LEVEL

Office of Naval Research
Order No. N00014-78-F-0004
Task No. NR 099-404

Final Report
October 1977 to September 1978

EXPERIMENTAL TWO-PHASE LIQUID-METAL MAGNETOHYDRODYNAMIC GENERATOR PROGRAM

by

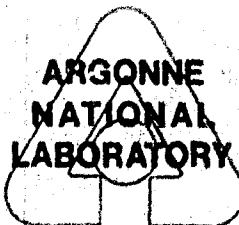M. Petrick, Project Scientist

G. Fabris

E. S. Pierson

A. K. Fischer

C. E. Johnson

P. Gherson

P. S. Lykoudis

R. E. Lynch

D D C

AUG 21 1979

ARGONNE NATIONAL LABORATORY

U of C-AUA-USDOE

Engineering Division

April 1979

79 08 20 092

Best Available Copy

ARGONNE NATIONAL LABORATORY
9700 South Cass Avenue
Argonne, Illinois 60439

FINAL REPORT.
October 1977 to September 1978

EXPERIMENTAL TWO-PHASE LIQUID-METAL
MAGNETOHYDRODYNAMIC GENERATOR PROGRAM

by

M. Petrick, Project Scientist

G. Fabris

E. S. Pierson

A. K. Fischer

C. E. Johnson

P. Gherson**

P. S. Lykoudis**

R. E. Lynch**

Engineering Division

April 1979

* Chemical Engineering Division, ANL
** Purdue University

TABLE OF CONTENTS

TABLE OF CONTENTS (Cont'd.)

TABLE OF CONTENTS (Cont'd.)

TABLE OF CONTENTS (Cont'd.)

LIST OF FIGURES

LIST OF FIGURES

LIST OF FIGURES

LIST OF FIGURES

LIST OF FIGURES

LIST OF TABLES

NOMENCLATURE

SYMBOL	DEFINITION
a	Electrode spacing
a	Electrode half length, Section V
a_i	Activity of species i
A	Aspect ratio, Section V
b	Magnetic flux density distribution fraction
B	Magnetic flux density
B_0	Magnetic flux density at $x = 0$, Section V
C'_d	Bubble parameter
D_b	Typical bubble length scale
E	Electric field intensity
f	Friction factor
F	Load factor, $V_L/u_\ell aB$
Fr	Froude number, Eq. III.1
h	Electrode half spacing, Section V
H	Enthalpy
I_e	End current
J	Current density
K	Slip ratio
L	Generator length
L_e	Magnetic field e-fold length
ℓ	Length of insulating vane(s)
$\dot{m}$	Mass flow rate
n	Number of insulating vanes
p	Pressure
P_{st}, P_{out}	Pressure in separator tank
P_e	Electrical power output
Q	Volumetric flow rate
R	Gas constant
Re	Reynolds number, $\rho u d/\mu$
R_e	Equivalent external resistance

SYMBOL	DEFINITION
R_i	Internal generator resistance
R_L	Load resistance
S	Entropy
T	Absolute temperature
u	Velocity
v	x-axis location of vane end closest to electrodes
$\dot{V}'$	Effective average volumetric flow rate, Section II.2
V_L	Load voltage
V_{oc}	Open-circuit voltage of equivalent circuit
w	Channel height parallel to B
W	Flow work
x, y, z	Axis parallel to flow, current, and magnetic field, Section V
x_i	Atom fraction of species i
z	Distance from inlet of channel
α	Void fraction
α'	Weighted average void fraction, Section II.2
γ	Surface tension
Γ_i	Surface excess of component i
δ	Total air gap length
δ^*	$\delta^* = \delta/h$
η_i	Generator isentropic efficiency
η_t	Generator turbine efficiency
λ	Half length of magnet pole piece
μ	Absolute viscosity
μ_i	Chemical potential of component i
ρ	Density
σ	Electrical conductivity
ϕ	Electric field potential

NOMENCLATURE

<div>

nerator resistance

ance

perature

tion of vane end closest to

verage volumetric flow rate,
2

e

t voltage of equivalent circuit

ght parallel to B

el to flow, current, and magnetic
ion V

on of species i

om inlet of channel

on

verage void fraction, Section II.2

sion

ess of component i

ap length

sentropic efficiency

urbine efficiency

of magnet pole piece

scosity

otential of component i

conductivity

ield potential

</div>

x   Mixture quality, $\dot{m}_g/(\dot{m}_g + \dot{m}_\ell)$

DEFINITIONS

NAME	SYMBOL	DEFINITION
Bubble Parameter	C_d'	Empirical 'drag coefficient,' based on experimental data, used to calculate slip force between gas and liquid.
Load Factor	F	Ratio of load (electrode) voltage to induced voltage, $V_L/u_\ell aB$.
Void Fraction	α	Ratio of volume occupied by gas to total volume, or flow cross-sectional area occupied by gas to total cross-sectional area.
Mixture Quality	x	Ratio of gas mass flow rate to total mass flow rate, $\dot{m}_g/(\dot{m}_g + \dot{m}_\ell)$.
Slip Ratio	K	Ratio of gas to liquid velocity.

SUMMARY

The experimental results presented herein satisfy one major goal in demonstrating the technical feasibility of two-phase LMMHD (liquid-metal MHD), i.e., operating an MHD generator at power densities equal to or above that anticipated for practical power systems. Power densities of up to 32 MWe/m^3 and efficiencies higher than 0.6 at high void fractions were attained for a small 20-kWe generator. Slip ratio data, and more-extensive pressure distribution and voltage profile data are also given.

Barium has been identified as an attractive additive for the generation of foams with NaK, and bismuth is a back-up for barium. A guiding hypothesis for understanding the phenomena contributing to foamability in liquid metal systems has been developed, and basic data on surface tension obtained.

A computer code has been developed that will calculate the electrical end loss for any insulating vane geometry and magnetic flux density distribution, a significant accomplishment. Initial studies with this code have shown that generator efficiencies in excess of 0.8 are attainable.

Initial measurements of local flow parameters in a NaK-nitrogen two-phase liquid-metal MHD generator, using hot-film and resistivity probes, are reported. Although the results are preliminary, there is evidence that large electromagnetic force densities have a significant effect on the size and distribution of the gas bubbles or voids.

All results are very encouraging for the development of large high-efficiency LMMHD generators.

I. INTRODUCTION

The two-phase LMMHD (liquid-metal MHD) generator combines experimental and analytical studies designed to increase understanding of the physical processes occurring in two-phase generators and to establish the limits of generator performance. For eight years this program has been sponsored by the Power Branch of the Office of Naval Research.

The generator experiments are conducted with an ambient-temperature NaK-N$_2$ test facility, consisting of a two-phase mixer, MHD generator, magnet, and required auxiliary loop equipment. The original facility, used in all tests through July 1975, has been described in Pittenger et al (1972). The revised facility, completed in 1977, is described in Petrick et al (1977). Earlier experiments on generators different geometries have been performed and the results presented in previous annual reports [Amend et al (1973), Petrick et al (1975), Petrick et al (1976), Petrick et al (1977), and Petrick et al (1978)].

Analytical models of the generator have been developed to aid in the basic understanding of the flow characteristics in the generator and to provide a (one-dimensional) computer code capable of predicting approximations of generator performance from such independent input parameters as flow rate, magnetic field strength, and geometry. This computer code and the semiempirical technique by which the bubble parameter (churn-turbulent drag coefficient) used in the determination of the interfacial slip ratio is characterized have been reported in detail [Amend et al (1973), Petrick et al (1970)].

The channel contours used in generator experiments are compared in Fig. I.1. The first channel (LT-1) was designed for a slip ratio of unity,
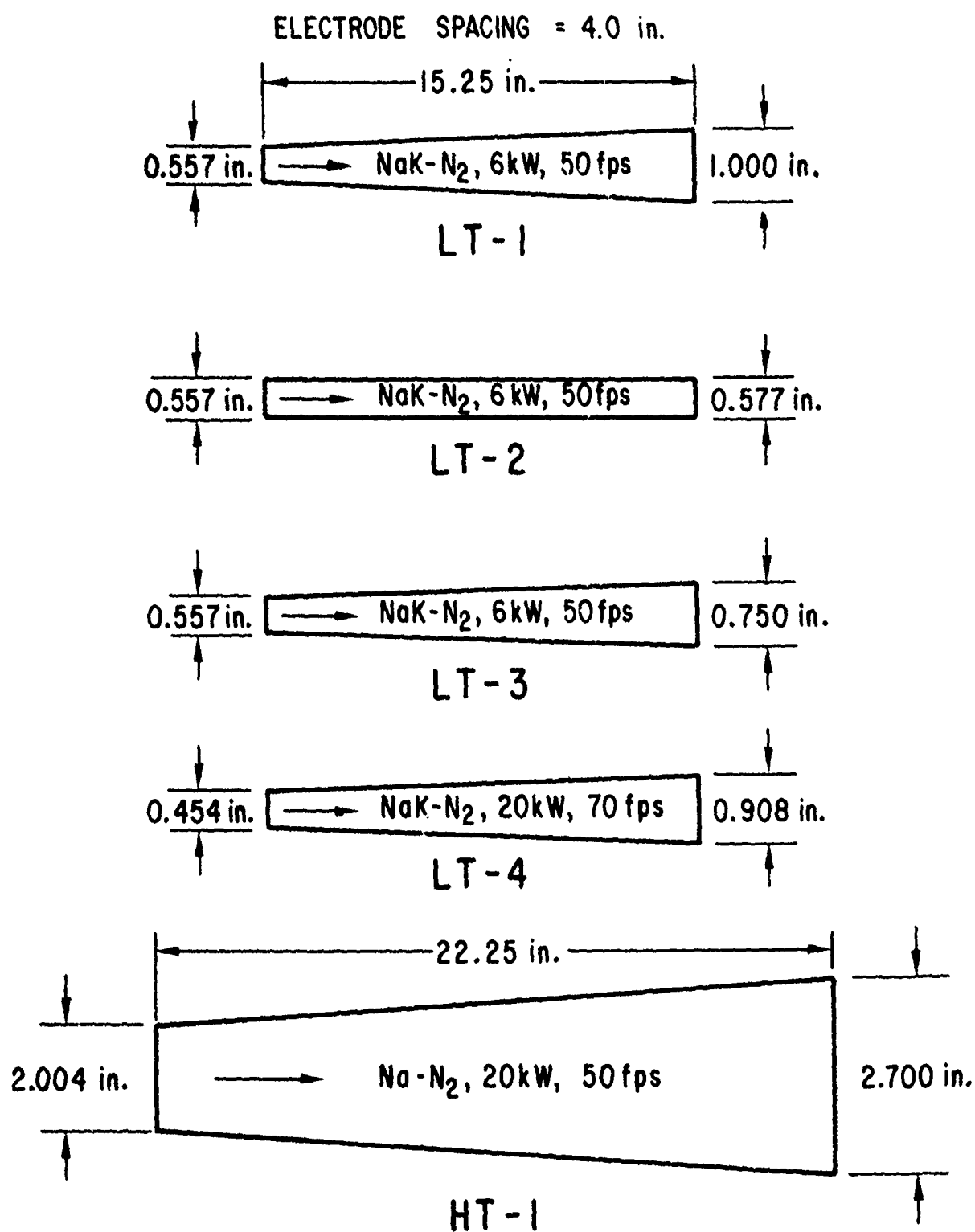
Figure I.1 Channel contours used in ANL LMMHD generator experiments

because the actual slip ratio was not known, but higher slip ratios were observed experimentally, and it was noted that the liquid velocity was not constant; it decreased along the generator [Amend et al (1973)]. A constant-area channel (LT-2) was then tested, and it was observed that the velocity increased along the channel [Amend et al (1973), Petrick et al (1975)]. The second diverging channel (LT-3) has a smaller angle than the first channel, as shown in Fig. I.1, to yield close-to-constant liquid velocity at the design point. As has been described [Petrick et al (1976), Petrick et al (1977)] improved generator performance was obtained with LT-3, and the liquid velocity was almost constant. LT-3 was also tested with the revised facility, and these tests demonstrated the expected reduction in slip ratio at higher liquid velocities (flow rates) [Petrick et al (1978), Fabris et al (1977a)]. The new high-pressure, high-velocity channel (LT-4) was designed to utilize the full NaK-nitrogen loop pressure and flow-rate capabilities, and test results are reported herein. The first channel for the high-temperature sodium-nitrogen test facility (HT-1) has been fabricated and tested at elevated temperatures under open-circuit conditions [Dunn et al (1979)].

The experimental and analytical aspects of the two-phase LMMHD generator program, with the exception of the high-temperature generator experiments, are described in Section II. The LT-4 test results, presented in detail in Section III, include the effects of liquid velocity on efficiency, power density, and slip ratio, and data on pressure distributions and voltage profiles. Further positive results on foams and surface-active agents are reported in Section IV. The results of an extensive analytical study of end effects are presented in Section V, and some initial data

-4-

on local measurements are summarized in Section VI. The conclusions drawn from the work presented herein are given in Section VII, and a brief review of the significant results from the eight-year program as a whole is in Appendix D.

II. PROGRAM

II.1 NaK-N$_2$ Generator Experiments

The NaK-N$_2$ ambient-temperature flow facility used for these tests has been described previously [see Petrick et al (1977)]. The contour of the new channel, LT-4, is compared with the other channel contours tested in Fig. I.1. This channel was designed for the higher pressures and flow rates of the revised facility and, thus, uses certain novel construction features. The channel contour is set by a filament-wound, fiberglass liner that forms the insulating walls and is relatively easy to replace. The liner was wound on a mandrel machined to the desired channel contour, and the exterior of the liner was then machined to the shape required to accept the copper electrode inserts and copper compensating bars. The copper structure absorbs all of the mechanical stress, the liner serves solely as the insulating channel walls. Because the liner is one piece, i.e., no glued joints, it is easy to seal the electrodes and end flanges to it with O-rings; thus, no leakage occurs.

The internal contour of the channel was designed, as for all previous two-phase MHD generator channels, using the generator portion of the system code described in Appendix A of Petrick et al (1970). In that code, the mass, momentum, and energy balances are solved in a stepwise fashion along the channel. The liquid velocity is held constant (constant u_ℓ gives constant induced voltage for constant B, and minimizes the internal circulating currents and losses), an ideal gas and perfect heat transfer* between

---

* See Petrick et al (1978) or Fabris and Pierson (1978) for experimental confirmation of this heat transfer.

the gaseous and liquid phases are assumed, and the liquid and gas properties are calculated at each step. The channel dimensions and powers are calculated for specified inlet conditions and outlet void fractions. The code can handle different working fluids (a version exists for steam in place of an ideal gas), different models for the two-phase electrical conductivity, and either no slip between the phases or a slip model with a bubble parameter, C_d' , that is an input va. able.

The contour calculate for the generator design conditions is shown in Fig. II.1 (note the expanded channel height scale). The bubble coefficient $C_d' = 2000$ m^{-1} was used for the design, based on the analysis of the most-recent LT-3 experiments. The extra expense of machining the calculated contour onto the liner mandrel was rejected as unnecessary; thus the two straight-line segments shown in Fig. II.1 were used. (Previous channels used only one straight-line segment, but they had much less divergence.) The straight-line segments were extended to the ends of the liner, 0.038 m (1.5 in.) outside of the electrodes.

The diagnostics for the experiment were improved for LT-4. The eight pressure transducers used previously along the electrode side of the channel and end regions were replaced by seventeen transducers, and eight transducers were added to the insulating side in the end regions just outside of the magnet pole face (four at the inlet, four at the exit). The six void fraction windows spaced along the channel were retained, and two each added in the entrance and exit sections. Three sets of eight voltage probes spaced between the electrodes, i.e., across the insulating wall, were incorporated, as used previously in LT-2. The sets are located 0.0127, 0.1937, and 0.3620 m downstream of the beginning of the electrodes.
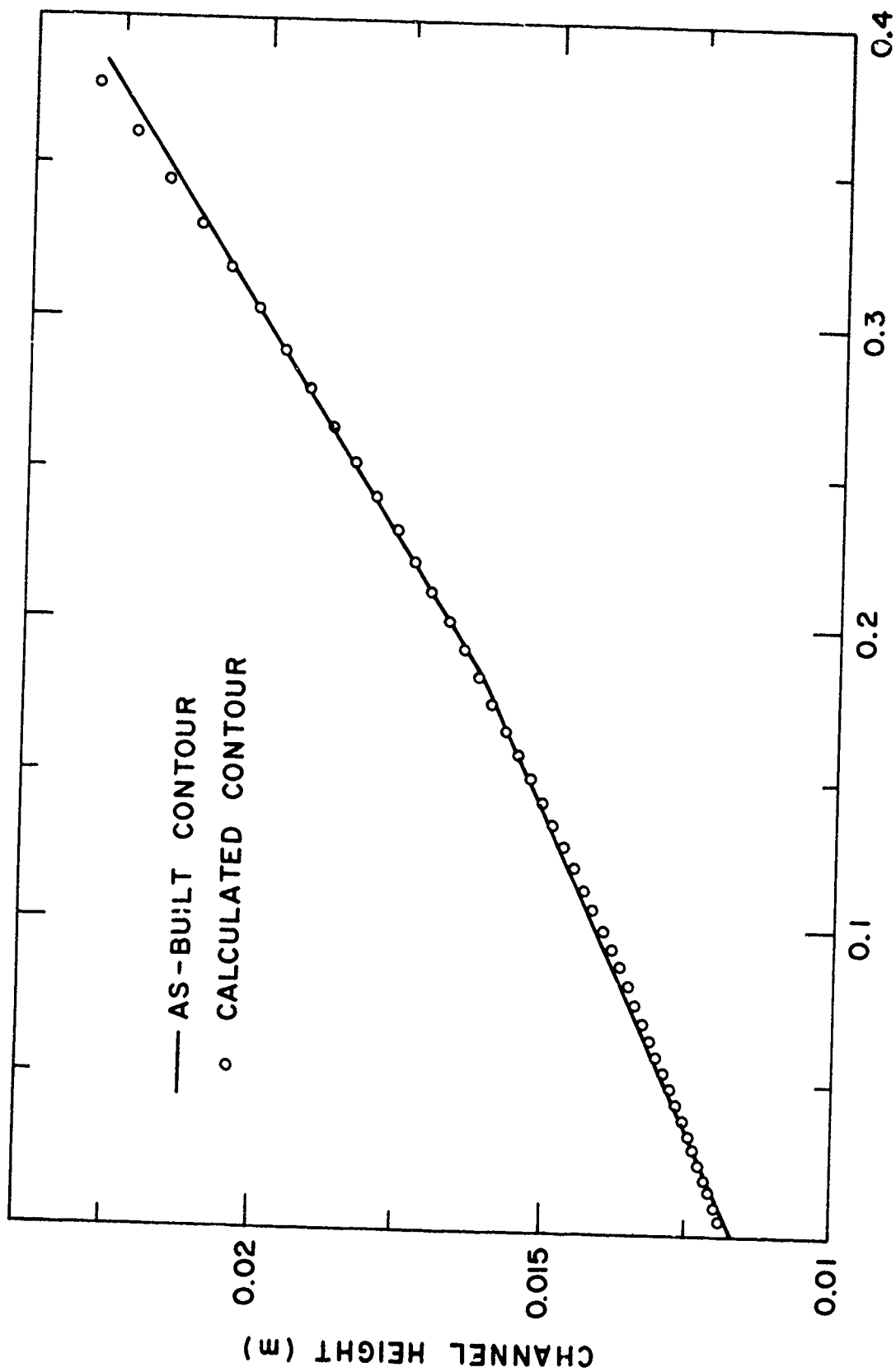
Figure II.1   Calculated and as-built channel heights for LT-4

DISTANCE ALONG GENERATOR (m)

CHANNEL HEIGHT (m)

— AS-BUILT CONTOUR
○ CALCULATED CONTOUR

-8-

The experimental data measured with LT-4 channel are discussed in Section III, and the significant parameters for all of the experimental runs from October 1977 to December 1978 are summarized in Appendix A. Significant results include the higher efficiencies obtained at higher liquid flow rates, the high power densities measured (comparable to or larger than those anticipated for large, practical LMMHD generators), and the reduction in slip into the liquid mass flow rate is increased.

II.2 Generator as Part of a Thermal Engine

In practically all thermal engines, only a gas (vapor) is used as the working fluid that, by its expansion, converts thermal to mechanical (or electrical) energy. In the two-phase LMMHD generator, the mechanical energy of the liquid is also converted to electricity. However, this does not represent the conversion of thermal energy, and the liquid mechanical energy must be replaced elsewhere in the cycle. Accordingly, instead of the generator isentropic efficiency

$$n_i = \text{electrical power output/isentropic power input}, \qquad (11.1)$$

a generator "equivalent turbine" efficiency

$$n_t = \frac{\text{electrical power out-ideal liquid mech. pump work}}{\text{isentropic power in-ideal liquid mech. pump work}} \qquad (11.2)$$

can be defined to characterize the LMMHD generator as a thermal energy converter. Note that n_t is useful in interpreting experimental generator performance because the liquid work is eliminated, a positive value shows that the electrical power out exceeds the ideal liquid pump work. However, n_i is used in system performance studies because the liquid pump work and flow losses are properly accounted for. The isentropic power input minus the ideal liquid mechanical pump work represents the contribution resulting from the presence of the gas. Note that the contribution of

-9-

the gas is much larger, because of the heat transferred to the gas from the liquid metal, than just the change in gas enthalpy, which is small because of the small temperature change across the generator. The specific expressions for each of these quantities are developed in Appendix B.

The equivalent turbine efficiency can be more easily interpreted in the following manner. The isentropic power input, ΔH_{mix}, can be written as

$$\Delta H_{mix} = \int \dot{V}_{mix} dp = (\dot{V}'_{\ell} + \dot{V}'_{g})\Delta p; \tag{II.3}$$

where $\Delta p = p_{in} - p_{out}$ is the pressure differences across the generator, and $\dot{V}'$ is the effective average volumetric flow rate such that $\dot{V}'\Delta p = \int \dot{V} dp$ for each component. In Eq. II.3, $\dot{V}'_{\ell}\Delta p$ is the ideal (isentropic) liquid mechanical pump work, and $\dot{V}'_{g}\Delta p$ represents the mechanical energy contribution from the gas. Note that the latter is not the enthalpy change of the gas (most of the energy actually comes from the temperature change of the liquid), but is the extra isentropic power available from the mixture because of the presence of the gas and the heat transfer from the liquid to the gas. If the weighted average mixture void fraction is defined as

$$\alpha' = \dot{V}'_{g}/(\dot{V}'_{g} + \dot{V}'_{\ell}), \tag{II.4}$$

it follows that

$$\dot{V}'_{\ell}\Delta p/\text{isentropic power input} = 1 - \alpha' \tag{II.5}$$

and

$$\dot{V}'_{g}\Delta p/\text{isentropic power input} = \alpha' \tag{II.6}$$

The resultant relations between "equivalent turbine" efficiency, isentropic efficiency, and weighted void fraction are shown in Figs. II.2 and II.3 for assumed isentropic efficiencies of 0.90 and 0.50, respectively. One notes that, when α' exceeds $1 - n_i$ the electrical power output exceeds the pump work input and the "turbine efficiency" is positive. Further, at high void fractions n_t approaches n_i.
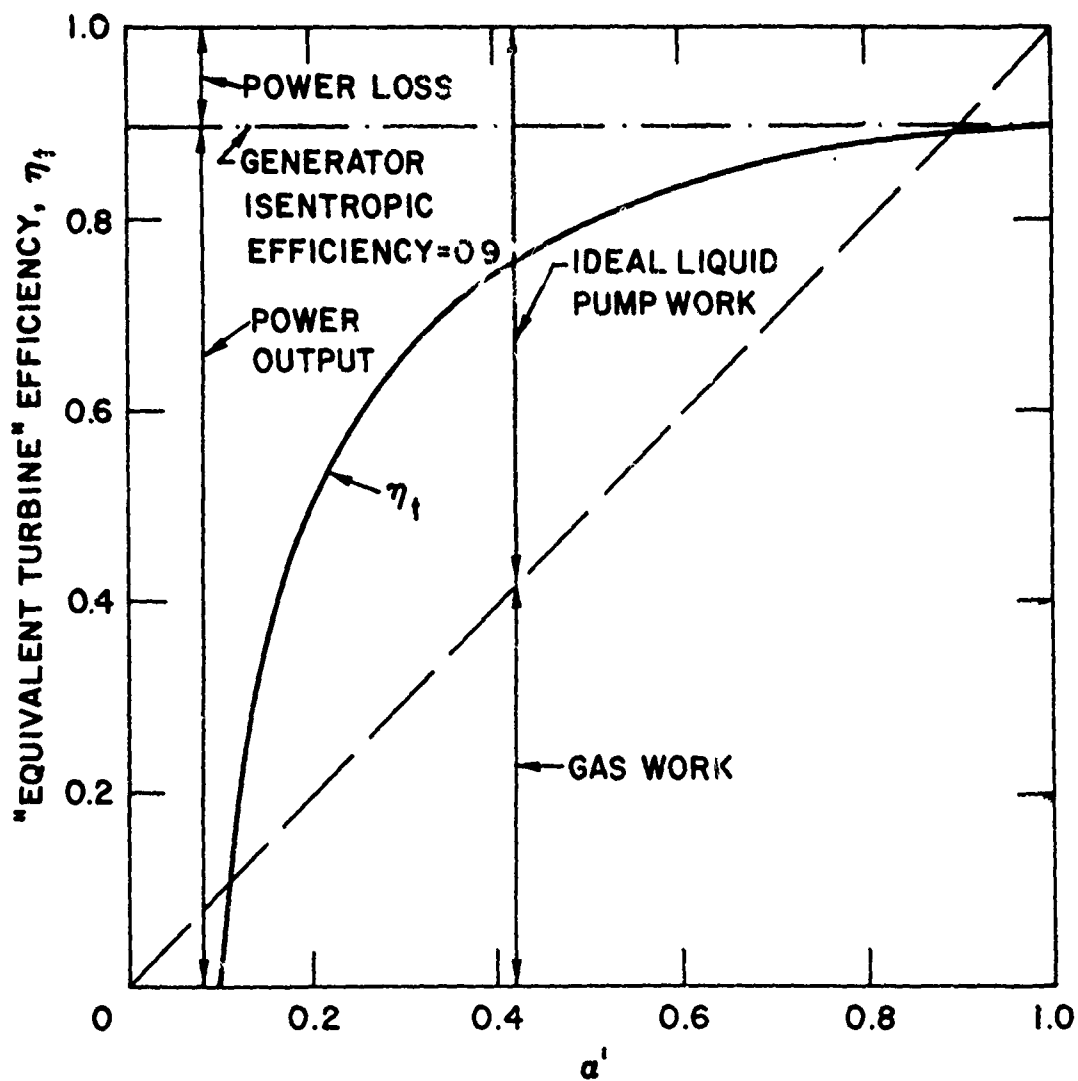
Figure II.2 "Equivalent turbine" efficiency vs weighted mixture void
fraction for a generator isentropic efficiency of 0.9
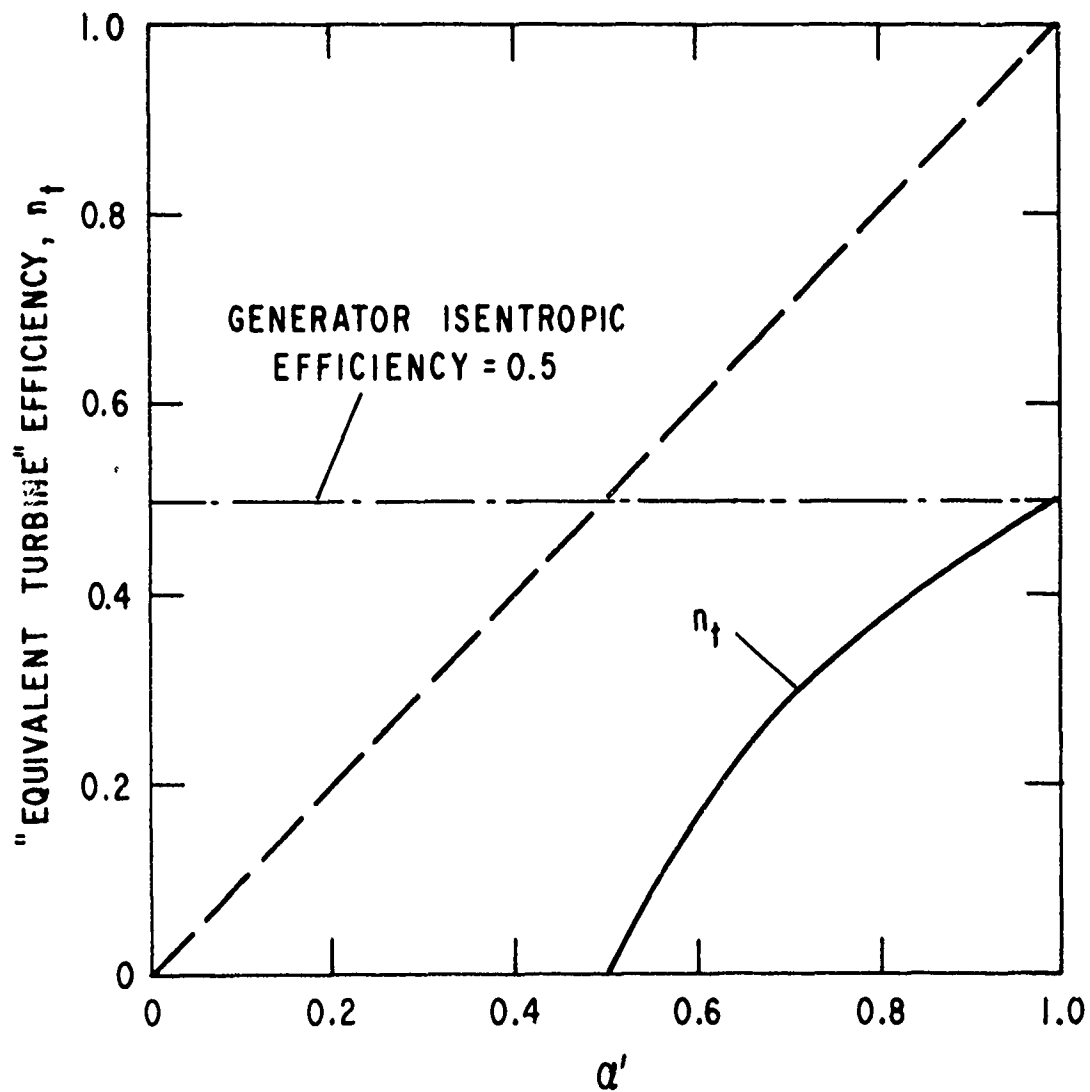
Figure II.3 "Equivalent turbine" efficiency vs weighted mixture void
fraction for a generator isentropic efficiency of 0.5

Experimental data for the LMMHD generator experiments can be recast in terms of η_t, Table II.1, shows that the net electrical output exceeds the net pump work input at higher void fractions, with only a slight departure from isothermal operation. The "equivalent turbine" efficiencies are low for these cases because of the low generator efficiencies and low average void fractions, but are consistent with Fig. II.3. With operation at higher average void fractions (such as foam flow), much higher isentropic and turbine efficiencies are expected, Fig. II.2. Note that the temperature difference along the generator is not measured directly, but is calculated from the experimental data using Eq. B.8, Appendix B.

TABLE II.1

Experimental Data for "Equivalent Turbine" Efficiencies

Run	8/18/ 76-2	8/18/ 76-3	2/17/ 77-6	2/18/ 77-7	7/12/ 78-1	11/29/ 78-3
Average α	0.59	0.68	0.64	0.70	0.61	0.58
Net Pump work (W)	2566	2544	1673	881	9760	5550
Electrical power out (W)	3205	3764	4214	4554	21600	12500
ΔT generator (K)	0.4	0.6	0.5	0.6	2.2	2.2
η_i	0.464	0.430	0.524	0.530	0.606	0.487
η_t	0.147	0.197	0.399	0.476	0.457	0.346

II.3 Foams

The most significant advance of the year in the surfactant program was the discovery that barium markedly stabilizes bubble lifetime and promotes foaming in a NaK alloy. A number of other systems were also tested, but none yielded beneficial effects approaching those of barium. Bubble tests and surface tension measurements proceeded in parallel, with the surface tension data yielding the scientifically interesting information that barium raises the surface tension at concentrations effective for bubble stability. Exploration of this finding leads to the development of a guiding hypothesis for understanding the phenomena contributing to foamability in liquid metal systems. This hypothesis invokes a tendency for attractive interatomic interactions to enhance film elasticity and, hence, bubble stability. The extent of the applicability of this hypothesis can only be determined by more detailed laboratory studies. Details of all aspects of the work are reported in Section IV.

NaK was chosen for these initial experiments because it allows room temperature tests, eliminating the special problems associated with handling hot liquid metals. Thus, the concept of using surface-active agents in MHD generators can be evaluated more rapidly and inexpensively with NaK, the existing NaK facility is available for future flow tests, and a generator of known performance properties with pure NaK will be available to observe the changes with a foam.

II.4 Local Measurements*

The operation of two-phase LMMHD generators depends on the processes occurring at the local level, i.e., interactions between the gas bubbles and the liquid metal. To date, however, all reported experiments have measured only gross or terminal parameters (voltage, current, pressure) or averages over (part of) the channel (pressure, void fraction). To obtain a better understanding of the local processes, the generator experiments have been expanded to include some local measurments. Both hot-film and resistivity probes were tested in the previous channel, LT-3. The initial results, reported in Section IV, give evidence that large electromagnetic force densities have a significant effect on the size and distribution of the gas bubbles or voids.

II.5 Analytical Studies

II.5.1 End Effects

End effects in LMMHD generators can be a significant loss mechanism, particularly because the coupling between increased terminal voltage and increased end loss limits the attainable voltage in high-efficiency generators. A computer code has been developed that will calculate the electrical end loss (fringing currents) for any insulating vane geometry and magnetic flux density distribution, a significant accomplishment. The development of the code and some initial results are presented in Section V, and the code is described in Appendix C.

II.5.2 Imperfect Compensation

Unless compensation is provided for the induced magnetic field caused by the currents in the conducting fluid, the total magnetic field varies exponentially along the channel and, for a generator, most of the energy conversion occurs in the downstream end of the channel. The result is a reduced generator efficiency. (A similar phenomenon, called armature reaction, occurs in dc rotating machines.) To eliminate the induced field or compensate the generator, the fluid current is returned through the air gap of the electromagnet. If the compensation is perfect, i.e., the return current is at the same axial location as the fluid current, the induced field lies along the flow and has no effect on the generator. However, because of both the end currents and the varying fluid properties and velocity along the flow, the compensation will be imperfect, as has been shown experimentally [see Petrick et al (1976)]. The objective of this analytical study is to model the distortion in the magnetic field caused by imperfect compensation and assess the consequent effect on generator performance.

The study has been divided into a one-dimensional model and a two-dimensional model. In the one-dimensional model, each vector quantity has only one component, which is a function only of axial position. In the two-dimensional model the magnetic flux density and magnetic intensity have two components that are functions of two variables, whereas all other vector quantities have one component that is a function of one variable. The one-dimensional model is restricted to infinitely-permeable iron and is used to indicate general trends, whereas the two-dimensional model considers real-iron effects.

-16-

The solution of the nonideal compensation problem can be reached to the solution of two subproblems, 1) the determination of the current distribution in the air gap caused by a given magnetic flux density distribution, and 2) the determination of the magnetic flux density produced by a given air gap current distribution.

The whole solution is achieved by iterating between two subproblem solutions. To start, the applied magnetic field is assumed to be the total field and the current distribution for that field is calculated (using the circuit model described below). The magnetic field produced by the current distribution is then calculated and compared to the field used to calculate the current distribution. If the difference is not within acceptable tolerances for a solution (specified input), the calculated magnetic field is used to determine a new current and field distribution. This new field is compared to the field calculated in the previous iteration, and the iteration process is continued until the field converges to a solution.

The subproblem of the current produced by a given magnetic field is best considered by using a circuit model to include the effects of the external circuit connections. Both the one- and two-dimensional models use the same circuit model. The channel is divided into a number of sections, and the magnetic field and current density are assumed constant over each section. The compensating bar is also divided into a number of sections, not necessarily the same number as in the channel. The end resistances are estimated from a theoretical model, assuming that a specified percentage of the end currents from the model are eliminated by insulating vanes or field overhang. The electrodes can be modeled

as real conductors by considering the resistance in the electrodes between the channel sections. An example of the circuit model for five channel sections and five compensating bar sections is shown in Fig. II.4. The known magnetic flux density determines the generated voltages, and the circuit model is solved for the currents in the channel and compensating bar sections, using the fundamental tie-set matrix, a standard method of circuit analysis.

The second subproblem, the determination of the magnetic flux density produced by a given air-gap current distribution, is handled differently in the two models. The magnetic field is determined directly from Ampere's law in the one-dimensional model but, in the two-dimensional model the magnetic vector potential is calculated by using the magnet design code, TRIM, which also considers nonlinear iron relationships.

Codes for the one-dimensional and two-dimensional models have been written in PL/1 and have been debugged. These codes are now being used to run parameter sweeps.
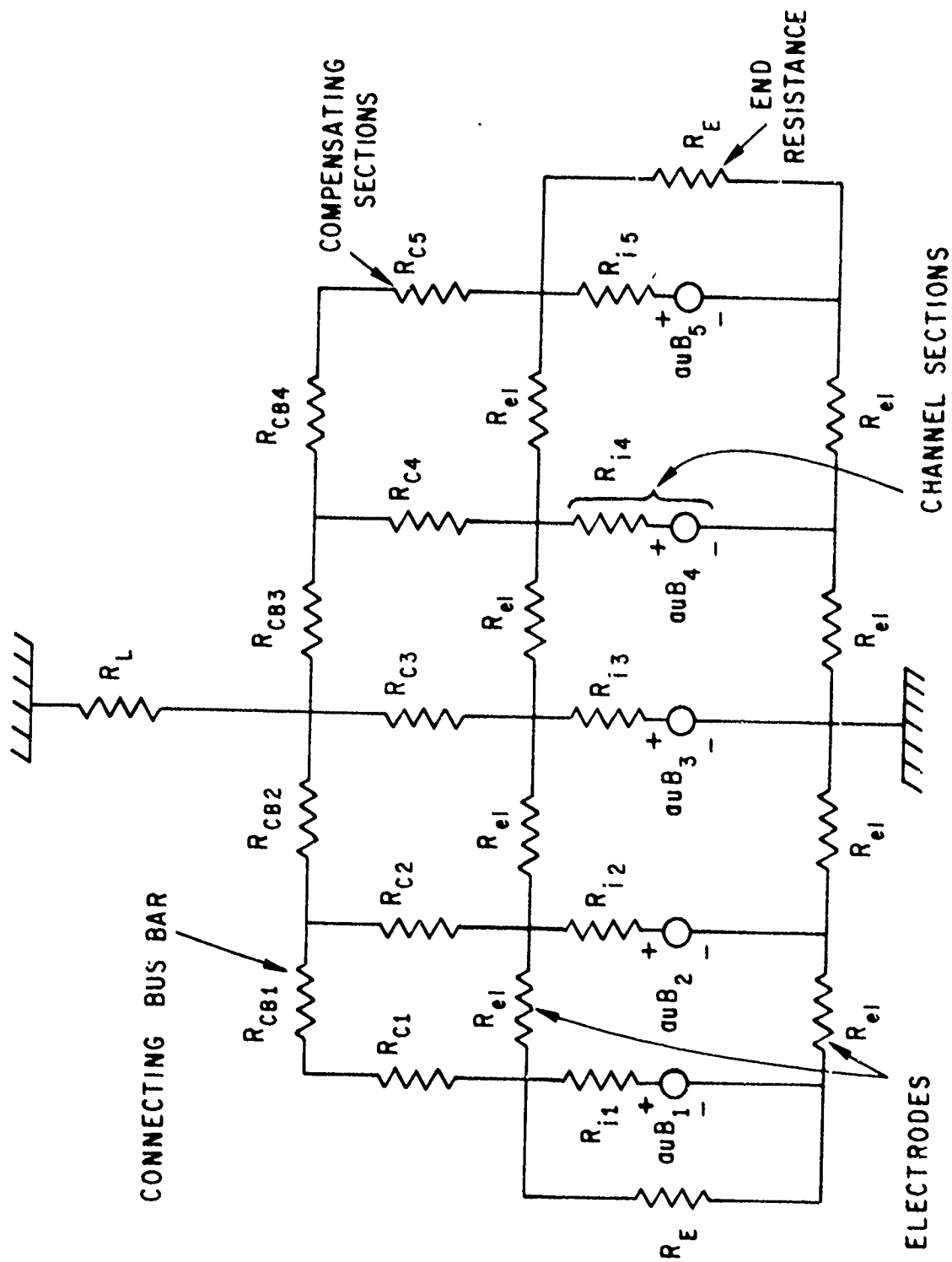
Figure II.4 Circuit model for imperfect compensation, five sections

III. GENERATOR PERFORMANCE

The data presented here includes all that obtained with the LT-4 channel. In contrast to the recent data reported for LT-3 [see Petrick et al (1978)], the LT-4 channel allowed operation at high velocity and high pressure (high magnetic flux density) and, thus, generator operation was extended to significantly-higher power densities. The emphasis in the following data is on high-power-density operation, but comparisons with previous LT-3 low-power data are given as appropriate. The measured efficiencies and power densities are discussed in Sections III.1 and III.2, respectively. The slip ratio data, pressure distributions, and voltage distributions are presented in Sections III.3, III.4, and III.5, respectively. A summary of all of the experimental data for the period October, 1977 to December, 1978 is given in Appendix A.

III.1 Efficiency

The generator isentropic efficiency is plotted in Fig. III.1 for all LT-4 data with R_L = 0.4 mΩ, B = 1.2 T, and a separation tank pressure of p_{st} = 0.14 MPa gauge (20 psig). Measurements were made for liquid flow rates, $\dot{m}_\ell$, of 3, 6, 9, and 12 kg/s. The emphasis was on obtaining high average void fractons, $\bar{\alpha}$, and the data were very encouraging, because the efficiency remained high at the high void fractions. (High generator average void fractions are necessary for good system performance or equivalent turbine efficiency, see Section II.2.) The efficiency increases sharply with increasing liquid flow rate (velocity), as anticipated, because of the reduced slip ratio (ratio of gas velocity to liquid velocity). There is only a single point at 12 kg/s because some experimental difficulties
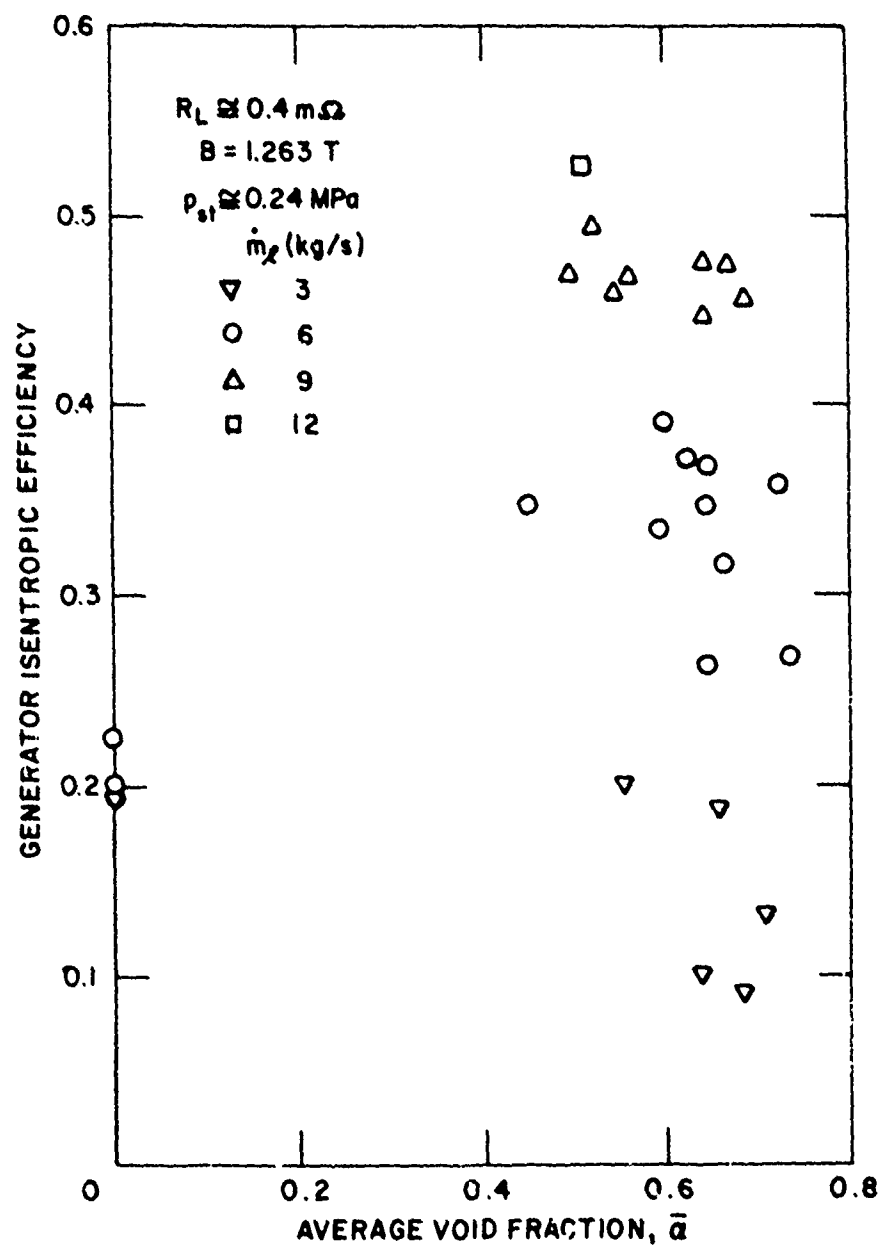
Figure III.1   Influence of flow rate on generator
efficiency, R_L = 0.4 mΩ

-21-

occurred with the resulting high gas flow rate (above the facility design value). Some of the lower-efficiency data points at 3 and 6 kg/s were obtained with very high gas flow rates, and this probably resulted in transitions to semiannular flow with high slip ratios (see Section III.3 and Appendix A)

The generator isentropic efficiencies measured with LT-4 are compared with similar data for LT-2 and LT-3 in Fig. III.2, all measured for R_L = 0.25 mΩ, B = 1.2 T, and p_{st} = 0.14 MPa gauge. Note that there is no data for $\dot{m}_\ell$ greater than 6 kg/s for LT-2 and LT-3 at B = 1.2 T, because the older channels were not designed for the higher pressures required. The efficiencies for LT-3 and LT-4 at $\dot{m}_\ell$ = 6 kg/s and high void fractions are in very good agreement. This is in spite of the different taper for the two channels and the fact that LT-4 is operating far off design conditions, and indicates that efficiency is not strongly sensitive to off-design operation. (At α = 0 the efficiency for LT-4 is significantly lower, because the larger taper or cross sectional area change results in increased circulating currents and losses, and, for the LT-3 case, there was flow separation, which significantly decreased the circulating currents.)

The higher liquid flow rates, $\dot{m}_\ell$, for LT-4 resulted in substantial increases in efficiency at the higher void fractions, see Fig. III.2, and efficiencies in excess of 0.60 were measured for $\bar{\alpha}$ greater than 0.5. This justifies the effort in extending the experiments to higher liquid flow rates (velocities) and pressures. To place these efficiencies in perspective, they were obtained with a small generator (approximately 20 kWe) that is basically wall limited, used ordinary NaK without any surfactive agent (see Section IV), and had no provision for insulating vanes or a special field profile to minimize end loss (see Section V). Thus, these

-22-
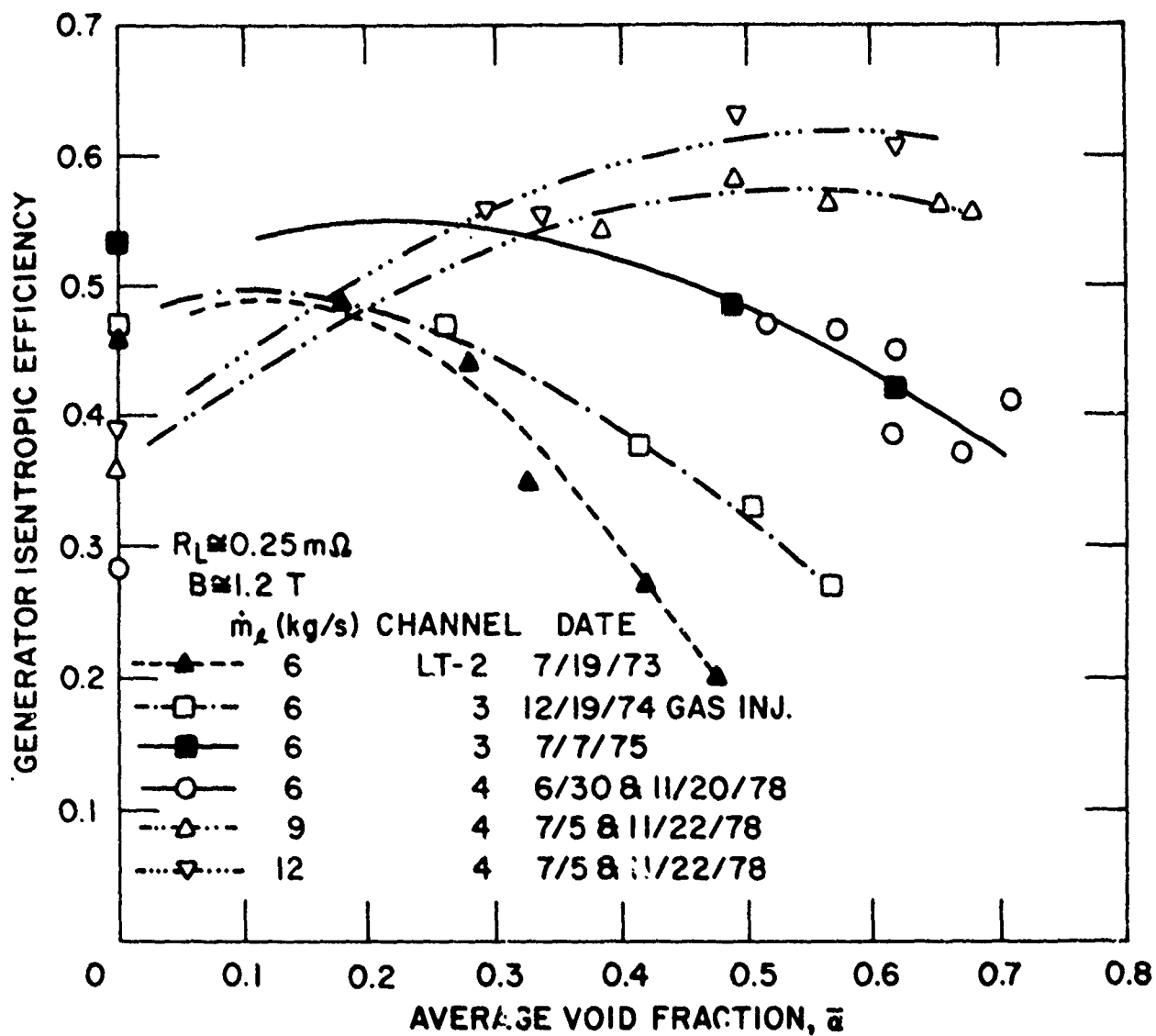
Figure III.2   Generator efficiency for LT-2,
LT-3, and LT-4, R_L = 0.25 mΩ

results present very encouraging evidence that large LMMHD generators can be built with efficiencies of 0.8 or higher.

III.2 Power Density

Power density, i.e., electrical power output per unit volume, in LMMHD generators is important because higher power densities mean smaller generators, which are cheaper to build and easier to integrate into the power plant, smaller and less expensive magnets, and reduced heat losses. In testing small LMMHD generators, it is important to reach power densities typical of those anticipated for large, practical generators, so that a comparable degree of electromagnetic interaction is obtained, thus minimizing the chances of encountering unanticipated problems in scaling to larger generators.

The electrical power output and power density for the R_L = 0.25 mΩ data are shown in Fig. III.3. The power density (and power) are proportional to the velocity squared and, thus, increase rapidly with increasing $\dot{m}_\ell$. The maximum power output, 21.6 kWe, corresponds to a power density of 31.8 MWe/m^3 at an average liquid velocity of 22.4 m/s. This is probably the highest power density obtained to date for any MHD generator that operated continuously for more than one minute. For comparison, the LMMHD generator design for the ECAS study had a power density of 11.1 MWe/m^3 at $\bar{\alpha}$ = 0.75 and a velocity of 30.5 m/s.

III.3 Slip Ratio

As described in the previous report [Petrick et al (1978)], the two-phase slip ratio is expected to decrease with increasing magnetic Froude number, defined as the ratio of the inertial to the Lorentz forces, or
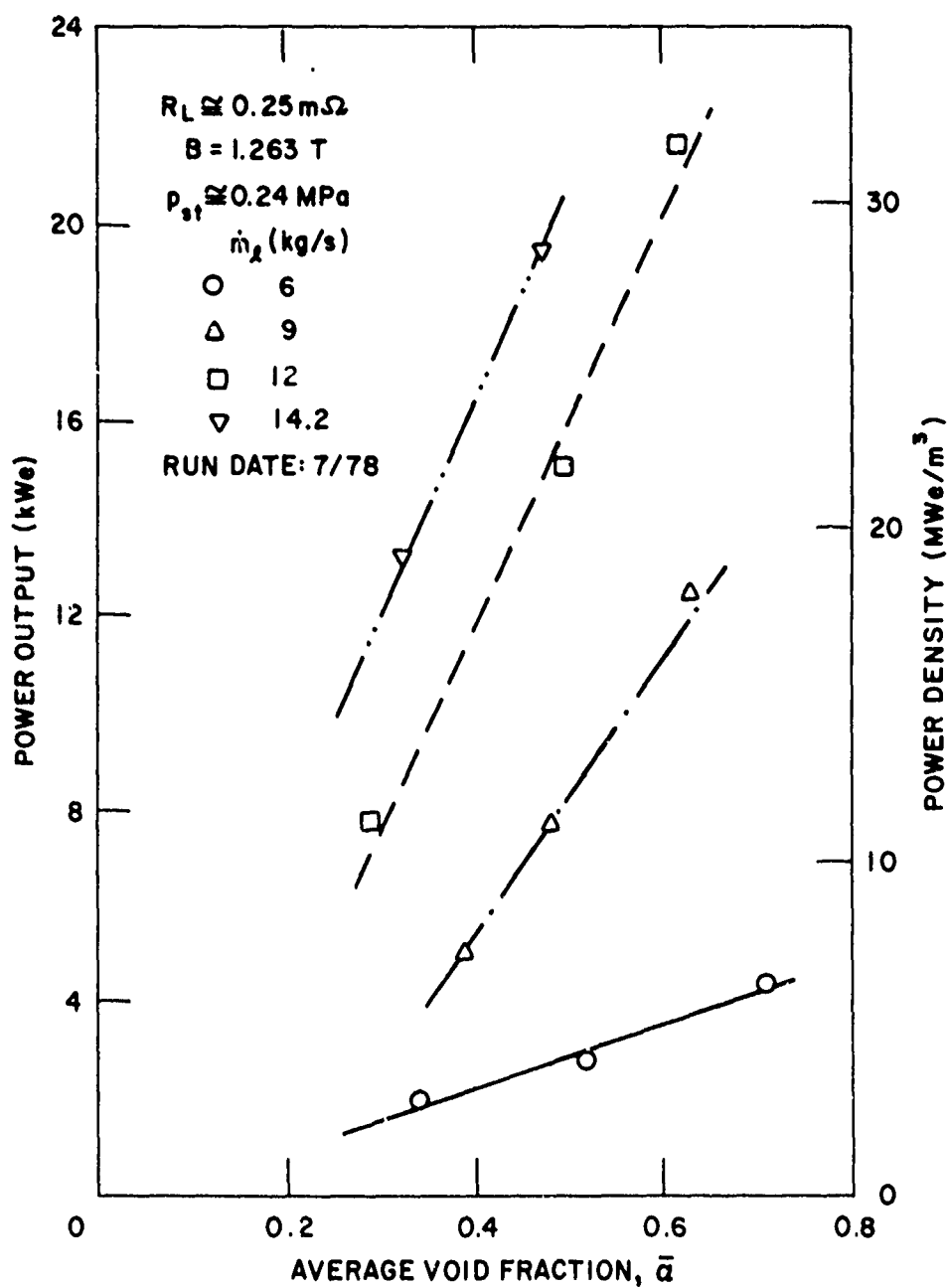
Figure III.3 Generator power output and power density, $R_L = 0.25$ mΩ

$$Fr_M = \frac{\rho_\ell u_\ell^2}{\sigma u_\ell B^2 (1 - F) D_b} \cdot \qquad\qquad (III.1)$$

Here, ρ_ℓ is the liquid density, u_ℓ the liquid velocity, σ the electrical conductivity of the two-phase mixture, B the magnetic flux density, F the load factor (ratio of terminal voltage to generated voltage), and D_b the typical bubble-length scale. From Eq. III.1, Fr_M increases as u_ℓ increases, and the resulting decreases in slip ratio and slip loss are the primary motivations for operating the LMMHD generator at higher liquid flow rates (velocities) and pressures. (The use of surfactants and foams, Section IV, will have a similar effect by decreasing the bubble size, D_b).

The average slip ratios, R, for all LT-4 data are shown as functions of $\bar{\alpha}$ and $\dot{m}_\ell$ in Figs. III.4 and III.5 for $R_L = 0.25\ m_\Omega$ and $0.4\ m_\Omega$, respectively. As $\dot{m}_\ell$ (or u_ℓ) is increased, R decreases and approaches unity (within the the accuracy of the experimental data).

The variation of R with $\dot{m}_\ell$ is shown in Fig. III.6 for $\bar{\alpha} = 0.54$ and 0.71. As $\dot{m}_\ell$ increases, R decreases very sharply, contributing significantly to the increase in generator efficiency with higher flow rates. The curve for $\bar{\alpha} = 0.71$ terminates at a lower $\dot{m}_\ell$ value, because of the facility design limitations. Note that similar results were reported previously [Petrick et al (1978) or Fabris et al (1977a)], but only at B = 0.6 T, a quarter of the present power density.

III.4 Pressure Distributions

The new generator channel, LT-4, was provided with 23 pressure transducers, rather then eight pressure gauges, as previously to provide
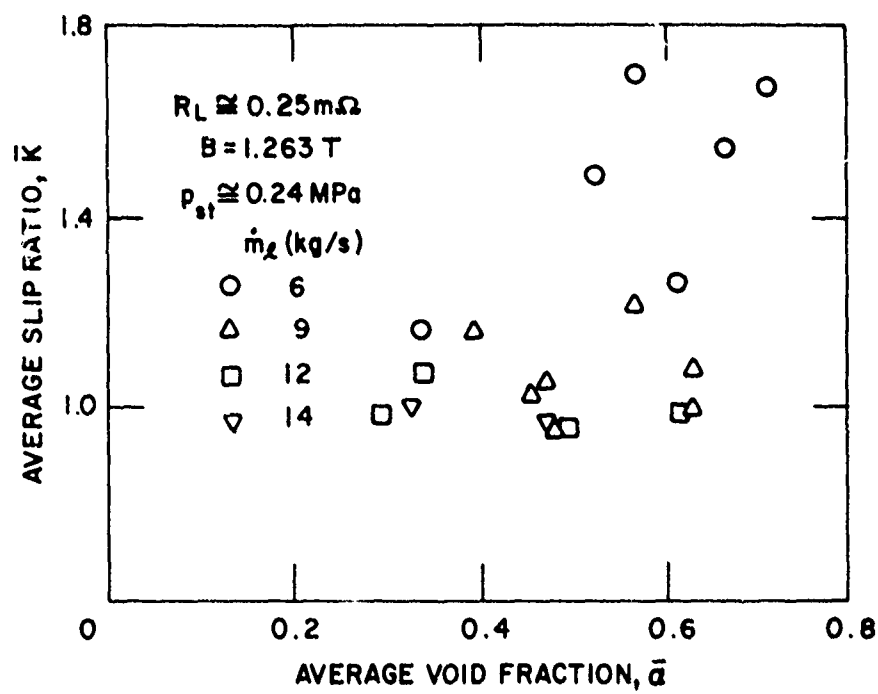
Figure III.4 Average slip ratio vs average void fraction, $R_L = 0.25$ mΩ
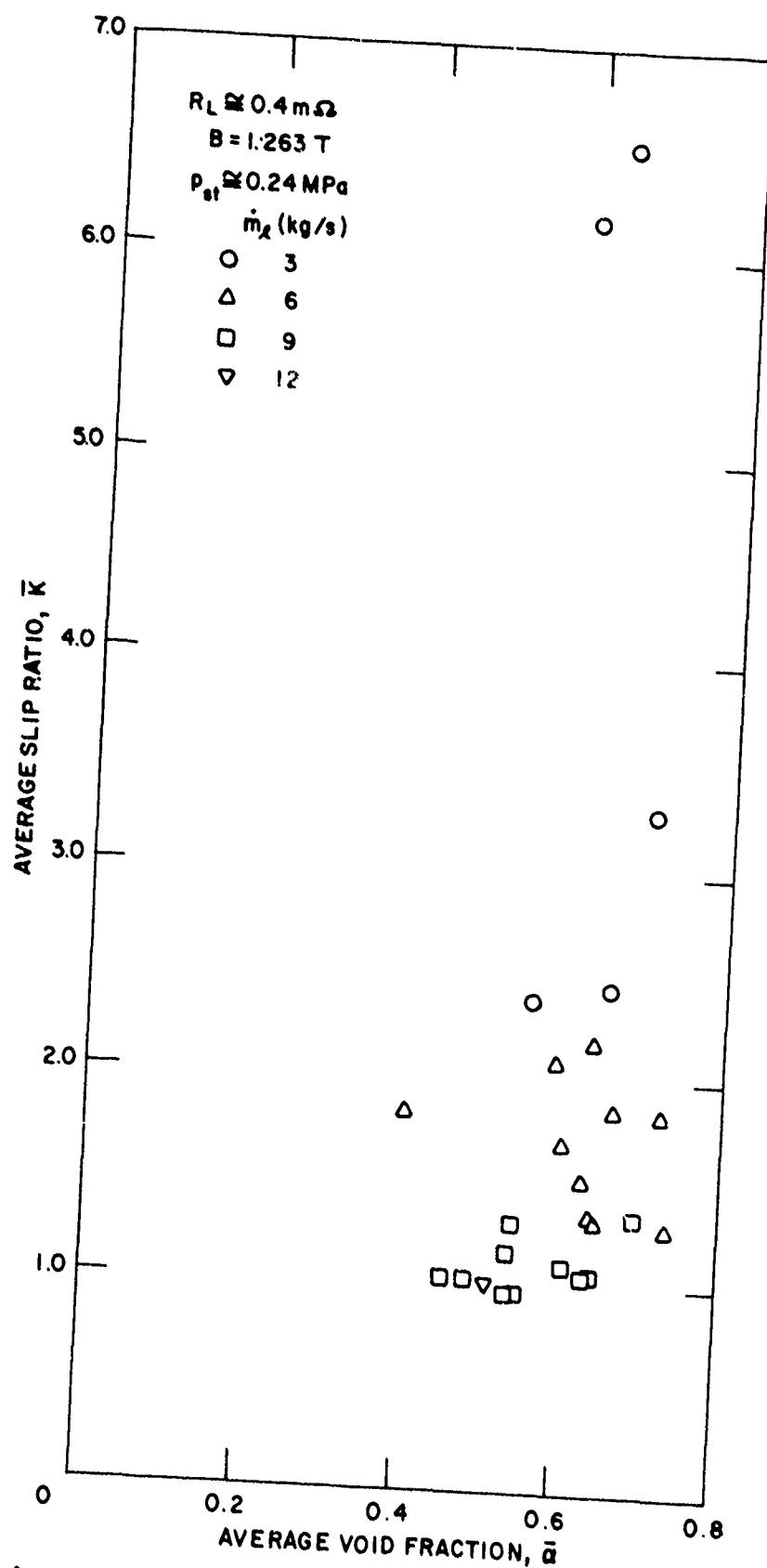
Figure III.5 Average slip ratio vs average void fraction, $R_L = 0.4$ mΩ

Figure III.6   Slip ratio as a function of liquid mass flow rate

A plot of VELOCITY SLIP RATIO, $\bar{K}$ (y-axis, from 0.6 to 3.4) versus LIQUID METAL FLOWRATE, $\dot{m}_\ell$ (kg/s) (x-axis, from 0 to 12).

$R_L \cong 0.4\,m\Omega$
$B = 1.263\,T$
$p_{st} \cong 0.24\,MPa$
$\bar{a}$
—◯— 0.54
– –△– – 0.71
RUN DATE: 7/78 + 9/78
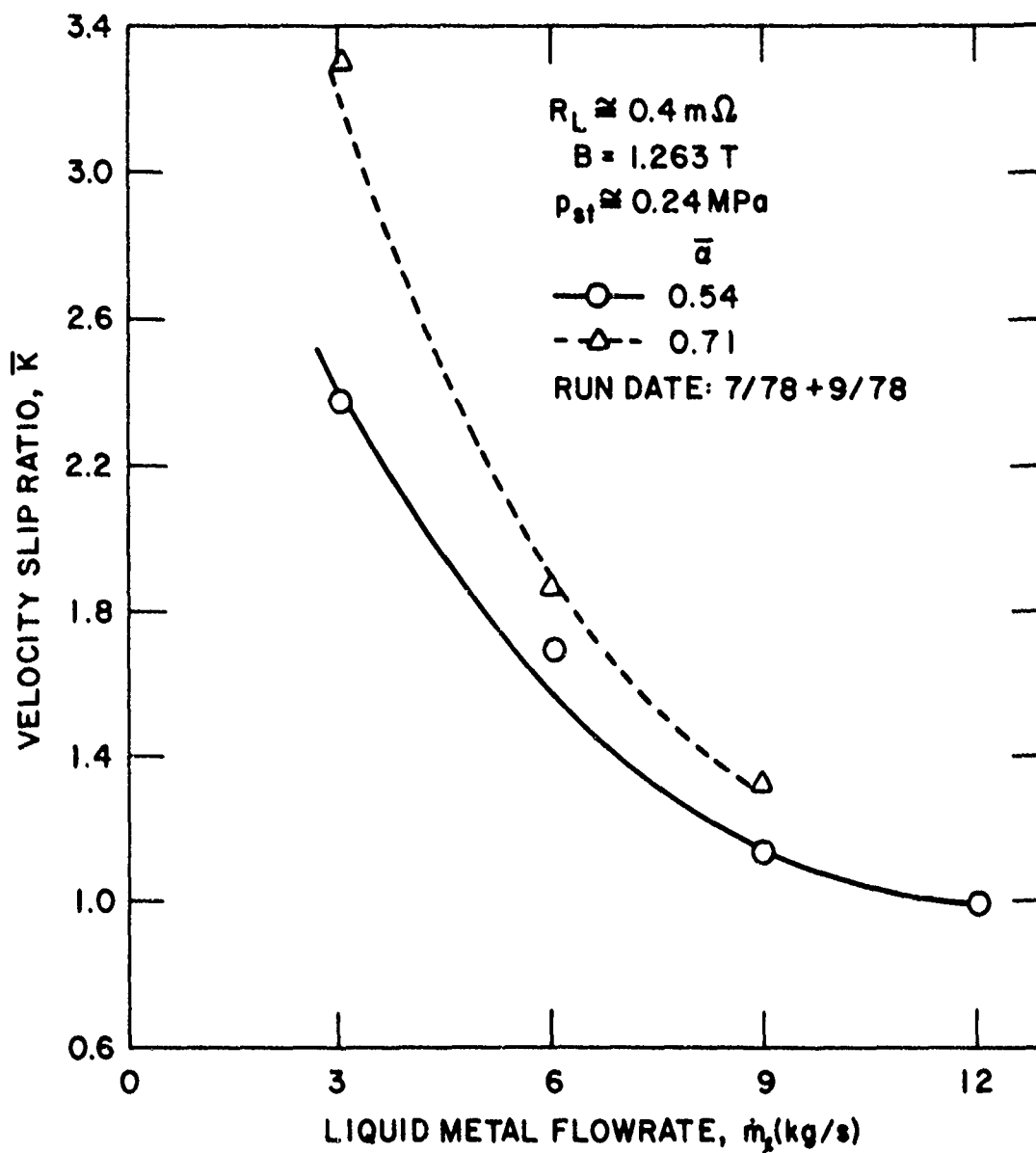
Figure III.6   Slip ratio as a function of liquid mass flow rate

additional information on the pressure distribution inside the generator channel. Seventeen transducers were spaced along the short (electrical) side of the channel, to provide a detailed picture along the generator length, including the end regions, and six transducers were located in the center of the wide (insulating) side of the channel just outside of the magnet, to provide information on the behavior in the end regions. The pressure behavior in the end regions is of interest because it is anticipated that the end currents circulating within the channel will cause the pressure to be higher in the center of the wide side than along the electrodes at the generator inlet, and this results in a higher velocity close to the electrodes, commonly referred to as M-shaped velocity profiles [see Branover (1974)].

The pressures for two pure-liquid runs are shown in Fig. III.7. Note the rapid pressure drop in the first portion of the channel and the pressure recovery near the downstream end; this is characteristic of pure-liquid MHD flows in a diverging channel. Circulating currents cause power generation near the inlet and pumping near the outlet for either loaded or open-circuit conditions. The pressure in the center of the wide side is higher than at the walls at the generator inlet by approximately 140 kPa (20 psi), a significant amount, so that M-shaped velocity profiles would be anticipated. Note that the use of insulating vanes to suppress end loss (circulating currents) will also suppress M-shaped profiles.

The pressures for two typical two-phase runs are shown in Fig. III.8. Note the relatively-smooth pressure decreases along the electrode length, and the pressure difference of up to approximately 100 kPa (15 psi) near the generator entrance. For two-phase flow, this pressure difference could cause some gas-liquid separation in addition to M-shaped profiles; again these would be suppressed by insulating vanes.
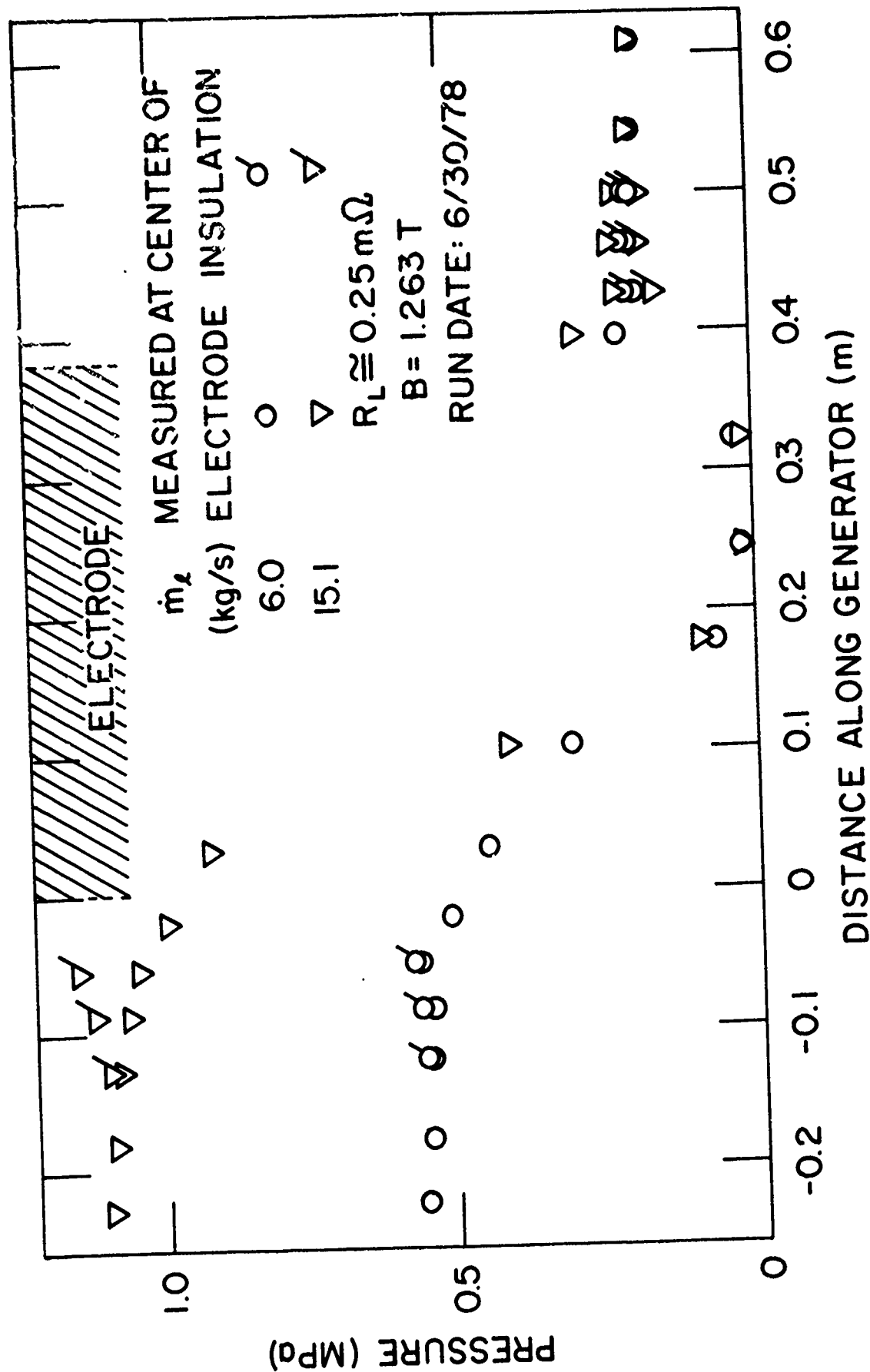
Figure III.7 Pure liquid pressure profiles along channel
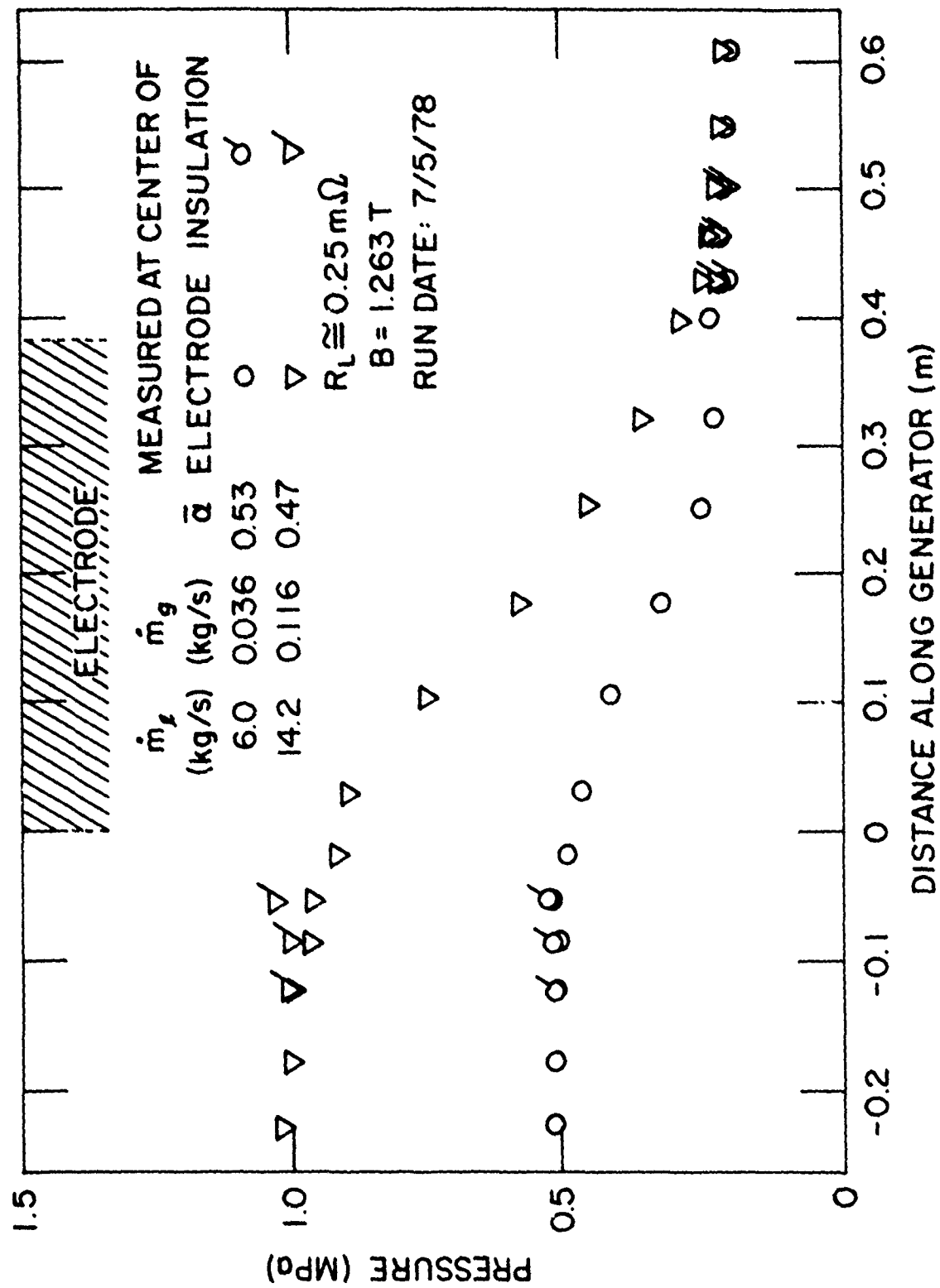
Figure III.8 Two-phase pressure profiles along channel

III.5 Voltage Profiles

Three sets of eight voltage probes were equally spaced between the electrodes to determine the voltage profiles across the insulating walls. The probes were mounted flush with the wall, and were located 0.0127, 0.1937, and 0.3620 m downstream from the beginning of the electrodes. To interpret the resulting voltage profiles, note that Ohm's Law can be written as

$$\frac{J}{\sigma} = u_\ell B - E . \qquad (III.2)$$

Because the load factor $F = E/u_\ell B$ is typically about 0.85, both $u_\ell B$ and E are large compared with J/σ, and the shape of the voltage curve between the electrodes is determined primarily by the variation of u_ℓ, rather than the variation of σ between the electrodes. Thus, the spatial variation of u_ℓ can be inferred from the voltage profiles.

One set of voltage profiles for pure liquid flow (Fig. III.9) shows convincing evidence for M-shaped velocity profiles, as expected from the pressure data for this case (Fig. III.7). The magnitude of the M-shaped variation seems to increase slightly along the channel. The reason for the asymmetry between the two sides is not known.

The voltage profiles for one two-phase case are shown in Fig. III.10. It is harder to interpret two-phase voltage profiles, because σ may vary. However, it appears that the voltage gradient is reduced close to the electrodes, perhaps because u_ℓ is reduced. (A decrease in σ, i.e., α, would have a similar effect.) Adjacent to the two regions of reduced
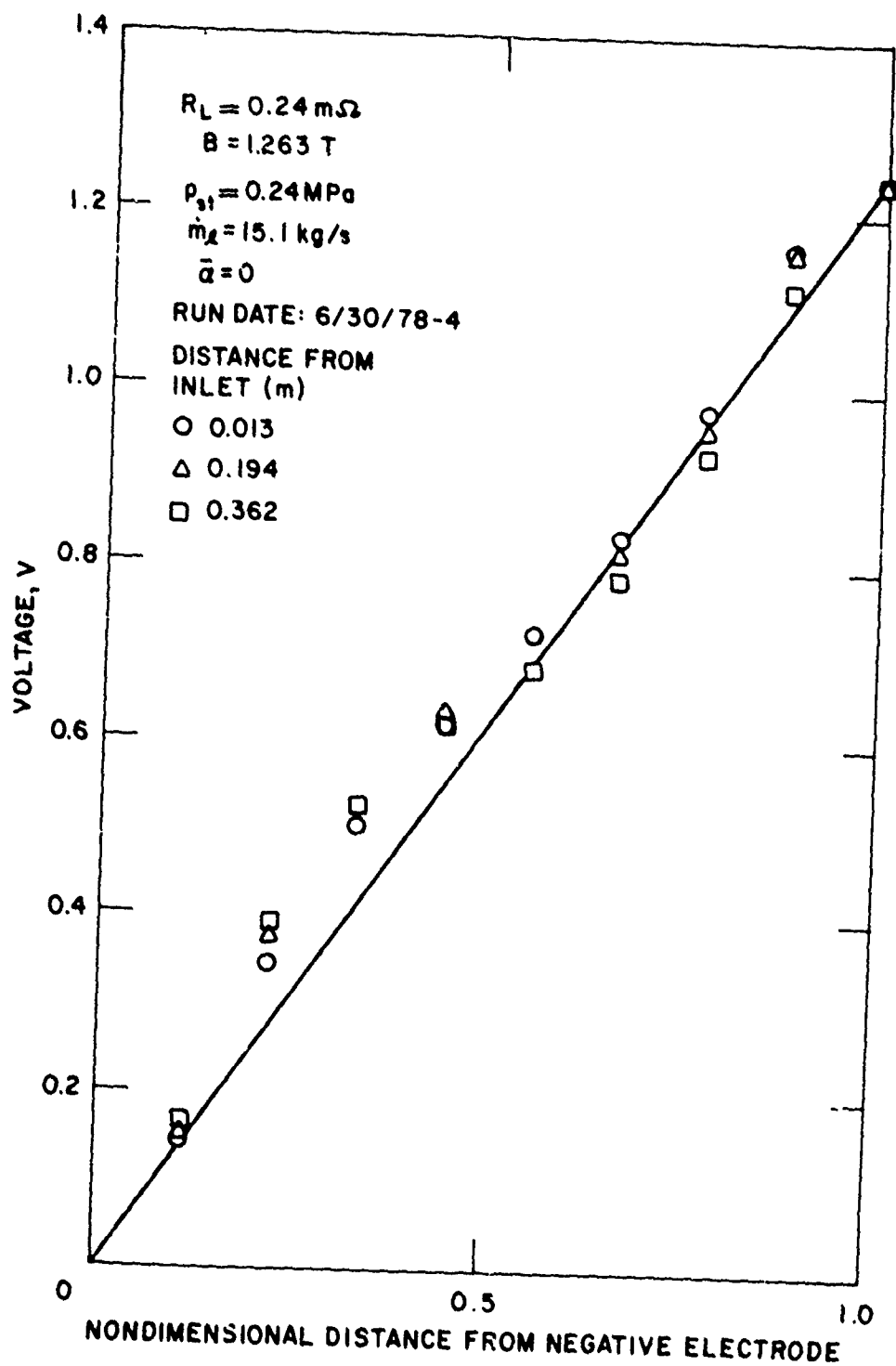
Figure III.9 Pure liquid voltage profiles between electrodes
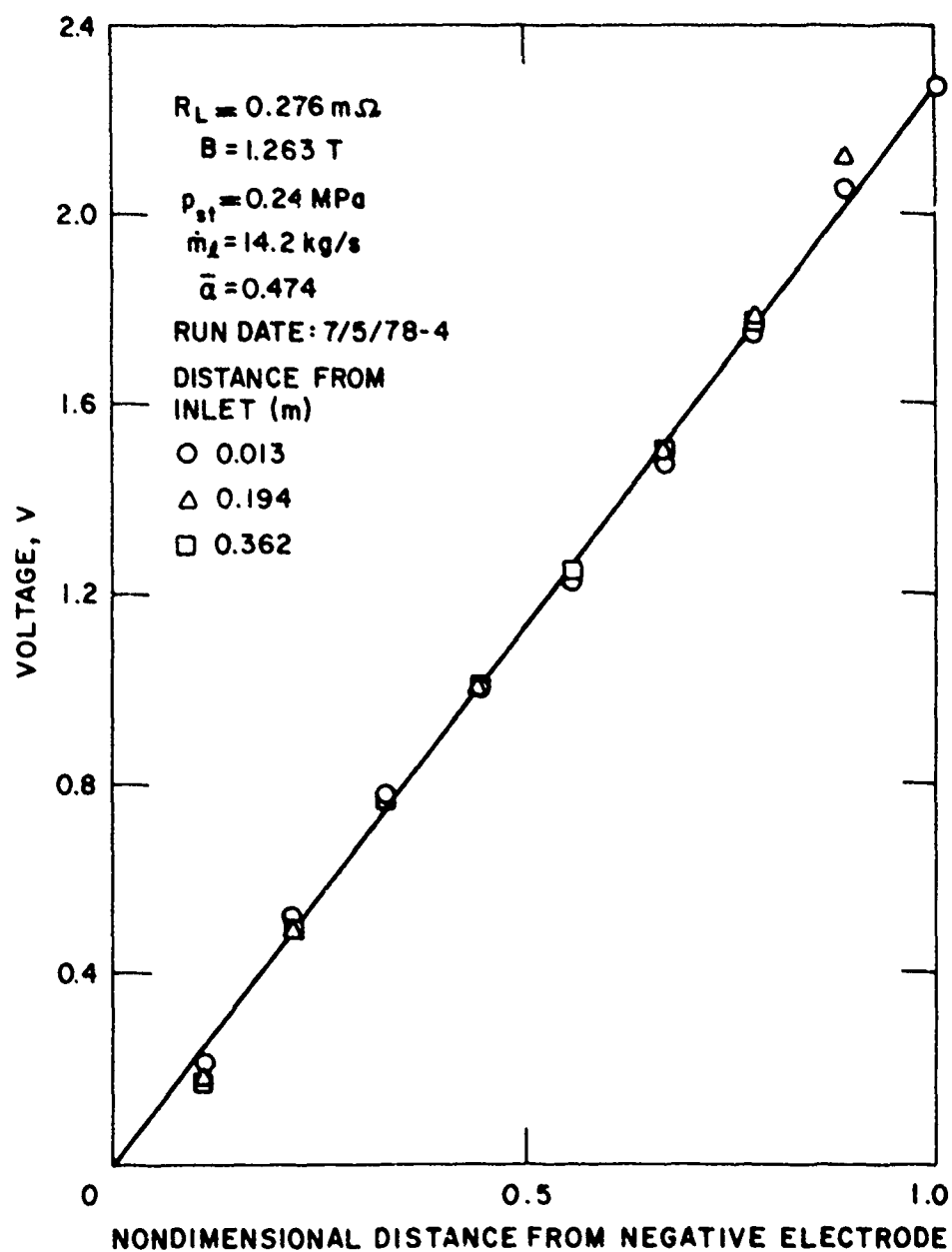
Figure III.10 Two-phase voltage profiles between electrodes

voltage gradient are regions of high voltage gradient; these would correspond to an M-shaped velocity profile, with the peaks of the M closer to the electrodes than in the pure-liquid case.

One important result of the new pressure distribution and voltage profile data is to emphasize the importance of the end regions on influencing the local behavior of the generator even far from the ends. The analytical studies aimed at understanding and minimizing end loss are described in Section V.

IV. LIQUID-METAL FOAMS AND SURFACE-ACTIVE AGENTS

The program has concentrated on bubble tests (Section IV.1) and surface tension measurements (Section IV.2) because the former indicate foamability directly, and surface tension is one quantitative measure of surface activity. As previously, the program is focussed on NaK alloy at ambient temperature, as it would be used in the initial foam LMMHD generator experiments.

IV.1 Bubble Tests in NaK Alloy

IV.1.1 Barium as an Additive

Early in the fiscal year, it was discovered that barium was effective in promoting bubble formation in NaK 77 (76.7 wt % K nominal). The initial mixture contained 0.45 wt % (0.11 mole %) barium. In the standard test, a single orifice in a Pyrex tube was used for gas introduction; full surface coverage by bubbles was achieved immediately on starting the gas flow (helium at 5 cc/min). At 375 cc/min, a column of bubbles several centimeters high was observed. It is appropriate to describe this aggregation of bubbles as a foam. When the Ba-NaK solution was transferred, helium was blown under the surface of the liquid metal with the transfer pipet in a manner analogous to blowing bubbles in a beverage with a soda straw. Surface coverage of the liquid metal with bubbles in the 5-cm diameter vessel was achieved quickly.

When nitrogen, instead of helium, was used as the bubble-blowing gas, it was observed that bubble performance did not degrade over a two day test period at ambient temperature. In this test, the system contained 0.22 wt % Ba. There was immediate surface coverage by bubbles. Two minutes after

gas flow was stopped, one bubble still survived, and broke only when the apparatus was shaken to determine whether it actually was a bubble.

Barium was also observed to act as a wetting agent in NaK. Stainless steel or Pyrex surfaces that normally do not become wetted on immersion in NaK at ambient temperature were wetted immediately on immersion in NaK containing small amounts of barium.

Some tests were made of bubble performance at higher temperatures. A sample of NaK 77 with 0.43 wt % barium was tested at 493 K. The tube was wetted immediately on immersion, and the bubbles were larger than those generated at ambient temperature and seemed to break faster. Approximately one-half the surface would be covered with bubbles, which persisted only approximately 5 seconds after the gas flow stopped. For comparison, at ambient temperature, the same sample showed nearly the same or slightly greater coverage with bubbles lasting approximately 7 seconds.

Pure NaK 77 at 448 K did not wet the tube on immersion or after a three-minute soak. Only approximately 20 % of the surface was covered, by a few large bubbles that lasted only 1 to 2 seconds. Clearly, barium enhances bubble stability even at higher temperatures, although there appears to be some decline in this stability at the higher temperatures.

IV.1.2 Calcium and Magnesium as Additives

NaK 77 containing 0.71 wt % calcium did not support bubble formation, nor did it wet Pyrex or stainless steel as barium-NaK solutions were observed to do. However, when barium (0.75 wt %) was added to the mixture, the excellent bubbling and wetting characteristics were again observed. The results indicate that barium is effective as a bubble promoter in the presence of calcium, despite the fact that calcium itself is ineffective in promoting bubbles.

-38-

With 0.11 wt % magnesium in NaK 77, there were favorable signs of bubble enhancement. This and subsequent bubble tests were performed in the tensionmeter pot, the vessel for surface tension measurements, using the same stainless steel orifice tube used earlier in the Pyrex bubble test apparatus. This change was made to eliminate any question of the Pyrex contributing a bubble-promoting surfactant. Adding 0.21 wt % barium to the magnesium-containing mixture conferred bubble stabilization and wettability much the same as seen for the calcium-containing system.

IV.1.3 NaK 46 (Sodium as an Additive to NaK 77)

In bubble tests with pure NaK 46 (46.2 wt % K), it was noticed that the geometry of the test setup can influence bubble formation, a result that indicates the importance of mechanical design in exploiting foaminess in a LMMHD machine. It was found that bubbles lasting 2 to 4 seconds would appear at the liquid surface if the L-shaped bubbler tube was held so that bubbles rose up away from the main shaft of the tube. No bubbles appeared at the surface if the tube was held in the inverted position. In that case bubbles presumably coalesced on the shaft on impact. Adding 0.072 wt % barium to the NaK 46 caused a dramatic improvement in bubble performance. Bubbles could easily be blown to cover the 2-inch (6-cm) diameter surface. Bubbles could be formed regardless of the position of the orifice tube, and it took 35 to 45 seconds for all of them to break after the gas flow was stopped. A lower concentration of barium, 0.020 wt %, was not effective in improving bubble performance.

IV.1.4 NaK 85 (Potassium as an Additive to NaK 77)

With pure NaK 85 (85.15 wt % K), approximately 20 % of the surface was covered with bubbles that lasted 3 to 5 seconds, and no wetting of the stain-

less steel orifice tube was noted on immersion in the liquid alloy. With 0.029 wt % barium, essentially the same results were obtained. With 0.16 wt % barium, the orifice tube became progressively wetted on repeated immersions. The bubbles covered approximately one-half of the surface and lasted 3 to 5 seconds. Further, bubbles would form with the tube in any position. Overall, the results of tests of NaK 46 and NaK 85 show better performance with NaK 46 and an apparent threshold of effectiveness for the barium.

IV.1.5 Silicon as an Additive

NaK 77 treated with high-purity silicon was tested. The solubility of silicon appears low, so the system was probably saturated. On immersion, the orifice tube was not wetted. The performance was no better than that of NaK 77 alone; approximately 25 % of the surface would be covered with bubbles that lasted about 3 seconds. When 0.080 wt % barium was added to the Si/NaK solution, bubble performance and wettability tended to be improved.

IV.1.6 Lead as an Additive

NaK 77 with 0.083 wt % lead was tested. The orifice tube was not wetted, even after repeated immersion. Approximately one third of the surface would be covered with bubbles lasting 3 to 5 seconds, and a single surviving bubble would last 8 to 10 seconds. The performance is slightly better than that with NaK 77 alone. Barium (0.075 wt %) was added to the Pb/NaK solution. The orifice tube was not wetted, and approximately one-third of the surface became covered with bubbles lasting some 3 seconds. With an increased concentration of barium (0.18 wt %), wetting was easily achieved, and approximately one-half of the surface would be covered with bubbles lasting about 5 seconds. The threshold for the effectiveness of

barium in this case is influenced by the fact that extensive compound formation is possible in the Ba-Pb system.

With still higher concentrations of lead and at higher temperatures, the following results were obtained. In a sample of NaK 77-1.05 wt % Pb, the orifice tube did not become wetted on immersion or on swirling at 315 and 463 K. At both temperatures, bubbles lasted approximately 2 seconds; at the lower temperature, however, somewhat more surface coverage--as much as half--could be obtained. At the higher temperature, 25 to 30 % coverage was observed. This performance does not appear to be significantly better than is found with NaK 77.

IV.1.7 Gallium as an Additive

Gallium, probably at the saturation level, was found to confer slightly better bubble performance than NaK 77 alone, but no wetting occurred. With 0.17 wt % barium also present, the orifice was wetted after three immersions; 30 to 50% of the surface would be covered with bubbles lasting approximately 5 seconds.

IV.1.8 Cadmium as an Additive

Cadmium, which was reported on as an additive last year, was reexamined. A mixture with 0.20 wt % Cd did not wet the orifice tube, and no bubbles could be formed with the orifice tube in the inverted position. In the upright position, up to 4 bubbles could exist for 4 to 5 seconds, a performance slightly better than that of pure NaK 77 under these conditions. This situation was essentially unchanged when barium was added to bring the barium concentration to 0.20 wt %, and then to 0.43 wt %. However, at 0.70 wt % Ba, the bubbler tube was wetted immediately and approximately 75 % surface coverage with bubbles lasting about 6 seconds was obtained. A single

bubble would survive approximately 12 seconds. The reason for the ineffectiveness of initial barium additions is probably the reaction between cadmium and barium; compounds ranging from $BaCd_{11}$ to Ba_2Cd are known. The final stoichiometry in this test mixture was equivalent to $Ba_{2.9}Cd$, i.e., enough barium was included to exceed the cadmium capacity for formation of Ba_2Cd and, thus, to be effective in bubble stabilization.

A test with cadmium at higher temperature was also included. NaK 77 with 0.58 wt % cadmium at 333 K did not wet the bubble test orifice tube, and provided approximately 25 % surface coverage by bubbles lasting 2 to 3 seconds. This performance was not as good as that obtained with barium.

IV.1.9 Bismuth as an Additive

In a bubble test with NaK 77 containing 1.15 wt % bismuth, the orifice tube was not wetted on immersion or swirling. Bubbles could be blown to produce approximately 50 % surface coverage lasting 5 to 7 seconds. At higher temperatures, the performance decreased, as with barium, so that only 25 % surface coverage could be achieved at 453 K with the bubbles lasting 1 to 2 seconds. Overall, the performance was about as good as with some barium-containing systems, but not as good as that found in the most favorable cases with barium. Further work should be done with bismuth to confirm and extend these data, particularly if nitrogen reacting with barium at ambient temperature becomes a problem.

IV.1.10 Selenium as an Additive

Selenium was retested under the new conditions. A saturated sample did not wet the orifice tube. Approximately 30 to 50 % surface coverage could be achieved, with bubbles lasting 2 to 3 seconds. This is, perhaps, slightly better performance than that achieved with pure NaK 77, and might

be the result of bubble stabilization by undissolved selenium particulate.
The same performance prevailed after addition of 0.17 wt % barium. With
0.34 wt % barium, the bubbler tube was nearly completely wetted on immersion.
Approximately half the surface was covered with bubbles lasting 5 to 7
seconds, and the bubbler tube was effective either upright or inverted.

IV.1.11 Pure Potassium and Potassium-Barium Systems

Studies of pure potassium and potassium-barium mixtures were included,
to provide reference data for the NaK 77 system, which is a potassium-rich
system. At 348 K (potassium melts at 337 K), the potassium did not wet the
stainless steel bubbler tube, and bubble stability was not observed. This
behavior is to be expected from a pure material.

With mixtures of potassium containing 0.11 wt % barium at 358 K, and
0.33 and 0.63 wt % barium at 353 K, the same lack of wetting and absence
of bubble stability was observed. Barium is not effective, at least at
these concentrations, in promoting bubble stability in potassium; this is
consistent with the observation of the elevation of surface tension by
barium in potassium.

The sodium concentration, then, is an important variable in relating
the nonfoaming K-Ba systems to the foaming NaK 77-Ba system. A sample of
potassium containing 1.19 wt % sodium and 0.62 wt % barium, held at 353 K,
was found to support an occasional, fairly large bubble that lasted for
a fraction of a second. Although there was no wetting of the orifice tube,
this bubble test did indicate a tendency for increased film stability.
However, using the same material with more sodium added, to increase the
composition to 15.8 wt % sodium (and 0.53 wt % barium), resulted in a
marked change in solution characteristics. The orifice tube was wetted
almost completely on the first immersion. As regards bubble stabilization,

approximately one-third of the surface became covered, with the last surviving bubble remaining for approximately one minute. At a higher temperature, 498 K, and when compared with other experiments at this temperature, some improvement in performance was found. The orifice tube was wetted after a single brief immersion, but the bubble lifetime was shorter. Approximately 25 % of the surface was covered with bubbles, with the last surviving bubble breaking after 5 to 7 seconds.

IV.1.12 NaK 83 with Barium as an Additive

The composition of NaK 83 (82.96 wt % potassium) is about the most potassium-rich NaK alloy that has potential use at ambient temperature in a LMMHD machine. Bubble performance in pure NaK 83 indicated only slight bubble persistence. However, when the system contained 0.27 to 0.99 wt % barium, the wetting characteristics of the solution improved markedly, and bubbles lasting as long as 5 seconds covered 20 to 35 % of the surface. For a mixture containing 1.28 wt % barium, a test at 478 K showed bubbles covering 50 % of the surface and lasting for approximately 5 seconds.

IV.1.13 Effect of Nitrogen on Bubble Performance with Barium as an Additive

The 1.28 wt % barium system mentioned above was used for a test of the reactivity of the dissolved barium with nitrogen. After three days of bubbling N_2 through the sample at temperatures that were increased stepwise (323, 373, 423, and 468 K), a bubble test at 468 K showed that the orifice tube was not wetted initially, but did wet after swirling during immersion. Bubbles could be blown to give approximately 25 % surface coverage and lasted for about 1 second. The effect of the barium was definitely diminished, quite possibly because of reaction with nitrogen at the higher temperature. However, when the same sample was cooled to

ambient temperature and retested, 35 to 50 % of the surface was covered with bubbles that lasted 5 to 7 seconds, with lone survivors lasting for 10 to 15 seconds. It appears that, even if considerable barium was removed from solution by reaction with nitrogen at high temperatures, sufficient barium remained for bubble stabilization to be appreciable at ambient temperature.

IV.2 Surface Tension Measurements

During the year, apparatus was installed to measure surface tension as a function of temperature. Data obtained with this equipment for a particular system are more extensive and are regarded as more reliable than the earlier measurements, in part because of their greater range and also because of the accumulated experience with the technique. Linear regression equations expressing the surface tension-temperature data are tabulated in Table IV.1, and curves for these data appear, where appropriate, in the following discussion. Table IV.2 contains a complete tabulation of surface tension data for temperatures at and above ambient.

IV.2.1 The Na-K-Ba System and the Rationale for Bubble Stabilization
by Surfactants

The most noteworthy observation gleaned from our studies on surface tension in the NaK 77-Ba systems was that, for systems showing enhanced bubble stability, the surface tension was not depressed but was, in fact, higher than that of pure NaK 77. Usually, foamability and film stability are correlated with lower values of surface tension. Actually, it is more accurate to state that the phenomenological correlation is between film stability and surface activity of a solute. The question, then, is one of reconciling surface activity with increased surface tension.

Table IV.1

Linear Regression Equations for Surface Tension Data

γ (mN/m) $= a - bT(C°)$[*] with 95% Confidence Intervals Shown

System	b	a
K	0.0717 ± 0.0069	111.9 ± 0.3
K + 0.33 wt % Ba	0.0777 ± 0.0093	113.2 ± 0.5
K + 0.63 wt % Ba	0.0781 ± 0.0045	121.7 ± 0.3
K + 0.62 wt % Ba + 1.19 wt % Na	0.0724 ± 0.0234	123.4 ± 1.2
K + 0.53 wt % Ba + 15.8 wt % Na	0.0679 ± 0.0134	125.7 ± 0.7
NaK77.17 (Na 77)[**]	0.0690 ± 0.0069	120.3 ± 0.4
NaK77 + 0.15 wt % Ba	0.0518 ± 0.0043	110.4 ± 0.2
NaK77 + 0.43 wt.% Ba	0.1773 ± 0.0258	169.4 ± 1.6
NaK77 + 0.58 wt % Cd	0.0618 ± 0.0042	117.2 ± 0.2
NaK77 + 1.15 wt % Bi	0.1276 ± 0.0099	148.7 ± 1.4
NaK77 + 1.05 wt % Pb	0.0583 ± 0.0049	102.2 ± 0.3
NaK 82.96 (NaK83)	0.0601 ± 0.0062	116.4 ± 0.4
NaK83 + 0.27 wt % Ba	0.0569 ± 0.0091	125.6 ± 0.6
NaK83 + 0.52 wt % Ba	0.0396 ± 0.0084	125.4 ± 0.5
NaK83 + 0.75 wt % Ba	0.0667 ± 0.0061	140.7 ± 0.3
NaK83 + 0.99 wt % Ba	0.0599 ± 0.0070 (high temp.)	140.4 ± 0.3
	0.0195 ± 0.0169 (low temp.)	136.7 ± 0.4
NaK83 + 1.28 wt % Ba	0.0623 ± 0.0099	138.5 ± 0.5

[*]Temperature range 25-200°C (298-473 K)

[**]The number in a designation such as NaK77 refers to the mass percentage of potassium.

Table IV.2

Surface Tension Measured by Maximum Bubble Pressure Method at Ambient Temperature

Identification Number	Description	Surface Tension mN/m
1	NaK77 previously treated with butanol. Orifices freshly cleaned.	113.7
2	Fresh supply of NaK77. No additives.	114.8
3	NaK77 treated with dicyclopentadiene at 323-333 K.	117.9
4	Same system after additional treatment with dicyclopentadiene at ∿388 K and after standing overnight.	114.3
5	Fresh NaK sample.	114.0
6	Same sample with 0.22 wt % Hg.	113.0
7	Same system one day later and after developing hot-wetting technique for orifices.	114.4
8	Same system with 1.18 wt % Hg.	114.3
9	Same system with 6.38 wt % Hg.	116.6
10	Fresh NaK. Helium is bubble-blowing gas.	114.7
11	Same system, but using nitrogen to blow bubbles.	113.6
12	Same system with 0.070 wt % barium. He is bubble gas.	114.4
13	Same system, two days later.	115.2
14	Same system with 0.45 wt % Ba.	118.3
15	Fresh sample of NaK77 with 0.17 wt % calcium. Helium bubbles.	116.0
16	Same sample seventeen hours later.	115.8

Identification Number	Table IV.2 (continued) Description	Surface Tension mN/m
17	Same sample after heating.	120.4
18	Same sample after additional heating.	116.7
19	Same sample three days later.	120.1
20	Additional calcium added to preceeding sample to make concentration 0.45 wt %.	117.9
21	Same sample after standing overnight.	118.4
22	Same sample after exploratory bubbling test with Pyrex pipet.	118.5
23	Same sample after heating.	118.3
24	Same sample after standing overnight.	119.1
25	Additional calcium added to same sample to bring calcium content to 0.71 wt %. Helium bubbles.	118.2
26	Same sample after standing five days.	118.9
27	Same sample with 0.18 wt % barium.	118.8
28	Same sample with additional Ba to give 0.51 wt % barium.	124.6
29	Same sample after heating for 47 minutes.	124.1
30	Same sample with additional Ba to give 0.75 wt % barium.	122.1
31	Same sample after bubbling through for 3 days.	122.4
32	NaK77 sample with 0.005 wt % magnesium.	121.7
33	Same sample with additional Mg:0.029 wt % Mg.	137.4
34	Same sample after reheating.	130.3
35	Same sample after bubbling helium through overnight.	130.1

Table IV.2 (continued)

Identification Number	Description	Surface Tension mN/m
36	Same sample with additional Mg:0.11 wt % Mg.	126.7
37	Same sample after reheating.	124.0
38	Same sample after bubbling helium through for three days.	124.1
39	Same sample after bubble tests and reheating.	123.4
40	Same sample with 0.21 wt % barium (no heating).	123.2
41	Same sample after heating.	123.8
42	Same sample three hours later.	124.0
43	Same sample after bubbling helium through overnight.	124.4
44	NaK with 46.43 wt % K, designated NaK46.	126.8-127.5
45	Same sample with 0.020 wt % Ba.	125.0
46	Same sample two weeks later.	127.9
47	Same sample with 0.072 wt % Ba.	127.0
48	NaK with 85.15 wt % K, designated NaK85.	109.9
49	Same sample 16 hours later.	109.5
50	Same sample with 0.029 wt % Ba.	120.1
51	Same sample after bubble test and cleaning tensionmeter.	121.8, 118.0
52	Same sample with 0.16 wt % Ba.	118.0, 119.3
53	Pure NaK77.	116.0
54	Same sample with 0.068 wt % selenium.	116.5
55	Same sample with 0.017 wt % barium.	116.4
56	Same sample with 0.34 wt % barium, total.	114.8

In developing an understanding of the behavior of surfaces in NaK 77-Ba alloy systems, it is important to recognize that NaK 77 is a two-component system. Bradhurst and Buchanan (1961) have reported a few surface tension values for the sodium-potassium system, which indicated that potassium is surface active in sodium. According to their data, the general nature of which is consistent with the results reported here, the surface tension decreases slightly as potassium concentration increases on the potassium-rich end of the system. NaK 77 is potassium-rich with a potassium atom fraction of 0.66. The slight bubbliness achievable with pure NaK 77 might derive from the surface tension gradient still present at this concentration.

Adding barium to the NaK alloy results in a three-component system, rather than the simpler two-component system. It is a potassium-rich mixture, and it seems more reasonable to examine the phenomena from the viewpoint of a potassim system, rather than a sodium system.

The surface tension data in Figure IV.1, all for measurements coming from this study, show that the dissolution of sodium in potassium increases the surface tension of the sodium-potassium mixture. The NaK 83 system was chosen because it is as close as is possible to the potassium-rich end of the binary, while still maintaining a liquid at ambient temperature. To give a feel for the precision, data points are shown in Fig. IV.1. This precision is typical of most cases examined. For simplicity, only the linear regression lines are shown in other figures.

Figure IV.2 shows that, for concentrations in the range of interest, barium raises the surface tension of pure potassium, in other words, that barium is surface inactive. From the data given in Figs. IV.1 and IV.2, the conclusion may be drawn that both sodium and barium are surface inactive
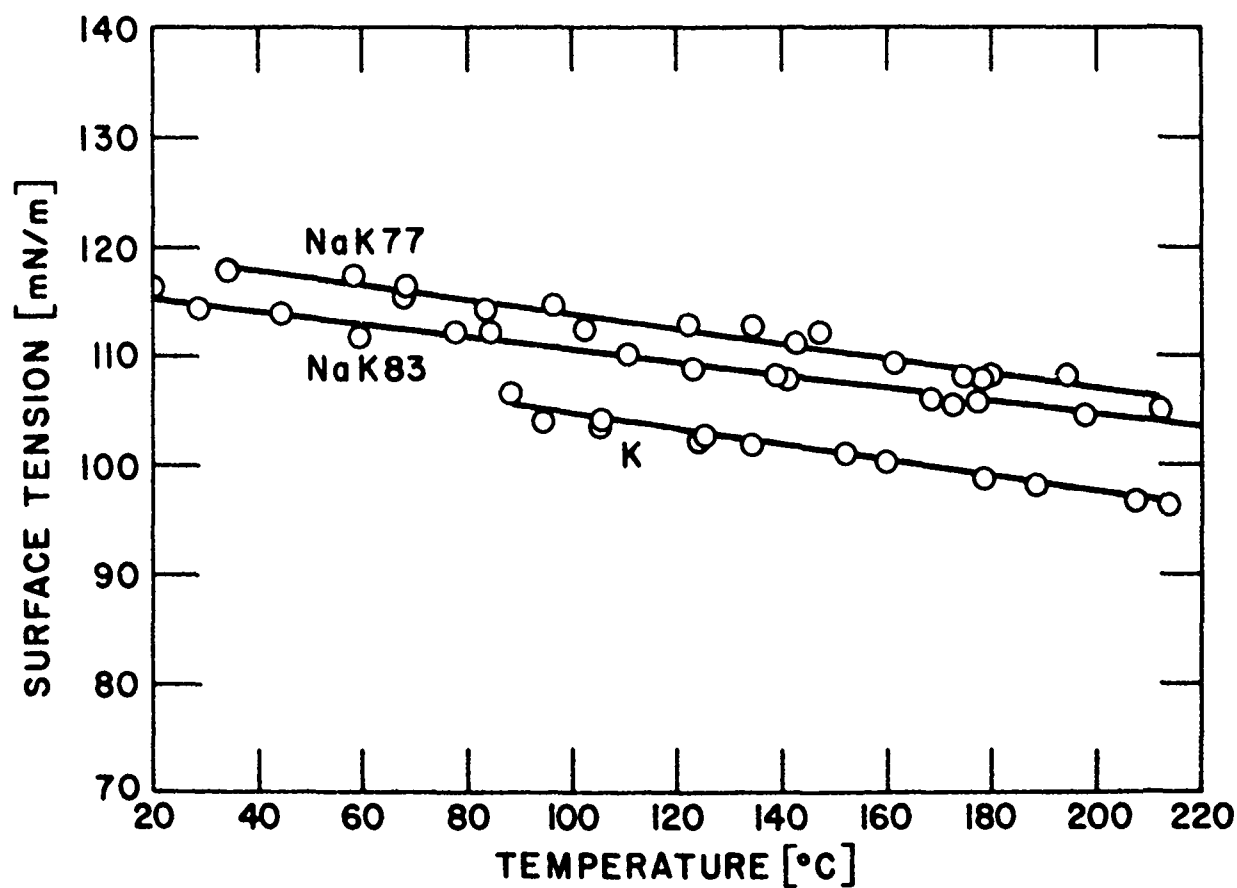
Figure IV.1 Surface tension vs temperature for NaK 77, NaK 83, and K
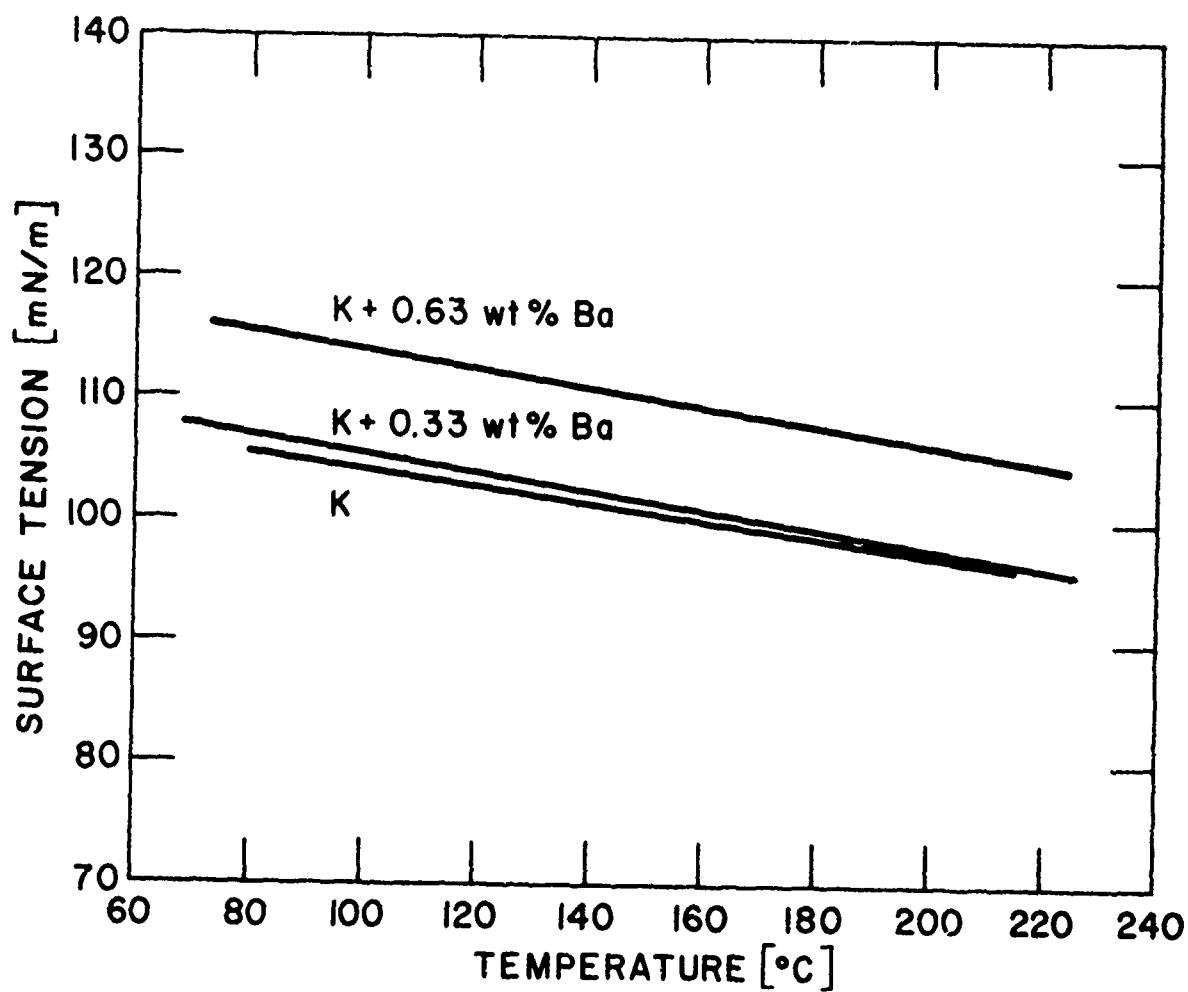
Figure IV.2 Surface tension vs temperature for potassium-barium combinations

in, or raise the surface tension of potassium. When both additives are present, the situation is like that shown in Fig. IV.3, where all the relevant data are plotted. Here substantial increases in surface tension are seen with increasing additions of sodium to a "base" system containing 0.63 wt % Ba in K. Furthermore, the system with 15.8 wt % sodium is virtually the same composition as NaK 83 in respect to the sodium and potassium components. Therefore, the uppermost curve implies that adding barium to NaK 83 will also raise the surface tension.

This expectation is supported, at least over the limited concentration range shown in Fig. IV.4. The surface tension of NaK 83 (the lowest curve) is taken as the reference case. Generally, the surface tension increases on adding barium to NaK 83, at least up to the 0.99 wt % Ba composition. However, surface tension data for 1.28 wt % barium in NaK 83 parallel, and are slightly below the curve for 0.99 wt % Ba, implying that a maximum surface tension was reached at 0.99 wt % Ba. The individual data are not shown in the figure, but are tabulated in Table IV.1. Although appearing to indicate a maximum in surface tension in this concentration region, these two curves are close enough together that the experimental error associated with both of them does not yet allow an unequivocal conclusion about a maximum. At this stage of understanding, only a tentative statement about a maximum is offered, for use in the following discussion.

Figure IV.4 also shows values for the slopes of these curves. For 0.99 wt % barium, there is a break in the curve at approximately 90°C (363 K). Examining all the data above 90°C (363 K), one can see that the slope goes through a minimum for the solution containing 0.52 wt % barium. Further, for the data above 90°C (363 K) the values of the slopes are the same within a 95 % confidence range. On the low temperature side [below 90°C

-53-
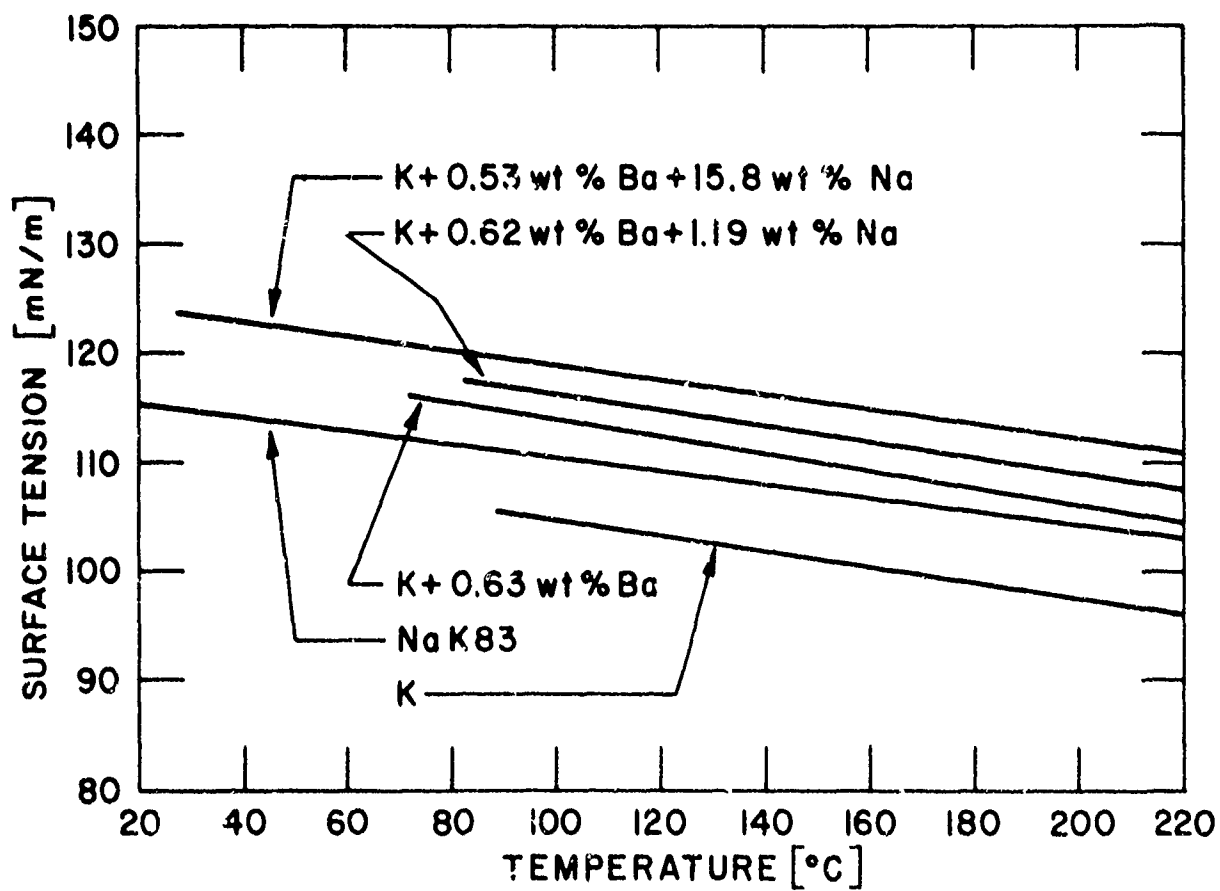
Figure IV.3 Surface tension vs temperature for potassium-
sodium-Barium combinations
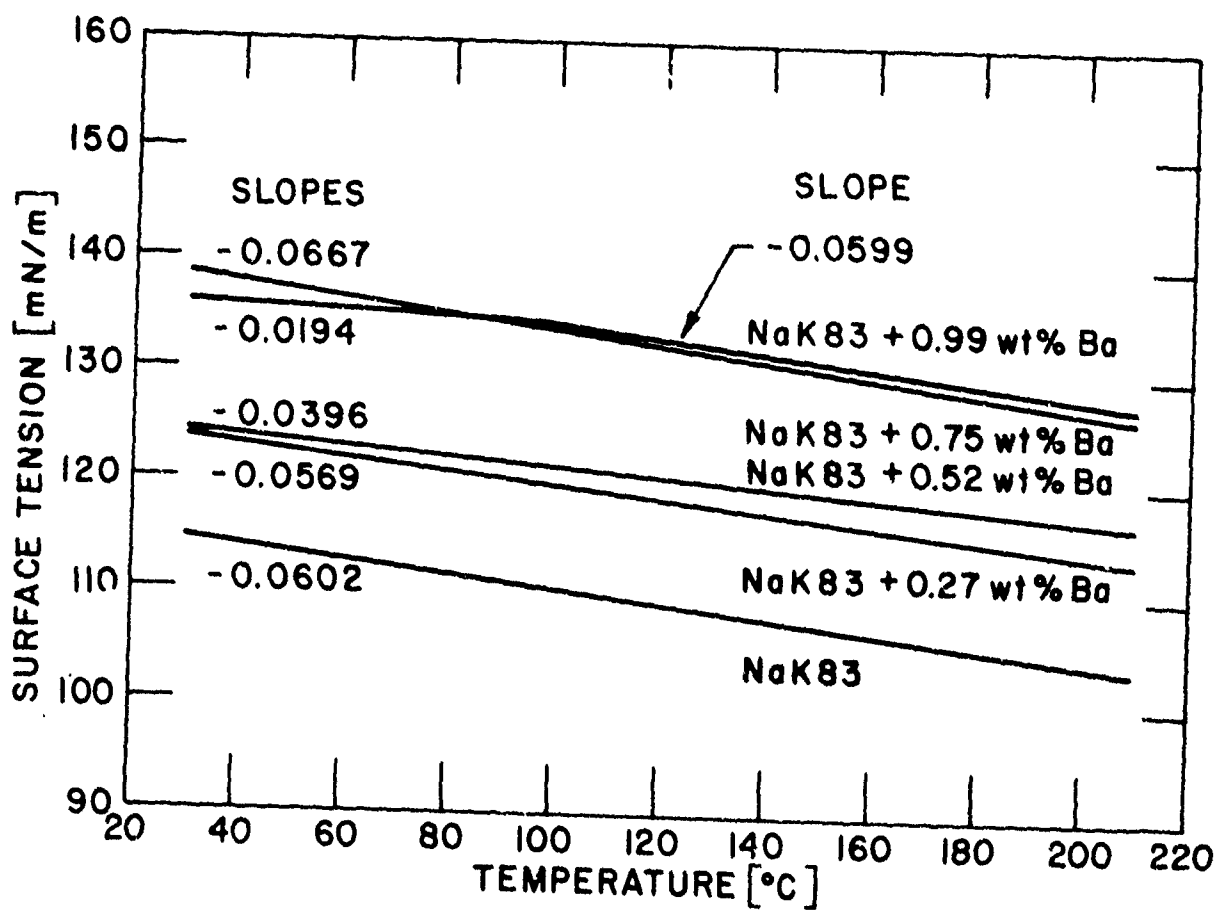
Figure IV.4 Surface tension vs temperature for NaK 83-Barium combinations

(363 K)], the 1.28 wt % barium system did not show a break, so that there

are two minima in the values of the slopes in the low temperature region--one

for the 0.52 wt % barium case, and one for the 0.99 wt % barium system.

Assuming that the slopes of the surface tension-temperature curves reflect

surface entropy ($S = -\frac{d\gamma}{dT}$, where S is entropy, γ is surface tension, and T

is temperature), it appears that surface entropy goes through two minima

below 90°C (363 K) and through one minimum above 90°C (363 K).

A rationalization for this occurrence can be developed on the assumption

that barium is surface active in NaK in the sense of positive adsorption,

rather than in the sense of depressing the surface tension of the mixture.

How surface activity coupled with increasing surface tension can come about

can be understood in terms of the general form of the Gibbs absorption

isotherm

$$d\gamma = - \sum_i \Gamma_i \, d\mu_i \ , \qquad\qquad (IV.1)$$

where γ is the surface tension, Γ_i is the surface excess of component i,

and μ is the chemical potential of component i. For the three component

Na-K-Ba system it is

$$d\gamma = -\Gamma_{Na} \, d\mu_{Na} - \Gamma_K \, d\mu_K - \Gamma_{Ba} \, d\mu_{Ba}. \qquad\qquad (IV.2)$$

On adding barium to a NaK sample, one can be sure of a positive sign for

$d\mu_{Ba}$. To the extent that dilution is influential, $d\mu_{Na}$ and $d\mu_K$ will

be negative. Conceivably, therefore, a positive sign for Γ_{Ba} (positive

adsorption of barium) could be coupled with positive signs for Γ_{Na} or

Γ_K. However, chemical interactions could also lead to positive signs for

$d\mu_{Na}$ or $d\mu_K$, instead of the negative signs assumed on the basis of

dilution. In the absence of detailed thermodynamic information, the point

to be made from these considerations is that one may consider the possibility of positive adsorption, coupled with a rise in surface tension, when dealing with a three-component system, whereas this coupling is not allowed thermodynamically in a two-component system. If barium is positively adsorbed, the barium-enriched surface can be viewed as having a composition markedly different from the composition of the bulk, with behavior different from the bulk in terms of the phase diagram relationships.

Unfortunately, a ternary phase diagram for the Na-K-Ba system is not available; thus, the changes in surface tension must be correlated from knowledge of the compounds identified in the Na-Ba and K-Ba binary systems. Of the two, only the Na-Ba diagram (Fig. IV.5) has been worked out in sufficient detail, the K-Ba diagram (not shown) is rather featureless and without strong interactions. The significant feature of the Na-Ba diagram is that Na and Ba form two compounds, NaBa and Na_4Ba. Furthermore, the temperature range of NaBa stability is greater than that of Na_4Ba. Although it is not claimed that compound formation occurs in the surface film, it seems reasonable to expect that the attractive interactions that lead to such compounds in the bulk could also persist, and could lead to ordering in the surface film. In addition, these attractive interactions are expected to have an elasticity-enhancing effect, favoring film and bubble stability.

It is of interest to speculate further on the correlation between the information given in the Na-Ba phase diagram and the slopes of the surface tension curves for the NaK 83-Ba mixtures. At low temperature, the phase diagram shows that two compounds or two kinds of interactions are possible, whereas only one such interaction persists at higher temperature. This situation might be regarded as being reflected in the two minima in surface
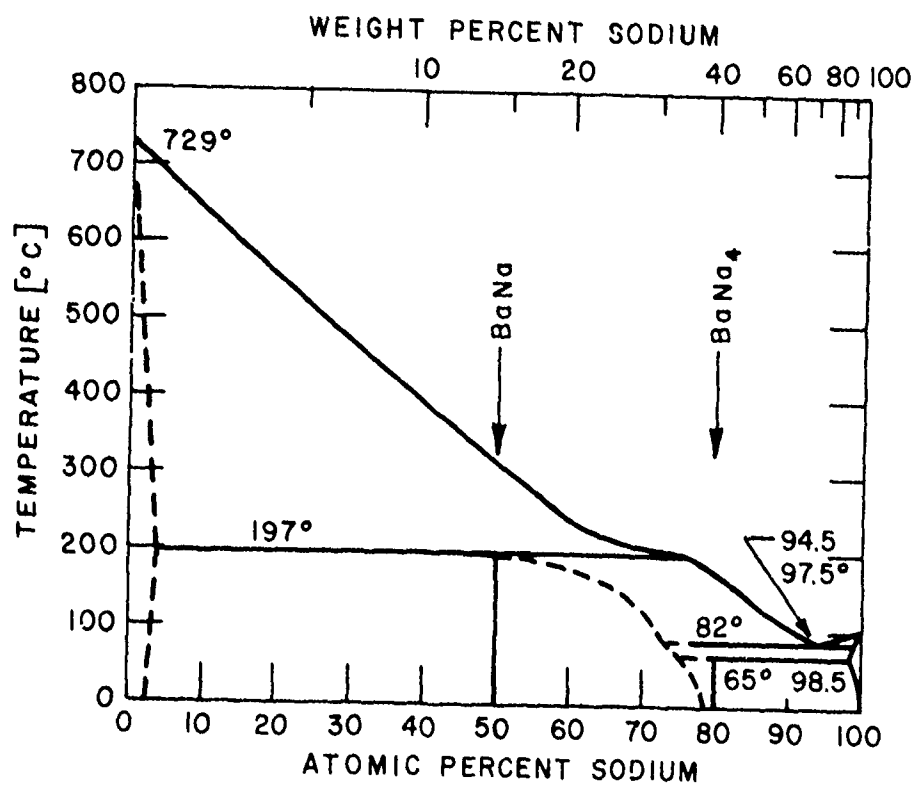
Figure IV.5 Sodium-Barium phase diagrams

entropy below 90°C (363 K), and in the single minimum above 90°C (363 K).

With the conceptual framework for understanding the potassium-rich systems developed on the basis of NaK 83, similar reasoning can be applied to the NaK 77 alloy system that is of present interest in the LMMHD program. Figure IV.6 shows a series of surface tension-temperature curves for pure NaK77, and, for reference, pure potassium is included. For the NaK77 alloy, an increase in surface tension is noted for the 0.43 wt % barium system. This increase is very substantial, as is the steepness of the slope. Both features need further checking, but the increase in surface tension is qualitatively consistent with data collected in earlier measurements of several NaK 77-Ba alloy mixtures at ambient temperature. However, an additional feature of interest is the decrease in surface tension observed with the 0.15 wt % barium mixture. The decrease in surface tension values at low barium concentration might be viewed as a vestige of the behavior of barium in pure sodium, as reported by Addison et al (1962). Some of the Addison data are shown in Fig. IV.7. The curve for 150°C (423 K) has been displaced upward by 50 mN/m for clarity. The minimum in the surface tension at about 4 at % is at a rather high concentration on a weight basis, approximately 20 wt %. It seems indicated that, in comparing the present data with the Addison data, the minimum in surface tension should shift to lower barium concentrations with increase in potassium content.

The hypothesis that attractive interactions of the type tending to form compounds occur in the surface receives additional support from two types of calculations. The first relates to the variation in the surface entropy invoked in connection with the minimum values of the slopes of the surface tension-temperature curves of the NaK 83-Ba systems. On the assump-
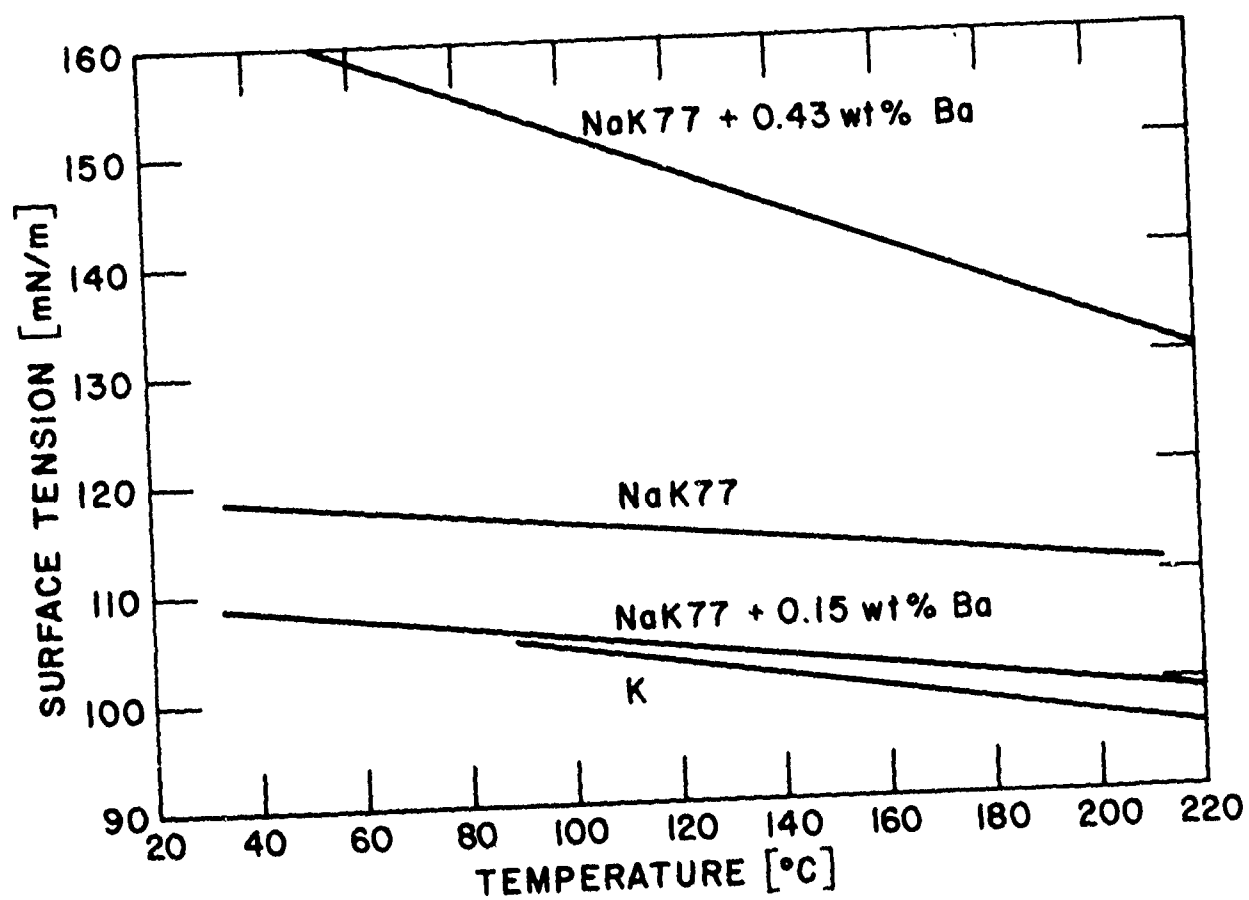
Figure IV.6   Surface tension vs temperature for K and
NaK 77-Barium combinations
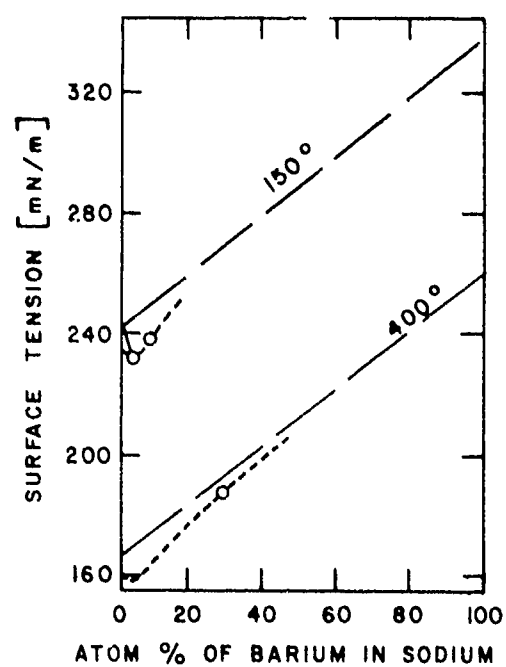
Figure IV.7 Surface tension vs atom % barium in sodium at 150 and 400°C

tion that there is an analogy between the entropy of mixing and the surface entropy of a mixture, an investigation was made of the effect that the addition of a third component makes on the entropy of mixing in the binary system, with the added condition that one or two compounds can form. The calculation uses the expression for the entropy of mixing,

$$S = - R \, \Sigma_i x_i \, \ln x_i \, , \qquad\qquad (IV.3)$$

where x_i is the atom fraction of species i, and R is the gas constant. It is further assumed that one of the binary components is decreasing in concentration with formation of the compound in which it is involved, and concurrently the concentration of that compound is increasing. If further addition of the reactive third component results in the formation of a second compound at the expense of the first, then the concentrations of all species are adjusted accordingly. The result of such an approach is that the entropy of mixing could be made to go through either one or two minima, depending on whether one or two compounds are invoked. Recalling that, in a given temperature regime, one or two minima were found in the slopes of the surface tension-temperature curves for a series of compositions for the NaK 83-Ba mixture, this calculation can be regarded as supporting the idea that attractive interactions could be operating in the surface to stabilize a preferred atom aggregate composition.

Again using the data for the NaK 83-Ba system, the second calculation follows a rigorous application of the Gibbs definition of a surface, which sets the contribution of the solvent equal to zero in the overall calculation. In the NaK 83 series, the barium additions were in small increments, and simultaneous equations for the Gibbs adsorption isotherm were set up as

$$d\gamma = -\Gamma_{Na} \, d\ln a_{Na} - \Gamma_{Ba} \, d\ln a_{Ba} \, , \qquad\qquad (IV.4)$$

where a is the activity, and the other terms are as defined previously. (The term for potassium does not appear because the conventional Gibbs definition of the surface is being followed.) When activities were taken equal to atom fractions, the values for Γ_{Na} and Γ_{Ba} were physically nonsensical, values of the order of -10^{-5} mole/cm^2 were obtained, whereas 10^{-10} mole/cm^2 would be reasonable. Further, using values of dγ that were at the extremes of the 95 % confidence ranges resulted again in nonsensical values. However, more physically acceptable values for Γ could be obtained if the values of a_i were reduced, as they would be for nonideal solutions with an activity coefficient of less than one. Such nonideality is typical of systems exhibiting, or showing tendency toward, compound formation. The calculations with reduced activity are, therefore, taken to be supportive of the idea of attractive interactions existing in the surface.

As for the more practical problem of stabilizing a liquid metal foam, it is suggested that liquid metal films cannot have available one of the mechanisms that operates to stabilize aqueous and organic films, namely, the repulsive effect of electrical double layers on opposite sides of the film. The conductive, metallic medium, in effect, short circuits such a condition. In dealing with liquid metals, greater reliance must, therefore, be placed on the film-stiffening effects of attractive interatomic forces.

On the basis of these ideas, systems with the potential for such film enhancing effects can be chosen from among those in whch a component is positively absorbed and for which there is evidence for compound formation in the bulk.

IV.2.2 Surface Tensions of Systems of NaK 77 with Additives Other Than
Barium

IV.2.2.1 Cadmium

Figure IV.8 shows the results from surface tension measurements on a
NaK 77-0.58 wt % cadmium alloy. Cadmium is seen to lower the surface
tension of NaK 77.

IV.2.2.2 Bismuth as an Additive

Data for the NaK 77-1.15 wt % Bi system show, Fig. IV.9, that bismuth
raises the surface tension of NaK 77. A linear regression line for the
surface tension of pure NaK 77 is shown for reference. The scatter for the
points as shown is considerably greater than in prior work, and might be
the result of increased tendencies to precipitate alkali metal bismuth
compounds on the orifice lips.

A significant feature of the regresssion line is that the slope (a
measure of surface entropy) is approximately double that of the curve for
pure NaK 77, i.e., 0.123 mN/m deg vs 0.068 mN/m deg. It may prove significant
that instances of increased surface entropy have been observed in the
systems that favor film stability, i.e., Ba and Bi in NaK 77. It is
noteworthy, too, that bubble stability has been associated in these studies
with increases, rather than decreases, in surface tension.

IV.2.2.3 Lead as an Additive

Surface tension data for the NaK 77-1.05 wt % Pb system, Fig. IV.10,
indicate significant reductions in surface tension. This fact, together
with the negligible effect of lead on bubble stability, further weakens the
conventional correlation between foamability and decreased surface tension.
If the lowered surface tension is an indication of positive absorption of
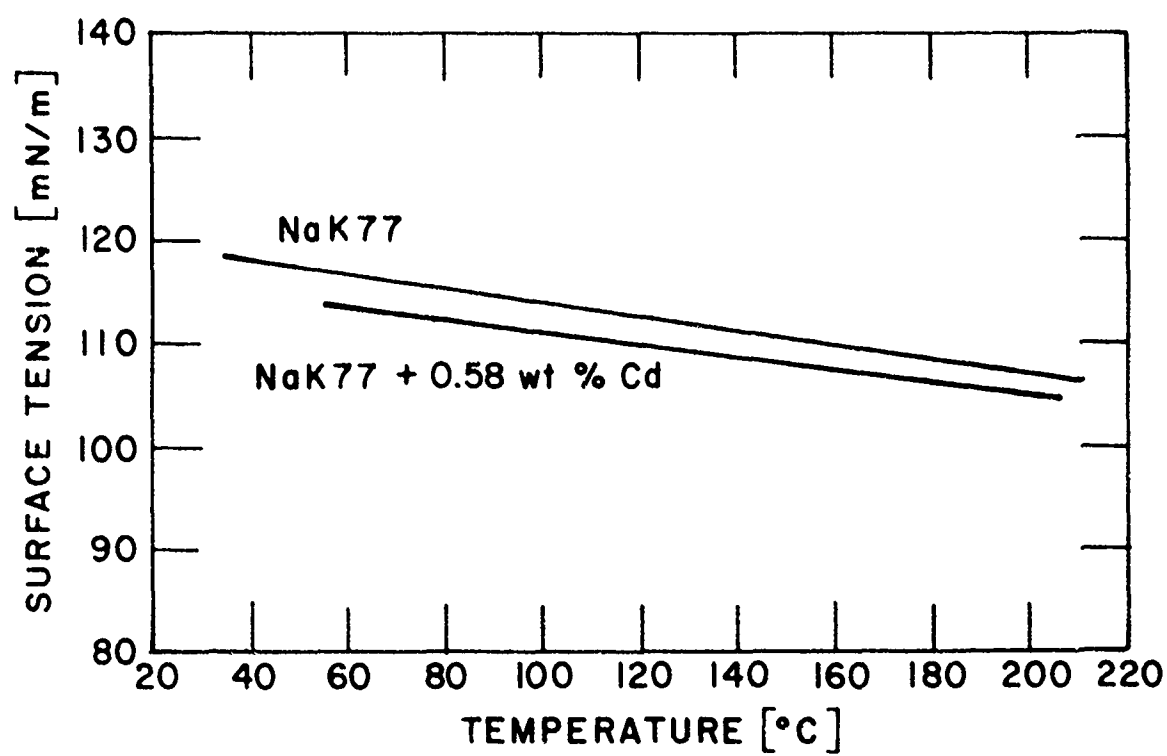
Figure IV.8 Surface tension vs temperature for NaK 77-Cadmium combinations
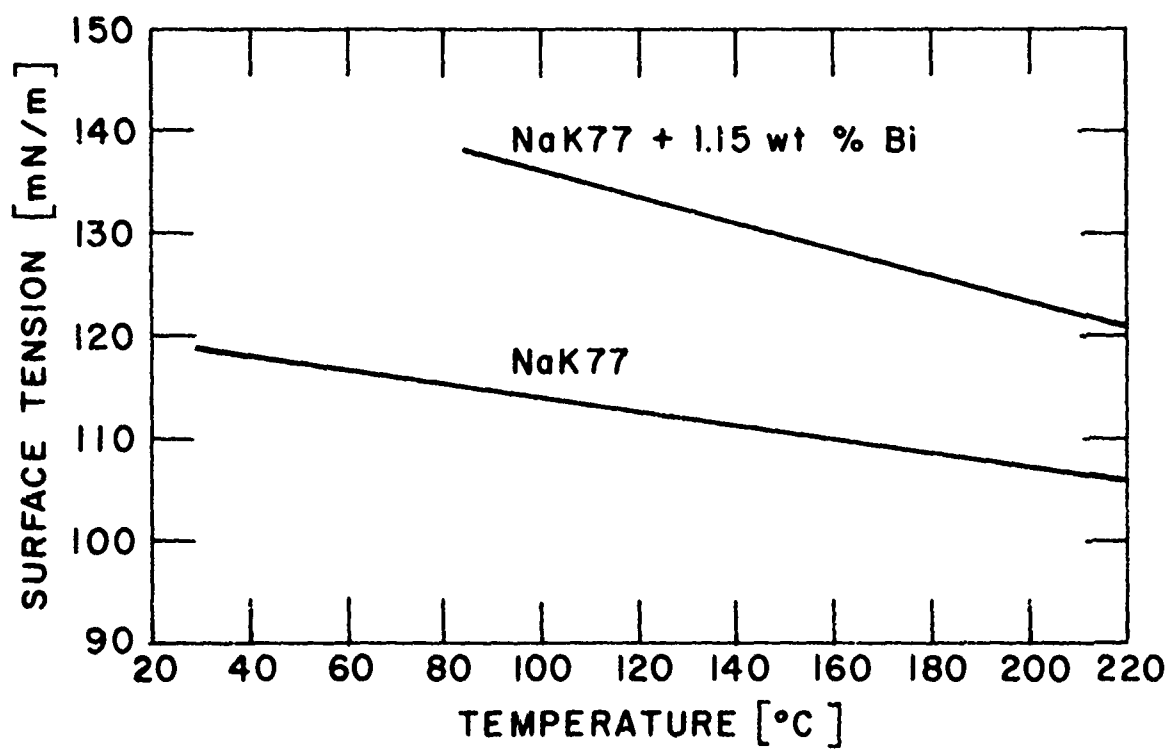
Figure IV.9 Surface tension vs temperature for NaK 77-Bismuth combinations
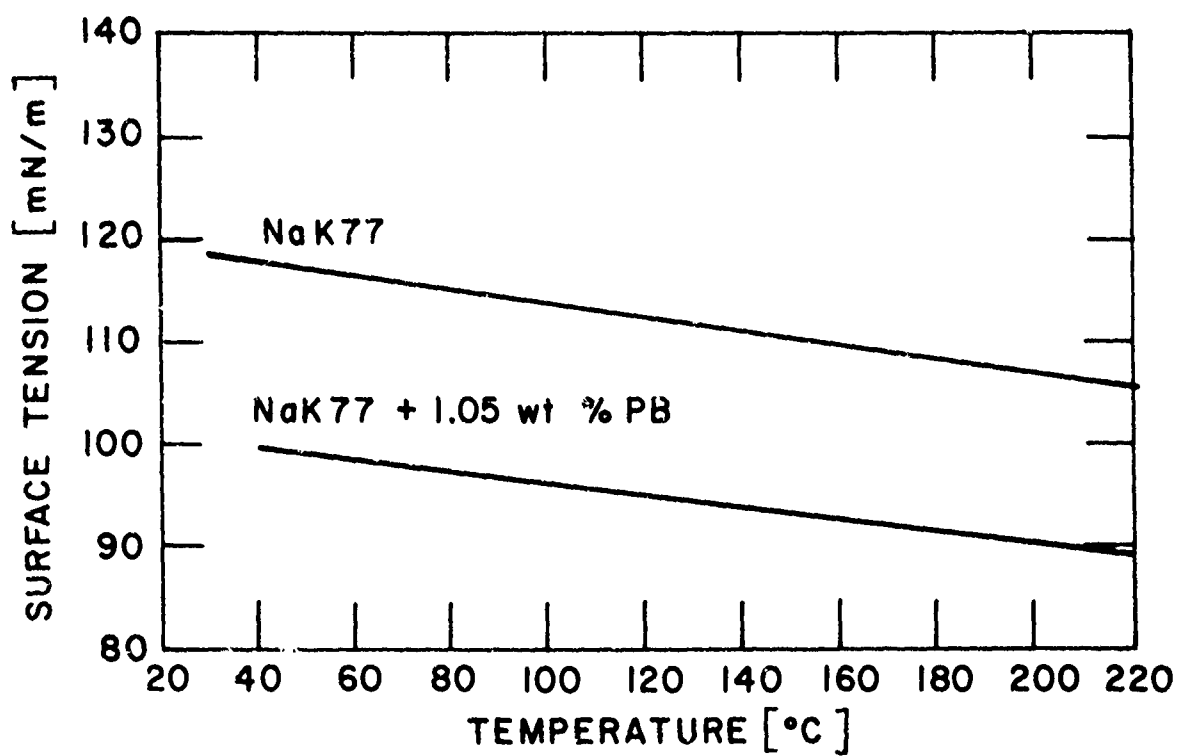
Figure IV.10 Surface tension vs temperature for NaK 77-lead combinations

-67-

lead, it might be possible to take advantage of this phenomenon to promote compound-like surface interactions with an additional solute, to stabilize films and bubbles.

IV.2.3 Effect of Nitrogen/Barium Interaction on Bubble Stabilization

Because nitrogen reacts with bulk barium to form Ba_3N_2 and is known to react with barium in molten sodium at high temperatures to form Ba_3N, the potential for a Ba-N_2 reaction in NaK should be evaluated for cases in which barium is used as a foam promoter. In the present experimental program, no change in surface tension was observed for a NaK 77-0.22 wt % Ba solution after nitrogen had been bubbled through it for two days at ambient temperature. A further examination of the reactivity question was done in a series of surface tension measurements at higher temperatures using a NaK 83-1.28 wt % Ba alloy (as in Section IV.1.13) Nitrogen flowed continuously through t̪ orifice tubes of the apparatus and measurements were made at nominal temperatures of 323, 373, 423, and 468 K. The results are plotted in Fig. IV.11, with reference curves for pure NaK 83 and NaK 83 containing 0.27 and 1.28 wt % barium. The data indicate that, over a period of about 3 days, during which the temperature rose stepwise from 323 to 423 K, the surface tension values were essentially parallel to the surface tension curve for the initial liquid metal system. The near parallelism tends to indicte a relatively slow reaction rate below 423 K. However, at 468 K, the surface tension departs from the curve noticeably, even in 2 to 4 hours, and in 3 days has unmistakably fallen to a value below that characteristic of a system with 0.27 wt % barium. This is taken to indicate that barium has been removed from the solution by combining in a compound with nitrogen.
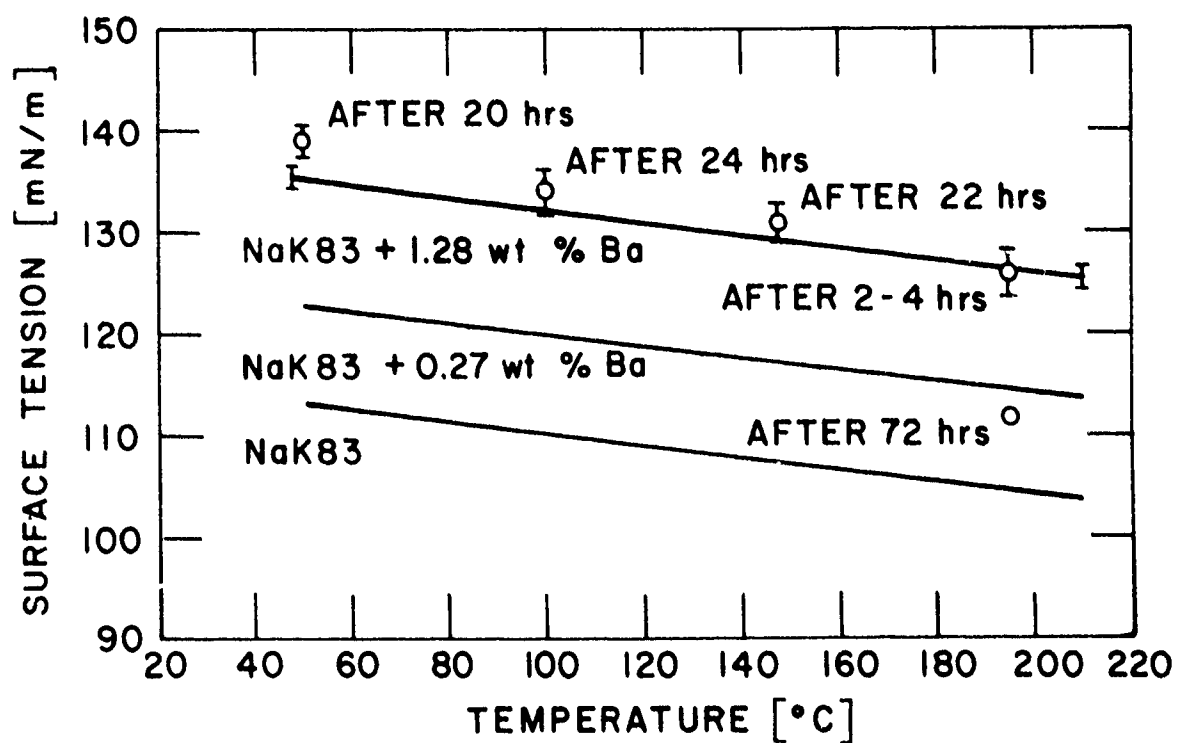
Figure IV.11 Surface tension of NaK 83-1.28 wt% Ba after exposure to
bubbling nitrogen. Indicated times are for length of
exposure at the respective temperatures, times are cumulative

-69-

For the perspective of utilization of a NaK-Ba alloy in a LMMHD machine, the results indicate that the depletion of barium by reaction with nitrogen at ambient temperature is a slow process. The fact that, even at 373 to 423 K, the rate is low, together with the fact that the system, which became depleted in barium at 468 K, still showed good bubble characteristics when retested at ambient temperature, suggests that good bubble performance at ambient temperature could be expected for long periods of operation. Exactly how long remains to be determined by further laboratory/engineering evaluation of the kinetics of the Ba-N_2 reaction in NaK.

V. END EFFECTS

V.1. Introduction

The overall efficiency of LMMHD generators can be significantly decreased by the effects associated with the passage of the working fluid through the regions at the upstream and downstream edges of the electrodes, where a strong gradient of the magnetic flux density exists, unless care is taken in the design of the generator. These effects, usually called "end losses", include:

a) short-circuiting electric current loops closing through the fluid regions beyond the electrodes (where the magnetic flux density is lower), i.e., the "end current loss"; and

b) an additional pressure drop due to the net ponderomotive force determined by the above-mentioned end currents, further referred to as "the end pressure loss." This is in excess of the pressure drop caused by the load current.

The effect of the end loss on the generator efficiency can be better understood by the aid of the equivalent electric circuit shown in Fig. V.1. The current density inside the channel is given by Ohm's law. The component perpendicular to the electrodes is

$$J_y = \sigma\left(-\frac{\partial\phi}{\partial y} + uB\right);\tag{V.1}$$

where σ is the electric conductivity of the working fluid, ϕ the electric field potential created by the voltage difference between the electrodes, and u the (constant and uniform) fluid velocity. The distribution of the
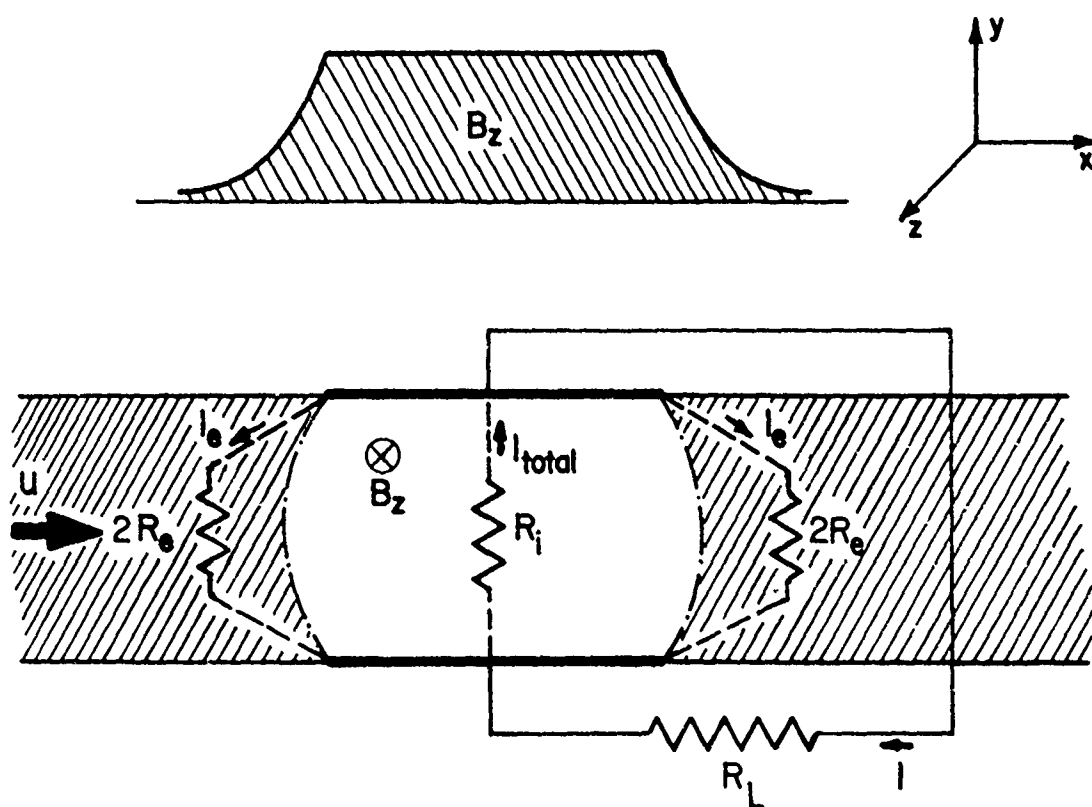
Figure V.1 The equivalent electric circuit of the generator

z component of the flux density B is represented in Fig. V.1; the x and y components of B are taken as zero.

In the region between the electrodes, the current density has the sign of the "velocity-induced" term of Eq. V.1, uB. Beyond the electrodes, where the magnetic field strength is reduced, the "electrostatic" term $-\frac{\partial \phi}{\partial y}$ becomes predominant and J_y changes sign, giving rise to a counter-current or end current I_e. Thus, beyond a certain curve where the current changes sign the fluid acts as an electric shunt, whose resistance (the end resistance) is represented by R_e. Note that R_e includes the effect of both ends. The generator internal resistance is $R_i \approx \frac{h}{\sigma A w}$; where h is the electrode half spacing, A the aspect ratio (ratio of electrode length 2a to electrode spacing 2h), and w the channel height parallel to B. The expression for R_i is approximate because, depending on the magnetic flux density distribution, some of the generated current may flow outside of the region between the electrodes.

Various methods are available to control end losses, including:

1. Increasing the aspect ratio A. This leads to a decrease in the value of R_i without affecting R_e, and thus proportionally less end loss. However, attainable values of A are limited by the available pressure difference and the required terminal voltage.

2. Shaping the decay of the magnetic flux density beyond the electrodes in such manner as to increase R_e (and decrease R_i. This method will be evaluated in Sections V.4 through V.6.

3. Inserting electrically insulating vane(s) parallel to the flow in the regions outside of the electrodes, thereby increasing the end current path length and R_e without affecting R_i [Rossow et al (1961)]. This method implies a certain increase in the viscous losses in the end regions; the increased viscous loss has to be weighted against the reduced end loss. Vanes are considered throughout the remainder of Section V.

Several aspects of the above methods have been treated in the literature by analytic two-dimensional [Fishman (1959), Sutton et al (1961), Lavrentiev (1967, 1968), Gubarev et al (1970)] and three-dimensional [Vasiliev and Lavrentiev (1970)] approaches, as well as by analog modelling [Moszynski (1967)]. A few experimental investigations have been reported [Moszynski (1967), Petrick et al (1968)]. The effect of the fringing magnetic field on the pressure losses has also been estimated [Hoffman and Carlson (1971)]; however, no investigation has been reported on the effect of the fringing field upon the viscous losses associated with the insertion of insulating vanes in the flow. Methods for the reduction of the end losses in a two-phase flow have also been proposed [Petrick et al (1968), Moszynski and Agrawal (1968), Branover et al (1977)] and recently tested experimentally [Branover et al (1978)].

The purpose of the present study is to give a quantitative evaluation of the effectiveness of different methods for end loss reduction and to supply useful data for the design of the LMMHD generators. The model is described in Section V.2, and the reference case--no magnetic field extension past the electrode ends--covered in Section V.3. Previous analytical solutions are summarized in Section V.4, and the numerical solution is

described in Section V.5. The numerical results are compared with the analytical solutions and analog data in Section V.6 with zero or one insulating vane. The results with insulating vanes are presented in Section V.7 for an exponential magnetic field extension and Section V.8 for a natural extension. The recommendations for the reduction of end losses are in Section V.9.

V.2 Model

Like most of the previous studies, the present investigation is based on a two-dimensional approach (ignoring the direction parallel to B). The channel configuration, magnetic field distributions considered, and the notations used are presented in Fig. V.2.

The assumptions made are:

a) The fluid velocity u is uniform and constant everywhere in the channel, and is directed along the x-axis. Viscous effects are neglected.

b) The magnetic field is directed along the z-axis and depends only on x. The magnetic Reynolds number is negligible (compensated channel).

c) The electrodes are perfect electrical conductors; the walls and vanes are perfect insulators.

d) The vanes are of infinitesimal thickness and do not disturb the flow.

V.3 The Reference Case: No Magnetic Field Extension

A magnetic field of constant flux density along the electrodes and of zero flux density beyond them was chosen as the "reference case" for

Figure V.2 The channel configuration and magnetic field distributions
          considered: 1.-The reference case; 2.-Exponentially de-
          caying overhang; and 3.-Natural overhang.
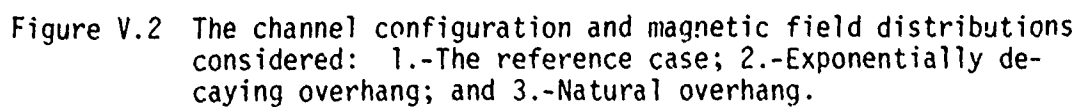
estimating the effectiveness of the different methods chosen for the reduction of the end losses because of its simplicity and the availability of established analytical solutions. Note that it is neither realistic nor desirable as the abrupt termination leads to large end currents. The above case has been studied both analytically [Sutton et al (1961), Fishman (1959)] and by analog modelling [Moszynski (1967)]. Also, a preliminary attempt at optimizing the number of insulating vanes to give the maximum efficiency is available for this case [Moszynski (1967)].

It was found by Sutton et al (1961) that for an aspect ratio $A > 0.7$, the resistance ratio R_i/R_e can be approximated by

$$\frac{R_i}{R_e} \simeq \frac{1}{A} \; \frac{2 \ln 2}{\pi} . \qquad (V.2)$$

In this case the maximum attainable efficiency can easily be related to the aspect ratio, as plotted in Fig. V.3. They also determined efficiency curves as a function of aspect ratio and load factor F, as shown in Fig. V.4 for $A = 1$, 2, and 3. (The other curves in Fig. V.4 will be explained later, and all curves are used for comparison with the numerical solutions.)

V.3.1 The Effect of Insulating Vanes on the End Resistance

If it is assumed that an "infinitely-long" insulating vane at the center line has the effect of "doubling" the apparent aspect ratio of the channel, and that n infinitely-long equidistant insulating vanes multiply the aspect ratio by a factor n+1, then the effect of the vanes on the maximum attainable efficiency is easy to infer from Eq. V.2 and Fig. V.3. However, there is no analytical or experimental confirmation for this.

An electric analog model [Moszynski (1967)] seemed to indicate that a vane of a length 7h (2h being the distance between the electrodes)
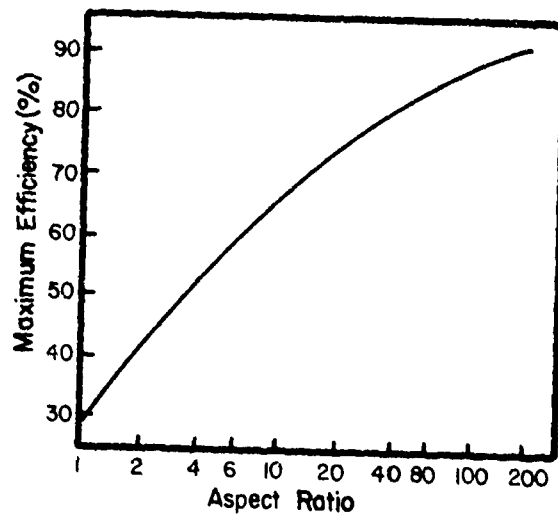
Figure V.3 The maximum attainable efficiency as a function
of aspect ratio with no magnetic field extension.
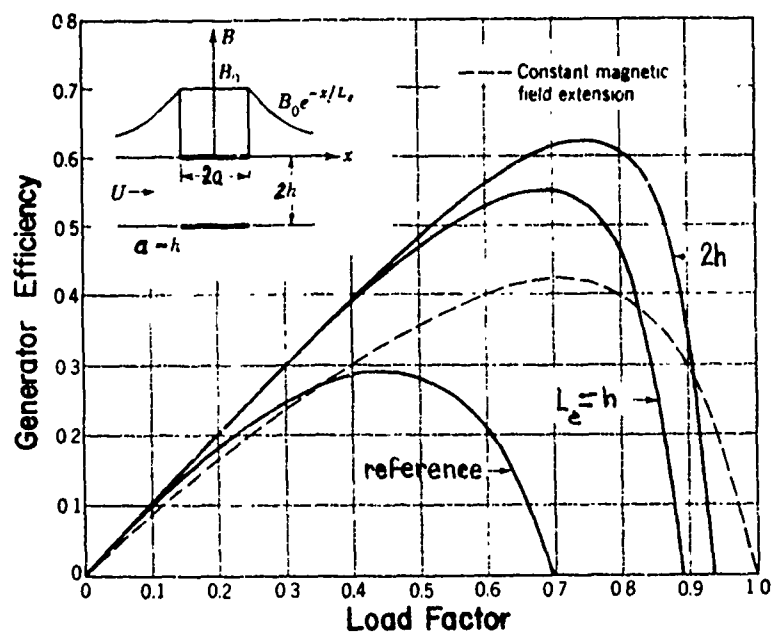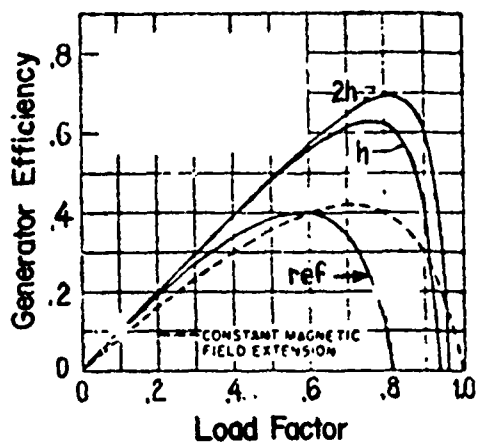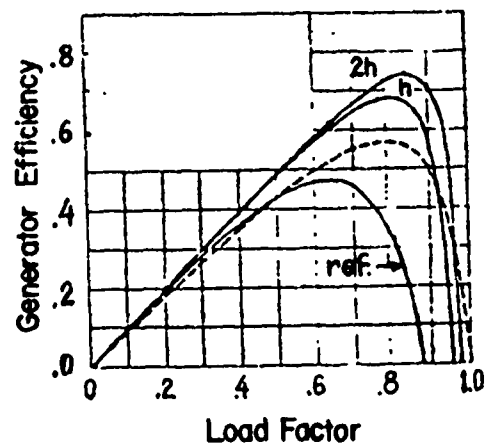
Figure V.4   Analytical efficiency curves from Sutton et al
(1961) for aspect ratios 1, 2, and 3.

has practically the same effect on R_e as an infinitely-long vane. A
later analytical solution by Lavrentiev (1968) found that to attain a
shunt resistance R_e within 5% of that for an infinitely-long vane,
the finite vane should have a length of at least 22h. Also, a vane
7h long would yield a value for R_e 15% lower than for an infinite vane.

The data from Moszynski's (1967) analog experiment may also be used to
find the influence of the number and length of the insulating vanes on
the ratio R_i/R_e and, hence, on the efficiency. The analog data seem
to be well correlated by

$$(\frac{R_i}{R_e})_n = (\frac{R_i}{R_e})_{nv} \quad \exp[-\frac{\sqrt{n}}{6.5}(\frac{\ell}{h})^{0.7}] \quad \text{for} \quad 0 \leq \ell \leq 4h, \qquad (V.3)$$

as shown in Fig. V.5, where n is the number of vanes, ℓ is the vane length,
and the index nv refers to the case with no vanes. The analog data do not
confirm the hypothesis that n infinitely-long equidistant vanes multiply
the apparent aspect ratio by a factor of $n+1$, as shown in Fig. V.5. However,
if the R_e values are corrected by 15%, as suggested by the study of
Lavrentiev (1968), an infinitely-long vane would indeed have the effect of
doubling the apparent aspect ratio.

V.3.2 The Effect of the Insulating Vane(s) on the Viscous End Loss

To calculate the viscous loss caused by the insertion of the vanes,
the assumptions needed are [Moszynski (1967)]:

   a) The friction factors for fully-developed pipe flow apply,

   b) The vanes are thin and shaped to eliminate contraction and enlarge-
       ment losses, and

   c) The electromagnetic interactions have a negligible effect on the
       pressure drop.
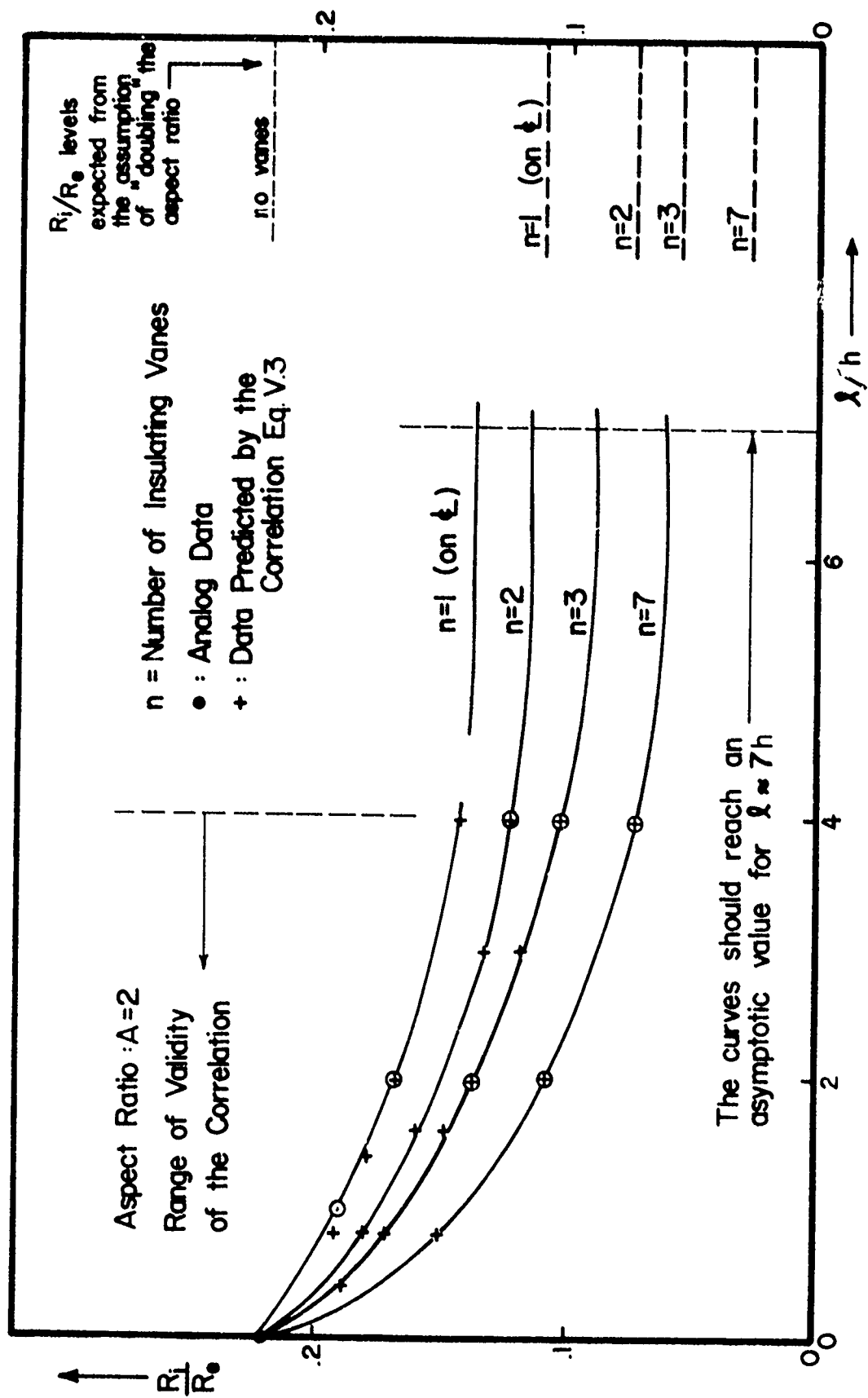
Figure V.5   The dependence of R_i/R_e on the number and length of the insulating vanes.

Experimental measurements of the pressure drop in a vaned rectangular channel [Moszynski (1967)] have proven that the first two assumptions are valid within 10% accuracy. The third assumption is clearly true for the reference case--no magnetic field exists beyond the electrodes where the vanes are situated. In an actual generator the velocity profile would be modified by the magnetic field and this assumption might not be valid.

V.4 Analytical Solutions for Magnetic Field Extensions

The cases of magnetic field overhang examined in the literature include: a "constant" overhang (magnetic field decreasing abruptly to zero at a certain point beyond the electrodes), a linearly decaying overhang, and an exponentially decaying overhang. The most significant reduction in the end losses was found by Sutton et al (1961) to be associated with the exponential overhang, as shown in Fig. V.4. The characteristic length of the exponential field overhang, the distance from the point where the decay begins to the point where the flux density has decreased to 1/e of its initial value, is referred to as "the e-fold length" L_e (see Fig. V.2).

The results presented in Fig. V.4 suggest that an increase in the e-fold length L_e brings about an increase in efficiency. This dependency will be quantitatively analyzed in Section V.7.2.1. Note that for L_e = 2h the maximum efficiency is almost twice that of the reference case (see also Table V.1).

V.5 The Numerical Technique

The analytical studies referenced above determine the electric field distribution in a longitudinal section of the MHD channel by solving the Laplace equation in a domain obtained by conformal mapping of that section or of a part of it. The insertion of an insulating vane at the center-line

of the channel makes the conformal mapping more difficult, but the case
of a semi-infinite insulating vane at center-line was solved analytically
by Lavrentiev (1967) for the case of a magnetic field with arbitrary longi-
tudinal distribution. However, no analytic solution is available for the
cases of exponential or arbitrary field overhangs and one or more vanes of
finite length. To evaluate the reduction in end losses in this latter
case, a numerical solution was sought in the present study, as described
below.

A computer program (ELLPACK) for solving elliptical partial equations,
presently being developed in a cooperative effort by Harvard, Texas and
Purdue Universities, was adapted for finding the electric field distribution
and the efficiency of the LMMHD generator. In an early stage of this investi-
gation, the ELLPACK program [Rice (1977)] was used to solve the Laplace equa-
tion in a rectangular domain with Dirichlet, Neumann, and mixed-type boundary
conditions. However, the solution with more than one insulating vane present
required significant modifications in the program. The final form of the
program is described in Appendix C.

V.5.1 The Mathematical Model

A schematic drawing of the channel and the magnetic flux densities
considered is given in Fig. V.2. Because of symmetry, a complete solution
for the electric field can be obtained by solving the Laplace equation in
one quadrant of the x-y plane.

The mathematical model used for the upper right quadrant is:

$$\partial^2 \phi(x,y)/\partial x^2 + \partial^2 \phi(x,y)/\partial y^2 = 0, \qquad 0 < x < x_{max}, \; 0 < y < h \qquad \text{(V.4a)}$$

$$\phi(x,h) = F h u B_0, \qquad 0 < x < a \qquad \text{(V.4b)}$$

$$\partial \phi(x,h)/\partial y = u B_0 b(x), \qquad a < x < x_{max} \qquad \text{(V.4c)}$$

$$\phi(x_{max}, y) = 0, \qquad\qquad 0 < y < h \qquad\qquad (V.4d)$$

$$\phi(x, 0) = 0, \qquad\qquad 0 < x < x_{max} \qquad\qquad (V.4e)$$

$$\partial\phi(0, y)/\partial x = 0, \qquad\qquad 0 < y < h \qquad\qquad (V.4f)$$

The presence of an insulating vane on the axis between the points $(v, 0)$ and $(v_{max}, 0)$ was modelled by requiring that the electric current density normal to the vane is zero, i.e., by replacing Eq. V.4e with:

$$\partial\phi(x, 0)/\partial y = uB_0 b(x), \qquad\qquad v \leq x \leq v_{max}. \qquad\qquad (V.4g)$$

A convenient feature is to normalize the distance between the electrodes as $2h = 2$ or $h = 1$. In this way, the x coordinate of the electrode end becomes numerically equal to the aspect ratio, i.e., $a = A$. The infinite-length channel is approximated by a finite-length one, with end points $\pm x_{max}$, where x_{max} is much larger than either a or h.

The magnetic flux density is written as $B = B_0 b(x)$, where B_0 is the flux density at $x = 0$. For the exponential overhang case the distribution function is

$$b(x) = \begin{cases} 1, & 0 < x \leq a \\ \exp[-(x-a)/L_e], & a < x. \end{cases} \qquad\qquad (V.5)$$

The boundary condition Eq. V.4d requires some prior knowledge of the electric potential distribution, namely the distance from the electrodes where the electric potential can be considered to be zero. In the analog experiments of Moszynski (1967) it was found that the region between $x = 10h$ and $x = 20h$ contributed no more than 2% to the end current shunt resistance. This was used in choosing $x_{max} = 16h$.

V.5.2 The Efficiency Computation

To determine the net current which can be drawn from the system (per unit channel width in the z direction), J_y has to be integrated along a line parallel to the x-axis; by symmetry this can be $2J_y$ from $x = 0$ to $x = \infty$ (to $x = x_{max}$ in the program). The value obtained should be independent of y for y between -h and +h. The total electric power P_e to the load per unit channel width is the product of this current and the load voltage

$$V_L = 2F\phi_0 = 2FuB_0h. \qquad (V.6)$$

The result is

$$P_e = 4FuB_0h\sigma \int_0^\infty [-\partial\phi(x,y)/\partial y + uB_0b(x)]dx. \qquad (V.7)$$

The generator efficiency is

$$n_i = P_e/W, \qquad (V.8)$$

where W is the rate of flow work done against the pressure difference Δp per unit width,

$$W = u \cdot \Delta p \cdot 2h \cdot 1 \cdot. \qquad (V.9)$$

The pressure difference Δp is found by integrating the ponderomotive force $\vec{J} \times \vec{B}$ along the channel and averaging over y, i.e.,

$$\Delta p = \frac{1}{2h} \int_{-h}^{+h} dy \int_{-\infty}^{+\infty} [J_y(x,y)B(x)]dx =$$

$$= \frac{4\sigma}{2h} \int_0^h dy \int_0^\infty dx[-\partial\phi(x,y)/\partial y + uB_0b(x)]B_0b(x). \qquad (V\ 10)$$

It can be shown (see Appendix C) that the group $\sigma u^2 B_0^2$ is a common
factor in the expressions for both P_e and W, and that the terms do not appear
separately. Therefore, in this model the efficiency η does not depend on
any of these parameters.

To check the validity of the current calculations, the electric current
integration was performed at three different parallel locations--$y=h/4$, $h/2$,
and $3h/4$. This resulted in differences of up to 8% between the first and
last level locations. However, when the integration was performed along
the path MNP in Fig. V.2 this difference fell below 1%. An alternative way
to reduce to about 1% the differences between the integration results is to
set the right boundary of the domain at $x_{max} = 32h$. Therefore, for all
the cases with no more than one insulating vane the value $x_{max} = 32h$ is
used.

V.5.3 Plots of the Electric Potential Inside the Channel

The solution of Eq. V.4 was provided by the computer both as tabulated
values of the electric potential $\phi(x,y)$ for every mesh point, and/or as
plots of the equipotential lines of ϕ. The latter form of output is useful
for getting a better understanding of the physical effect of different
magnetic field parameters, insulating vanes, etc. on the electric
field (and implicitly the current density) distribution inside the channel.
Some typical plots are presented in Figs. V.6 and V.7.

V.6 Comparison of the Numerical Results with the Existing Analytical
Solutions and Analog Data

A useful test of the computer program's accuracy is a comparison of
its results with those of a few of the existing exact solutions resulting
from an analytical approach.
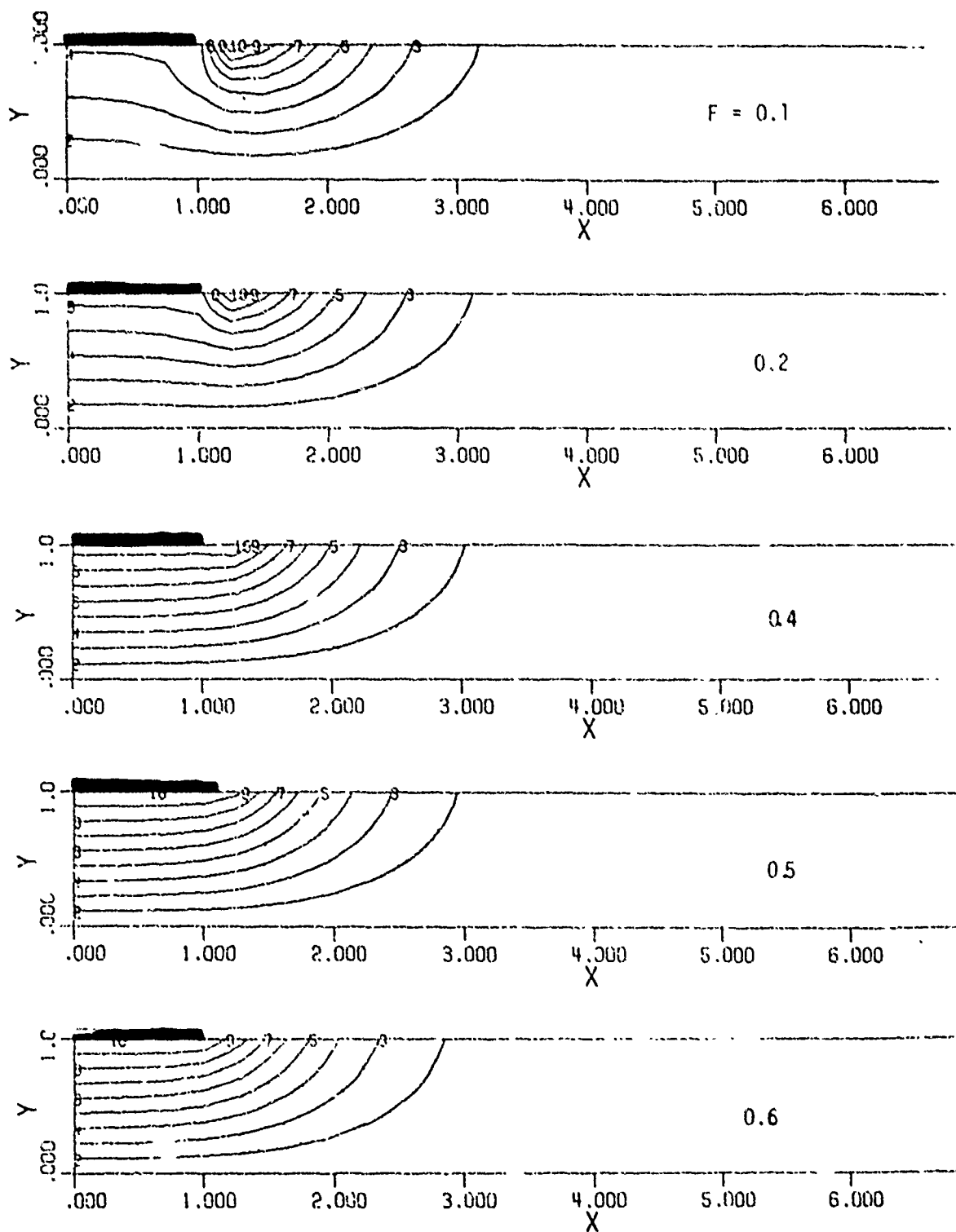
Figure V.6 Electric potential distributions for different load factors, $A = 1$, $L_e/h = 1/2$, and no insulating vanes.
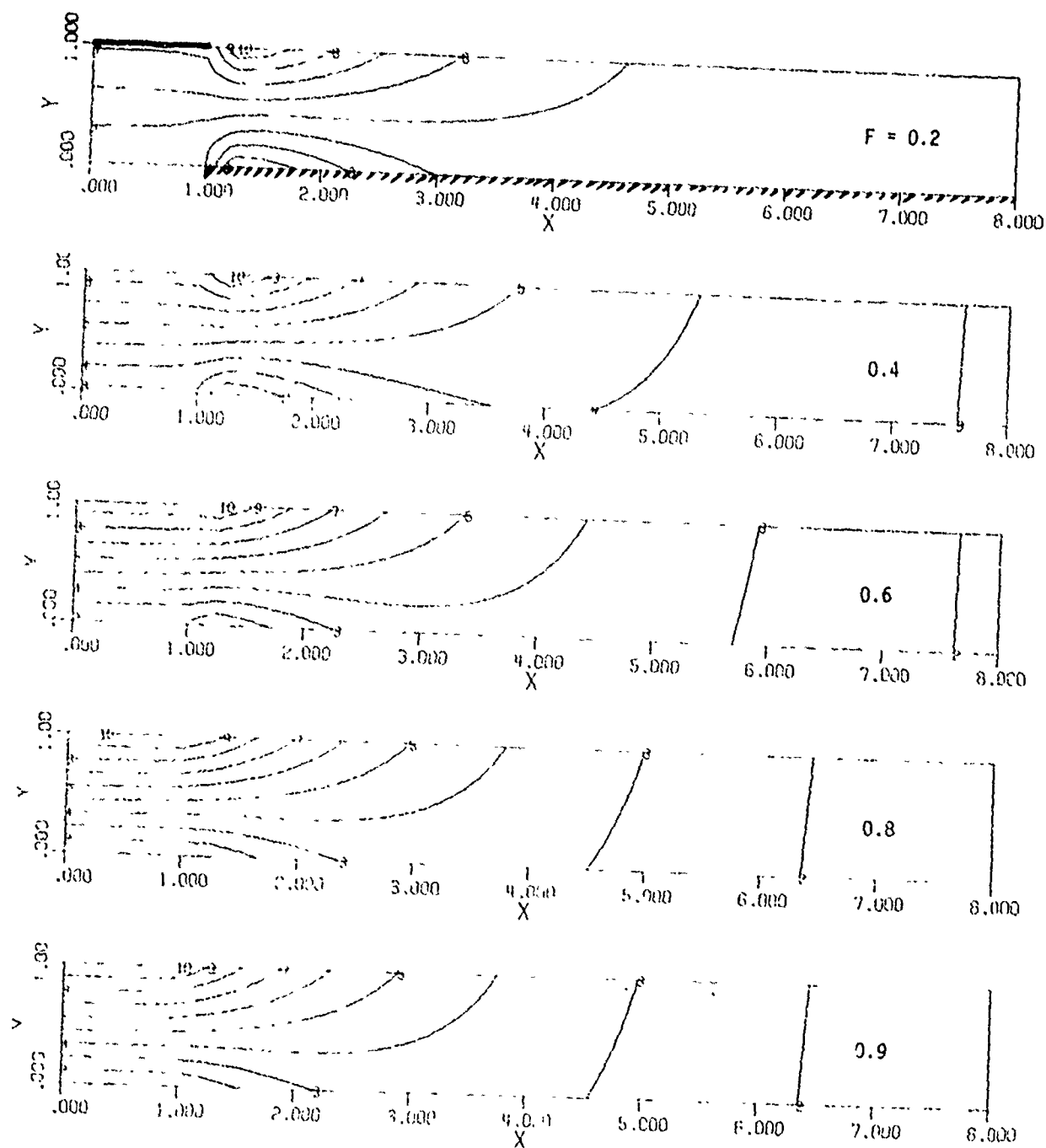
Figure V.7 Electric potential distributions for different load factors
A = 1, $L_e/h = 1$, and one "infinitely long" vane on the centerline

V.6.1 The Reference Case

The maximum efficiencies reported by Sutton et al (1961), about 0.29 and 0.40 for A = 1 and A = 2, respectively, as well as the efficiency vs. load factor curves, are reproduced by the computer code with an accuracy within 1%. This is demonstrated by comparing Figs. V.4.a and V.4.b with Fig. V.8. Note that on Fig. V.8 and the following figures all distances are normalized by h, the half distance between the electrodes, V and V_{max} are the positions of the left and right edges of the insulating vanes, MAXEFF is the maximum value of the efficiency, and MAXLOAD is the load factor at MAXEFF.

V.6.2 An Exponential Magnetic Field Overhang with No Vanes

The dependence of the efficiency on the load factor has been computed by Sutton et al (1961) on the basis of an analytical solution for the electric potential, see Fig. V.4. The computer code reproduced the data for L_e = h and 2h with less than 3% error for both A = 1 and A = 2 (see Figs. V.9 and V.10). In addition, the computer results for L_e = h/2 (one-quarter of the interelectrode distance) are shown.

V.6.3 No Magnetic Field Overhang with an Insulating vane on
the Center Line

The electric analog of this configuration reported by Moszynski (1967) was intended to determine the ratio R_i/R_e for a variety of vane lengths and positions in order to compute the generator efficiency according to the equation

$$\eta_i = \frac{F}{1 - F} [1 - F(1 + R_i/R_e)]. \tag{V.11}$$
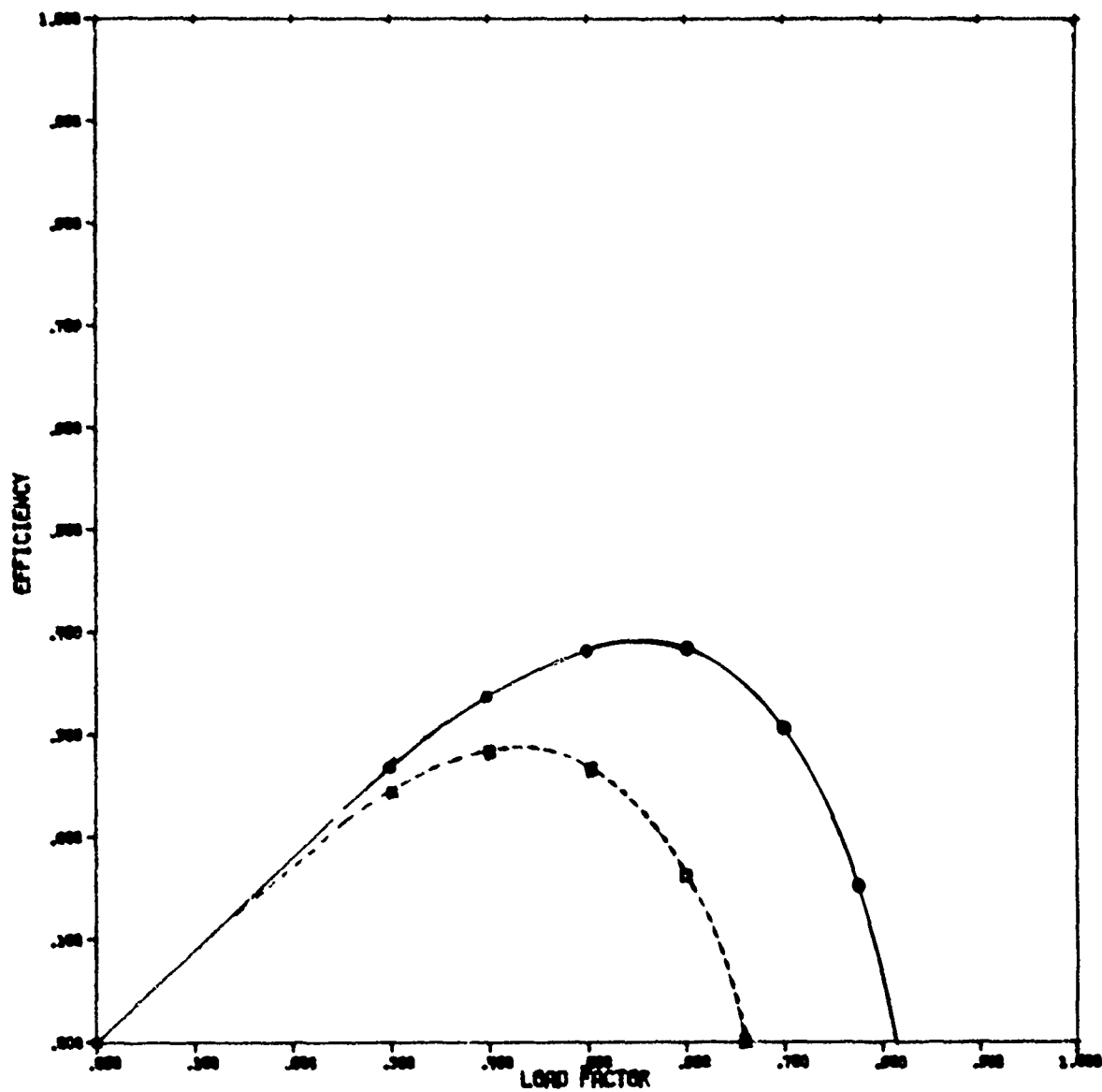
L_e/h	A	V	VMAX	XMAX	MAXEFF	MAXLOAD
.0	1.00	31.50	32.00	32.00	.28	.44
.0	2.00	31.50	32.00	32.00	.40	.50

Figure V.8 Efficiency vs Load Factor for the reference case, A = 1 and 2
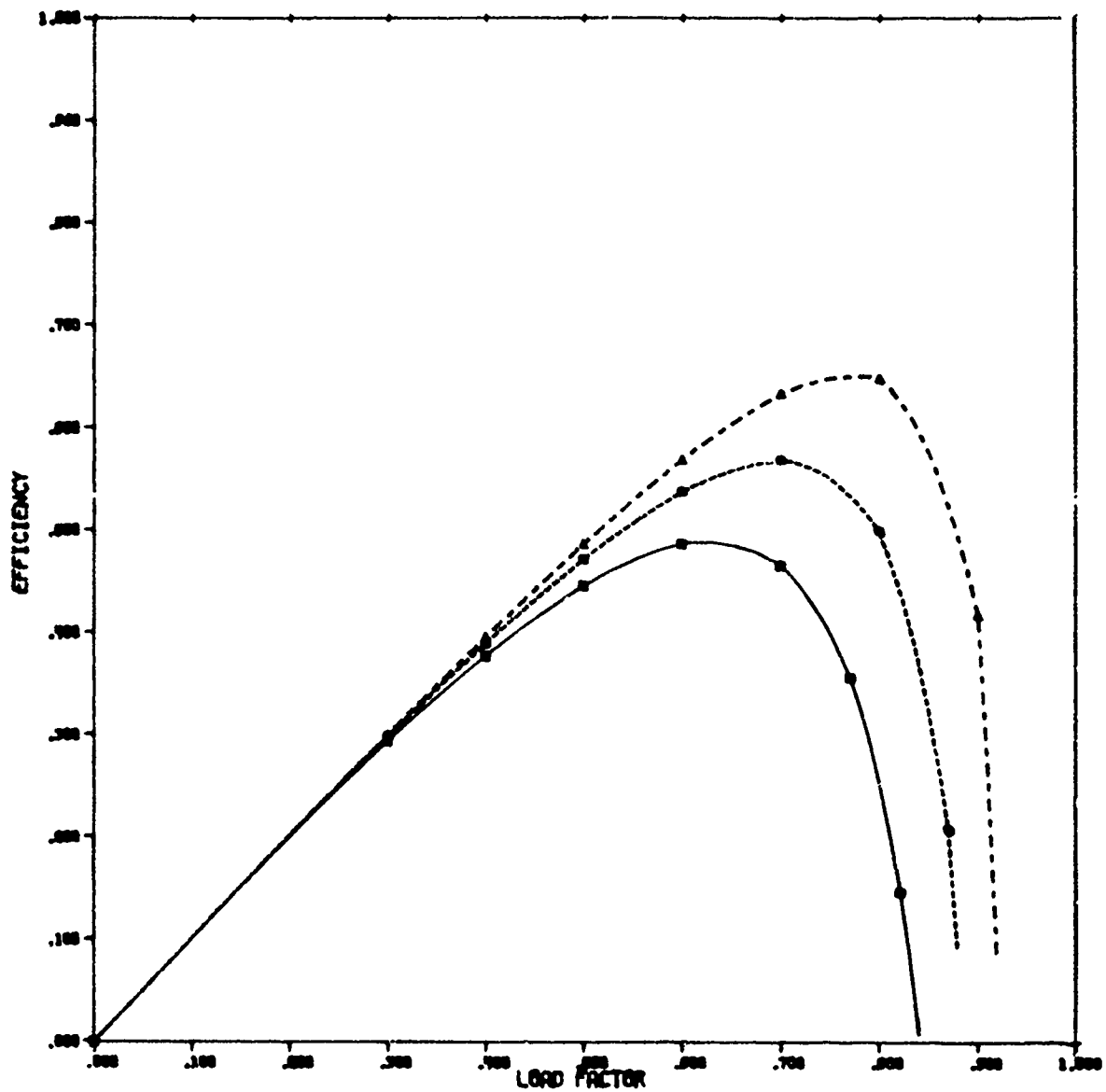
L_e/h	f_i	V	VMAX	XMAX	MAXEFF	MAXLOAD
.50	1.00	31.50	32.00	32.00	.49	.62
1.00	1.00	31.50	32.00	32.00	.57	.70
2.00	1.00	31.50	32.00	32.00	.65	.77

Figure V.9 Efficiency vs load factor for an exponential field
overhang with no vanes, A = 1
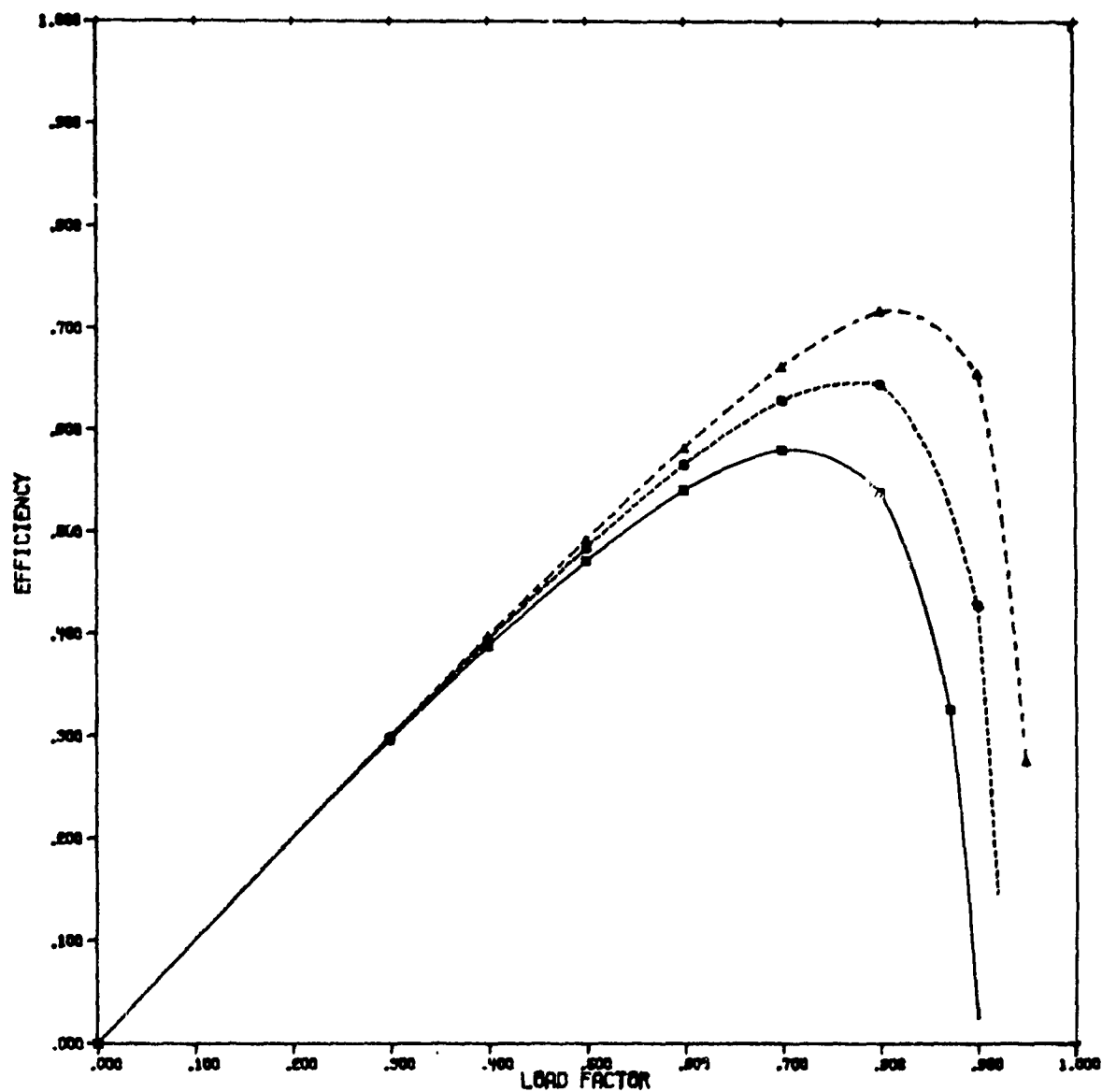
-91-

Figure V. 10 Efficiency vs load factors for an exponential
field overhang with no vanes, A = 2

-92-

Moszynski found that increasing the vane length ℓ beyond a value of 7h (3.5 times the interelectrode distance) does not have any significant effect on the R_i/R_e ratio; and, therefore, a vane of this length would be practically equivalent to an infinite-length vane. Using the data for R_i/R_e reported by Moszynski (1967), the efficiency vs. load factor curves for the cases of no vanes and center-line vanes of lengths 4h and 6h are plotted in Fig. V.11.

The computer code accurately (within 1%) reproduced the curve for the "no vane" case of Moszynski (1967), Fig. V.12. However, a significant difference was found for the last two cases(ℓ = 4h and ℓ = 6h). This difference is apparently due to the fact that the analog experiment was based on measuring the currents set up by the electric potential between the electrodes and could not simulate the "velocity induced" current due to $\vec{u} \times \vec{B}$. Moreover, increasing the vane length beyond ℓ = 7h in the computer code brought about a further increase in efficiency. This means that the asymptotic limit found by Moszynski (1967) was not confirmed by the numerical technique. This agrees with the theoretical work reported by Lavrentiev (1968).

V.7   An Exponential Magnetic Field Extension With Insulating Vanes

V.7.1   One Infinitely-Long Insulating Vane at the Center Line

When the magnetic field extends exponentially beyond the electrodes, the insertion of insulating vanes on the center line from the points x = ± a where the electrodes end up to the boundaries x = ±x_{max} increases the maximum attainable efficiency, as shown in Table V.1 for L_e/h = 1 and 2. The efficiency curves for aspect ratios of 1 and 2 and for vanes with ℓ = 15h and ℓ = 14h are shown in Figs. V.13 and V.14, respectively.
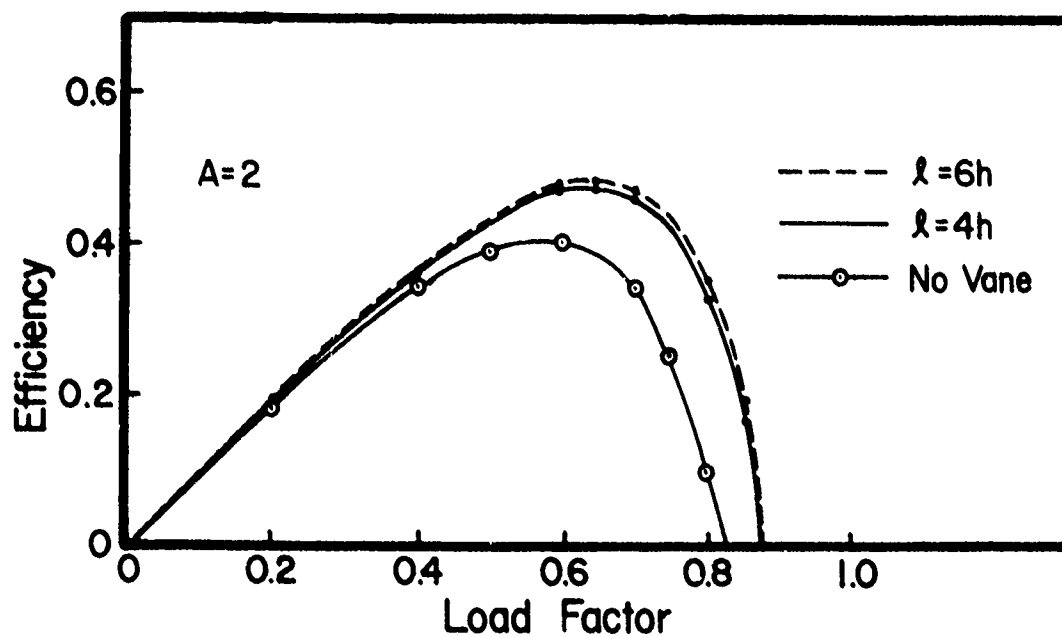
Figure V.11 Efficiency curves computed with the analog data
for R_i/R_e from Moszynski (1976) for A = 2

Figure V.12 Efficiency vs load factor for no fringing field
and one vane at center-line, A = 2
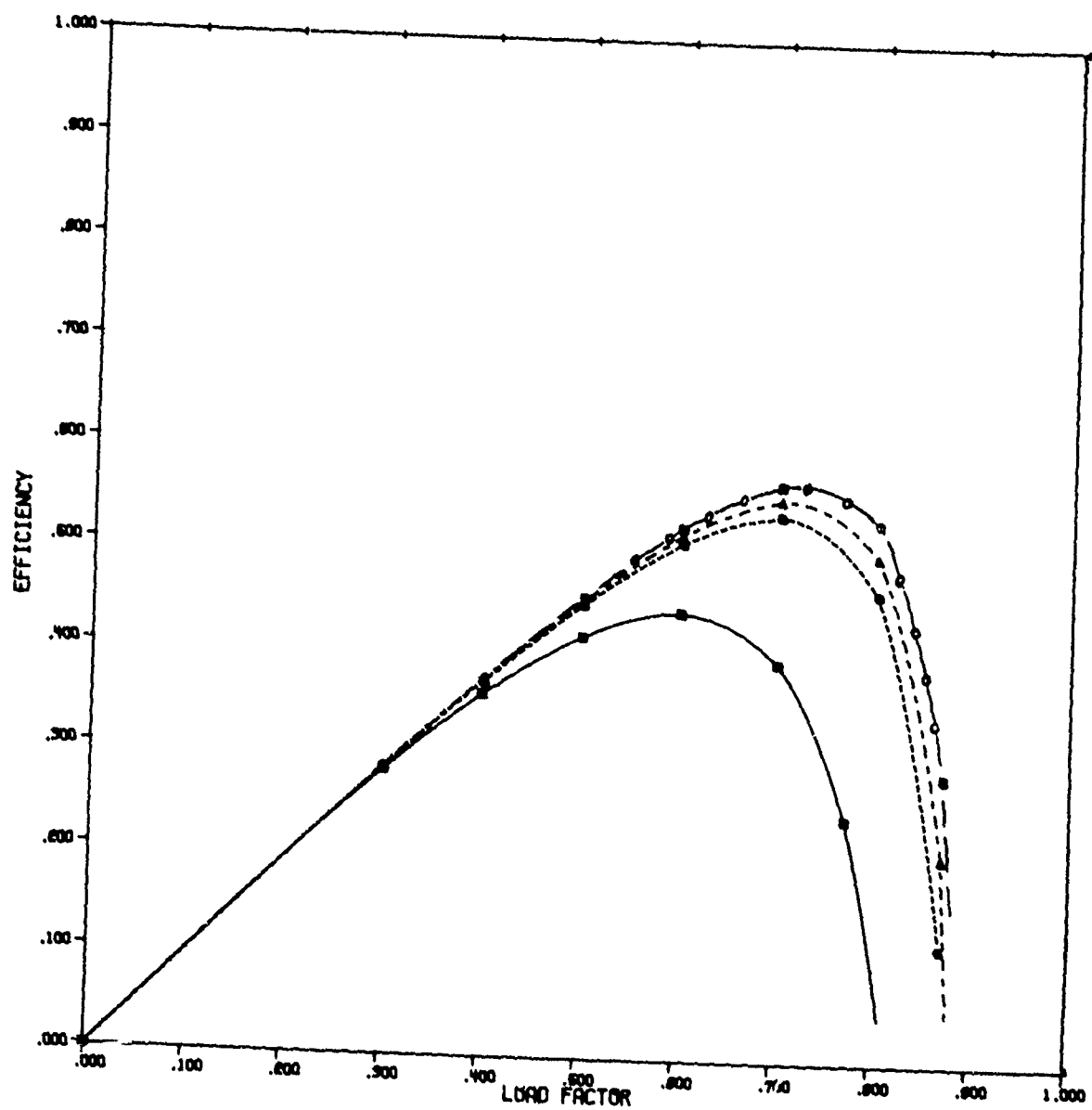
	L_e/h	A	V	VMAX	XMAX	MAXEFF	MAXLOAD
	.0	2.00	31.50	32.00	32.00	.40	.56
	.0	2.00	2.00	6.00	32.00	.54	.70
	.0	2.00	2.00	8.00	32.00	.55	.70
	.0	2.00	2.00	12.00	32.00	.57	.72
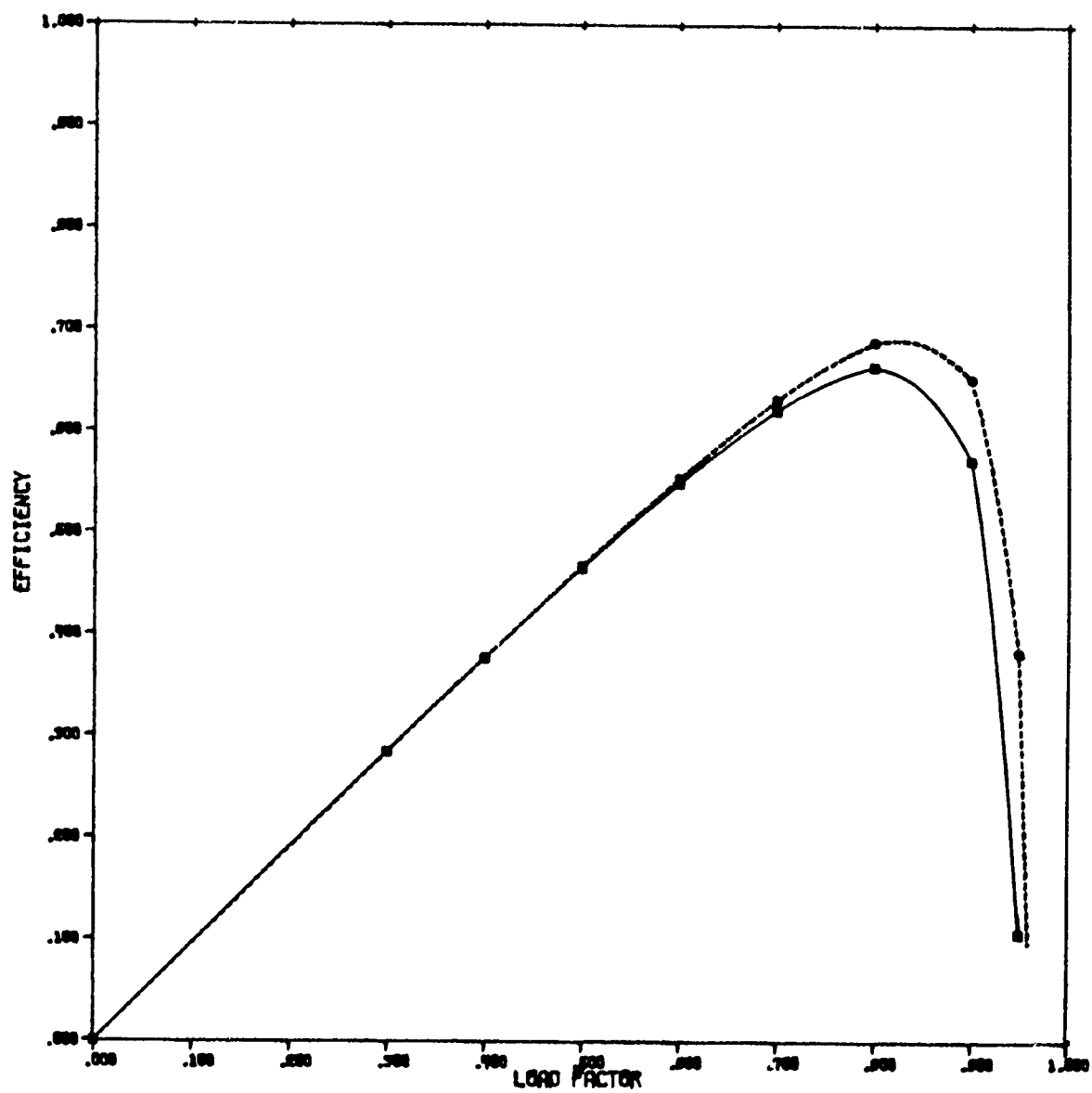
L_e/h	A	V	VMAX	XMAX	MAXEFF	MAXLOAD
1.00	1.00	1.00	16.00	32.00	.66	.80
2.00	1.00	1.00	16.00	32.00	.69	.82

Figure V.13 Efficiency vs load factor for an exponential field
overhang and an insulating vane of length ℓ/h=15, A = 1
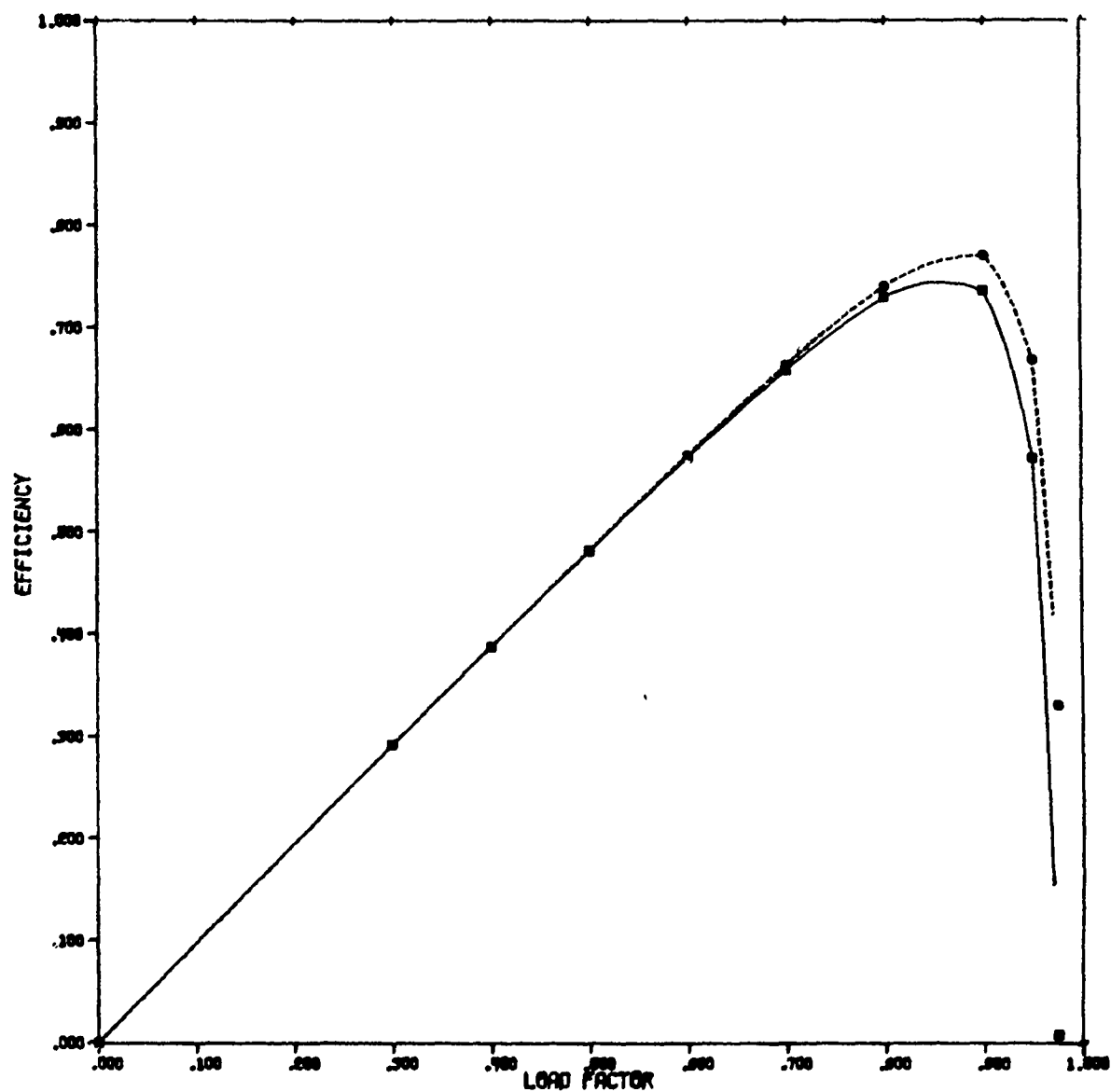
Le/h	A	V	VMAX	XMAX	MAXEFF	MAXLOAD
1.00	2.00	2.00	16.00	32.00	.74	.86
2.00	2.00	2.00	16.00	32.00	.77	.89

Figure V.14 Efficiency vs load factor for an exponential field overhang
and an insulating vane of length ℓ/h = 14, A = 2

TABLE V.1

Maximum Attainable Efficiencies for Exponential Field Overhang and One

"Infinitely-Long" Vane

(The percentages in the brackets indicate the increase with respect to

the reference case)

Aspect ratio	Maximum Efficiency				
	Reference Case	Exponential overhang, no vanes		Exponential overhang, one "infinitely long" vane	
		Le/h=1	Le/h=2	Le/h=1	Le/h=2
1	.28	.57 (203%)	.65 (232%)	.66 (235%)	.69 (246%)
2	.40	.65 (162%)	.72 (180%)	.75 (185%)	.77 (192%)

V.7.2 The Influence of the Magnetic Field Distribution and the

Insulating Vane Length

V.7.2.1 Magnetic Field Overhang Length

For the case of an exponentially decaying magnetic field overhang

it is obvious that an increase in L_e leads to an efficiency increase, see

Figs V.13 and V.14. While this increase is not large for an infinitely-long

vane on the center line (see the last two columns of Table V.1), better

results may be attained by optimizing the vane length and position (especially

when viscous loss is included).

V.7.2.2 Vane Length

Since it is obvious that an infinitely-long insulating vane would

be technologically inconvenient, it seems reasonable to choose a length

such that only a small efficiency improvement would be obtained by a

further increase in length. The maximum attainable efficiency for A = 2

and L_e = h is plotted in Fig. V.15 against the insulating vane length.

V.7.2.3 Vane position

The axial position of a short vane has been found to influence

significantly the efficiency. The efficiency curves of Fig. V.16 for

different axial positions of a short vane of constant length ℓ = 8h indicate

that the best efficiency is obtained when the vane begins at a distance

equal to $L_e/2$ outside of the electrode end. This was confirmed by

computations made for both L_e/h = 1 and 2.

V.7.3 The Influence of Additional Insulating Vanes

As mentioned in Section V.5.2, the computer program was modified

to provide the solution for the electric field with insulating vanes at the

center line and/or at intermediate positions within the channel. Since the

numerical integration technique was modified for the new version of the

program, tests were run for cases with an available analytical solution and

for the case of one insulating vane on the center line. The results

obtained previously (see Sections V.6.2 and V.7.2) were reproduced within

the accuracy allowed by the discretization mesh employed.

To run the new program, which required an increased number of horizontal

mesh lines, within a memory field length of 150 K, the right boundary of

the domain had to be reduced from x_{max} = 32h to x_{max} = 16h, then to

x_{max} = 14h. This change did not affect the results by more than about

3% (compare the maximum efficiency from the first case of Fig. V.16 with that

of line 4 of Table 5.2).

V.7.3.1 Two Insulating Vanes

For a certain vane length, the best efficiency was obtained when

the two insulatiing vanes were approximately equidistant (within the accuracy

-99-
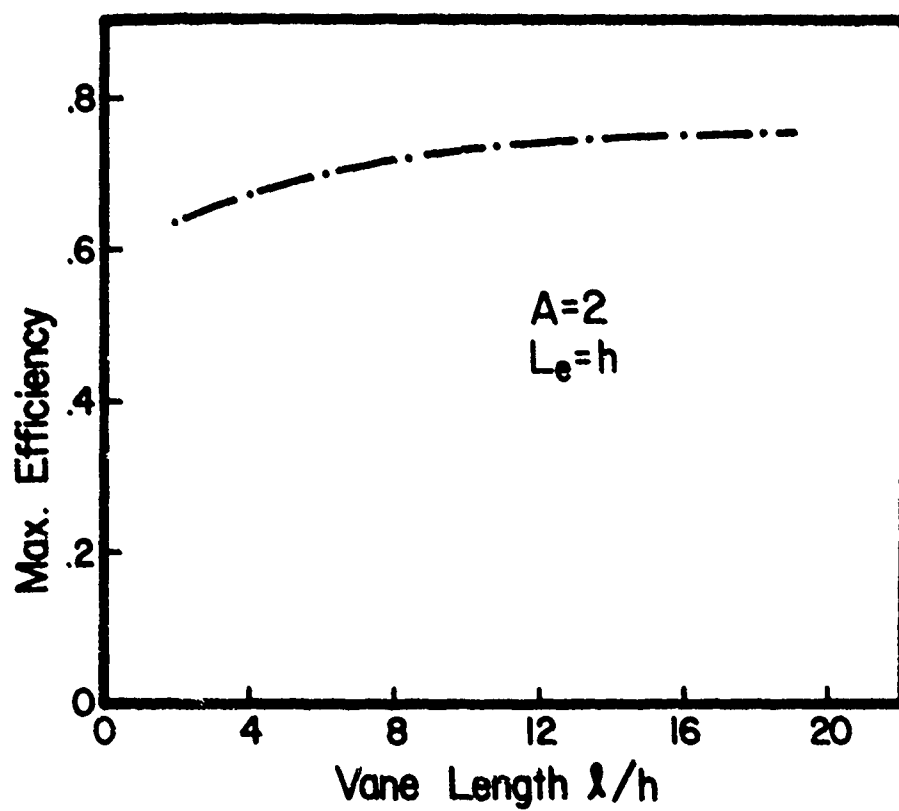
Figure V.15   The influence of vane length on efficiency
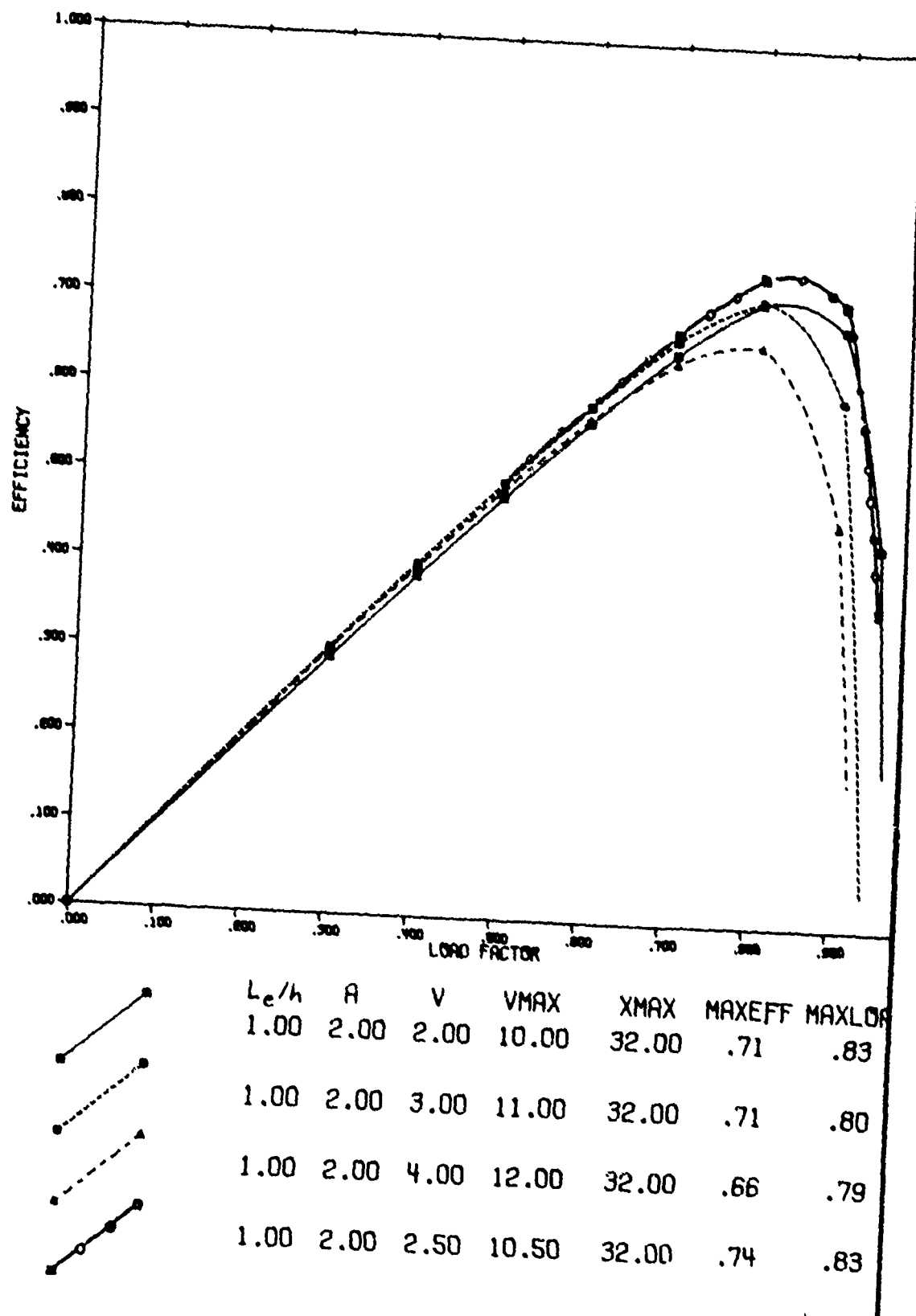
Figure V.16 Efficiency vs load factor as a function of
the axial location of one vane.

of the mesh spacing), Table V.2 and Fig. V.17. (With two vanes, there is
no vane on the center line.) The optimum axial position for the edge of
the vanes was found to be between $x = a$ and $x = a + L_e/2$ (probably around
$a + L_e/4$) for $A = 2$, Fig. V.18. With two insulating vanes, the influence
of L_e is relatively weak, as shown in Fig. V.19.

The efficiency increase caused by an increasing vane length does not
seem to reach an asymptotic value even for $\ell = 10h$, Figs. V.20 and V.21.

Quantitatively, the improvement in efficiency obtained by the inser-
tion of two vanes of a certain length with respect to a single vane of the
same length was found to be about 4%, as shown by lines 4 and 12 of Table
V.2.

V.7.3.2   Three or More Insulating Vanes

The increase in efficiency attained by the insertion of three vanes,
with respect to the two-vane case, is only about 1.5%, Fig. V.22. The
influence of L_e is again very weak, Fig. V.23.

With five vanes, only about 1.5% increase in efficiency is obtained
with respect to the case of three vanes of the same length, lines 15 and 16
of Table V.2.

V.8   The Natural Magnetic Field Overhang with Insulating Vanes

While the exponential extension of the magnetic field was proven to
be more efficient than a "constant" or "linearly decaying" field overhang,
it was not shown how it compares in shape or efficiency with a real magnetic
field distribution. This should determine the magnetic field shape that
yields the best efficiency.

Table V.2

Maximal Efficiency Attainable with Various Insulating Vanes

LINE NO.	ASPECT RATIO	X-AXIS VANE		FIRST INTERMEDIARY VANE PAIR			SECOND INTERMEDIARY VANE PAIR			RIGHT BOUNDARY	MAXIMUM ATTAINABLE EFFICIENCY L_E/h		
	A	ℓ/h	v/h	ℓ_1/h	y_1/h	v_1/h	ℓ_2/h	y_2/h	v_2/h	x_{max}	0.5	1	2
1	1									16	0.49	0.57	0.654
2	2									16	0.58	0.65	0.72
3	2	8	2.5							16	0.687	0.737	0.773
4	2	8	2.25							14	0.69	0.725	0.765
5	2			8	0.5	2.25				14	0.73	0.745	0.773
6	2			8	0.5	2.0				14		0.743	
7	2			8	0.5	2.25				14		0.754	
8	2			8	0.5	2.5				14		0.745	
9	2			8	0.37	2.25				14		0.757	
10	2			8	0.5	2.25				14		0.749	
11	2			8	0.63	2.0				14		0.721	
12	2			8	0.37	2.25				14		0.757	
13	2			8	0.37	2.5				14		0.751	
14	2			8	0.37	2.75				14		0.731	
15	2	8	2.25	8	0.5	2.0				14	0.77	0.77	0.79
16	2	8	2.25	8	0.33	2.25	8	0.66	2.25	14	0.78		

-103-

EFFICIENCY

	X AXIS VANE FROM X TO X	INTERMEDIATE VANE FROM X TO X	VANE Y	MAX. EFF.	MAX. LOAD.
1	.00 .00	2.25 10.25	.37	.76	.85
2	.00 .00	2.25 10.25	.50	.75	.85
3	.00 .00	2.00 10.00	.63	.72	.83
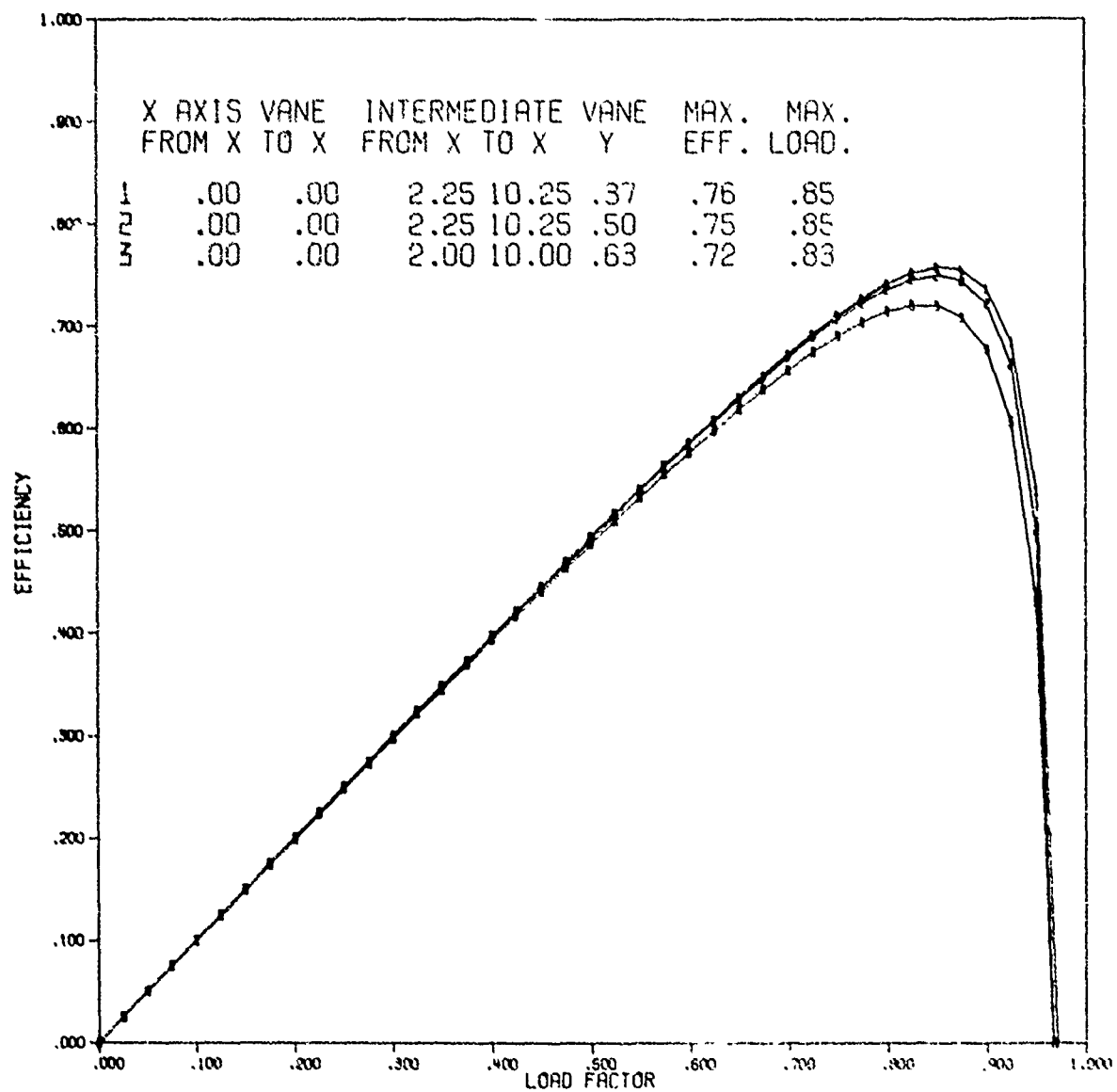
LOAD FACTOR

Figure V.17 Efficiency vs load factor as a function of vane position for two insulating vanes, $L_e/h = 1$ and $A = 2$

-104-
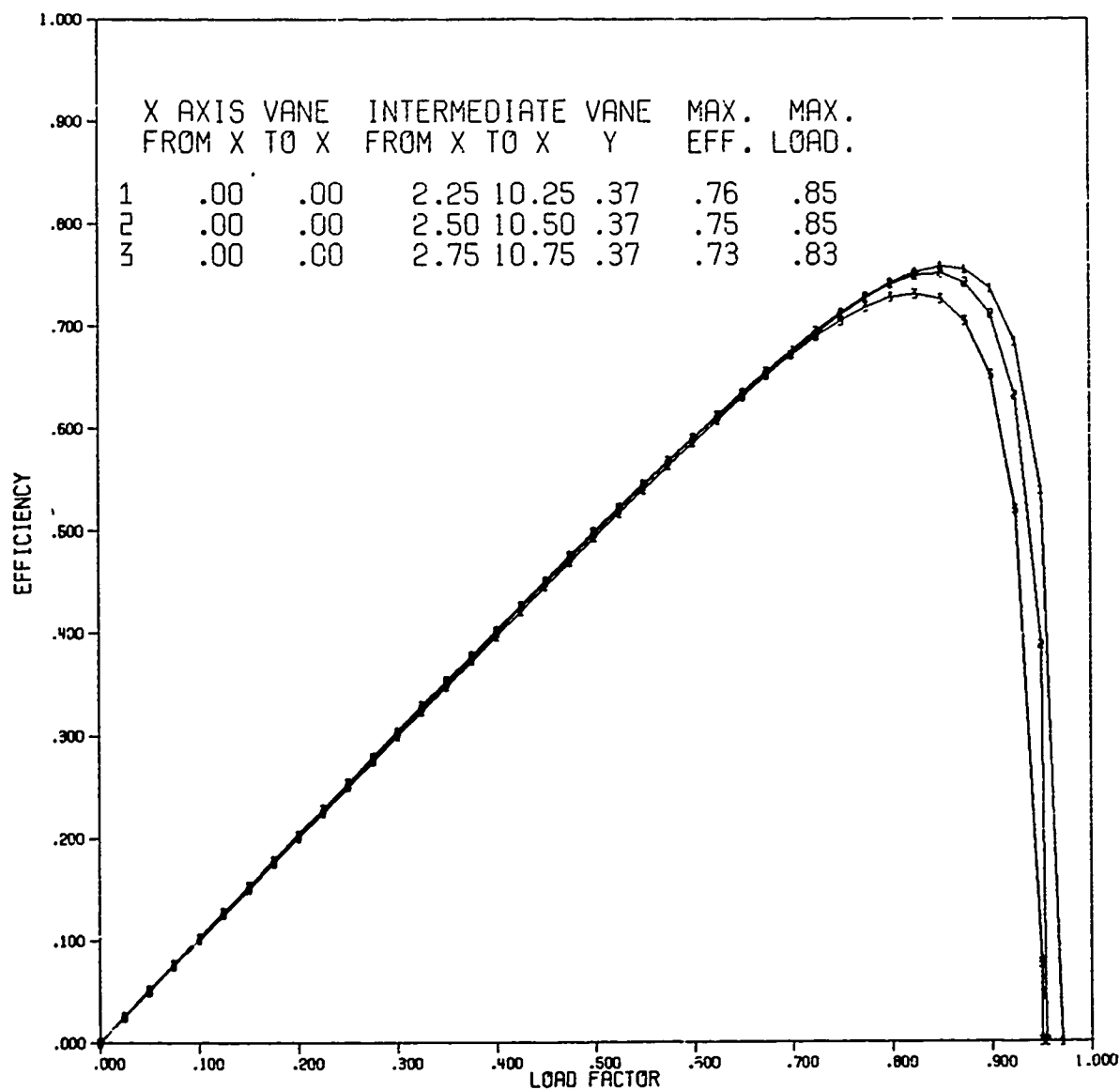
Figure V.18 Efficiency vs load factor as a function of vane position for two insulating vanes, $L_e/h = 1$, and $A = 2$
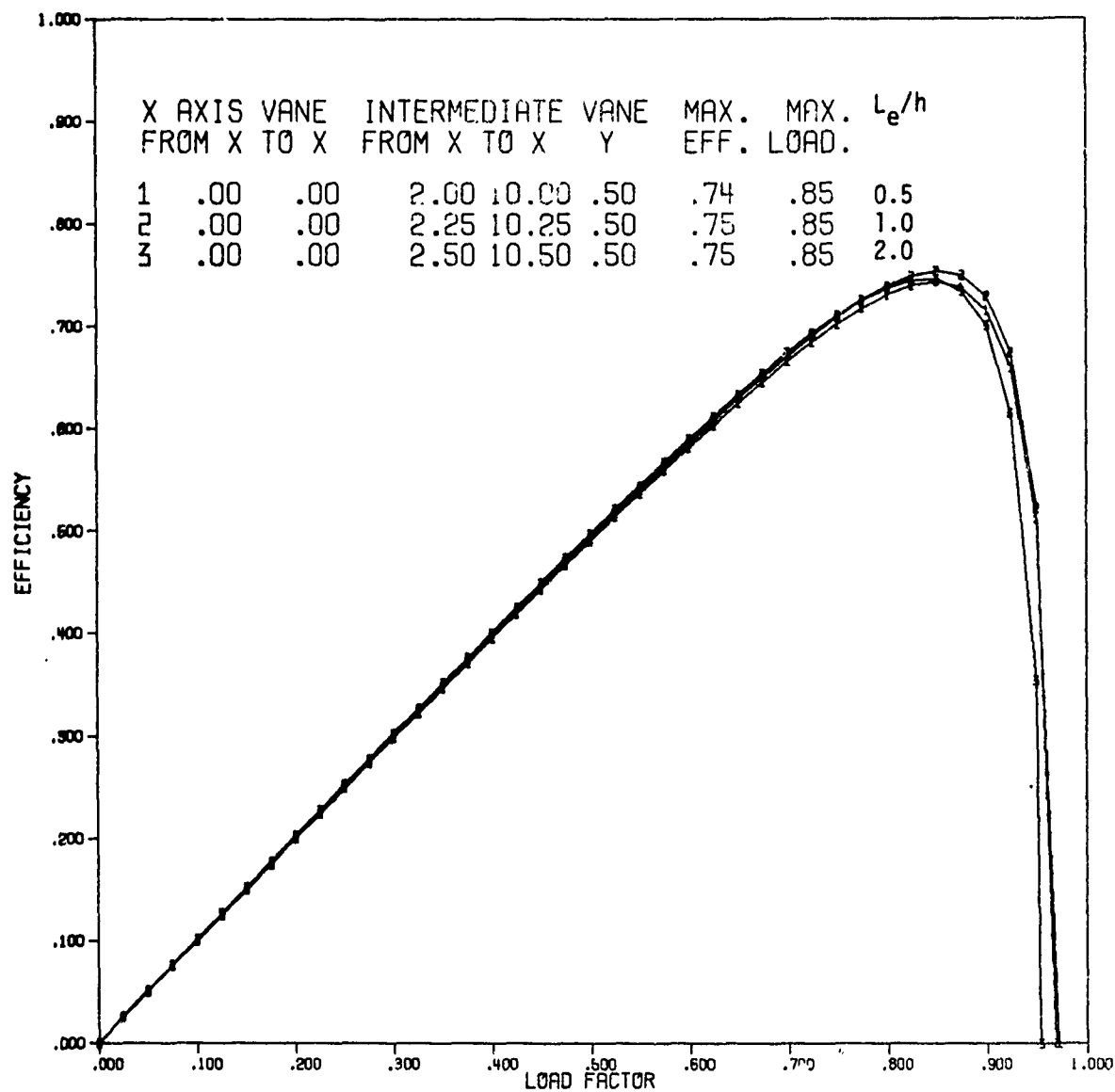
Figure V.19 Efficiency vs load factor as a function of L_e for two insulating vanes of length $\ell/h = 8$, $\varepsilon_\Lambda = 2$
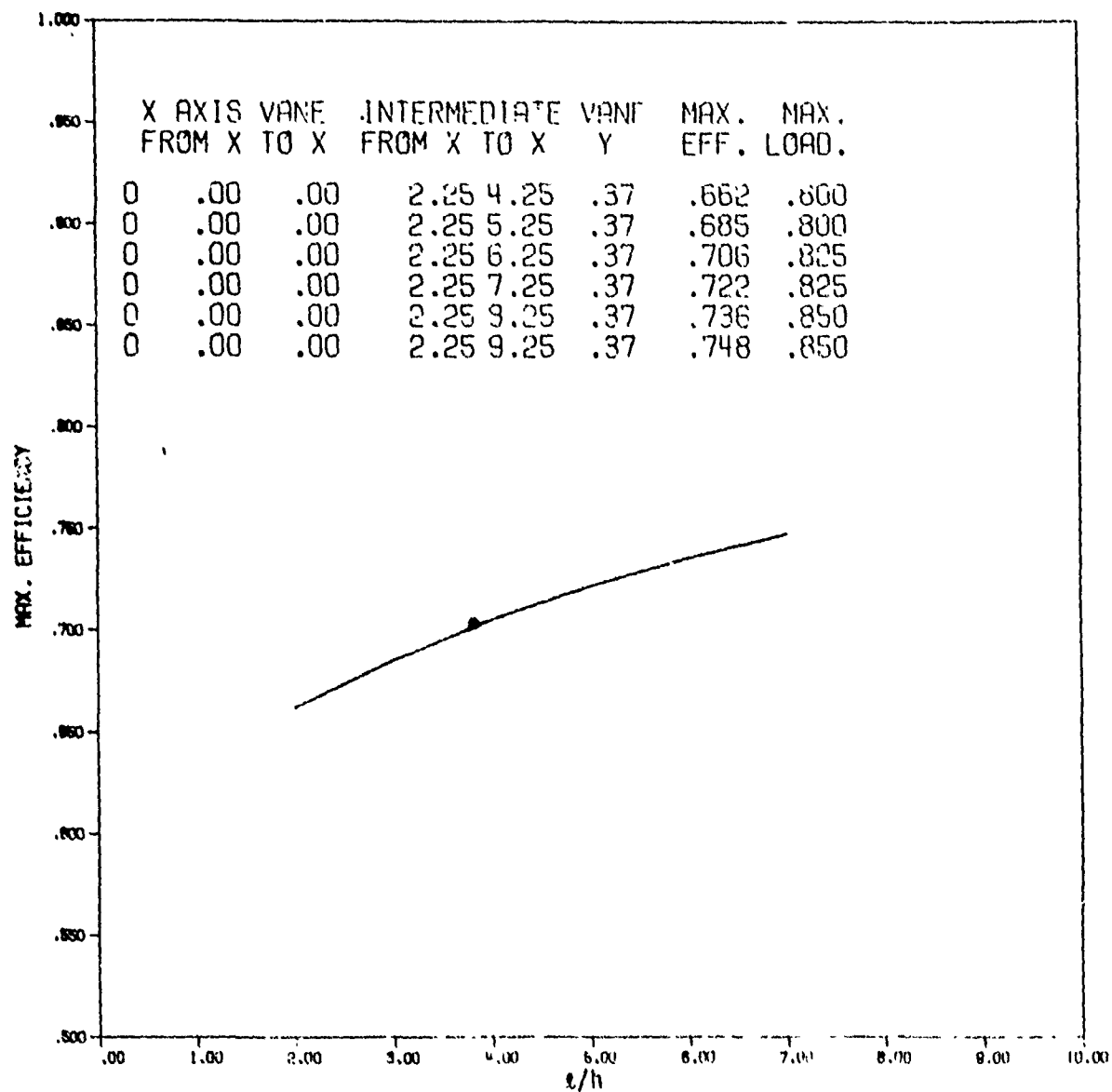
Figure V.20 Efficiency vs the length of two insulating equidistant vanes, $A = 2$ and $L_e/h = 1$

-107-

X AXIS VANE FROM X TO X		INTERMEDIATE VANE FROM X TO X		VANE Y	MAX. EFF.	MAX. LOAD.
0	.00 .00	2.25	4.25	.50	.663	.800
0	.00 .00	2.25	5.25	.50	.685	.800
0	.00 .00	2.25	6.25	.50	.705	.825
0	.00 .00	2.25	7.25	.50	.720	.825
0	.00 .00	2.25	8.25	.50	.733	.850
0	.00 .00	2.25	9.25	.50	.744	.850
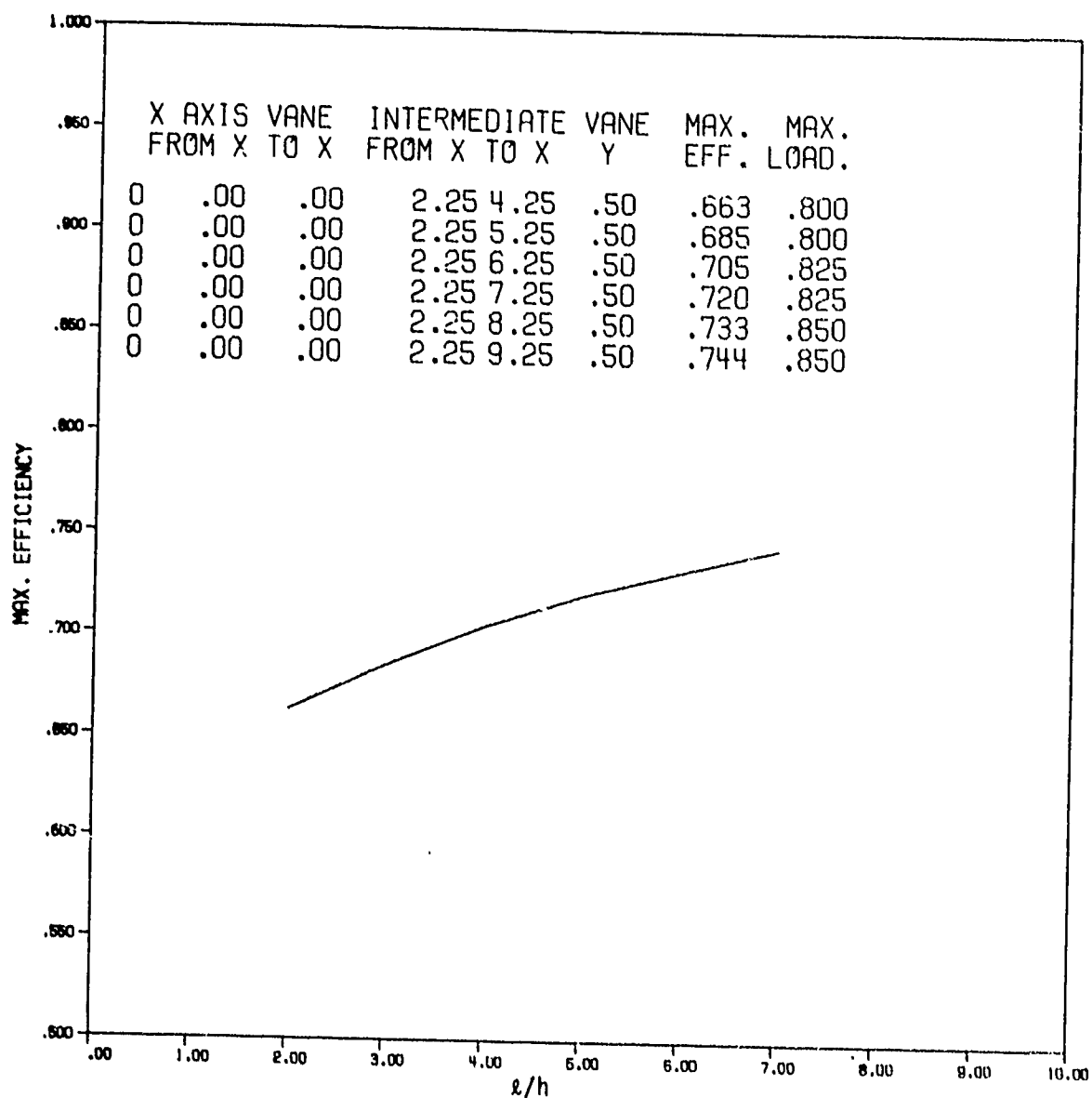
Figure V.21   Efficiency vs the length of two insulating equidistant vanes, A = 2, and $L_e/h = 1$

-108-
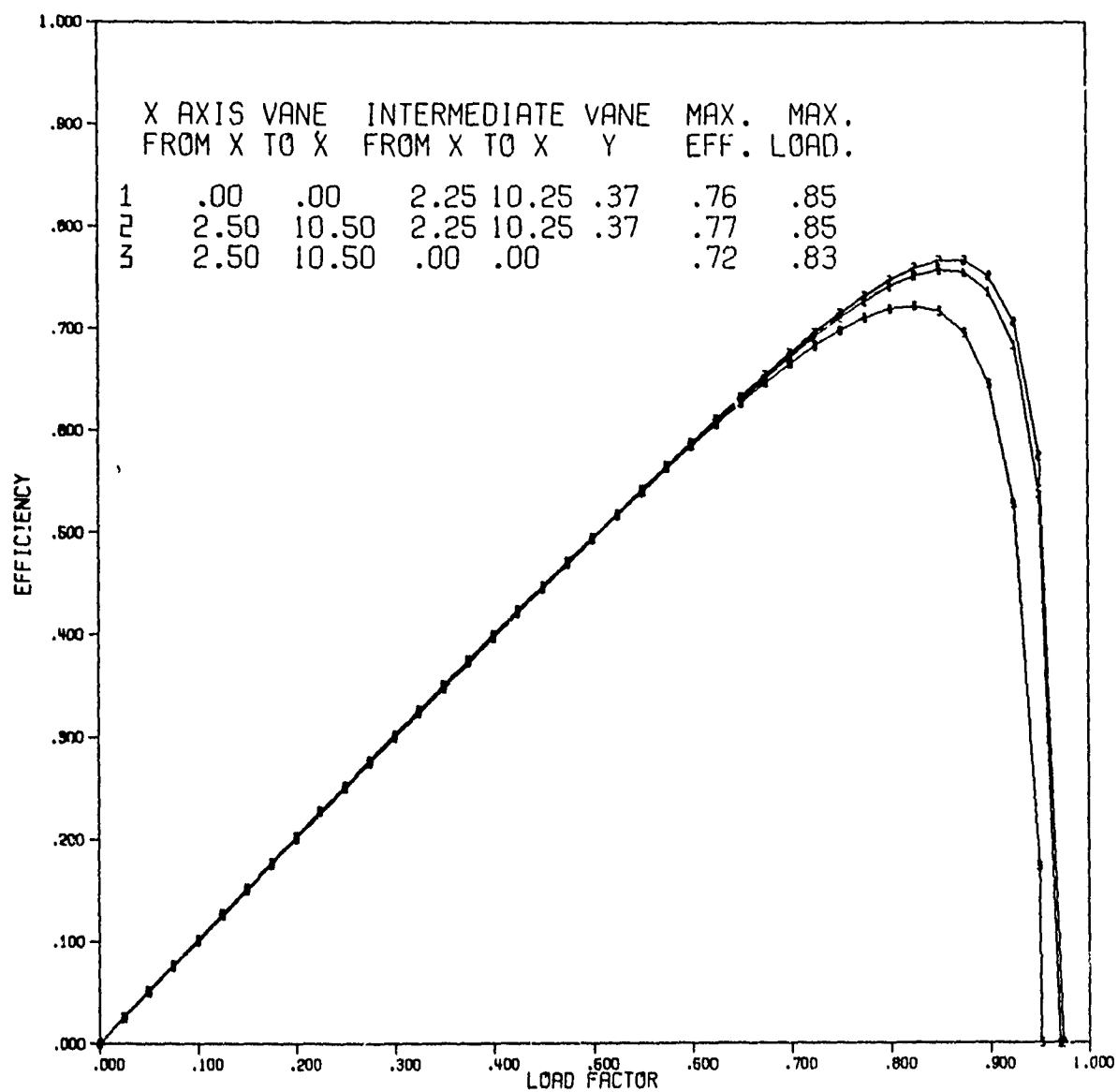
Figure V.22 Efficiency curves for vanes of length $\ell/h = 8$, $A = 2$, and $L_e/h = 1$

-109-
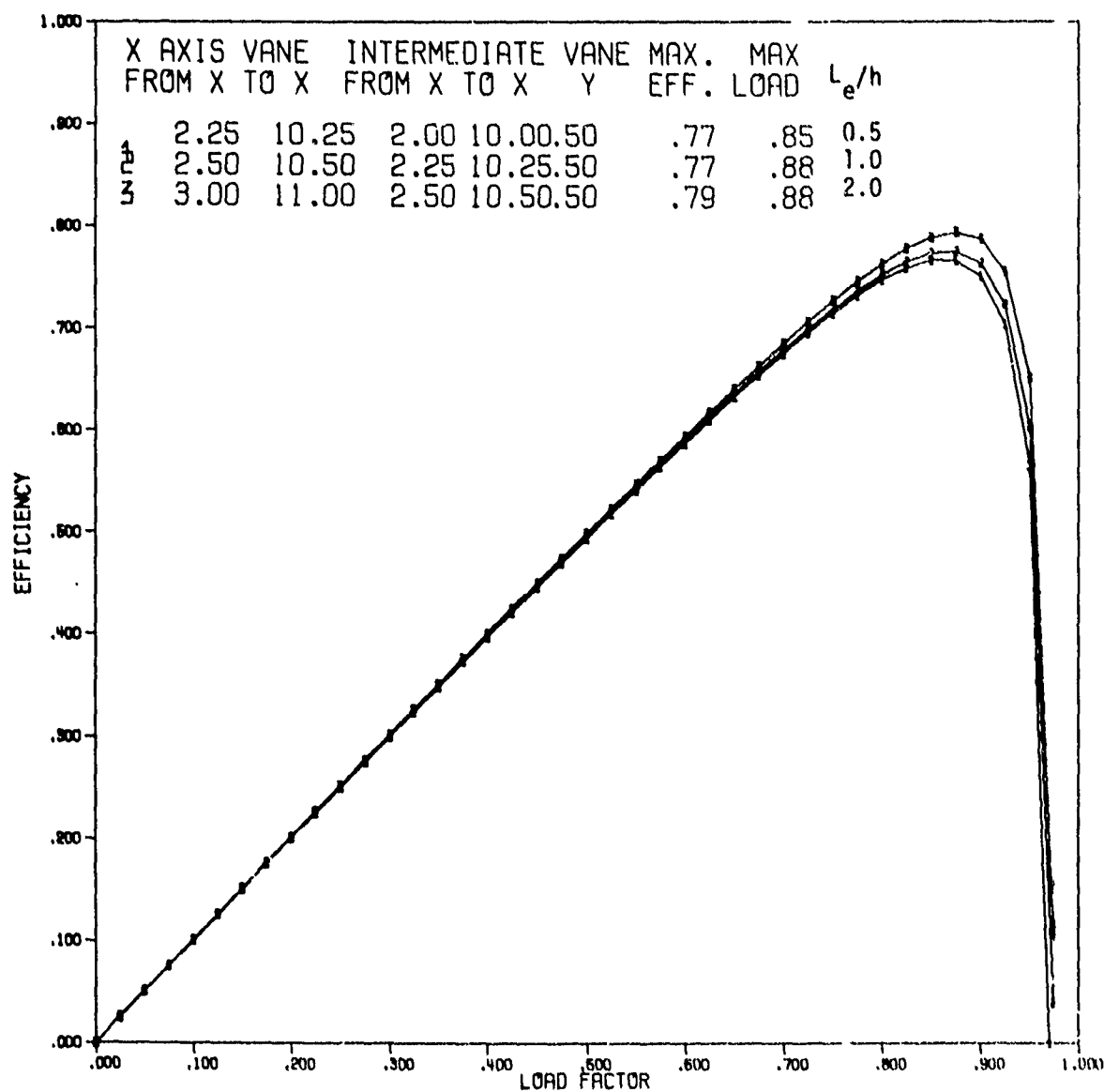
Figure V.23   The effect of L_e on efficiency for
3 vanes of length $l/h = 8$, $A = 2$

-110-

The longitudinal distribution of the magnetic field created by two plane-parallel pole pieces can be described with a good approximation by [see Laverentiev (1968)]

$$b(x) = \begin{cases} 1 - A_1 \exp[\nu_1(|x| - \lambda)/h] & \text{for } |x| < \lambda \\ A_2 \exp[-\nu_2(|x| - \lambda)/h] & \text{for } |x| \geq \lambda, \end{cases} \tag{V.12}$$

where $A_1 + A_2 = 1$,

$$A_1 \nu_1 = A_2 \nu_2,$$

and 2λ the length of the pole piece. This magnetic field distribution is shown in Fig. V.24 for values of $\delta^* = \delta/h$ (the total air gap δ between the magnetic poles normalized by the interelectrode distance h) of 0.2...1.4. The slope of the field decay is determined by the gap δ; a smaller gap leads to a more abrupt decay. The actual values used in Eg. V.12 for Fig. V.24 were $A_1 = 0.17$, $A_2 = 0.83$, $\nu_1 = 5.29/\delta^*$, and $\nu_2 = 1.07/\delta^*$.

It should also be noted that, if the length of the pole piece is equal to the electrode length, $\lambda = a$, then at the edge of the electrode the magnetic field has decreased to 83% of its value at $x = 0$. Since the magnetic field is not constant (and equal to B_0) between $x = 0$ and $x = a$, the voltage between the electrodes will be taken as

$$V_L = \frac{Fu2h}{a} \int_0^a B_0 b(x) dx. \tag{V.13}$$

In Fig. V.25 the real distribution of the magnetic field for $\delta^* = 0.5$, 1.0, and 1.5 is compared with the exponential decay for $L_e = 0.5$, 1.0, and 1.5, respectively. This comparison will be useful for the interpretation of the following results. For instance, it seems evident that if the magnet edge is beyond the electrode edge, $\lambda > a$, the voltage between the electrodes given by Eq. V.13 will be higher for the same B_0, improving

-111-
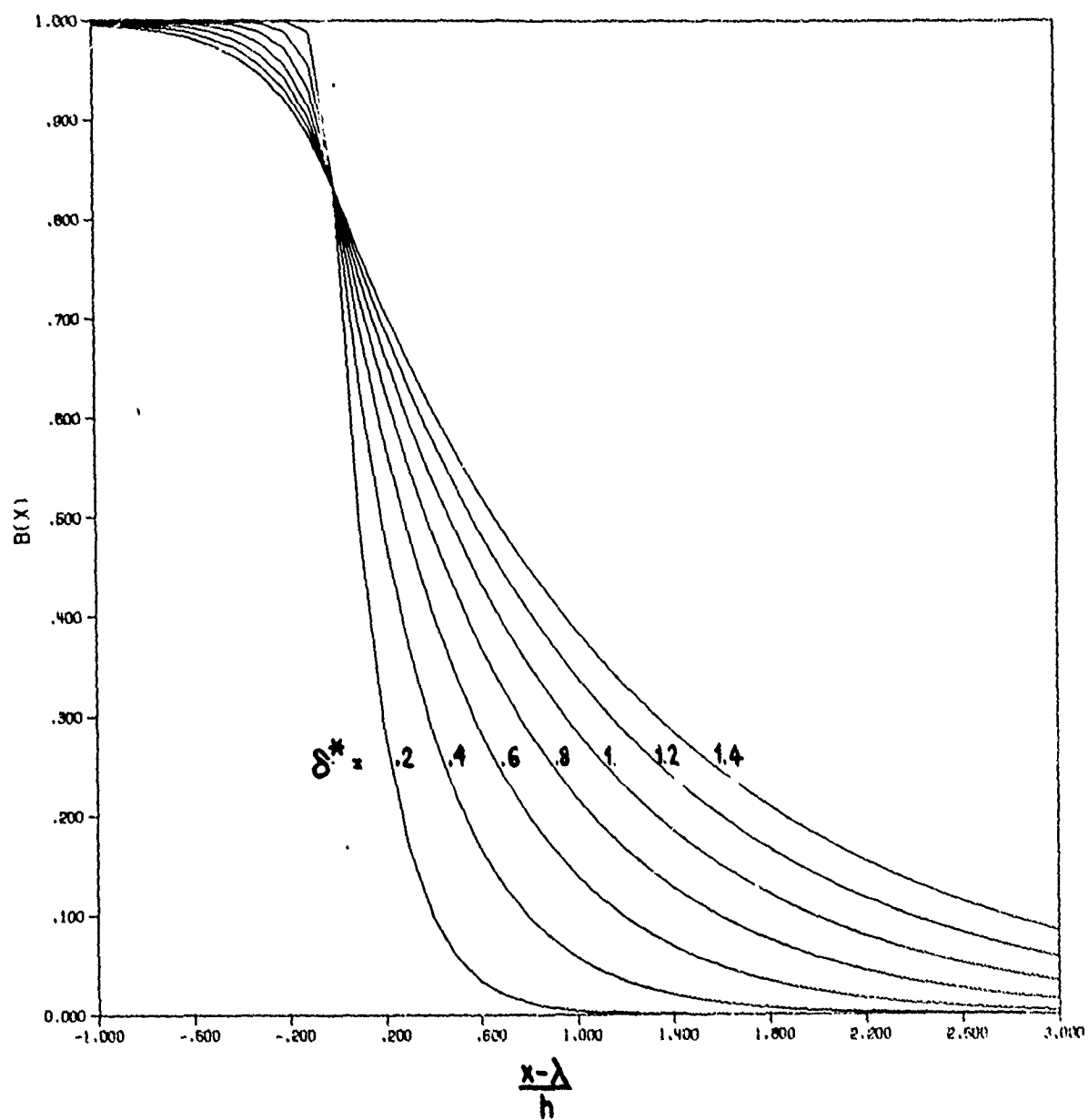
Figure V.24 The approximated variation of the real
magnetic field shape for different gaps
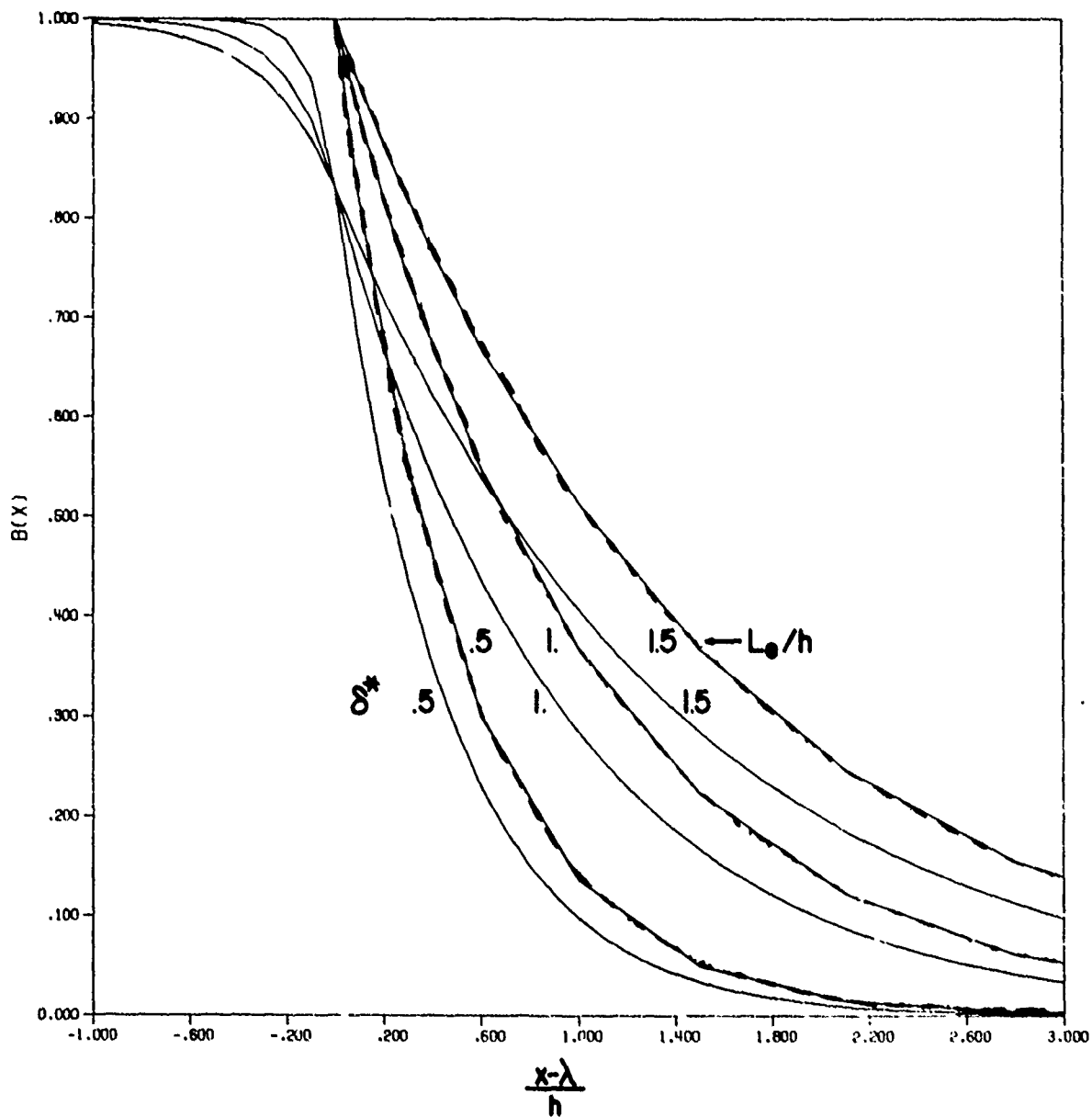
Figure V.25 Comparison of the real distribution of the magnetic
flux density with the exponential approximation

-113-

the efficiency. Quantitatively, this can be seen in Fig. V.26, where the electrode edge has the position a = 2, i.e., A = 2. The less-predictable result is that, even for $\lambda > a$, the efficiency is about 20% lower than it was for the case of an exponential field overhang. For instance, with $\delta * = 0.5$ and $\lambda = 2.5 = 1.25a$, the efficiency is about 0.49, as compared with 0.58 for an exponential overhang with $L_e = 0.5$ (see Table V.2, line 2). The insertion of an insulating vane at the center line improves the efficiency, Fig. V.27, but the latter still remains below the value attainable with an exponential field overhang, line 3 of Table V.2.

Again, the axial position of the vane influences the maximum attainable efficiency, Fig. V.27.

V.9 Recommendations for the Reduction of End Losses

In the preceding sections three ways to reduce the end current losses were considered:

a) increasing the aspect ratio of the channel,

b) providing a magnetic field distribution approximating an exponential decay beyond the electrodes. and

c) inserting insulating vane(s) in the regions where the fluid enters and leaves the magnetic field.

The choice of the channel aspect ratio is primarily determined by the rated electric power and the allowable pressure drop. However, from the point of view of the end losses, a larger aspect ratio leads to a better efficiency. The data obtained in the present study indicate, curve 1 of Fig. V.28, that for aspect ratios above 5 a maximum efficiency higher than 0.80 can be obtained without any insulating vanes, provided a proper shape of the magnetic flux density distribution is achieved.
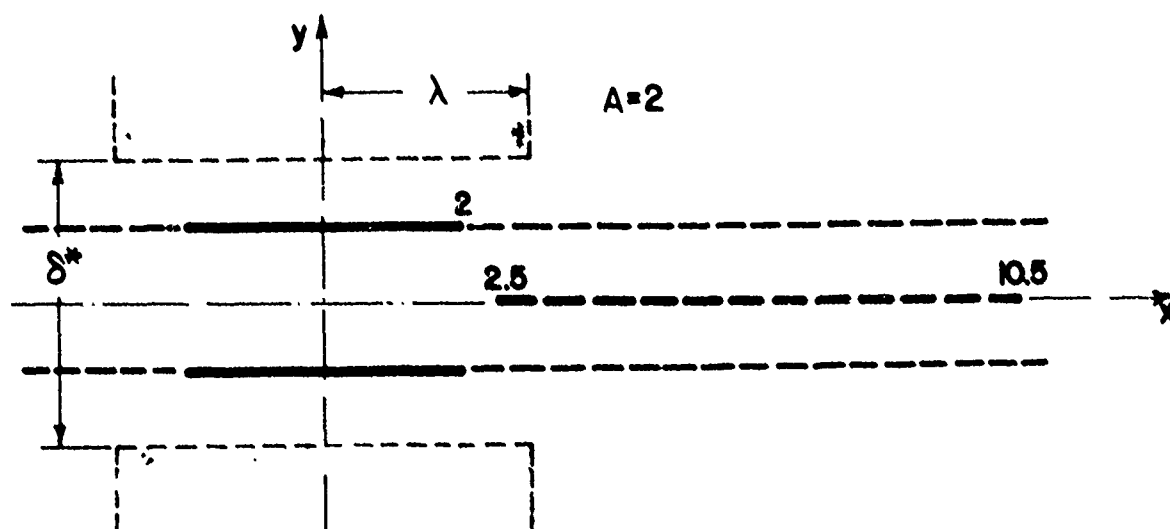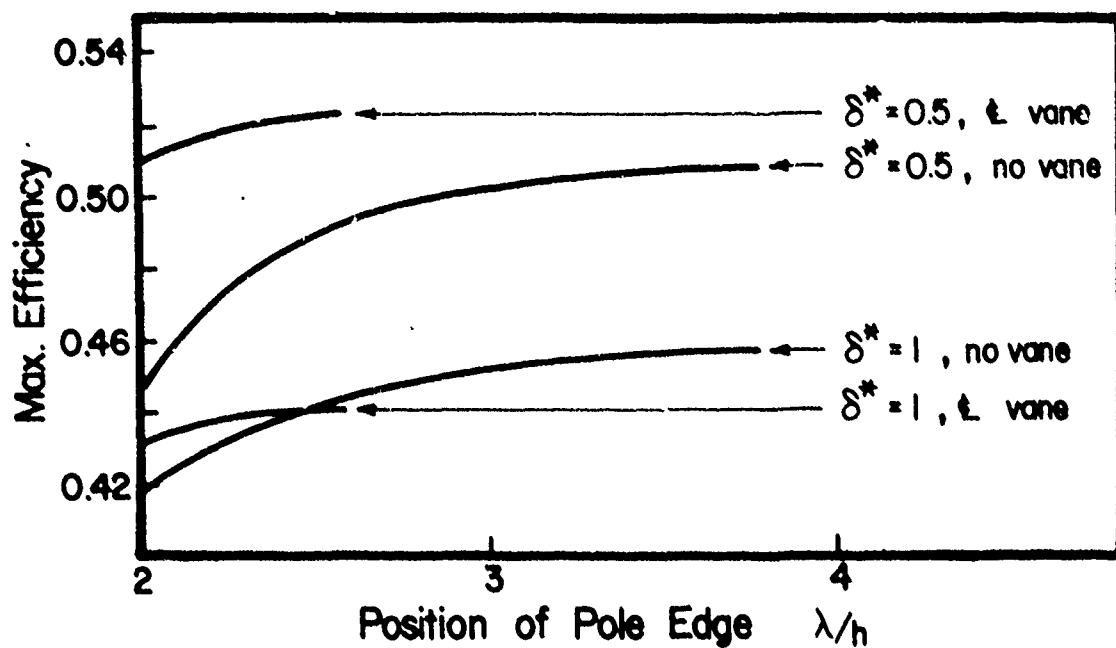
Figure V.26   The influence of the position of the magnet edge on the
maximum efficiency attainable with a "real" field decay. A=2
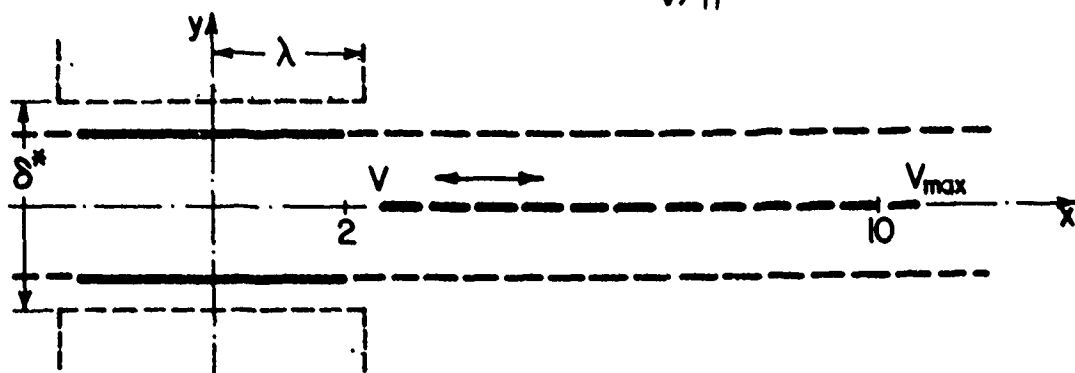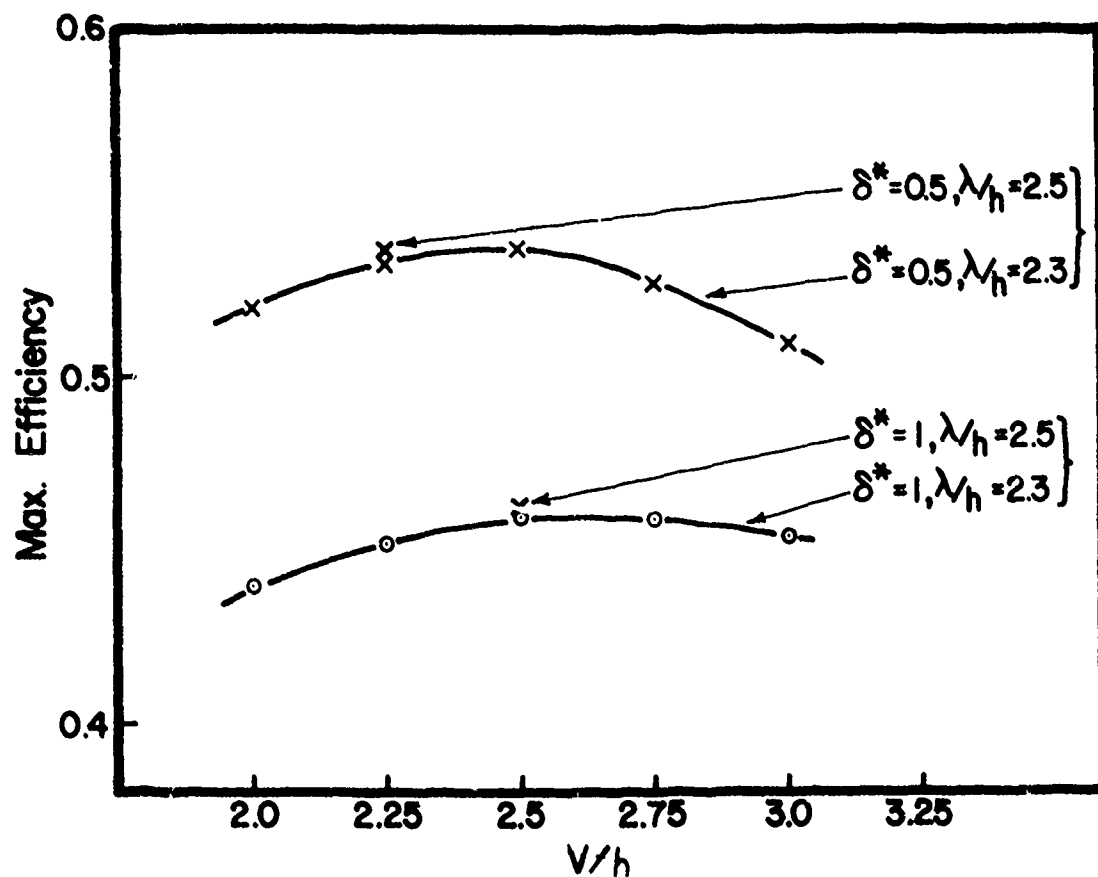
Figure V.27   The optimum position of a center-line vane
edge for the real decay of the magnetic field

-116-
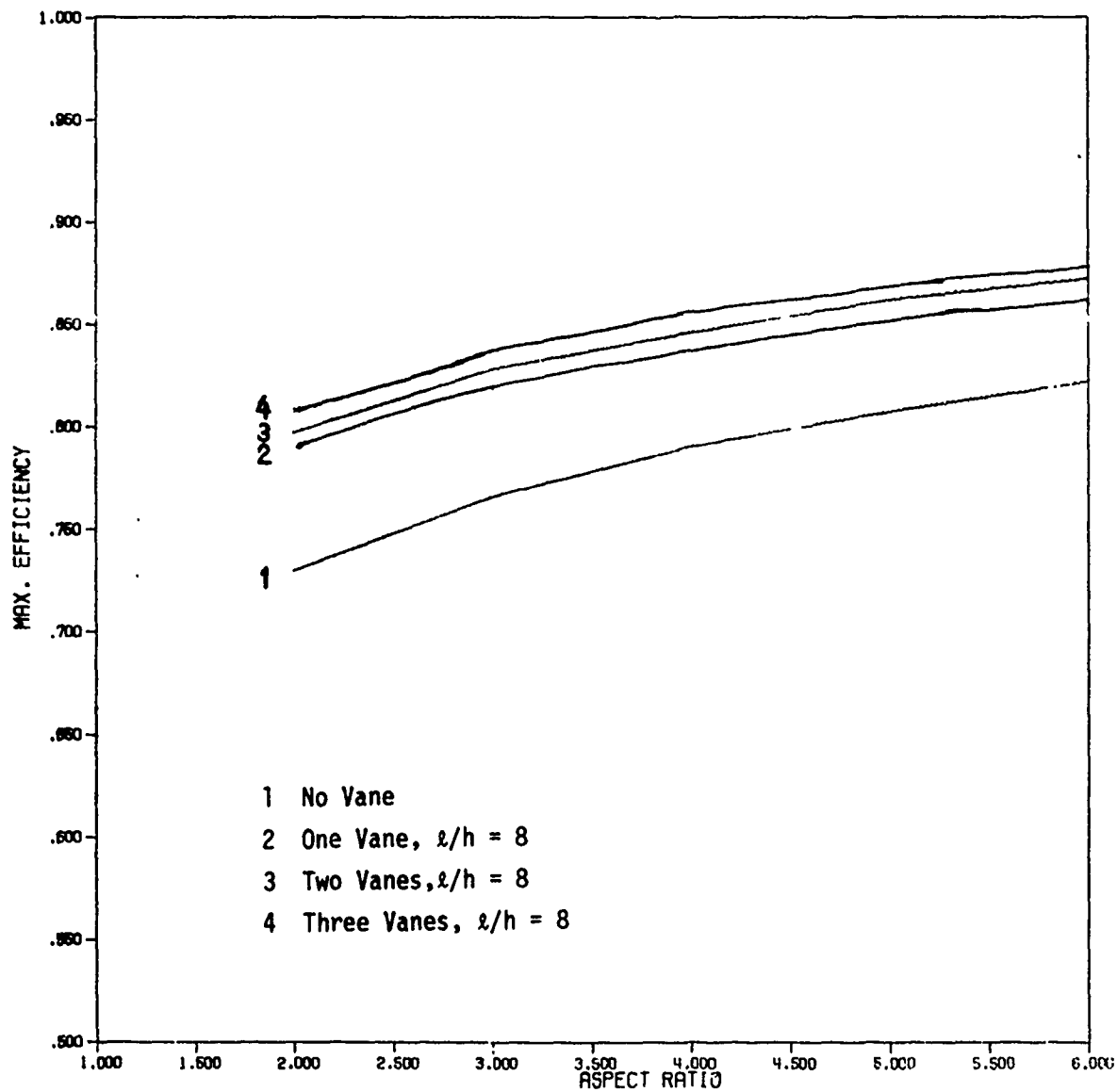
Figure V.28 The maximum attainable efficiencies for aspect ratios up to
A=6 and an exponential magnetic field decay with L_e = 21

Once a specific aspect ratio is chosen for the channel, the most important parameter affecting the efficiency was found to be the magnetic field distribution along the longitudinal axis. If the field is created by plane-parallel poles of a length equal to the electrode length, its strength decays toward the ends of the electrodes leading to a lower average voltage between them and, therefore, to an efficiency lower than that obtained with a magnetic field of uniform amplitude over the entire electrode length (due to added circulating currents). If this situation is compensated for by making the magnetic poles longer than the electrodes, to obtain a uniform field along the latter, then the field intensity beyond the electrodes will not decay sharply enough, giving rise to currents which increase the ponderomotive force without contributing to the electric power drawn from the generator so that the efficiency is not improved. The best solution, according to the results of this study, is to shape the magnetic field to achieve a field of uniform strength over the entire length of the electrodes and decaying (quickly) beyond the electrode edge according to an exponential curve.

The efficiency was found to be higher as L_e is increased. For a channel without insulating vanes, the increase in efficiency is not linearly dependent on L_e. For instance (see Fig. V.29), for $A = 2$, $L_e = 2h$ increases the efficiency by 92% with respect to the reference case (for which $L_e = 0$); and doubling L_e (to $4h$) brings about a further efficiency increase of only 2.5%. The dependence shown in Fig. V.29 remains qualitatively correct for channels with a higher aspect ratio; however, a relatively larger value of L_e would be required to obtain the same percentages of efficiency increase.
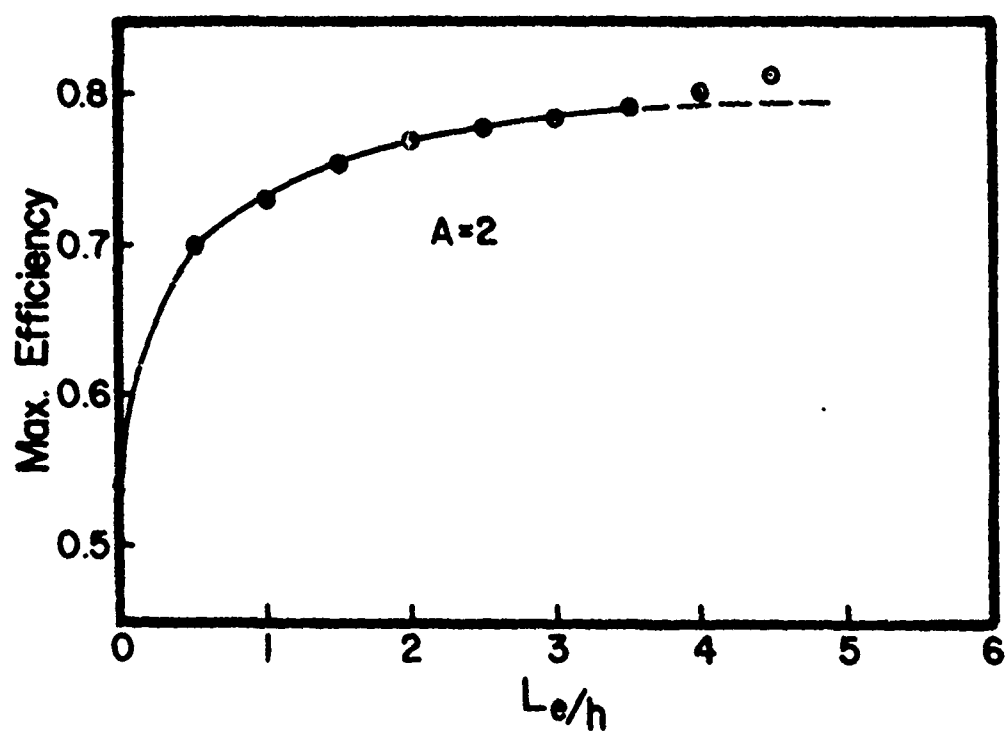
Figure V.29 The influence of L_e on the maximum attainable efficiency
for an "infinitely long" insulating vane, A = 2

It should be noted that, if insulating vanes are present in the region beyond the electrodes, the dependence of the efficiency on L_e is different. For aspect ratios of A = 3 and 5, for instance, an asymptotic value for the maximum attainable efficiency seems to be reached for L_e of about 3h, Fig. V.30.

The emphasis in the present study was on the influence of the insulating vanes on the efficiency. For L_e = 2h, a further efficiency increase of 10% can be achieved by the insertion of a center-line vane of a length $\ell \approx$ 8h. Additional vanes of the same length lead to a further increase in the maximum attainable efficiency of only a few percent, Fig. V.28. This fact, together with the technological difficulties implied by an increased number of vanes, seem to indicate that the most efficient solution for the end loss reduction would be the insertion of a single insulating vane on the center line. It has to be stressed that not only the length, but also the axial position of the vane, is of critical importance. With the magnetic field "shaped" to approximate an exponentially-decaying longitudinal distribution, the best efficiency is obtained when the vane edge is positioned at a distance of about $L_e/2$ (measured axially) from the electrode end. Since for different load factors the electrostatic field created by the electrodes has different intensities, the optimal position of the vane is dependent on the load factor. However, the distance from the electrode end indicated above may be considered valid for the range of load factors which correspond to maximum generator efficiency (F = 0.8 ....0.95).

Obviously, the same increase in efficiency may be attained in two or more different ways. For instance (see Fig. V.32), for a channel with A = 2
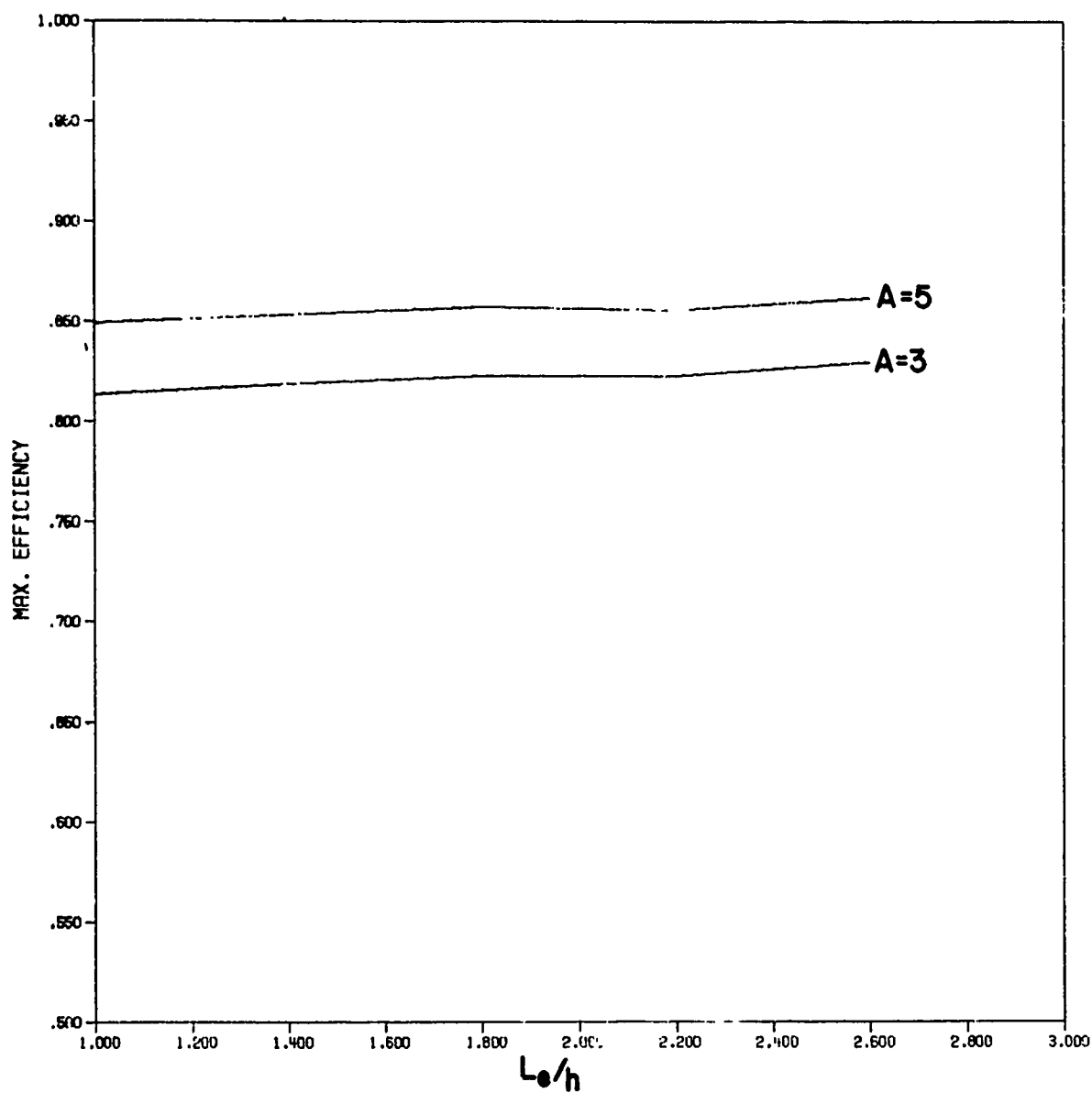
Figure V.30 The influence of L_e and A on the maximum attainable efficiency for one vane, $\ell/h = 8$
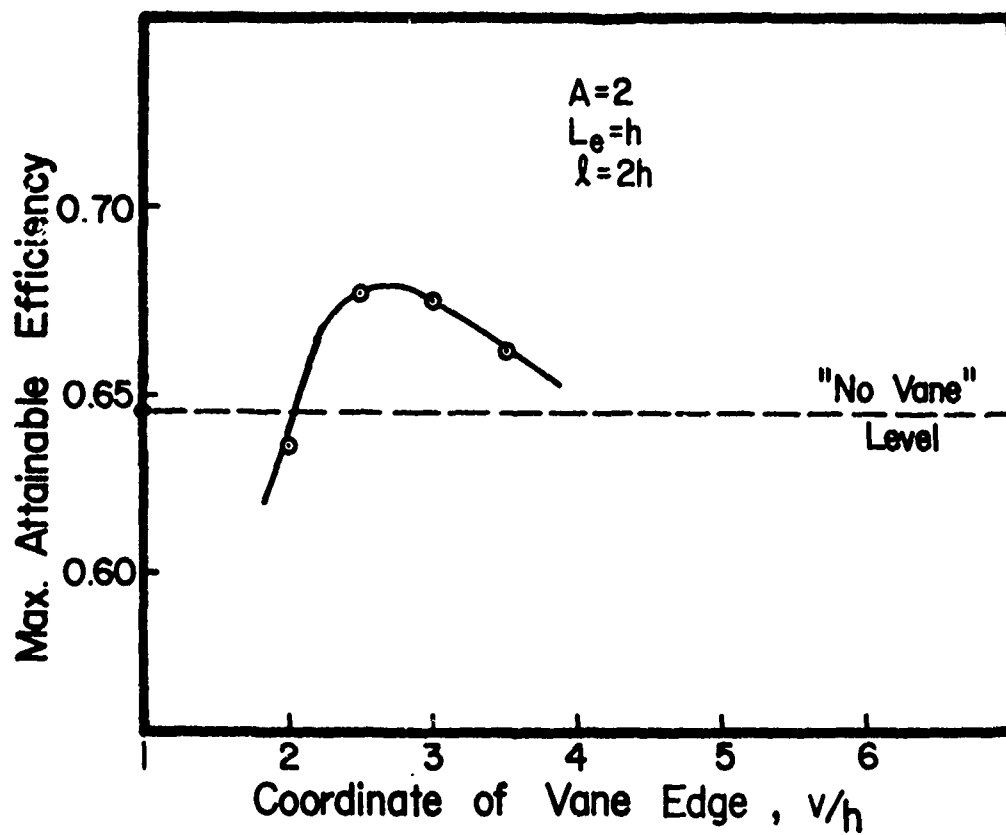
Figure V.31 The influence of the position of a short center line vane on the maximum attainable efficiency, A=2, $L_e/h=1$, and $\ell/h=2$
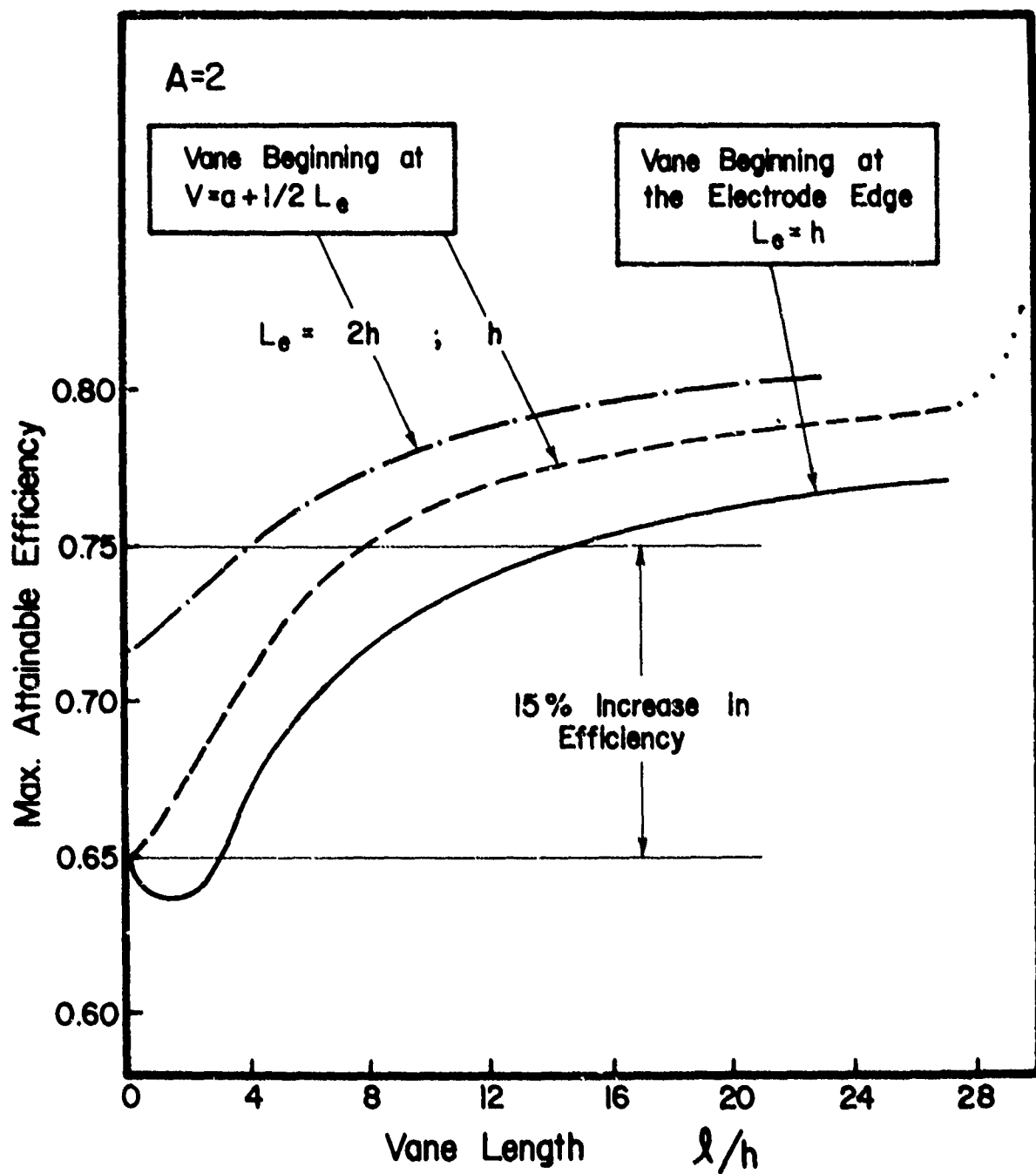
Figure V.32 Equivalent solutions for efficiency improvement

and an exponential field overhang characterized by $L_e = h$, the efficiency can be increased by 15% by either a) a center-line insulating vane of length 14h beginning at the end of the electrodes, b) a center-line vane of length 8h beginning at a better axial position, or c) a center-line vane of length 4h and an increase in L_e to 2h.

The choice between the last two alternatives would depend upon technological considerations. In its last version, the computer program used in this study can provide data describing the dependence of the maximum attainable efficiency with respect to any one of the parameters characterizing the vanes and the magnetic field. A few examples are given in Figs. V.29-V.32. In Figs. V.28 and V.30, the values of the aspect ratio are comparable with the LMMHD generator models presently being tested (see Section III). For the specific parameters chosen the maximum attainable efficiencies are in excess of 80%.

VI. LOCAL MEASUREMENTS

VI.1 Introduction

The two-phase LMMHD generator is complex fluid dynamically because it employs two working fluids--a gas as the thermodynamic fluid and a liquid metal to provide the high electrical conductivity. [For a description of the cycle, see Brunsvold and Pierson (1976), Pierson (1978), or Pierson et al (1979).] The gas expands and performs work on the liquid metal in the generator, but the very large electromagnetic force acts solely on the liquid. In addition, because of the high ratio of liquid to gas mass flow rates and liquid to gas heat transfer, the gas expansion occurrs at almost constant temperature (hence two-phase LMMHD cycles have high thermodynamic efficiencies, a significant attractive feature) and the enthalpy change in the two-phase mixture comes almost entirely from the liquid. To maintain high generator and cycle efficiency, good interfacial heat and mechanical energy transfers are required, as has been demonstrated, see Fabris and Pierson (1978) or Petrick et al (1978). These gas-liquid interactions are very dependent on the two-phase flow pattern.

System studies have shown that cycle efficiency will improve greatly as the average void fraction in the generator is increased, because this reduces the amount of recirculating liquid and associated loss. However, as the void fraction is increased, two-phase flow-pattern transitions may occur, limiting generator (and cycle) performance. Good generator performance has been measured at average void fractions up to approximately 0.7, with efficiencies in excess of 0.60 and power densities up to approximately 32 MWe/m^3 (see Section III). The use of foams has been proposed by Fabris et al (1975) to prevent flow transitions and allow higher average void fractions, but this has yet to be tested in a generator.

All reported experimental measurements have been terminal or average parameters. No experimental data is available on local gas and liquid velocities, bubble sizes, local temperatures, etc. Local measurements in any two-phase flow, with or without a magnetic field, are difficult, and no measurements inside a LMMHD generator with a magnetic field have been reported.[*] There is not even published data on hot-film measurements in pure-liquid alkali-metal flows. Thus, it was necessary to develop the experimental techniques, and this should be read as an initial report, not a presentation of data obtained by established measurement methods. The experimental facility is described briefly in Section VI.2, and the hot-film probe and resistivity probe results are in Sections VI.3 and VI.4, respectively. Hot-film probes yield both velocity and void fraction data, while resistivity probes yield only void fraction directly but are smaller, i.e., respond to smaller bubbles, and easier to use.

VI.2 Experimental Facility

The ambient-temperature NaK-nitrogen LMMHD facility used for the two-phase LMMHD measurements has been described in Petrick et al (1977). The generator channel used is 387 mm long, with 102-mm electrode spacing and height that varies linearly, from 1.41 mm at the inlet to 1.91 mm at the outlet, parallel to the applied magnetic field. The load resistance

---

[*]Recently some LMMHD resistivity-probe pipe-flow data have been published, but they are not in the correct parameter range. For example, Michiyoshi et al (1977) studied bubbles in mercury at low velocities, less than 1 m/s, where the electromagnetic force density is not dominant. Also, it is important to be aware that mercury behaves differently than NaK in two-phase flows because of the substantial difference in their Weber numbers (ratio of inertial to surface tension forces) that govern the disintegration of liquid sheets [see experimental result of Dombrowski and Fraser (1954)]. The ratio of mercury to NaK Weber numbers is four.

is continuously variable and is connected to the electrodes by means of compensating bars located on both sides of the channel. The electromagnet has a 406 mm diameter pole face and is capable of flux densities in excess of 1.2 T at the required air-gap length. Instrumentation is provided for measurement of terminal voltages and currents, gas and liquid flow rates, pressures, temperatures, and average void fractions.

For the NaK-nitrogen hot-film experiments a TSI quartz-coated ruggedized side-flow probe 3.18 mm in diameter, Model 1269 W, was used. The probe was connected to a TSI Series 1050 constant-temperature anemometry system, and the output was displayed on an oscilloscope screen and recorded on a Sangamo/Tandberg Model TIR 115 four-channel FM tape recorder. The analog signals were subsequently digitized at the rate of 4000 samples per second, and the digital signals used for some of the figures in Section VI.3. The minimum detectable bubble size is limited to approximately 10 mm by the probe size, sample rate, and two-phase velocity.

Appreciable dc drift was observed in the output signal from the hot-film probe, but is not considered important here because only qualitative behavior and gas-liquid changes are of interest, rather than absolute velocities. (After the experiments reported herein, the probe was gold-plated by vapor deposition, resulting in reduced dc drift because of improved NaK wetting of the probe.) A sample calibration curve, taken from the digitized data, is shown in Fig. VI.1 only to give an indication of the voltage-velocity magnitudes for the data in Section VI.3. (The voltage is the anemometery system output with the probe at the center of the channel for B = 0 and a pure-liquid flow; the velocity is calculated as the average velocity from the measured volume flow rate multiplied by 1.225, the 1.225 being the correction factor based in the velocity profile shape in a
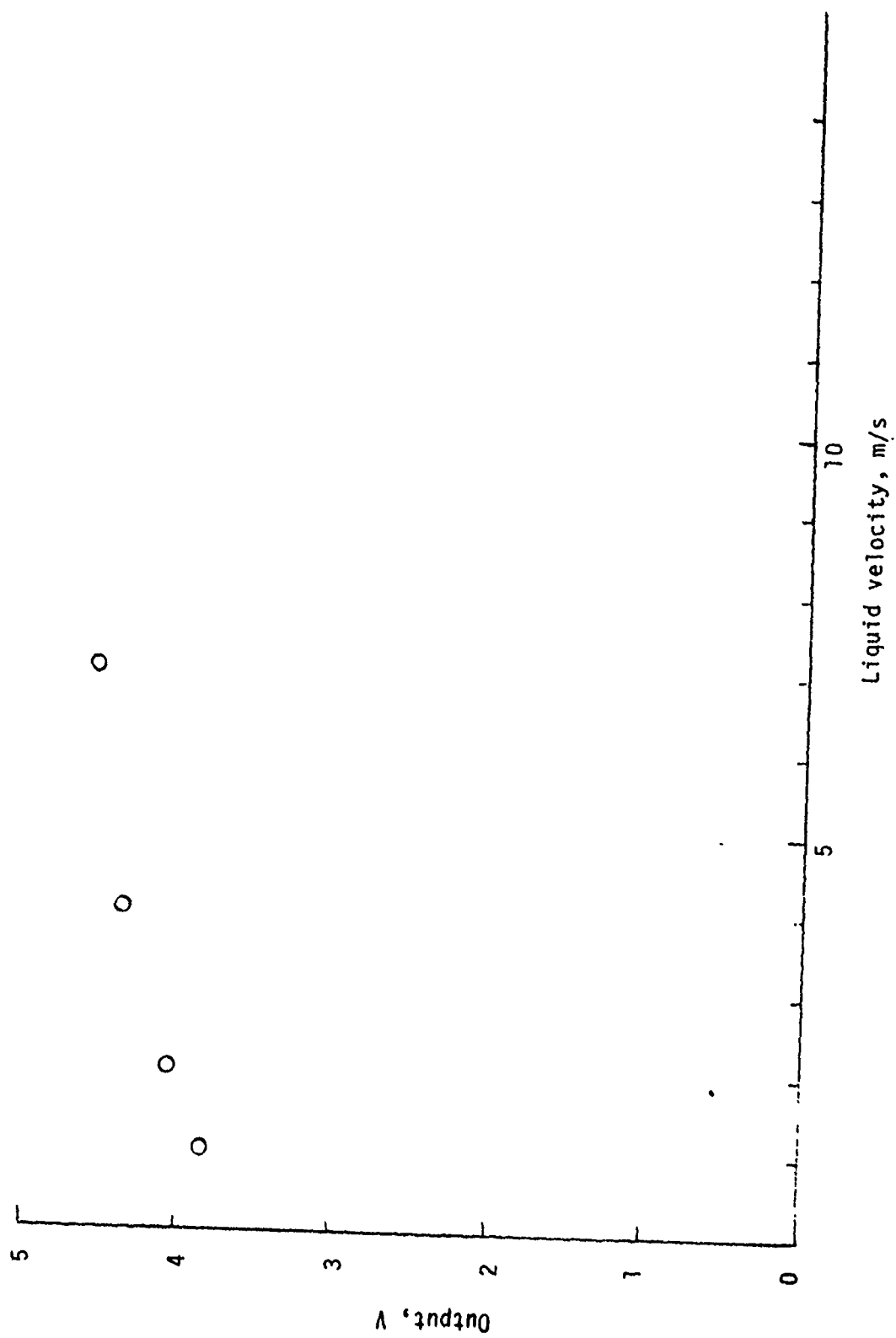
Figure VI.1 Calibration curve of the hot-film probe and anomometry system

rectangular channel at high Reynolds numbers.) The voltages shown in
Fig. VI.1 must be multiplied by four for use with the oscilloscope signals.

The resistivity probes, basically thin wires insulated except at the
very tip, were made by one of the authors. To improve the void fraction
and bubble frequency measurements, a discriminator circuit was developed by
Dunn (1978) that produces a square-wave signal with the value 1 V when the
probe is in gas and 0 V when the probe is in liquid; thus, a dc voltmeter
connected to this signal reads local void fraction directly. Note that the
time response of the probe is typically one order of magnitude faster
with NaK-nitrogen than with air-water.

A resistivity probe with the discriminator circuit was calibrated
against the more established γ-ray attenuation measurements by Gawor
(1978). Agreement to within three percentage points was obtained where
bubble diameters were greater than approximately 0.5 mm.

VI.3 Hot-Film Probe Results

Oscilloscope traces of the hot-film probe-anemometry system output
signals are shown in Fig. VI.2 for pure-NaK non-MHD flows (B = 0) with the
probe at the center of the channel cross section, i.e., halfway between
the electrodes and centered between the insulating walls, and 250 mm from
the beginning of the electrodes. As expected, a substantial increase in
the frequency and the intensity of the fluctuations is apparent as the mass
flow rate, $\dot{m}_\ell$, is increased. The influence of B is shown in Figs. VI.3
and VI.4, as measured 25 and 38 mm, respectively, from the center of the
channel, i.e., toward one electrode. (The distance from the center to
either electrode is 51 mm.) The magnetic field clearly damps the fluctua-
tions, although some weak large-scale "eddies" remain. Comparison of the

$\dot{m}_\varrho$ = 1.47 kg/s

$\dot{m}_\varrho$ = 2.31 kq/s

$\dot{m}_\varrho$ = 3.07 kg/s

$\dot{m}_\varrho$ = 5.07 kq/s
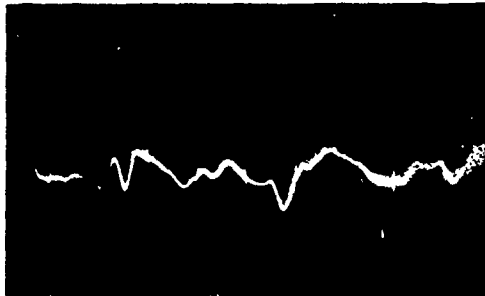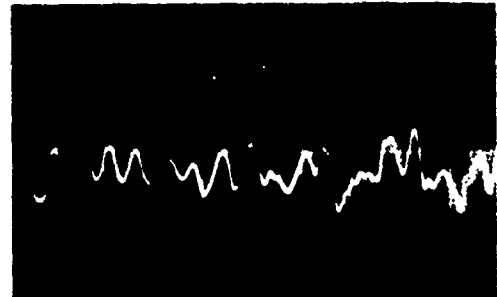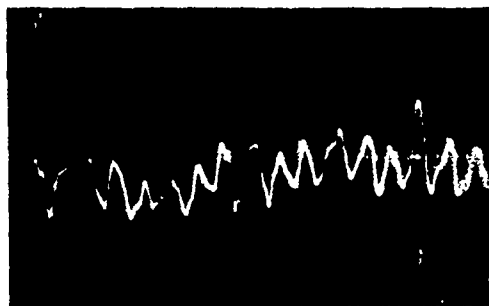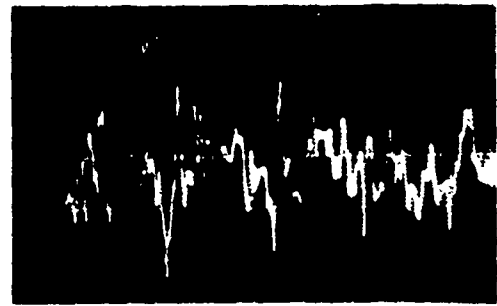
$\dot{m}_\varrho$ = 6.55 kg/s
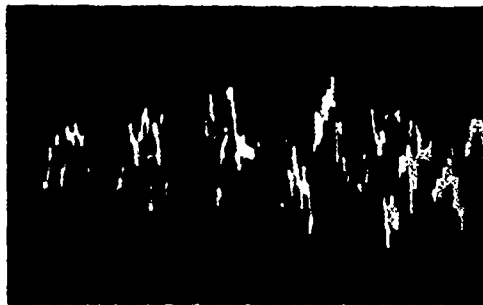
$\dot{m}_\varrho$ = 7.56 kq/s
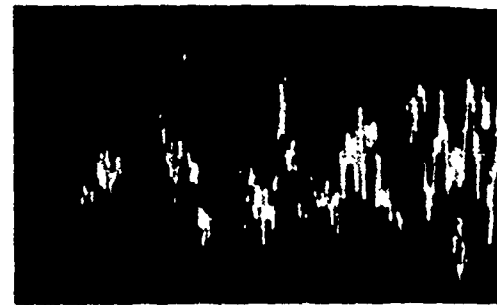
Figure VI.2 Hot-film probe signals in pure NaK flow: B=0T, measured at
channel centerline, 5 ms/DIV on abscisa, 100 mV/DIV on ordinate

$\dot{m}_\ell$ = 6.18 kg/s
B = 0.15 T

$\dot{m}_\ell$ = 6.11 kg/s
B = 0.6 T

$\dot{m}_\ell$ = 5.58 kg/s
B = 0.9 T

$\dot{m}_\ell$ = 6.27 kg/s
B = 0.0 T
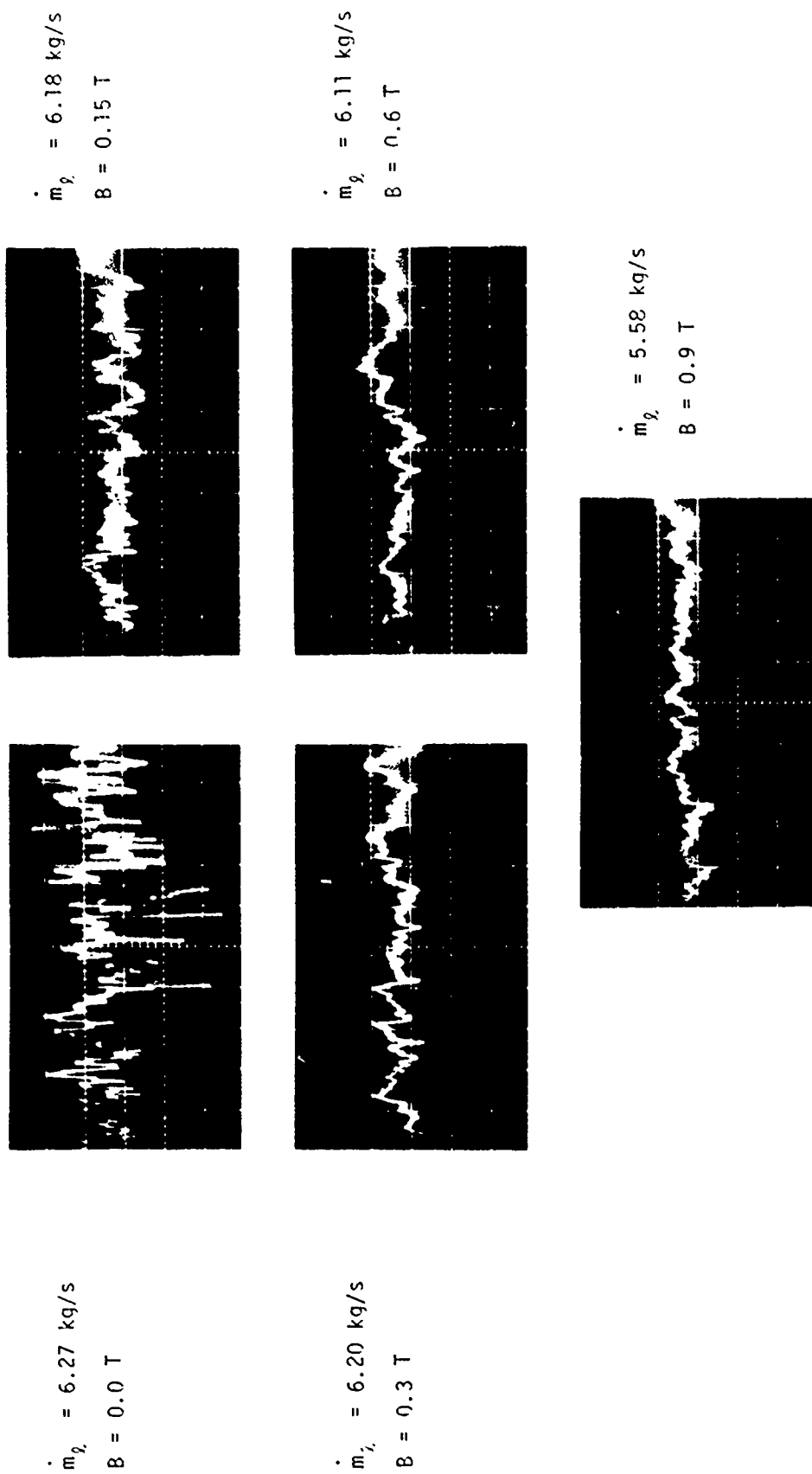
$\dot{m}_\ell$ = 6.20 kg/s
B = 0.3 T

Figure VI.3 Hot-film probe signals in pure NaK flow: measured 38 mm from the channel center-line, 5 ms/DIV on abscisa, 10 mV/DIV on ordinate

$\dot{m}_\ell$ = 6.16 kq/s, B = 0.05 $\dot{m}_\ell$ = 6.29 kq/s, B = 0.15T

$\dot{m}_\ell$ = 6.28 kg/s, B = 0.3T $\dot{m}_\ell$ = 6.20 kq/s, B = 0.6T
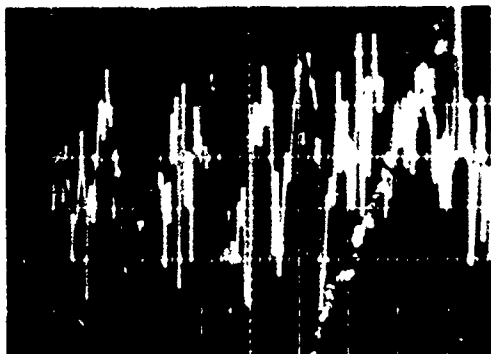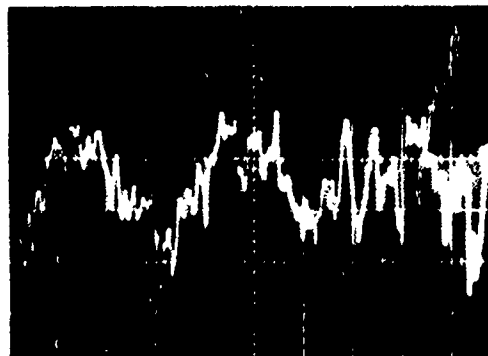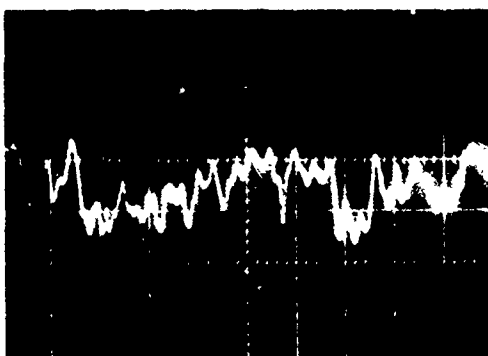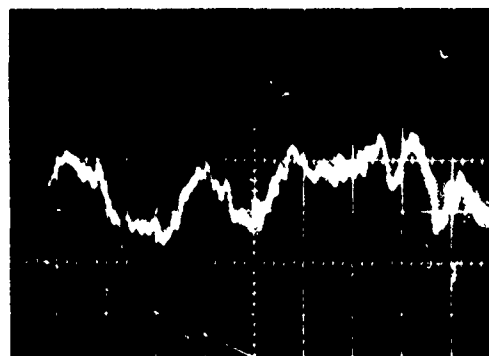
$\dot{m}_\ell$ = 5.63 kq/s, B = 0.9 T
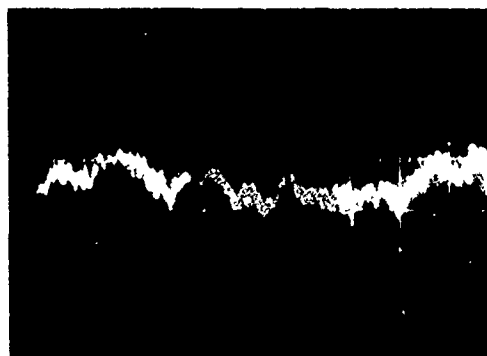
Figure VI.4 Hot-film probe signals in pure NaK flow: measured 25.4 mm from the channel centerline, 5 ms/DIV on abscisa, 10 mV/DIV on ordinate

-132-

curves is limited because of signal drift, but, for the same conditions, there is more fluctuation closer to the electrodes. Similar measurements in mercury have been reported previously [see, for example, Gardner and Lykoudis (1971)].

Plots of the digitized probe signals for two-phase NaK-nitrogen flows are shown in Figs. VI.5 to VI.10, all taken at the channel center. The square of the bridge output voltage from the anemometer is proportional to the heat transfer rate; thus, the high voltages occur when the probe is in contact with NaK and the low voltages (except, possibly, for a liquid film) when the probe is in contact with nitrogen. The rate of voltage increase is greater than the rate of voltage decrease, because, when the probe starts to encounter liquid, the increase is governed by the time constant of the probe and the electronics, whereas, when the probe starts to en- counter gas, the probe remains wetted by a liquid film (at least for a short time). The frequency response of the recording-digitizing process was not determined, hence, the plots should be regarded only as qualitative data.

To interpret the hot-film signals, it is helpful to refer to previous- ly obtained results with a conical hot-film probe 0.5 mm in diameter in an air-water flow with and without the addition of small amounts of liquid soap. Without the soap, the bubbles were approximately 3-4 mm in diameter and were clearly visible in the output signal, whereas with the soap the bubbles were much smaller in diameter and very few bubbles were indicated by the signal.

Figures VI.5, VI.6, and VI.7 were all obtained for $B = 0$. The first two are for the same flow conditions, but Fig. VI.6 shows the signal at a time when larger numbers of smaller bubbles were observed. In Fig. VI.7,

-133-
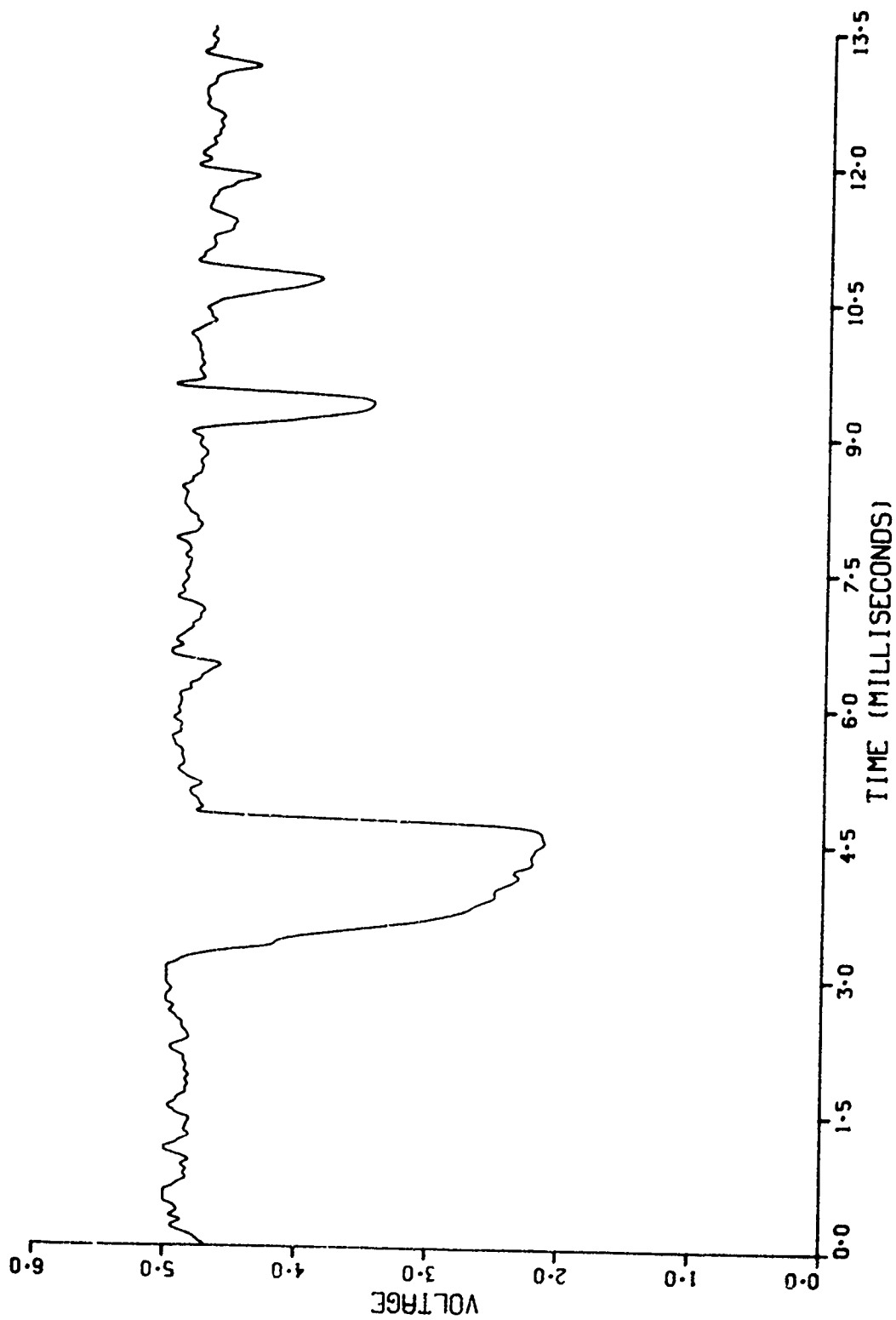
Figure VI.5 Hot-film probe signals in NaK-N_2 flow: measured at the channel centerline, B = 0 T, $\dot{m}_g$ = 0.017^{2}kg/s, $\dot{m}_\ell$ = 5.96 kg/s
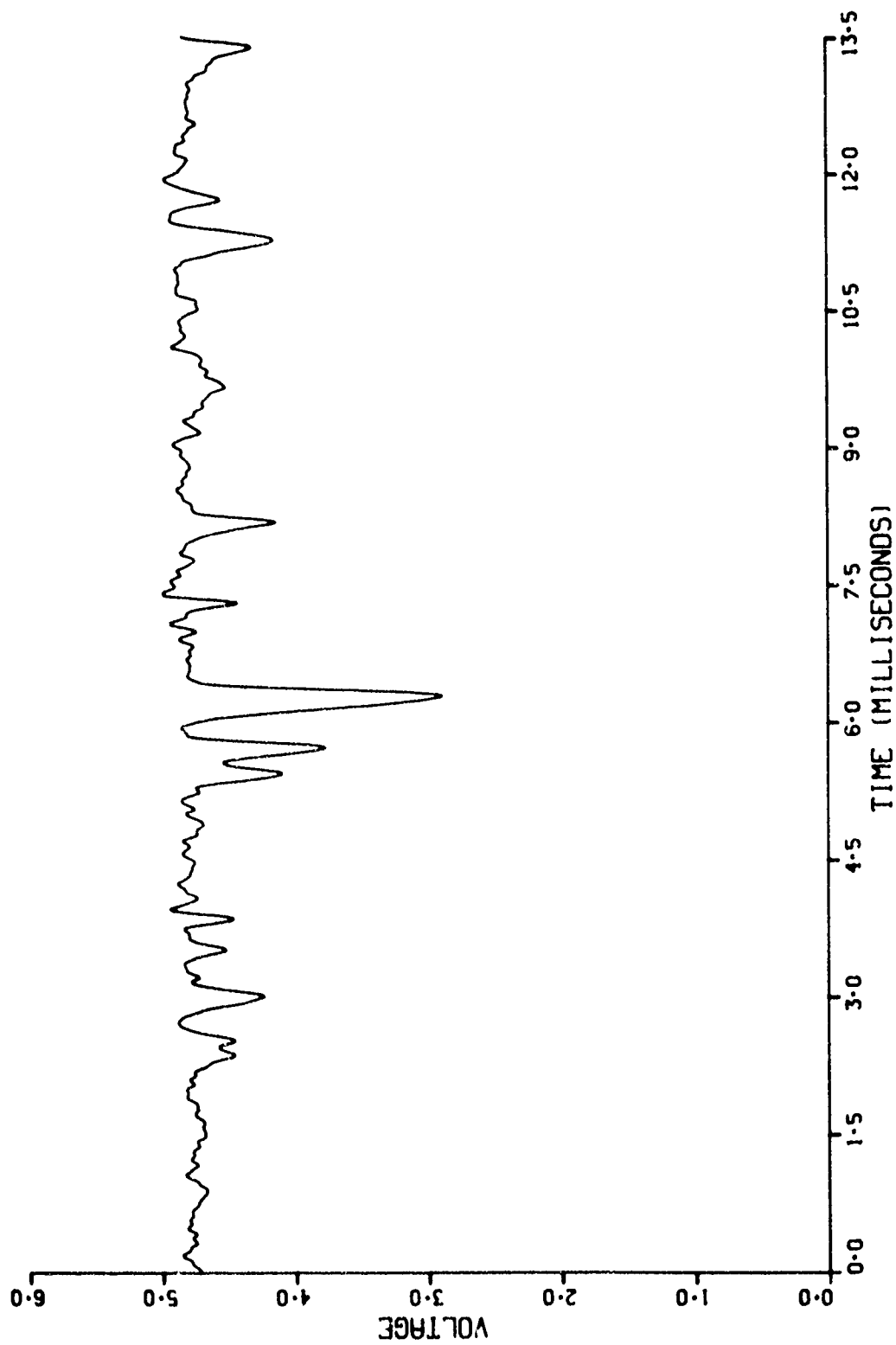
Figure VI.6 Hot-film probe signals in NaK-N_2 flow: measured at the channel centerline, B = 0 T, $\dot{m}_g$ = 0.017 kg/s, $\dot{m}_\ell$ = 5.96 kg/s
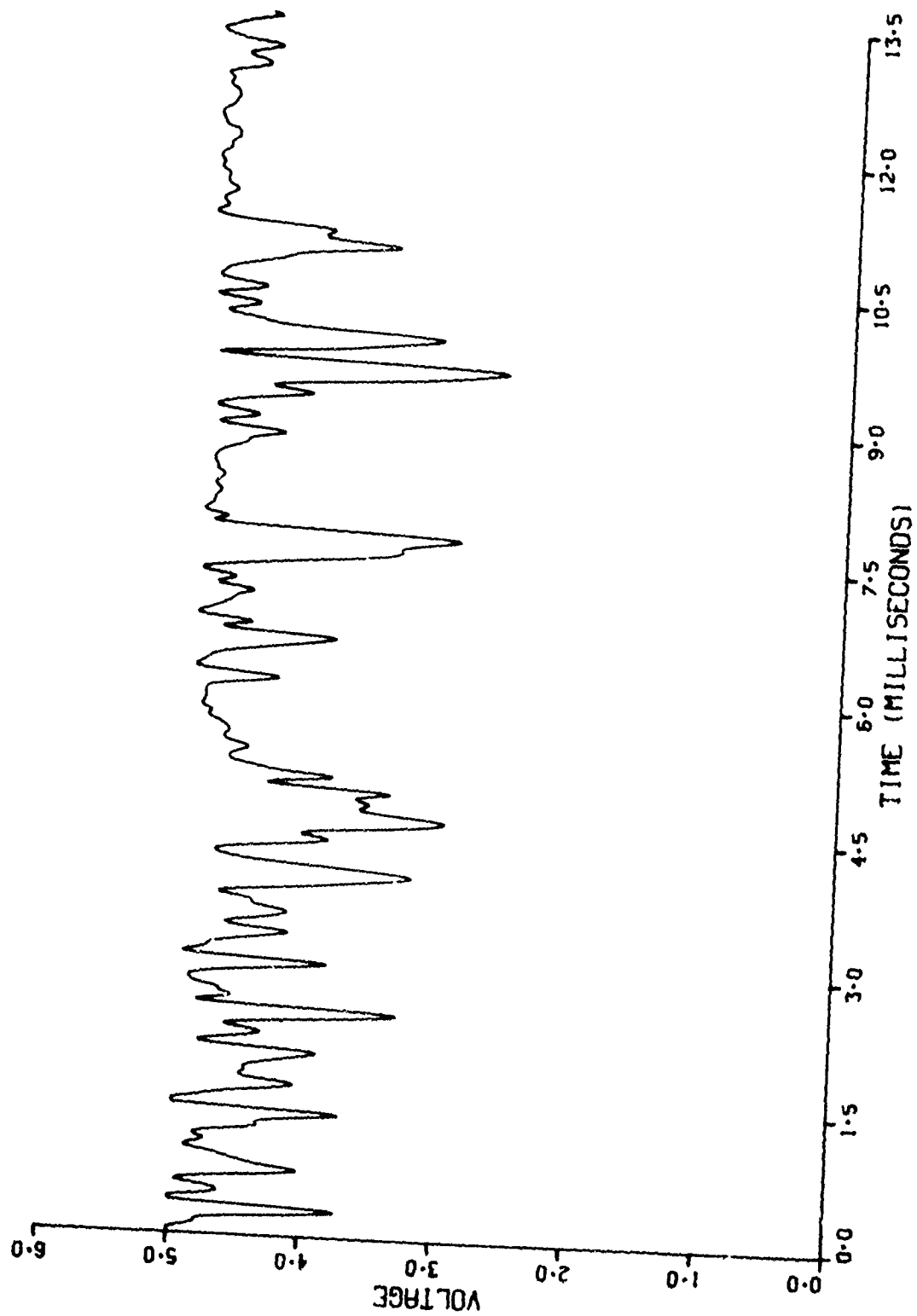
Figure VI.7 Hot-film probe signals in NaK-N$_2$ flow: measured at the channel centerline, B = 0 T, $\dot{m}_g$ = 0.067 kg/s, $\dot{m}_\ell$ = 5.65 kg/s
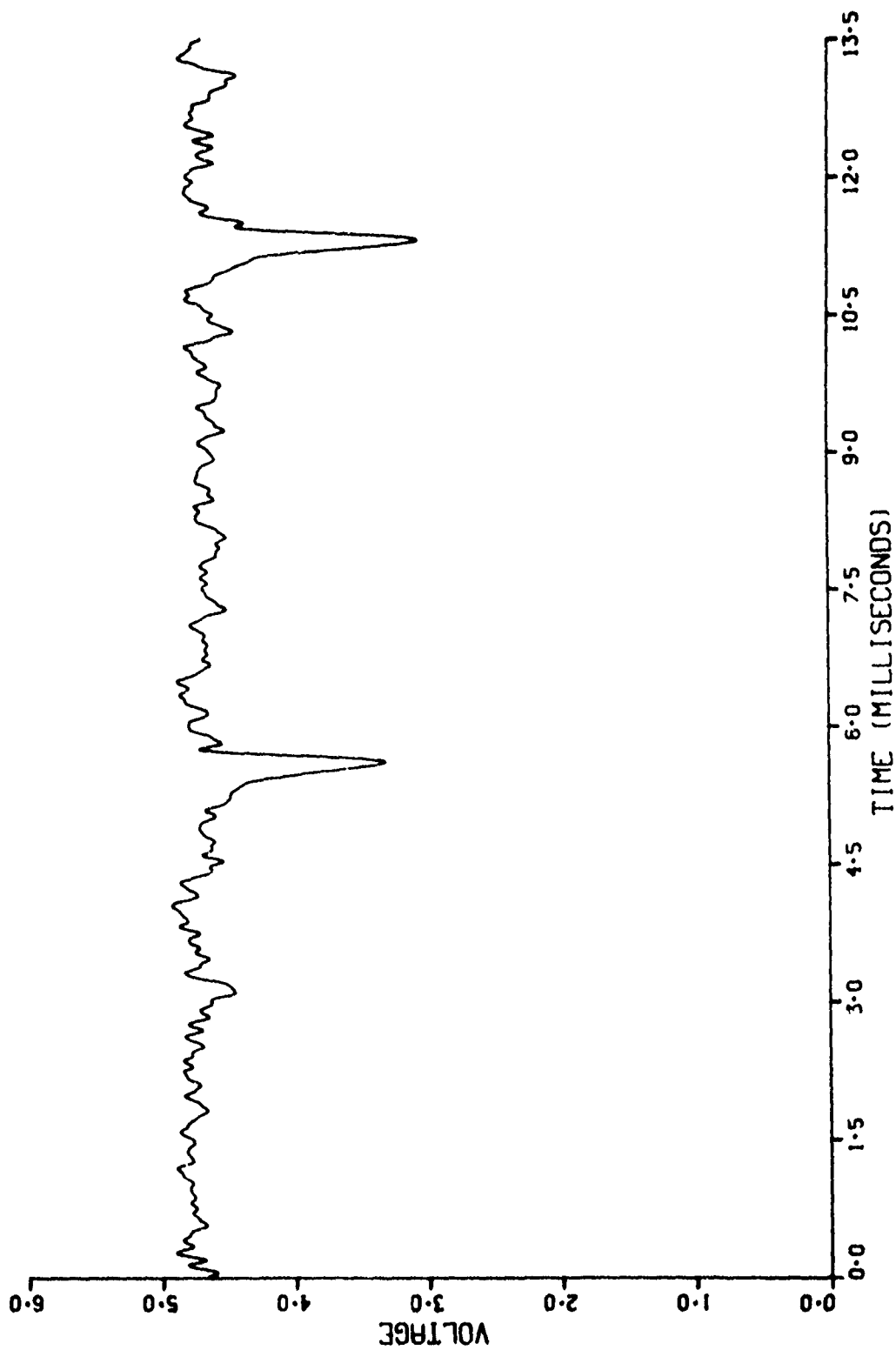
Figure VI.8 Hot-film probe signals in NaK-N$_2$ flow: measured at channel centerline, B = 0.3 T, $\dot{m}_g$ = 0.018 kg/s, $\dot{m}_\ell$ = 5.82 kg/s
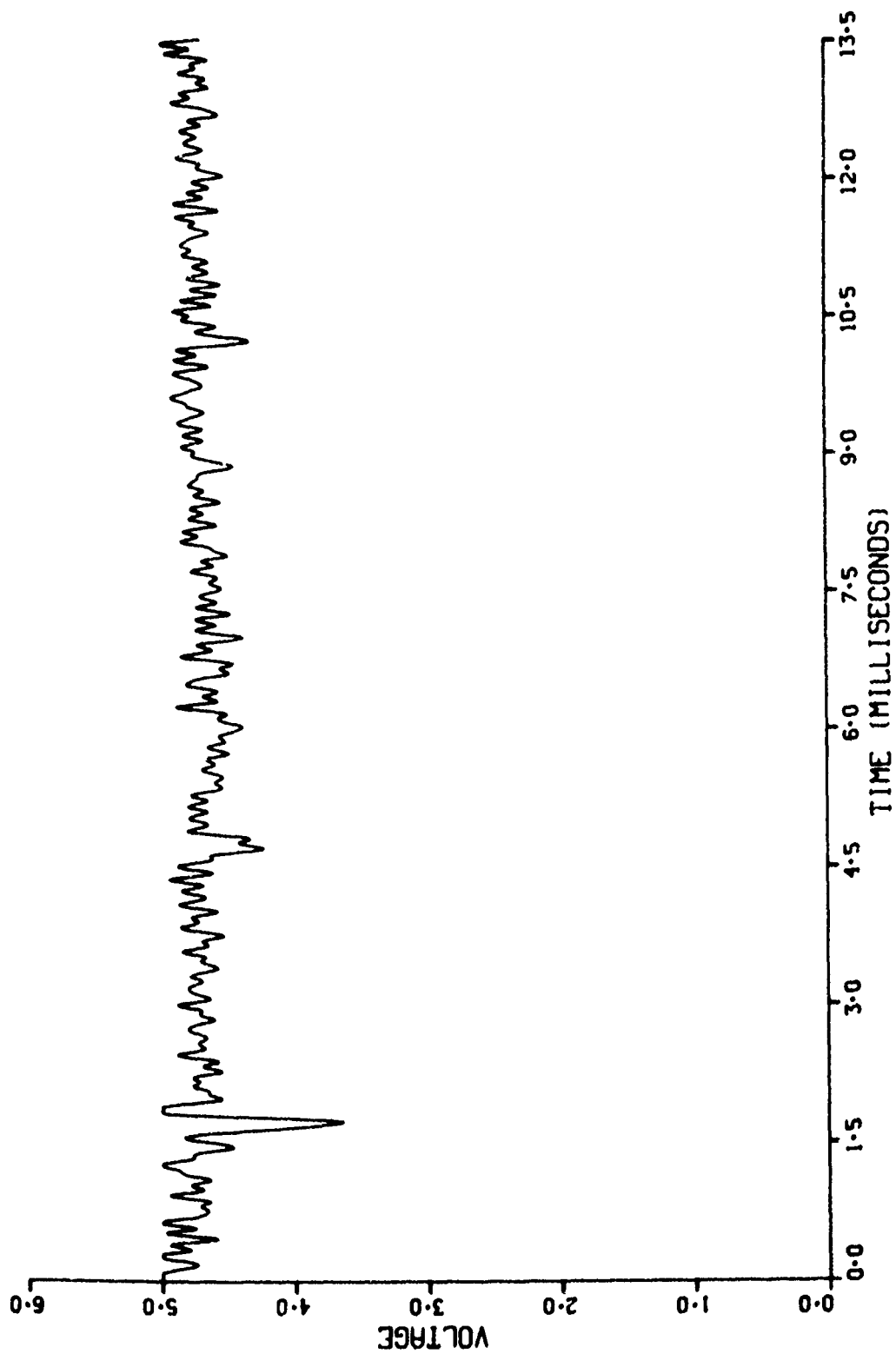
Figure VI.9 Hot-film probe signals in NaK-N$_2$ flow: measured at the channel centerline, B = 0.6 T, $\dot{m}_g$ = 0.065 kg/s, $\dot{m}_\ell$ = 5.0 kg/s
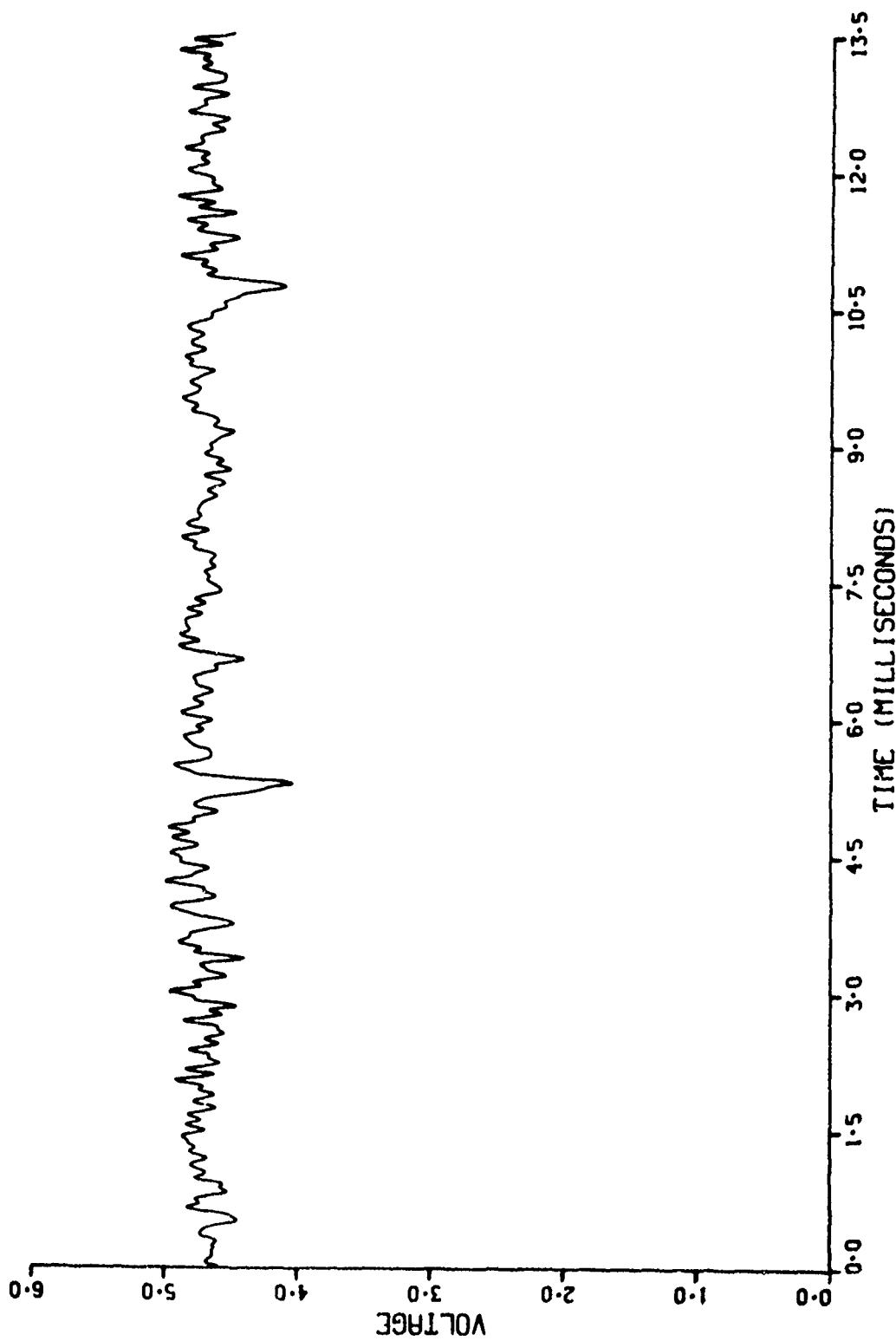
Figure VI.10 Hot-film probe signals in NaK-N$_2$ flow: measured at the channel centerline, B = 1.2 T, $\dot{m}_g$ = 0.06 kg/s, $\dot{m}_\ell$ = 3.96 kg/s

the gas flow rate is four times as high and corresponds to an average void fraction of approximately 0.65. In all cases, bubbles (voids may be a more-appropriate term, because they are not necessarily spheres) appear to differ in size and distribution with time. Especially for the last figure, there may be many pieces of liquid (drops, threads, sheets, etc.) inter-mingled with the voids; this is characteristic of churn-turbulent flow.

Figures VI.8, VI.9, and VI.10 were measured for two-phase MHD flows with a load resistance of 0.1 mΩ, a relatively-small resistance value that results in heavy loading of the channel, and magnetic flux densities of B = 0.3, 0.6, and 1.2 T, in that order. The mass flow rates of Fig. VI.8 are the same as those of Figs. VI.5 and VI.6, whereas Figs. VI.9 and VI.10 are close to the mass flow rates of Fig. VI.7. For all cases with an applied magnetic field, especially at the higher flux densities, there is an apparent decrease in the number of detectable bubbles. Also, the fluctua-tions in the liquid flow appear to increase in magnitude as B increases, and the higher-frequency components appear to be damped. The cause of the apparent decrease in the number of bubbles is unknown at present. The probe was moved to different locations (but still halfway between the insulating walls) with similar results. Note that, for two-phase flows, the fluctuations appear to increase in magnitude with increasing B, whereas for pure-liquid flows, the fluctuations are damped.

VI.4 Resistivity Probe Results

The resistivity probe used to obtain the data shown in Figs. VI.11 to VI.13 was inserted through a pressure tap located 250 mm downstream of the beginning of the electrodes. The probe used a stainless steel wire with an uninsulated tip approximately 0.1 mm in diameter and 0.25 mm in length, on
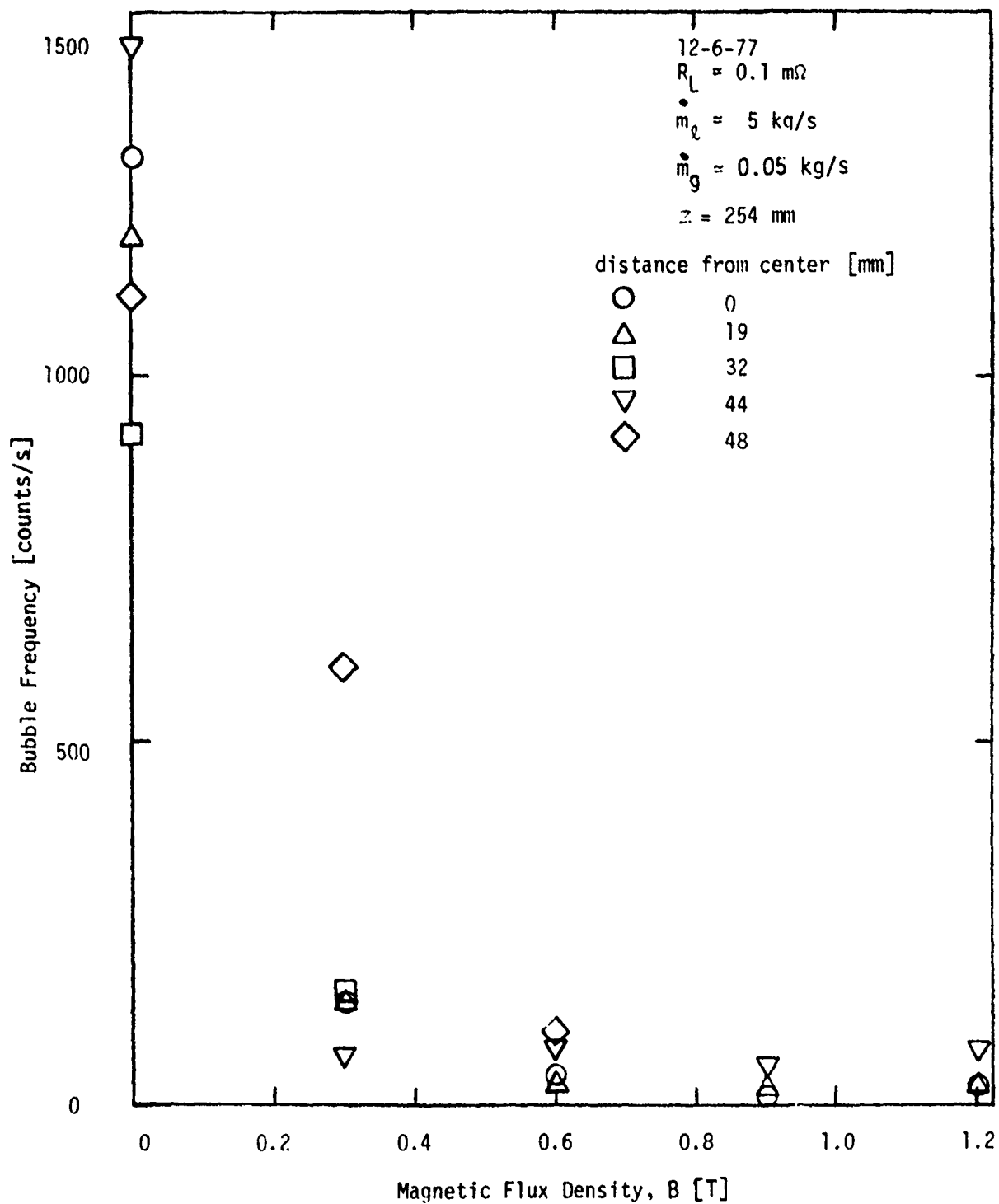
Figure VI.11 Bubble frequency in NaK-N$_2$ MHD generator, obtained by resistivity probe
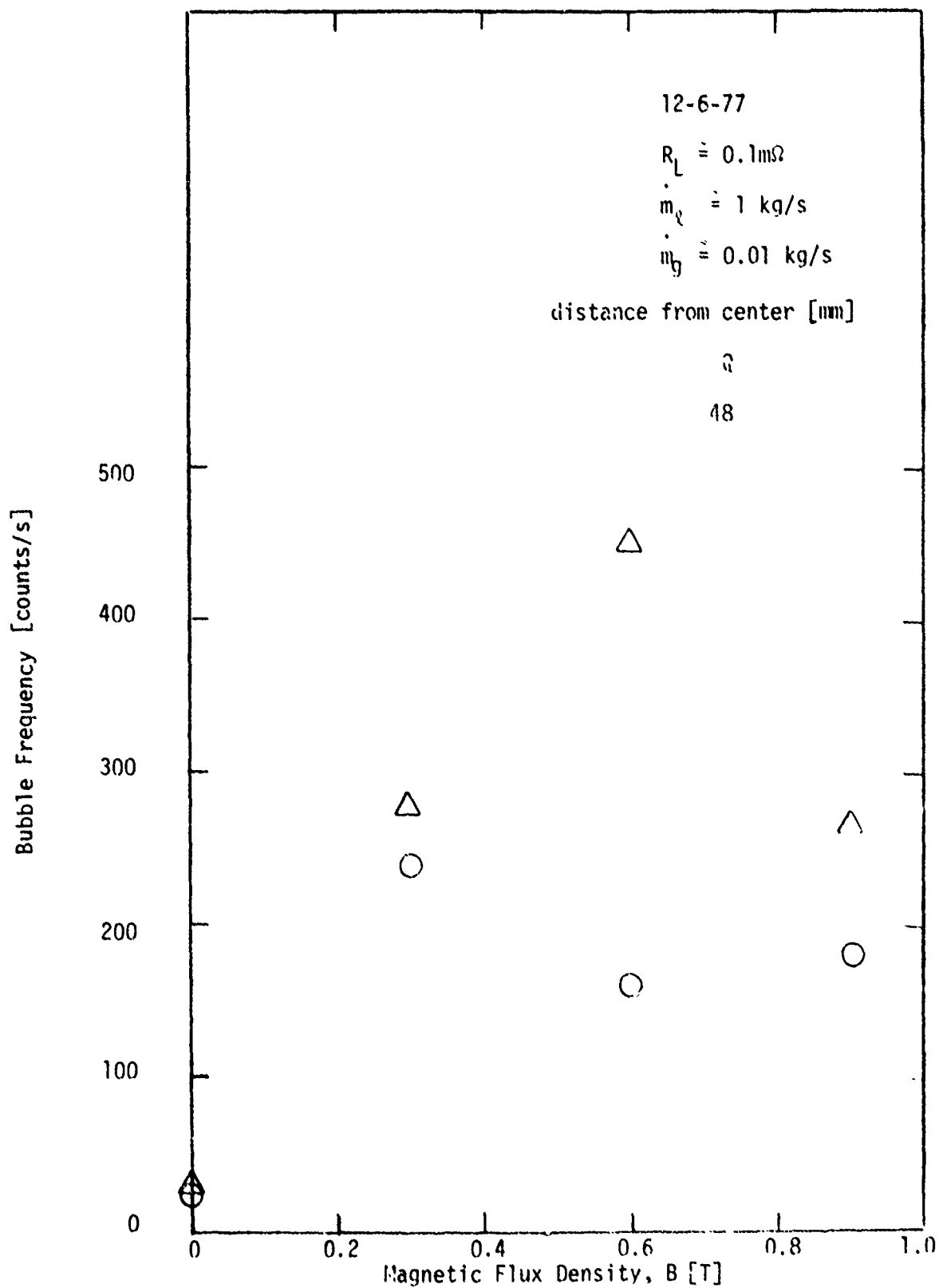
Fig. VI.12 Bubble frequency in NaK-N$_2$ MHD generator, obtained
by resistivity probe
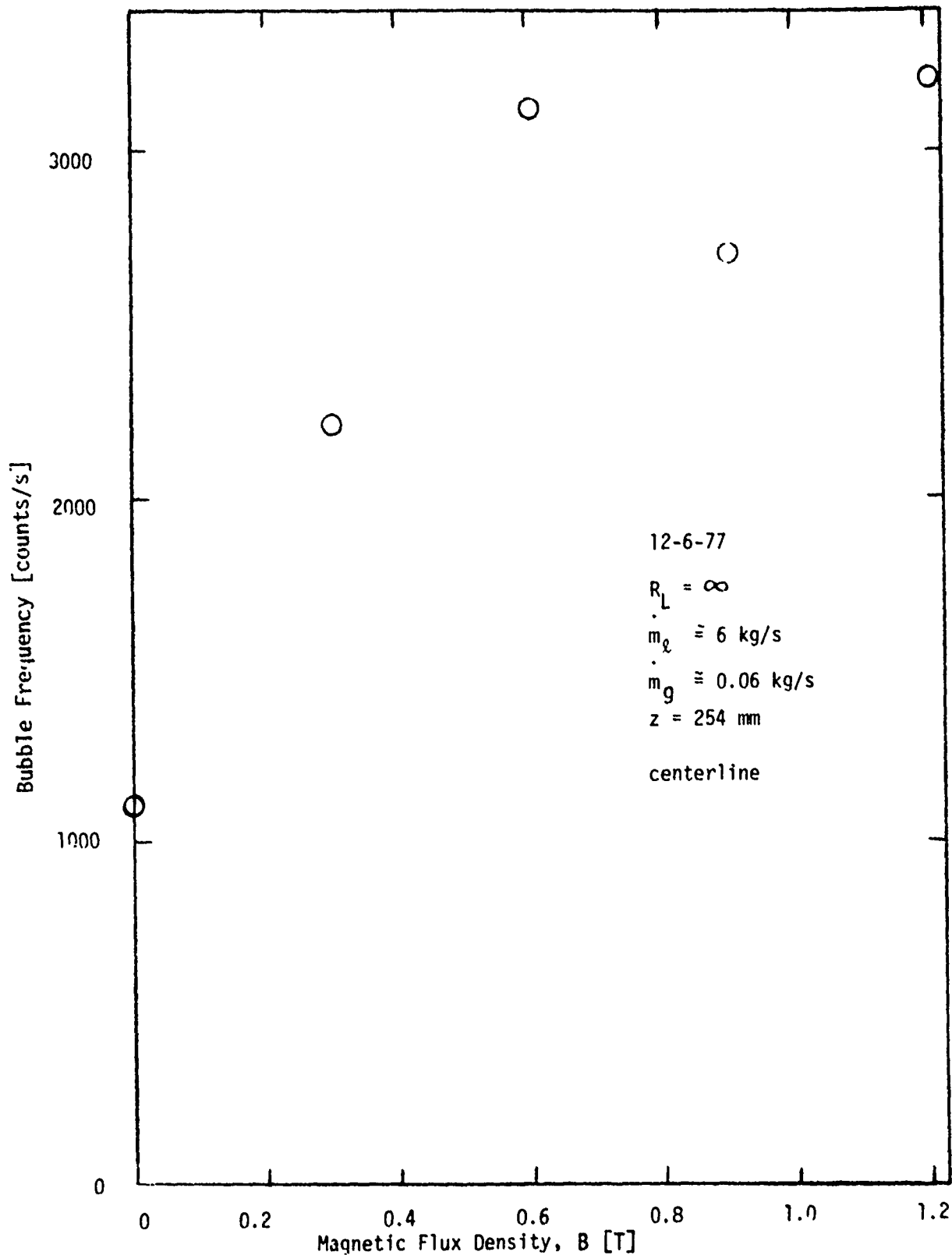
Figure VI.13 Bubble frequency in NaK-N$_2$ MHD generator, obtained by resistivity probe

a stem approximately 5 mm long, which was pointed into the flow. (Note that the length of the uninsulated tip is also the dimension of the smallest detectable bubble or void parallel to the flow.) It is convenient to use bubble frequency (bubbles/second) to interpret the resistivity probe data, because the discriminator circuit converts the signal to square waves that are easy to count.

Bubble frequencies for $\dot{m}_\ell$ = 5 kg/s and $\dot{m}_g$ = 0.05 kg/s are shown in Fig. VI.11 as functions of B and the distance of the probe from the center of the channel along the line to one electrode (total distance of 51 mm). For B = 0, the bubble frequencies show a triple maximum, similar to the void-fraction profiles obtained with a resistivity probe by Fabris et al (1977b) for air-water flow with an identical mixer geometry. As B is increased, the bubble frequency drops sharply to very low values. Note that the decrease in bubble frequency with increasing B is less closer to the electrodes; this might possibly indicate bubble migration toward the electrodes, as would be expected from the end-region currents that produce M-shaped MHD velocity profiles. (Recent measurements for a similar LMMHD generator confirm the existence of the pressure distribution in the end regions caused by these currents, see Section III.4.) The addition of one or more insulating vanes in the end regions to supress end currents would also suppress this bubble migration; thus migration is not a matter of concern in regard to practical LMMHD generators.

The most-significant feature shown in Fig. VI.11 is the low bubble count at all locations for high B; this confirms the hot-film data. Bubble migration toward the electrodes cannot be the sole cause, because so many bubbles there would break the current paths. The most-likely explanation is that the large electromagnetic force density and the resulting high

-144-

pressure gradient "shear" the gas bubbles or voids into smaller pieces, which may be too small to be detected clearly by either probe. (Such small voids could cause the high-frequency fluctuation shown in Figs. VI.8 through VI.10 for the hot-film probe.) Evidence of void break-up is discussed below. Another factor could be the influence of the electro-magnetic force density on the void shape and motion around the probe. Also, the voids are smaller because of the higher static pressure at the probe location with $B \neq 0$; however, this is not enough of a factor in itself.

Additional experiments were performed to clarify some of the effects. At low flow rates or velocities, the electromagnetic force density is reduced; thus, changes with B becomes more gradual and easier to detect. In addition, voids are easier to detect at lower velocities. Data are shown in Fig. VI.12 for flow rates one-fifth that of Fig. VI.11 for the same quality (same void fraction if pressure and slip ratio are the same). At B = 0, the bubble frequency is very low, indicating a slug flow pattern with large voids. As B is increased, the bubble frequency increases by more than one order of magnitude before decreasing. This indicates that the large voids are broken up into smaller voids and many are not detected at large B values, as discussed above. Significantly, more bubbles are observed close to the electrode, as occurred with the higher flow rate.

Data are shown in Fig. VI.13 for a high flow rate but with the gene-rator open-circuited, so that the electromagnetic force density is greatly reduced. Again, the bubble frequency increases as B is increased; this time without a decrease at larger B values.

VII. CONCLUSIONS

The new generator channel, LT-4, has been tested at high velocities
and high pressures (large magnetic interactions). Power densities of up to
32 MWe/m^3 were obtained in this small, 20-kWe generator, equal to or
better than those anticipated for LMMHD generators in practical power
systems. Efficiencies higher than 0.6 at average void fractions well above
0.5 were measured, which is very good performance for a small, wall-dominated
generator. The rapid decrease in slip ratio with increasing flow rate,
demonstrated previously at low power densities [Petrick et al (1978)], was
confirmed for high power densities. In addition, more-detailed pressure
and voltage data were obtained. These postive results meet the goals of
the revised facility and channel LT-4, and justify the existence of this
experimental program.

The use of foams in the two-phase LMMHD generators allows the generator
to operate at higher average void fractions, and leads to higher "equivalent
turbine" efficiencies, reduced losses, because there is less liquid to
recirculate, and higher system performance. The foam experiments have
concentrated on bubble tests and surface tension measurements, and much
basic data has been obtained. Barium has been identified as an attractive
additive for NaK because it 1) markedly stabilizes bubble lifetime, 2) pro-
motes foaming, and 3) is a wetting agent. Although barium is known to
react with nitrogen (but not helium), no degradation of bubble performance
was observed at temperatures close to ambient; some slow degradation was
observed at temperatures above approximately 400 K, with the rate of
degradation increasing with temperature. Bismuth was identified as a
back-up for barium. A guiding hypothesis for understanding the phenomena
contributing to foamability in liquid metal systems has been developed.

End current losses in LMMHD generators can be controlled by the proper choice of 1) channel aspect ratio, 2) magnetic flux density distribution outside of the electrodes, and 3) number and dimensions of insulating vanes. A computer code has been developd for the calculation of the end current loss as the above parameters are varied. Initial studies with this code have shown that generator efficiencies in excess of 0.8 are attainable.

Initial measurements of local flow parameters in two-phase LMMHD flows have been presented. Both hot-film and resistivity probes were used, and similar results were obtained. Clearly, the behavior of the voids is influenced when the electromagnetic interaction parameter is high, although definitive statements are limited at present by the inability of the probes to detect the smaller voids that result for higher electromagnetic force densities. There is, however, definite evidence of void break-up and migration.

Significant advances have been made in understanding the operation of two-phase LMMHD generators. All results are very encouraging, and indicate that large high-efficiency two-phase LMMHD generators can be developed.

REFERENCES

ADDISON, C. C., COLDREY, J.M., and HALSTEAD, W. D., 1962, J. Chem. Soc., 3868.

AMEND, W. E., COLE, R. L., CUTTING, J. C., and PITTENGER, L. C., 1973, "Experimental Two-Phase Liquid-Metal Magnetohydrodynammic Generator Program," ANL/ENG-73-02, Argonne National Laboratory, Argonne, IL.

BRADHURST, D. H., and BUCHANAN, A. S., 1961, Australian J. of Chem., 14, 397.

BRANOVER, H., 1974, "On Some Important Effects in Laboratory MHD Flows in Rectangular Ducts in Transverse Magnetic Fields, "Proc. of the 14th Symp. on Engrg. Aspects of MHD, Tullahoma, TN.

BRANOVER, H., GHERSON, P., and YAKHOT, A., 1977, "MHD Turbulence and Two-Phase Flow," ME 5-77, Ben Gurion University of the Negev, Beer-Sheva, Israel.

BRANOVER, H., ELBOCHER, A., HOCH, E., UNGER, Y., YAKHOT, A., and ZILBERMAN, I., 1978, "Hydrodynamic Investigation of Single and Two-Phase Flow in Liquid Metal MHD Generator Channels," ME 4-78, Ben Gurion University of the Negev, Beer-Sheva, Israel.

BRUNSVOLD, A. R., and PIERSON, E.S., 1976, "Liquid-Metal MHD Coupled to Coal-Fired Fluidized-Bed Combustors," III.8.1-III.8.8, Proceedings of the 15th Symposium on Engrg. Aspects of Magnetohydrodynamics, Phila-delphia, PA.

DOMBROWSKI, N., and FRASER, R. P., 1954, "A Photographic Investigation into the Disintegration of Liquid Sheets," Phil. Trans. A, 247 (A924), pp. 101-130.

DUNN, P. F., 1978, "Current-or-Voltage Clamp Impedance-Variation Probe Circuit," Patent Securement Proposal, submitted 8/17/78, DOE Case No. S-49,198.

DUNN, P. F., PIERSON, E. S., STAFFON, J. D., POLLACK, I., and DAUZVARDIS, P. V., 1979, "High-Temperature Liquid-Metal MHD Generator Experiments," Proceedings of the 18th Symposium on Engrg. Aspects of MHD, Butte, MT.

FABRIS, G., PIERSON, E.S., FISCHER, A.K., and JOHNSON, C.E., 1977a, "Initial Generator Tests with Revised Ambient-Temperature Liquid-Metal MHD Facility," Proceedings of the 16th Symposium on Engrg. Aspets of MHD, Pittsburgh, PA.

FABRIS, G., DUNN, P.F., CHOW, J.C.F., and KOLP, R., 1977b, "Studies on Two-Phase Flow Mixing Pertaining to Liquid-Metal Magnetohydrodynamic Power Generation," Proceedings of the Fifth Biennial Symposium on Turbulence, Rolla, MI.

FABRIS, G., and PIERSON, E. S., 1978, "The Role of Interfacial Heat and
    Mechanical Energy Transfer in a Liquid-Metal MHD Generator," ASME
    Paper 78-WA/HT-33, presented at the ASME Winter Annual Meeting, San
    Francisco, CA.

FISHMAN, F., 1959, "End Effects in Magnetohydrodynamic Channel Flow,"
    Research Report No. 78, Avco-Everett Research Laboratory, Everett,
    MA.

GARDNER, R. A., and LYKOUDIS, P.S., 1971, "Magneto-Fluid-Mechanic Pipe Flow
    in a Transverse Magnetic Field, Part 1, Isothermal Flow," J. Fluid
    Mech., 78, 261.

GAWOR, J.Z., 1978, "An Experimental Study of the Resistivity Probe Technique
    for the Measurement of Void Fraction in Air-Water Two-Phase Flow,"
    M.S. Project, Dept. of Energy Engrg., University of Illinois and
    Chicago Circle, Chicago, IL.

GUBAREV, A. V., DEGTYAREV, L. M., and FAVORSKII, A. P., 1970, "Longitudinal
    Edge Effect in Magnetohydrodynamic Channels," Magnitnaya Gidrodiuamica,
    6, No. 2, pp. 78-82.

HOFFMAN, M. A., and CARLSON, G. A., 1971, "Calculation Techniques for
    Estimating the Pressure Losses for Conducting Fluid Flows in Magnetic
    Fields," UCRL-51010, Lawrence Radiation Laboratory, Livermore, CA.

LAVRENTIEV, I. V., 1967, "Effect of Baffle Location on the Characteristics
    of an MHD Channel," Magnitnaya Gidrodinamika, 3, No. 4, pp. 89-95.

LAVRENTIEV, I. V., 1968, "Effect of the Length of a Nonconducting Barrier
    on the Characteristics of an MHD Generator," Magnitnaya Gidrodinamika,
    4, No. 1, pp. 27-32.

MICHIYOSHI, I., FUNAKAWA, H., KURA MOTO, C., AKITA, Y., and TAKAHASHI, O.,
    1977, "Local Properties of Vertical Mercury-Argon Two-Phase Flow in a
    Circular Tube under Transverse Magnetic Field," Int. J. Multiphase
    Flow, 3, pp. 445-457.

MOSZYNSKI, J. R., 1967, "Reduction of Electrical End Losses in MHD Generator
    Channels by Insulating Vanes," ANL-7188, Argonne National Laboratory,
    Argonne, IL.

MOSZYNSKI, J. R., and AGRAWAL, J. C., 1968, "Electrical End Losses in
    Liquid Metal MHD Generators with Variable Conductivity," Electricity
    from MHD Proceedings of a Symposium, Warsaw, Vol. III, pp. 1667-1680.

PETRICK, M., ROBERTS, J. J., LAMBERT, G., and SPLEHA, E., 1968, "Analytical
    and Experimental Studies of Single and Two-Phase Liquid Metal Faraday
    Generators," AFAPL-TR-68-93, Argonne National Laboratory, Argonne, IL.

PETRICK, M., AMEND, W. E., PIERSON, E. S., and HSU, C., 1970, "Investigation
    of Liquid-Metal MHD Power Systems," ANL/ETD-70-12, Argonne National
    Laboratory, Argonne, IL.

PETRICK, M., COLE, R. L., CUTTING, J. C., AMEND, W. E., and FABRIS, G., 1975, "Experimental Two-phase Liquid-Metal Magnetohydrodynamic Generator Program," ANL/ENG-75-02, Argonne National Laboratory, Argonne, IL.

PETRICK, M., FABRIS, G., COLE, R., HANTMAN, R., PIERSON, E., and CUTTING, J., 1976, "Experimental Two-Phase Liquid-Metal Magnetohydrodynamic Generator Program," ANL/ENG-76-04, Argonne National Laboratory, Argonne, IL.

PETRICK, M., FABRIS, G., PIERSON, E. S., CARL, D. A., FISCHER, A. K., and JOHNSON, C. E., 1977, "Experimental Two-Phase Liquid-Metal Magneto-hydrodynamic Generator Program," ANL/MHD-77-3, Argonne National Laboratory, Argonne, IL.

PETRICK, M., FABRIS, G., PIERSON, E. S., FISCHER, A. K., and JOHNSON, C. E., 1978, "Experimental Two-Phase Liquid-metal Magnetohydrodynamic Generator Program," ANL/MHD-78-2, Argonne National Laboratory, Argonne, IL.

PIERSON, E. S., 1978, "Central Station Applications of Brayton-Cycle Liquid-Metal MHD," Proceedings of the Rand Corporation Conference on Liquid-Metal MHD Power Generation, Pei, R. Y., and Purnell, S. W., Eds., R-2290-DOE, Washington, D. C.

PIERSON, E. S., PETRICK, M., SCHREINER, F., and COHEN, D., 1979, "Open-Cycle Coal-Fired Liquid-Metal MHD," Proceedings of the 18th Symposium on the Engrg. Aspects of MHD, Butte, MT.

PITTENGER, L. C., PIERSON, E. S., COLE, R., and PETRICK, M., 1972, "Experimental Two-Phase Liquid-Metal MHD Generator Program," Report No. ANL/ETD-72-07, Argonne National Laboratory, Argonne, IL.

RICE, J. R., 1977, "ELLPACK: A Research Tool for Eliptic Partial Differential Equations Software," in Mathematical Software III, (J. R. Rice, ed.) Academic Press, pp. 319-344.

ROSSOW, V. T., JONES, W. D., and HUERTA, R. H., 1961, "On the Induced Fow of an Electrically Conducting Liquid in a Rectangular Duct by Electric and Magnetic Fields of Finite Extent," NASA TN-D-347, Ames Research Center, Moffett Field, CA.

SUTTON, G. W., HURWITZ, H., JR., and PORITSKY, H., 1961, "Electrical and Pressure Losses in a Magnetohydrodynamic Channel due to End Current Loops," Trans. AIEE Part I, Communications and Electronics, 80, 687-695.

VASILIEV, V. F., and LAVRENTIEV, I. V., 1970, "Longitudinal Boundary-Vaue Problem of Electric Field Distribution in MHD Channels with Nonconducting Walls," Magnitnaya Gidrodinamika, 6, No. 2, pp. 83-89.

APPENDIX A

SUMMARY OF EXPERIMENTAL GENERATOR DATA[**]

OCTOBER 1977 TO DECEMBER 1978

Date (1978)	Run No.	Liquid Mass Flow Rate $\dot{m}_\ell$ [kg/s]	Load Resistance R_L [mΩ]	Load Voltage V_L [V]	Average Void Fraction $\bar{\alpha}$	Average Slip Ratio K	Average Load Factor F	Power Output P_e [kW]	Generator Eff. n_i	Equiv. Turbine Eff. n_t	Back Pressure P_{out} [psia]
6-21	1	6.120	∞	0.518	0	-	.974	0	0	-	20
	2	9.080	∞	0.799	0	-	.987	0	0	-	20
	3	12.100	∞	1.006	0	-	.956	0	0	-	20
	4	6.025	∞	0.973	.585	1.0[*]	.765	0	0	-	20
	5	9.080	∞	1.717	.571	1.0[*]	.920	0	0	-	20
	6	12.100	∞	2.424	.561	1.0[*]	.995	0	0	-	20
	7	15.200	∞	1.300	0	-	.984	0	0	-	20
	8	17.780	∞	1.593	0	-	1.031	0	0	-	20
6-30	1	5.980	.260	0.417	0	-	.802	0.669	.204	-	20
	2	9.083	.261	0.781	0	-	.989	2.341	.349	-	20
	3	11.825	.245	1.016	0	-	.988	4.219	.391	-	20
	4	15.108	.240	1.235	0	-	.940	6.352	.308	-	20

[*]K assumed 1 for these runs, not measured

[**]Magnetic Flux Density B = 1.263 T for all runs except as indicated

Date (1978)	Run No.	Liquid Mass Flow Rate $\dot{m}_\ell$ [kg/s]	Load Resistance R_L [mΩ]	Load Voltage V_L [V]	Average Void Fraction $\bar{\alpha}$	Average Slip Ratio $\bar{K}$	Average Load Factor F	Power Output P_e [kW]	Generator Eff. η_i	Equiv. Turbine Eff. η_t	Back Pressure P_{out} [psia]
7-5	1	5.980	.241	0.813	.525	1.0*	.726	2.744	.472	.043	20
	2	9.218	.246	1.382	.489	1.0*	.874	7.759	.585	.210	20
	3	12.140	.257	1.965	.492	1.0*	.919	15.017	.629	.333	20
	4	14.210	.276	2.271	.474	1.0*	.940	18.684	.599	.276	20
	5	6.025	.240	1.033	.709	1.0*	.556	4.452	.414	.207	20
	6	9.173	.251	1.765	.630	1.0*	.790	12.397	.566	.385	20
7-12	1	12.190	.276	2.444	.614	1.0*	.857	21.615	.605	.457	20
	2	6.025	.253	0.712	.338	1.0*	.885	2.002	.548	-.324	20
	3	8.990	.256	1.142	.392	1.0*	.870	5.088	.543	-.094	20
	4	11.960	.260	1.413	.294	1.0*	.939	7.677	.555	-.426	20
	5	12.050	.260	1.473	.341	1.0*	.907	8.352	.551	-.219	20
	6	15.153	.264	1.860	.323	1.0*	.935	13.120	.556	-.242	20
	7	6.025	.417	0.900	.597	1.0*	.678	1.942	.391	-.005	20
	8	9.038	.410	1.469	.535	1.0*	.848	5.266	.493	.095	20
	9	11.690	.409	1.973	.514	1.0*	.920	9.506	.525	.157	20

*K assumed 1 for these runs, not measured

Date (1978)	Run No.	Liquid Mass Flow Rate $\dot{m}_\ell$ [kg/s]	Load Resistance R_L [mΩ]	Load Voltage V_L [V]	Average Void Fraction $\bar{\alpha}$	Average Slip Ratio $\bar{K}$	Average Load Factor F	Power Output P_e [kW]	Generator Eff. η_i	Equiv. Turbine Eff. η_t	Back Pressure P_{out} [psia]
7-17	1	6.120	.408	1.086	.726	1.0*	.546	2.889	.357	.121	20
	2	8.903	.409	1.807	.693	1.0*	.695	7.978	.453	.272	20
9-29	1	5.935	.416	0.474	0	-	.919	0.540	.201	-	20
	2	5.935	.399	0.897	.451	1.831	.940	2.019	.344	-.104	20
	3	6.160	.394	1.143	.629	1.492	.775	3.317	.371	.135	20
	4	6.115	.394	1.197	.590	2.080	.893	3.635	.333	.126	20
	5	5.845	.391	1.206	.665	1.837	.775	3.717	.316	.135	20
10-3	1	6.025	.388	0.477	0	-	.911	0.587	.222	-	26
	2	5.755	.392	1.170	.642	2.190	.828	3.489	.263	.091	23
10-4	1	3.147	.380	0.240	0	-	.877	0.151	.198	-	25
	2	3.192	.391	0.466	.559	2.379	.729	0.555	.205	-.067	20
	3	3.282	.389	0.536	.653	2.446	.622	0.738	.188	-.024	20
	4	3.013	.390	0.555	.705	3.307	.598	0.790	.131	-.028	21
	5	2.878	.390	0.566	.641	6.556	.770	0.822	.099	-.034	22
	6	2.833	.388	0.570	.683	6.171	.697	0.837	.089	-.035	21

*$\bar{K}$ assumed 1 for these runs, not measured

-153-

Date (1978)	Run No.	Liquid Mass Flow Rate $\dot{m}_\ell$ [kg/s]	Load Resistance R_L [mΩ]	Load Voltage V_L [V]	Average Void Fraction $\bar{\alpha}$	Average Slip Ratio R	Average Load Factor F	Power Output P_e [kW]	Generator Eff. η_i	Equiv. Turbine Eff. η_t	Back Pressure P_{out} [psia]
11-13	1	6.210	.411	0.485	0	-	.898	0.572	.195	-	24
	2	5.980	.399	1.055	.638	1.333	.724	2.788	.345	.061	22
	3	6.070	.397	1.242	.736	1.117	.599	3.889	.268	.056	20
	4	9.310	.402	1.900	.605	1.076	.910	8.987	.473	.216	20
11-14	1	5.980	.386	0.470	0	-	.904	0.572	.203	-	24
	2	6.250	.399	1.090	.643	1.294	.733	2.976	.366	.087	22
	3	9.308	.401	2.118	.646	1.050	.911	11.195	.473	.287	19
11-15	1	5.980	.246	0.457	0	-	.879	0.848	.278	-	25
	2	5.980	.254	1.032	.566	1.689	.852	4.191	.464	.214	20
	3	8.948	.271	1.810	.569	1.215	.976	12.107	.562	.355	20
11-20	1	5.940	.244	0.461	0	-	.893	0.870	.290	-	26
	2+	5.980	0	0	0	-	-	0	0	-	26
	3	6.070	.258	1.060	.614	1.257	.755	4.358	.450	.200	20
	4	9.130	.269	1.838	.625	0.984	.847	12.573	.555	.354	18
	5	6.070	.261	1.205	.672	1.540	.730	5.555	.369	.193	20
	6	6.120	.259	1.089	.614	1.625	.778	4.579	.385	.198	5

+ B = 0

Date (1978)	Run No.	Liquid Mass Flow Rate $\dot{m}_\ell$ [kg/s]	Load Resistance R_L [mΩ]	Load Voltage V_L [V]	Average Void Fraction $\bar{\alpha}$	Average Slip Ratio $\bar{K}$	Average Load Factor $\bar{F}$	Power Output P_e [kW]	Generator Eff. n_i	Equiv. Turbine Eff. n_t	Back Pressure p_{out} [psia]
11-22	1	6.025	.247	0.463	0	-	.884	0.867	.275	-	22
	2+	6.000	∞	0	0	-	-	0	-	-	24
	3	5.980	.264	1.135	.700	1.650	.660	4.874	.312	.190	4
11-28	1	6.025	.242	.465	0	-	.888	0.892	.283	-	22
	2	6.025	.254	.932	.583	1.963	.730	3.422	.338	.112	5
	3	5.890	.253	1.008	.681	1.824	.620	4.011	.279	.156	5
	4	6.070	.255	1.102	.738	1.461	.544	4.755	.284	.176	5
	5	6.025	.256	1.111	.604	1.961	.604	4.844	.244	.121	5.5
	6	9.083	.244	.733	0	-	.928	2.200	.305	-	22
	7	9.083	.257	1.530	.576	1.001	.818	9.091	.537	.280	5
11-29	1	9.083	.243	0.724	0	-	.917	2.160	.295	-	20
	2	8.723	.260	1.655	.594	1.344	.870	10.543	.473	.317	5
	3	9.263	.264	1.820	.584	1.353	.927	12.537	.487	.346	6
12-06	1	6.025	.404	0.475	0	-	.907	0.559	.202	-	20
	2	6.115	.420	0.971	.619	1.440	.670	2.245	.309	.041	5

+ B = 0

Date (1978)	Run No.	Liquid Mass Flow Rate $\dot{m}_\ell$ [kg/s]	Load Resistance R_L [mΩ]	Load Voltage V_L [V]	Average Void Fraction $\bar{\alpha}$	Average Slip Ratio R	Average Load Factor F	Power Output P_e [kW]	Generator Eff. η_i	Equiv. Turbine Eff. η_t	Back Pressure P_{out} [psia]
12-06	3	6.070	.424	1.092	.729	1.058	.558	2.811	.280	.091	5
	4	6.025	.424	1.237	.713	1.640	.660	3.611	.259	.127	5
	5	9.128	.427	1.521	.516	1.034	.903	5.415	.469	.085	5
	6	9.083	.430	1.616	.540	1.255	.910	6.076	.429	.145	4.5
	7	8.948	.435	1.845	.662	1.015	.773	7.829	.410	.229	6
12-08	1	5.940	.401	0.464	0	-	.899	0.536	.201	-	21.5
	2	9.038	.425	1.420	.484	1.020	.910	4.743	.468	-.050	20.5
	3	9.128	.428	1.540	.541	0.956	.871	5.548	.458	-.006	31
	4	9.128	.428	1.579	.556	0.969	.864	5.831	.466	.078	21
	5	9.128	.434	1.836	.636	1.016	.821	7.774	.448	.187	20
	6	9.128	.245	1.339	.454	1.026	.898	7.324	.581	.151	20
	7	9.173	.249	1.470	.537	0.951	.830	8.680	.566	.240	19.5
	8	9.038	.254	1.672	.541	1.338	.955	11.015	.537	.306	19

APPENDIX B

GENERATOR POWER EQUATIONS

The electrical power output is determined from the measured generator terminal voltage V_L and the load resistance, R_L, i.e.,

$$\text{Electrical power output} = V_L^2/R_L. \qquad (B.1)$$

The ideal liquid mechanical pump work, the power input from the liquid to the generator, is the pump work plus the kinetic energy change of the liquid (assuming there are no losses and that the pumping process is isentropic),

$$\text{Ideal liquid mechanical pump work} = \frac{\dot{m}_\ell \nabla p}{\rho_\ell} + \frac{\dot{m}_\ell (u^2_{\ell,\text{in}} - u^2_{\ell,\text{out}})}{2}, \qquad (B.2)$$

where $\dot{m}_\ell$ is the liquid mass flow rate, ρ_ℓ the liquid density, $\nabla p = p_{\text{in}} - p_{\text{out}}$ the pressure difference across the generator for this idealized case, and u_ℓ the liquid velocity. The total power input is the enthalpy and kinetic energy changes across the generator for both the liquid and gas components,

$$\text{Total power input} = \dot{m}_\ell \left[\Delta h_\ell + \frac{(u^2_{\ell,\text{in}} - u^2_{\ell,\text{out}})}{2} \right] +$$

$$\dot{m}_g \left[\Delta h_g + \frac{(u^2_{g,\text{in}} - u^2_{g,\text{out}})}{2} \right] \qquad (B.3)$$

where $\nabla h = h_{\text{in}} - h_{\text{out}}$ denotes the enthalpy change. The enthalpy change for the liquid is

$$\Delta h_\ell = C_{p_\ell} (T_{\text{in}} - T_{\text{out}}) + (1 - \alpha_T \bar{T}) \frac{\Delta p}{\rho_\ell} , \qquad (B.4)$$

where T is the absolute temperature, C_{p_ℓ} the specific heat, the superscript "-" denotes an average, and

$$\alpha_T = \rho_\ell \left[\frac{\partial(1/\rho_\ell)}{\partial T}\right]_p . \tag{B.5}$$

For an ideal gas,

$$\Delta h_g = C_{p_g} (T_{in} - T_{out}) . \tag{B.6}$$

The isentropic power input is found by assuming that the expansion of the two-phase mixture through the generator is isentropic,

$$\Delta S = 0 = \dot{m}_g \left[C_{p_g} \ln \frac{T_{out}}{T_{in}} + R_g \ln \frac{p_{out}}{p_{in}} \right] +$$

$$\dot{m}_\ell \left[C_{p_\ell} \ln \frac{T_{out}}{T_{in}} - \frac{\alpha_T}{\rho_\ell} (p_{out} - p_{in}) \right]. \tag{B.7}$$

This leads to

$$T_{out} = T_{in} \exp \frac{\frac{\dot{m}_\ell}{\rho_\ell} \alpha_T (p_{out} - p_{in}) + \dot{m}_g R_g \ln(p_{out}/p_{in})}{(\dot{m}_g C_{p_g} + \dot{m}_\ell C_{p_\ell})} \tag{B.8}$$

for the exit temperature of the two-phase mixture. The isentropic power input is calculated from Eq. B.3 using T_{out} from Eq. B.8.

APPENDIX C

THE USE OF ELLPACK77 FOR SOLVING THE LAPLACE EQUATION ON A REGION WITH INTERIOR SLITS, APPLICATION TO A PROBLEM IN MAGNETOHYDRODYNAMICS

Robert E. Lynch[1], Paul Gherson[2], and Paul S. Lykoudis[2]

CSD-TR 275

July 1978

[1] Department of Computer Science and Mathematics, Purdue University, West Lafayette, Indiana 47907

[2] Department of Nuclear Engineering, Purdue University, West Lafayette, Indiana 47907

THE USE OF ELLPACK77 FOR SOLVING THE LAPLACE EQUATION ON A REGION WITH INTERIOR SLITS, APPLICATION TO A PROBLEM IN MAGNETOHYDRODYNAMICS

Robert E. Lynch[1], Paul Gherson[2], and Paul S. Lykoudis[2]

July 18, 1978

1. <u>Introduction</u>. We describe modifications of the Purdue University version of ELLPACK77 (see Rice [1977]) to solve the Laplace equation subject to mixed boundary conditions on the boundary of a rectangule and Neumann conditions on straight line segments in the interior of the rectangle.

In Section 2 a brief description is given of the physical origin of the problem, namely the analysis of the performance of a magnetohydrodynamic electric generator. Section 3 contains a mathematical model of the generator. Section 4 contains a new result: we show that one can determine the efficiency of the model for <u>all</u> values of one of its parameters by solving a <u>single pair</u> of boundary value problems. Section 5 very briefly describes how the efficiency of the generator can be increased by inserting insulating vanes in the fluid; in the mathematical model, these are modeled by slits in the interior of the rectangular domain on which Neumann boundary conditions are specified. Section 6 contains a brief outline of the ELLPACK system and its application to this problem. Section 7 gives the complete system of finite difference equations whose solution is taken as an approximation to the electric potential in the generator.

The ELLPACK module 5-POINT STAR, which was written by Ronald F. Boisvert of Purdue University, was modified to solve this problem. We thank him for his help during our modification of his routines.

---

[1] Departments of Computer Science and Mathematics, Purdue University.
[2] Department of Nuclear Engineering, Purdue University.

2. <u>Physical phenomenon.</u> In this section we describe the idealized physical situation which we consider.

An inviscid incompressible fluid flows with constant speed v in the x-direction in a channel between a pair of planes at $y = -h$ and at $y = h$. All variation in the z-direction is neglected. The fluid is electrically conductive with uniform conductivity σ.

Except between $x = -x_e$ and $x = x_e$, the channel walls are electric insulators. Between $-x_e$ and x_e they are electrodes with infinite electric conductivity.

A magnetic field of intensity $\overline{B}$ is imposed in the z-direction. It is uniform across the channel and its magnitude depends only on x. Its magnitude is symmetric with respect to x, it is constant for x between $-x_e$ and x_e, and it tends to zero as x tends to infinity; a special case is $\overline{B}(x) = 0$ for $|x| > x_e$.

The Lorentz force which acts on the electric charges in the fluid causes charge separation and charges of different sign collect near the walls of the channel. This creates an electric field in the fluid with potential ϕ. We use $2\phi_0$ to denote the resulting potential difference of the electrodes and take ϕ_0 to be the potential of the electrode on the wall at $y = h$. The channel height is $2h$ and it follows from Maxwell's equations that $2\phi_0$ is given by

$$2\phi_0 = 2hvB_0$$

The device becomes an electric generator when wires are attached to the electrodes and ends of an electric resistance; this produces an

electric current in the wires and resistance. The potential difference between the electrodes is reduced to a fraction η of its open curcuit value $2\phi_0$; the fraction depends on the load and η is called the load factor.

The current density $\bar{j}$ in tl.. fluid is

$$\bar{j} = \sigma(\bar{E} + \bar{v} \times \bar{B}) = \sigma(-\text{grad } \phi + \bar{v} \times \bar{B}).$$

We write the magnitude of the magnetic field as $B_0 b(x)$ with $b(x)$ equal to unity for x between $-x_e$ and x_e. The z-component j_z of the current density is zero and its other two components are

$$j_x(x,y) = \sigma(-\partial \phi(x,y)/\partial x),$$

$$j_y(x,y) = \sigma[-\partial \phi(x,y)/\partial y + v B_0 b(x)].$$

We call the term in j_y which involves ϕ the <u>electrostatic contribution</u> and the term which involves the magnetic field the <u>magnetic contribution.</u>

When there is an external current, then j_y is positive in the vicinity of the electodes because there the magnetic contribution dominates the electrostatic one. The magnetic field decreases rapidly as x increases from x_e and for large x, j_y is negative because there the electrostatic contribution dominates the magnetic one and this give rise to a <u>counter-current</u>. The net amount of current which can be drawn from the system is diminished by this counter-current. It is part of our research to determine the effect on the performance predicted by the mathematical model of thin insulators (vanes) placed in the fluid; as expected, these vanes decrease the counter-current.

To determine the net current which can be drawn from the system per unit channel width (in the z-direction), one integrates j_y along a line parallel to the x-axis and by symmetry, one can integrate $2j_y$ from $x = 0$ to $x = \infty$. The value obtained is independent of y for y between $y = -h$ and $y = h$. The total electric power P per unit channel width is the product of the current and $2\eta\phi_0 = 2\eta v B_0 h$. One obtains

$$P = 4\eta v B_0 h\sigma \int_0^\infty [-\partial\phi(x,y)/\partial y + v B_0 b(x)] \, dx, \quad P \text{ independent of } y.$$

The total power W per unit channel width needed to maintain the flow is the integral of $v j_y B_0 b$ over the whole channel. This is given by

$$W = 4v\sigma \int_0^h dy \int_0^\infty dx \, [-\partial\phi(x,y)/\partial y + v B_0 b(x)] \, B_0 b(x).$$

Considering only these two powers, the efficiency E of the device is taken to be

$$E = P/W.$$

[We remark that one of the things which is neglected in this model is the effect of viscosity which gives rise to friction effects and makes the fluid speed nonuniform across the channel. A second thing which is neglected is the variation of the magnetic field across the channel and between $-x_e$ and x_e. A third thing which is neglected is the finite width of the channel.]

-163-

3. <u>Mathematical model</u>. We approximate the infinite channel with a finite one with end points $\pm x_{max}$ where x_{max} is much larger than either x_e or h. The mathematical model of the idealized situation described in Section 2 is taken to be

(3-1a) $\partial^2 \phi(x,y)/\partial x^2 + \partial^2 \phi(x,y)/\partial y^2 = 0,$ $0 < x < x_{max},\ 0 < y < h,$

(3-1b) $\phi(x,h) = nhvB_0,$ $0 \le x \le x_e,$

(3-1c) $\partial\phi(x,h)/\partial y = vB_0\, b(x),$ $x_e < x < x_{max},$

(3-1d) $\phi(x_{max},y) = 0,$ $0 \le y \le h,$

(3-1e) $\phi(x,0) = 0,$ $0 \le x \le x_{max},$

(3-1f) $\partial\phi(0,y)/\partial x = 0,$ $0 < y < h.$

The function b which specifies the magnetic field is equal to unity for x between 0 and x_e and in some of our experiments it was equal to zero for x larger than x_e; in others it was

(3-2) $b(x) = \begin{cases} 1 & 0 \le x \le x_e \\ \exp(-[x-x_e]/\text{efold}), & x_e < x \end{cases}$

where efold is a constant which specifies the rate of decay of the magnetic field beyond the end of the electrode.

The channel half-width h is taken as the unit of length and we set

$x = hX,\quad y = hY,\quad \phi(x,y) = \phi(hX,hY) = \Phi'(X,Y),$

$x_e = hX_e,\quad x_{max} = hX_{max},\quad b(x) = b(hX) = B(X),\quad \text{efold} = h\text{EFOLD}$

$\partial\phi(x,y)/\partial x = (1/h)\partial\Phi'(X,Y)/\partial X,\quad \partial\phi(x,y)/\partial y = (1/n)\partial\Phi'(X,Y)/\partial Y.$

-164-

With the exception of (3-1c), the equations (3-1) and (3-2) are transformed by making the changes:

$$x \rightarrow X, \quad y \rightarrow Y, \quad \phi \rightarrow \Phi', \quad b \rightarrow B, \quad h \rightarrow 1, \quad \text{efold} \rightarrow \text{EFOLD}.$$

Equation (3-1c) becomes

$$\partial \Phi'(X,1)/\partial Y = hvB_0 B(X), \qquad X_e < X < X_{max}.$$

Now set $\Phi' = hvB_0 \phi$ to get the system

(3-3a) $\quad \partial^2 \phi(X,Y)/\partial X^2 + \partial^2 \phi(X,Y)/\partial Y^2 = 0, \quad 0 < X < X_{max}, \; 0 < Y < 1,$

(3-3b) $\qquad \qquad \phi(X,1) = \eta, \qquad \qquad 0 \leq X \leq X_e,$

(3-3c) $\qquad \qquad \partial \phi(X,1)/\partial Y = B(X), \qquad X_e < X < X_{max},$

(3-3d) $\qquad \qquad \phi(X_{max},Y) = 0, \qquad \qquad 0 \leq Y \leq 1,$

(3-3e) $\qquad \qquad \phi(X,0) = 0, \qquad \qquad 0 \leq X \leq X_{max},$

(3-3f) $\qquad \qquad \partial \phi(0,Y)/\partial X = 0, \qquad \qquad 0 < Y < 1,$

(3-4) $\qquad \qquad B(X) = \begin{cases} 1, & 0 \leq X \leq X_e, \\ \exp(-[X-X_e]/\text{EFOLD}), & X_e < X. \end{cases}$

The power P and the rate of work W then become

(3-5a) $\quad P = \eta 4v^2 B_0^2 \sigma \int_0^{X_{max}} [-\partial \phi(X,Y)/\partial Y + B(X)] \, dX$

(3-5b) $\quad W = 4v^2 B_0^2 \sigma \int_0^1 dY \int_0^{X_{max}} dX \, [-\partial \phi(X,Y)/\partial Y + B(X)] \, B(X)$

Thus, in this model, the efficiency $E = P/W$ does not depend on the value of $v^2 B_0^2 \sigma$.

An analysis of this mathematical model by conformal mapping is given by Sutton, Hurwitz, and Poritsky [1961].

4. <u>Efficiency as a function of load factor.</u> In this section we present a result which does not seem to be in the literature which significantly reduces the amount of computation to determine the efficiency $E = P/W$ as a function of load factor η. Namely, for a fixed geometry and magnetic field, the efficiency can be determined by solving a <u>single pair</u> of boundary value problems.

Suppose that the geometry and the function B are fixed. Then the solution of (3-3) depends only on the value of η. Let ϕ_1 denote the solution when η is equal to some given value η_1. Consider the solution ϕ for an arbitrary value of η. We can write

$$\phi = \phi_1 + (\eta - \eta_1)\, \Psi$$

where Ψ satisfies

(4-1a) $\quad \partial^2 \Psi(X,Y)/\partial X^2 + \partial^2 \Psi(X,Y)/\partial Y^2 = 0, \quad 0 < X < X_{max},\ 0 < Y < 1,$

(4-1b) $\quad \Psi(X,1) = 1, \qquad\qquad 0 \le X \le X_e,$

(4-1c) $\quad \partial \Psi(X,1)/\partial Y = 0 \qquad\qquad X_e < X < X_{max},$

(4-1d) $\quad \Psi(X_{max},Y) = 0, \qquad\qquad 0 \le Y \le 1,$

(4-1e) $\quad \Psi(X,0) = 0, \qquad\qquad 0 \le X \le X_{max},$

(4-1f) $\quad \partial \Psi(0,Y)/\partial X = 0, \qquad\qquad 0 < Y < 1,$

The efficiency $E(\eta)$ for a given value of load factor η is then given by

(4-2a) $\qquad E(\eta) = \eta[\alpha + (\eta - \eta_1)\beta]/[\gamma + (\eta - \eta_1)\delta]$

where the constants $\alpha, \beta, \gamma, \delta$ are given by

-166-

$$(4\text{-}2b) \qquad \alpha = \int_0^{X_{max}} [-\partial\Phi_1(X,Y)/\partial Y + B(X)]\, dX$$

$$(4\text{-}2c) \qquad \beta = \int_0^{X_{max}} \Psi(X,Y)\, dX$$

$$(4\text{-}2d) \qquad \gamma = \int_0^1 dY \int_0^{X_{max}} [-\partial\Phi_1(X,Y)/\partial Y + B(X)]\, B(X)\, dX$$

$$(4\text{-}2e) \qquad \delta = \int_0^1 dY \int_0^{X_{max}} [-\partial\Psi(X,Y)/\partial Y]\, B(X)\, dX$$

5. Reduction of the counter-current. The efficiency of the device
is limited by the amount of counter-current mentioned in Section 2.
This counter-current can be reduced by inserting insulating vanes
parallel to the X-axis in the fluid. These vanes are symmetric
with respect to $X = 0$ and to $Y = 0$ and a pair might be on the X-axis.
We denote the left (L) and right (R) endpoints of these vanes in
the first quadrant by

$$(X^{(L,k)}, Y^{(k)}) \quad \text{and} \quad (X^{(R,k)}, Y^{(k)}), \quad k = 1,2,\ldots$$

The mathematical models (3-3) and (4-1) are augmented by the boundary
conditions

(5-1a) $\qquad \partial\Phi(X,Y^{(k)})/\partial Y = B(X), \quad X^{(L,k)} < X < X^{(R,k)}, \quad k = 1,2,\ldots$

(5-1b) $\qquad \partial\Psi(X,Y^{(k)})/\partial Y = 0, \qquad X^{(L,k)} < X < X^{(R,k)}, \quad k = 1,2,\ldots$

If one of these vanes, say for $k = 1$, is on the X-axis, then
(3-3e) and (4-1e) are replaced with

(5-1c) $\qquad \Phi(X,0) = \Psi(X,0) = 0, \qquad 0 \le X < X^{(L,k)}, \quad X^{(R,k)} < X \le X_{max}$

together with (5-1a) and (5-1b) with $k = 1$.

The thickness of the vanes is neglected in the mathematical model
and thus the rectangle $[0, X_{max}] \times [0,1]$ contains slits. Although
the Y-derivative of the potential is continuous across these
slits (because of (5-1), the potential itself is discontinuous
at the slits.

6. Ganeral operation of ELLPACK. The ELLPACK system is a research
tool for testing the performance of the various components which make
up a program designed to obtain approximations to solutions of elliptic
partial differential equations. ELLPACK is made up a a number of
modules, for example, the DISCRETIZATION module constructs a set of
linear algebraic equations whose solution gives an approximation to
the solution of the user specified partial differential equation.
Each module has several different versions, for example there are
several different discretizations one can use which vary from the
standard divided central difference approximation to the most recently
developed methods of approximating elliptic partial differential equations.
There have been numerous contributors to the components which make
up ELLPACK and these include people at several different universities.
The current version of ELLPACK, called ELLPACK77, treats problems
with the domain of the partial differential ˄quation the interior
of a rectangle or a cube. A new version of ELLPACK is being prepared
which will treat general domains.

An ELLPACK progrm consists of (a) a series of statements written
in the ELLPACK user oriented language grouped to form ELLPACK segments
and (b) a set of user supplied Fortran FUNCTION and SUBROUTINE subprograms.

The ELLPACK77 segments are:

(i) EQUATION. which specifies the elliptic partial differential
     equation to be solved;

(ii) BOUNDARY. which specifies the rectangular domain and the
     conditions on the solution of the partial differential
     equation at the boundaries.

(iii) GRID. which specifies the number of vertical and horizontal mesh lines, a rectangular mesh is generated;

(iv) OPTIONS. which specifies, for example, the amount of ELLPACK generated information about the execution of the program;

(v) DISCRETIZATION. which specifies which of the discretization method is to be used;

(vi) INDEX. which specifies the indexing of the algebraic equations and the unknowns;

(vii) SOLUTION. which specifies which of several linear algebraic equation solvers is to be used;

(viii) OUTPUT. which specifies the ELLPACK generated output, for example: print a table of the values of the approximation at mesh points, construct a contour plot of the approximation;

(ix) SEQUENCE. which specifies the order of the exectuion of the ELLPACK segments and the number of times the sequence is to be executed;

(x) FORTRAN. which specified that the lines of the program which follow are user supplied Fortran FUNCTION and SUBROUTINE subprograms, these are for the boundary conditions and other needed routines as well as a SUBROUTINE called TEST which is described below.

The current version, ELLPACK77, of ELLPACK can be used to generate an approximation U to the potential Φ or Ψ, the solutions of (3-1) and (4-1). Paul Gherson of Purdue used ELLPACK77 to find estimates of Φ

for various values of the electrode endpoint X_e, the endpoint of the rectangle X_{max}, different magnetic fields B, different load factors n, and for various conditions on $Y = 0$, namely the boundary condition (3-3e) and the condition (5-1) for $k = 1$ and $Y^{(1)} = 0$. His results are given in the report by Gherson and Lykoudis [1978].

One of the discretization modules 5-POINT STAR which was written by Ronald F. Boisvert was modified by Robert E. Lynch to handle the case of insulator vanes in the interior of the rectangular domain. In addition to modifying the routines used by 5-POINT STAR, Gherson's BOUNDARY segment was changed slightly and an additional DISCRETIZATION module was specified in order to increase the sizes of certain of the ELLPACK generated arrays so that the modifed 5-POINT STAR would operator properly. Also, Gherson's FORTRAN seqmenc was completely rewritten in order to handle all the various cases to be treated; the new FORTRAN segment has about three times the number of lines of Gherson's. The new segment has about 900 lines with numerous comments.

In some of our recent test cases, the SEQUENCE. segment was:

```
SEQUENCE.   LOOP = 6
            DISCRETIZATION
            INDEXING
            SOLUTION
            OUTPUT
            TEST
```

The statement LOOP = 6 instructs the ELLPACK system to execute the SEQUENCE six times. As with Gherson's SUBROUTINE TEST, ours set initial values of parameters with DATA statements; some of these

specify values such as the location of the endpoints of the interior

insulating strips, the value of EFOLD, and so on; others control

the operation and they are "switches", for example the LOGICAL variable

MAGFON (MAgnetic Field ON) is set to .TRUE. when B is to be nonzero

and it is set to .FALSE. when B is to be zero. During the execution

of the SEQUENCE the odd numbers of times (1,3,5), MAGFON is set to

.TRUE. and the approximation U gives estimates of the potential Φ

for a fixed value of load factor n_1; a different value of EFOLD

is used so that Φ for n_1 is obtained for three different values

of EFOLD. During the even number of times (2,4,6), MAGFON is set to

.FALSE., the load factor is set to unity, and the approximation U

gives estimates of the potential Ψ. The values of the integrals

$\alpha,\beta,\gamma,\delta$ in (4-2) are estimated by the Trapezoid Rule, values

of efficiency for $\eta = 0,1/40,2/40,...$ is computed, and a graph

of efficiency versus load factor is generated. Sample output is shown below.
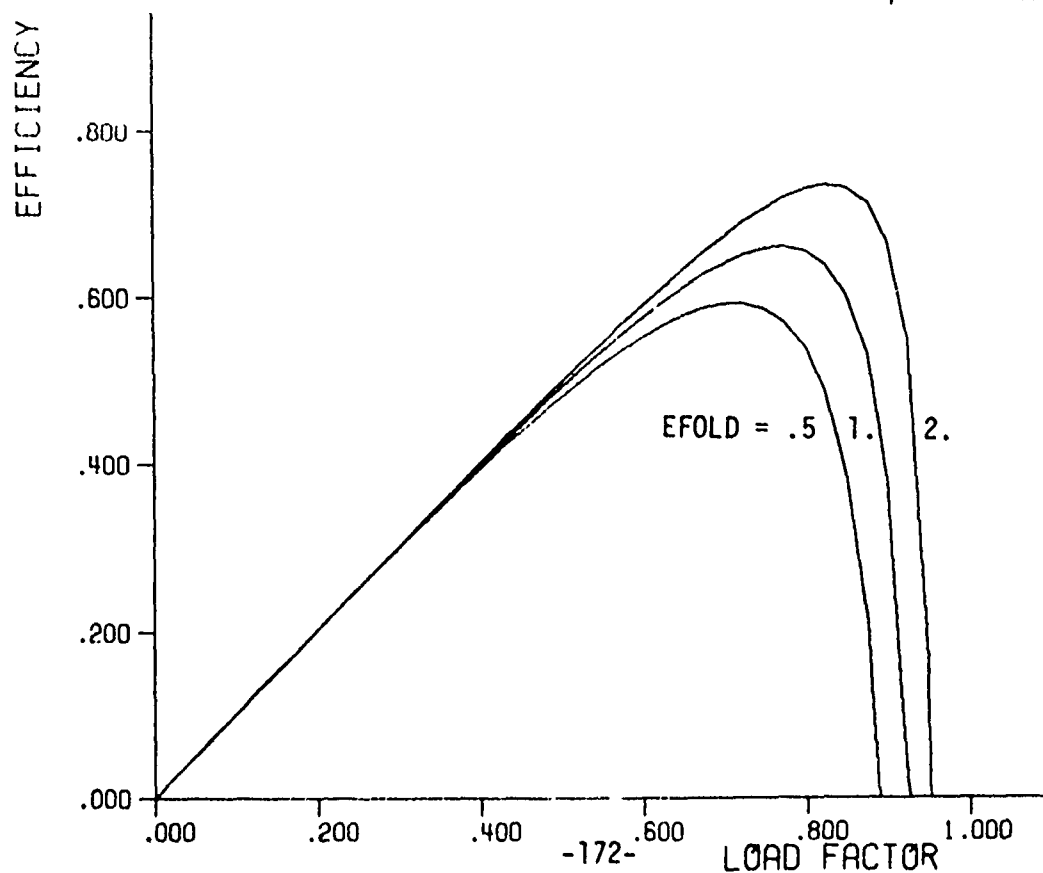
7. Discrete model. The ELLPACK module 5-POINT STAR which we
modified uses finite difference approximations to derivatives. There
are three basic ones which we display below in terms of a given function
u of z:

$$d^2u(0)/dz^2 = [u(-\Delta z) - 2u(0) + u(\Delta z)]/\Delta z^2 + (\Delta z^2/12)d^4u(0)/dz^4 + \ldots$$

$$du(0)/dz = [-3u(0) + 4u(\Delta z) - u(2\Delta z)]/2\Delta z - (\Delta z^2/3)d^3u(0)/dz^3 + \ldots$$

$$du(0)/dz = [u(-2\Delta z) - 4u(\Delta z) + 3u(0)]/2\Delta z - (\Delta z^2/3)d^3u(0)/dz^3 + \ldots$$

Use of the values of the divided differences as approximations to the
values of the derivatives leads to local error which is the order of
Δz^2. Provided that the u is smooth, then when one halves Δz one
expects the error to be approximately quartered. This applies to
finite difference approximations to elptic partial differential
equations for sufficiently small Δz and provided the solution has
continuous fourth derivatives in the region and at the boundary.
For the mathematical models decribed above for the potentials Φ
and Ψ, the solutions have derivatives with singularities at the
end of the electrode and at the ends of insulator vanes. Consequently,
one expect that the error does not decrease as the square of the
mesh spacing as this spacing tends to zero. The error probably
decreases as the first power of the mesh spacing as it tends to zero.

We now describe the approximations used in 5-POINT STAR and
their modifications which allow the slit-region problems to be treated.
We use some of the variable names of ELLPACK and our routines, such
as TEST so that this report will also serve as partial documentation

for the programs involved.

The horizontal sides of the rectangle are $AX \leq X \leq BX$ and the vertical sides are $AY \leq Y \leq BY$. Numerical values for AX, BX, AY, and BY are user supplied in the BOUNDARY. segement of the ELLPACK program. In our case, $AX = AY = 0.$, $BX = X_{max}$, and $BY = 1$.

The number of vertical and horizontal mesh lines are NGRIDX and NGRIDY, respectively. Numerical values of these are specified in the GRID segment of the ELLPACK program. Uniform mesh spacing is used by 5-POINT STAR and the spacing are HX and HY defined by

$$HX = (-AX+BX)/(NGRIDX-1),$$

$$HY = (-AY+BY)/(NGRIDY-1).$$

We denote the mesh points by (X_I, Y_J) and the values are stored in the ELLPACK arrays GRIDX and GRIDY. The values are

$$X_I = AX + (I-1)HX = GRIDX(I), \quad I = 1, \ldots, NGRIDX,$$

$$Y_J = AY + (J-1)HY = GRIDY(J), \quad J = 1, \ldots, NGRIDY.$$

The approximation to the solution of the partial differential equation is denoted by U and this can be considered as a two-dimensional array and, depending on which problem is solved,

$$U(I,J) \approx \Phi(X_I, Y_J) \quad \text{or} \quad U(I,J) \approx \Psi(X_I, Y_J).$$

At each interior mesh point, the Laplace equation is approximated with its usual divided central difference approximation (this is modified at certain points as explained below):

$$[U(I-1,J) - 2U(I,J) + U(I+1,J)]/HX^2$$

$$(6-1a) \quad + \quad [U(I,J-1) - 2U(I,J) + U(I,J+1)]/HY^2 = 0, \quad I = 2,\ldots,NGRIDX-1,$$

$$J = 2,\ldots,NGRIDX-1.$$

The vertical mesh line number of the endpoint of the electrode (conductor) is denoted by ICONDR and its value is set in a DATA statement in SUBROUTINE TEST. Since AX = 0, the X-coordinate of the endpoint of the conductor is

$$X_e = (ICONDR-1)HX = GRIDX(ICONDR).$$

The LOGICAL variable HAVANE (HAve VANE) is set to .TRUE. or .FALSE. in a DATA statement in TEST. When it is .TRUE., then there is an insulator strip (vane) on the X-axis, and in this case the horizontal mesh line numbers must also be set by a DATA statement in TEST. The endpoints are denoted by IVANEL (L for "left") and IVANER (R for "right"). The coordinates of the endpoints are then determined by the modified 5-POINT STAR to be at $(X^{(L,1)},0)$ and $(X^{(R,1)},0)$ where

$$X^{(L,1)} = (IVANEL-1)HX = GRIDX(IVANEL),$$

$$X^{(R,1)} = (IVANER-1)HX = GRIDX(IVANER).$$

The boundary conditions on the boundary of the rectangle are given below in the same order as in (3-3) [see also (5-1)]:

$$(6-1b) \qquad U(I,NGRIDY) = LOADFA, \qquad I = 1,\ldots,ICONDR,$$

(LOADFA for LOAD FActor; this is declared REAL and set in a DATA statment in SUBROUTINE TEST),

$$[U(I,NGRIDY-2) - 4U(I,NGRIDY-1) + 3U(I,NGRIDY)]/2HY$$

(6-1c)

$$= B(GRIDX(I)), \quad I = ICONDR+1,\ldots,NGRIDX-1,$$

(6-1d)
$$U(NGRIDX,J) = 0, \quad J = 1,\ldots,NGRIDY,$$

$$U(I,1) = 0, \quad I = 1,\ldots,IVANEL-1 \quad and$$

(6-1e)

$$I = IVANER+1,\ldots,NGRIDX-1,$$

$$[-3U(I,1) + 4U(I,2) - U(I,3)]/2HY$$

(6-1e')

$$= B(GRIDX(I)), \quad I = IVANEL,\ldots,IVANER,$$

$$[-3U(1,J) + 4U(2,J) - U(3,J)]/2HY$$

(6-1f)

$$= 0, \quad J = 2,\ldots,NGRIDY-1.$$

The total number of algebraic equations in (6-1) is equal to the total
number of mesh points NGRIDX*NGRIDY, hence there is one equation for
each mesh point and thus for each unknown U(I,J).

The equations (6-1) give the set of algebraic equations generated
by 5-POINT STAR and which are used in the case that there are no
insulator vanes in the interior of the rectangle. We now consider
ther case in which there are insulator vanes in the interior; we allow
for one or two such vanes or slits.

The horizontal mesh line number of a slit is set in a DATA statment
in TEST. The variable names are JYSL1D and JYSL2D (D for "down").
If one or both of these are nonzero, then this informs the system that
there is one or two interior slits and in this case the corresponding
vertical mesh line numbers for the endpoints must be set in a DATA

-176-

statement in TEST. The endpoints are denoted by

IXSL1L, IXSL1R for JYSL1D and

IXSL2L, IXSL2R for JYSL2D,

where "L" and "R" stand for "left" and "right". The boundary condition at the slit is $\partial\phi/\partial Y = B(X)$ and at the downward side of the slit, the difference equation approximation is

$$[U(I,JYSLkD-2) - 4U(I,JYSLkD-1) + 3U(I,JSLkD)]/2HY$$

(6-1g)
$$= B(GRIDX(I)), \quad I = IXSLkL,...,IXSLkR$$

$$\text{for} \quad k = 1 \quad \text{and/or} \quad k = 2.$$

The value of $\partial\phi/\partial Y$ is continuous across a slit, but the value of ϕ is discontinuous; that is

$$\lim_{\epsilon\to 0} [-\phi(X,Y^{(k)}-\epsilon) + \phi(\wedge,Y^{(k)}+\epsilon)] \neq 0 \quad \text{for} \quad X^{(L,k)} \leq X \leq X^{(R,k)}.$$

Since the value of U at both the bottom and the top of the slit are unknowns, we need to add another equation:

$$[-3U(I,JYSLkD+1) + 4U(I,JYSLkD+2) - U(I,JYSLkD+3)]/2HY$$

(6-1h)
$$= B(GRIDX(I)), \quad I = IXSLkL,...,IXSLkR$$

$$\text{for} \quad k = 1 \quad \text{and/or} \quad k = 2.$$

The mesh points $(I,JYSLkD)$ and $(I,JYSLkD+1)$ correspond to the same point $(X_I, Y^{(k)}_{JYSLkD})$ in the region. Consequently, in order to obtain an approximation to the potential in a rectangular region with interior slits, we double the number of horizontal mesh points

along each interior slit.

This is done by a modification of 5-POINT STAR. When the module is called to be executed, it calls a subroutine which determines whether or not there are interior slits and modifies the horizontal mesh line coordinates. We give three examples. Suppose that one wants estimates of ϕ on a mesh with horizontal mesh spacing $HY = .1$ and vertical mesh spacing $HX = 1$. where $X_{max} = 20$.

Example 1: no interior slits.

In TEST one includes the statement

DATA JYSL1D, JYSL2D / 0, 0 /

The GRID. segment of the ELLPACK program is

GRID. UNIFORM X = 21 $ UNIFORM Y = 11

Then NGRIDX = 21, NGRIDY = 11, HX = 20/20 = 1, HY = 1/10 = .1

Example 2: one interior slit with endpoints (4,.3) and (10,.3)

In TEST one includes the statement

DATA JYSL1D, JYSL2D, IXSL1L, IXSL1R / 4, 0, 5, 11 /

The GRID. segment of the ELLPACK program is

GRID. UNIFORM X = 21 $ UNIFORM Y = 12

Then NGRIDX = 21, NGRIDY = 12, and the ELLPACK system set $HY = 20/20 = 1$, $HY = 1/11 = .0909090...$ It also generates values for GRIDX and GRIDY with spacing 1. and 1/11, respecitively. The modified 5-POINT STAR determines that JYSL1D is nonzero so that there is an interior slit. It then knows that there is a pair of horizontal mesh lines which correspond to the same value of Y along the slit. It changes HY from 1/11 to 1/10 = .1 and it resets the

the values of the Y coordinates of the mesh lines:

$$Y_J = (J-1)HY = GRIDY(J), \qquad J = 1,\ldots,JYSL1D$$

$$Y_{JYSL1D+1} = Y_{JYSL1D} + HY*10^{-5} = GRIDY(JYSL1D+1)$$

$$Y_J = (J-2)HY = GRIDY(J), \qquad J = JYSL1D+2,\ldots,NGRIDY.$$

The values in GRIDY are then:

$$J = 1, 2, 3, 4, 5, \qquad 6, 7, 8, 9, 10, 11, 12$$
$$GRIDY(J) = 0.,.1,.2,.3,.3+10^{-6},.4,.5,.6,.7,.8,.9,1.$$

Example 3: two interior slits with endpoints (4,.3),(10,.3) and
(3,.7),(5,.7):

In TEST one includes the statements

        DATA JYSL1D, IXSL1L, IXSL1R / 4, 5, 11 /

        DATA JYSL2D, IXSL2L, IXSL2R / 9, 4, 6 /

The GRID. segment of the ELLPACK program is

        GRID. UNIFORM X = 21 $ UNIFORM Y = 13

The ELLPACK system sets HX = 20/20 = 1., HY = 1/12 = .08333...

and generates values of GRIDX and GRIDY with these spacing.

The modified 5-POINT STAR finds that both JYSL1D and

JYSL2D are nonzero so that there are two interior slits.

It then knows that there are two pairs of horizontal mesh

lines which correspond to the two values of Y along the slits.

It changes the value HY from 1/12 to 1/10 = .1 and it

resets the values of the Y coordinates of the mesh lines:

-179-

$$Y_J = (J-1)HY = GRIDY(J), \qquad J = 1,\ldots,JYSL1D$$

$$Y_{JYSL1D+1} = Y_{JYSL1D} + HY*10^{-5} = GRIDY(JYSL1D+1)$$

$$Y_J = (J-2)HY = GRIDY(J), \qquad J = JYSL1D+2,\ldots,JYSL2D$$

$$Y_{JYSL2D+1} = Y_{JYSL2D} + HY*10^{-5} = GRIDY(JYSL2D+1)$$

$$Y_J = (J-3)HY = GRIDY(J), \qquad J = JYSL2D+2,\ldots,NGRIDY$$

The values in GRIDY are then:

$$J = 1, 2, 3, 4, 5, \qquad 6, 7, 8, 9, 10, \quad 11,12,13$$
$$GRIDY(J) = 0.,.1,.2,.3,.3+10^{-6},.4,.5,.6,.7,.7+10^{-6},.8,.9,1.$$

By introducing these lines of "double" mesh points, we have added additional unknowns, namely the values of $U(I,JYSLkD)$ and $U(I,JYSLkD+1)$, $I = 1,\ldots,NGRIDY$. Equations corresponding to some of these are given in $(6-1g)$ and $(6-1h)$, specifically for $I = IXSLkL,\ldots,IXSLkR$. At points off of the slits, the potential is continuous, so we add the equations

$$U(I,JYSLkD) - U(I,JYSLkD+1) = 0, \quad I = 1,\ldots,IXSLkL-1 \quad \text{and}$$

(6-1i)
$$I = IXSLkR+1,\ldots,NGRIDX$$

In equation (6-1a) we give the approximation for the Laplace equation; but now that does not apply for (I,J) on these lines of double mesh points. In (6-1a) the range of the subscripts changes from

$$I = 2,\ldots,NGRIDX-1, \quad J = 2,\ldots,NGRIDX-1$$

to

(6-1a') $I = 2,\ldots,\text{NGRIDX-1},$ $J = 2,\ldots,\text{JYSL2D-2}$

$J = \text{JYSL1D+2},\ldots,\text{JYSL2D-2},$ $J = \text{JYSL2D+2},\ldots,\text{NGRIDY-1}$

The approximation to the Laplace equation for a mesh point with
JYSLkD and at a distance at least 2HX from the end of a slit
is taken as [note the "+2" in the second pair of square brackets]

$$[U(I-1,\text{JYSLkD}) - 2U(I,\text{JYSLkD}) + U(I+1,\text{JYSLkD})]/HX^2$$

(6-1j) $+ [U(I,\text{JYSLkD-1}) - 2U(I,\text{JYSLkD}) + U(I,\text{JYSLkD+2})]/HY^2 = 0,$

$I = 2,\ldots,\text{IXSLkL-2},$ and $I = \text{IXLSkR+2},\ldots,\text{NGRIDX}.$

For mesh points immediately to the right and to the left of the
end points of the slits, we incorporate the average value of U
at the top and bottom of the end of the slit and use [again, note the "+2"]

$$[U(I-1,\text{JYSLkD}) - 2U(I,\text{JYSLkD}) + U(I+1,\text{JYSLkD})/2 + U(I+1,\text{JYSLkD+1})/2]/HX^2$$

(6-1k) $+ [U(I,\text{JYSLkD-1}) - 2U(I,\text{JYSLkD}) + U(I,\text{JYSLkD+2})]/HY^2 = 0,$

for $I = \text{IXSLkL-1}$

and

$$[U(I-1,\text{JYSLkD})/2 + U(I-1,\text{JYSLkD+1})/2 - 2U(I,\text{JYSLkD}) + U(I+1,\text{JYSLkD})]/HX^2$$

(6-1ℓ) $+ [U(I,\text{JYSLkD-1}) - sU(I,\text{JYSLkD}) + U(I,\text{JYSLkD+2})]/HY^2 = 0$

for $I = \text{IXSLkR+1}$

These last two equations involve a linear combination of six
of the unknowns; the usual approximation to Laplace's equation involves

five as in (6-1a). The ELLPACK module 5-POINT STAR constructs a
set of difference equations which has at most five of the unknowns
in them; consequently, the ELLPACK system does not allocate a
sufficient amount of storage when the DISCRETIZATION. segement of
the ELLPACK program is

DISCRETIZATION. 5-POINT STAR

In order to obtain the necessary storage, we include a second
discretization module--this is not subsequently used, its purpose
is merely to obtain extra storage. Hence in an ELLPACK program
which estimates the potential of a region with slits, one uses

DISCRETIZATION(1)   5-POINT STAR
DISCRETIZATION(2)   HOLR 9-POINT (IORDER=40)

and in the SEQUENCE. segment, DISCRETIZATION is replaced with
DISCRETIZATION(1).

Caution: The locations of the end of the conductor, and
the endpoints of the slits and vane are given in terms of mesh
line numbers. Consequently, if the number of grid lines is changed
in the ELLPACK GRID. then the integer values ICONDR, JYSLID, and
so on, must be changed in order to obtain the same geometry.

Caution: Because a three term approximation is used for
the normal derivative at an insultor, for accuracy one must have
at least two interior (non-slit) mesh lines between any pair
of insulators. In Example 3 above, with two slits, note that
there are two interior mesh lines between the lower slit and Y = 0
$(J = 2,3)$ and two between the upper slit and $Y = 1$ $(J = 11,12)$

-182-

and these are the minimal number. There are three between the
pair of interior slits (J = 6,7,8) and this is one more than
the required minimum number.

Caution: The derivatives of the potential are singular
at the end point of the conductor and at the end of the
insulator slits and vane. One should run a few test cases to
determine the mesh spacing which yields sufficient accuracy.
In particular, the vertical mesh line spacing should be smaller
than the length of the electrode.

REFERENCES:

Gherson, Paul, and Paul S. Lykoudis, Analytical study of end effects in liquid metal MHD generators: Progress Report for March 1, 1978 to June 30, 1978 prepared for Argonne National Laboratory, Magneto-Fluid-Mechanics Laboratory, Purdue University, June 30, 1978.

Rice, John R., ELLPACK: A research tool for elliptic partial differential equations software, in Mathematical Software III, (J.R. Rice, ed.) Academic Press, 1977, pp 319-344.

Sutton, G.W., H. Hurwitz, Jr, and H. Poritsky, Electrial and pressure losses in a magnetohydrodynamic channel due to end current loops, Trans. AIEE Part I, Communications and Electronics 80, 687-695, 1961.

APPENDIX D

MAJOR ACCOMPLISHMENTS OF THE COMPLETE PROGRAM

This report covers the final ye.; of an eight-year experimental
and theoretical program aimed at developing practical two-phase
LMMHD generators. Thus, the significant accomplishments are summa-
rized below by subject area--generator experiments, code develop-
ments, facility developments, local measurements, foams, and
analytical studies. The goals of this program were to study the
basic phenomena and to demonstrate that practical, high-efficiency
LMMHD generators can be built, thus making possible the development
of high-efficiency LMMHD energy-conversion systems.

Generator Experiments

The four generator channels tested in this program are compared
in Fig.I.1. The basic channel dimensions were set by the facility
constraints--magnet gap length and pole-face size, available flow
rates, etc.--and the designs were done within these constraints,
using the generator design code extracted from the system code
(Section II.1). The structural design for the first three channels
used the same copper electrodes and compensating bars with different
side walls to set the different channel contours. For LT-4, an
improved design with a filament-wound liner was developed to provide
for different contours with a higher pressure rating and easier
sealing.

Diagnostic instrumentation has been an integral part of this
program since its initiation. Gas and liquid volume flow rates,
temperatures, pressures, void fractions (by means of γ-ray attenua-

tion), electrode voltages, load currents, and magnetic flux densities have been measured for all channels. For channels LT-2, LT-3, and LT-4, probes were built into one insulating wall to measure voltage profiles between the electrodes. As the scope of the program permitted, the measurement capability was improved. Recently local measurements were initiated, as described below.

The first channel, LT-1, was designed for a slip ratio of unity, because the actual slip ratio or bubble parameter, C_d', (based on experimental data) was unknown. As anticipated, slip ratios greater than unity were observed, with some values in excess of two, and, thus, the liquid velocity along the generator decreased. Experimental values of C_d' were determined.

Next, a constant-area channel, LT-2, was tested to obtain further basic data on slip ratios and values of C_d'. In general, C_d' values were less for LT-2 than for LT-1. The efficiency was higher for LT-2 than for LT-1 at zero or low void fractions, but lower at the higher void fractions. This was expected, because LT-2 would yield liquid velocities that were almost constant for zero or low void fractions, but not for high void fractions. (Constant liquid velocity is desired because it results in constant generated voltage and no or minimal circulating current loss.)

Analysis of the data from LT-1 and LT-2 showed that much of the discrepancy between the experiments and the models could be explained by the existence of a pure-liquid shunt layer on the insulating walls, where the shunt layer bypasses some of the current around the load. To eliminate this possible shunt layer, gas injection along the insulating walls was proposed. Gas injection was tested

with channels LT-2 and LT-3. For LT-3, substantially better performance was obtained without the injectors. Support studies showed that performance improved as the amount of gas injected was decreased, that the injected gas did not form the desired pure-gas wall layer, and that the partial flow obstruction of the gas injection ports degraded performance. A later analytical study has shown that liquid shunt layer losses will not be significant for large generators.

The second diversing channel, LT-3, was designed on the basis of data obtained from LT-1 and LT-2. Improved generator performance was obtained, with efficiencies of up to 0.50 at high void fractions. Channel LT-3 was also tested at higher liquid velocities in the revised facility (described below), and the reduction in slip ratio with increasing liquid velocity was demonstrated. Substantial increases in generator efficiency were obtained with higher liquid flow rates.

Experiments to demonstrate that good liquid-to-gas heat transfer exists in the generator were succssfully completed with LT-3. Good heat transfer is essential, becuse it is the almost-constant-temperature expansion of the gas (vapor) in the generator that yields the higher system efficiencies for LMMHD power cycles.

The design of LT-4 and the significant test results obtained are described in this report. Power densities of up to 32 MWe/m^3 were obtained in this small 20-kWe generator, equal to or better than that anticipated for LMMHD generators in practical power systems. Efficiencies higher than 0.60 at average void fractions well above 0.50 were measured. The rapid reduction in slip ratio with increasing liquid velocity was confirmed for high power densities.

Testing of HT-1 was also completed under open-circuit conditions over the temperature range of approximately 490 to approximately 740 K [Dunn et al (1979)]. The slip ratio was shown to decrease with increasing temperature, implying higher generator and system efficiencies; this anticipated result was a prime reason for performing the experiments.

Code Developments

The channel design code (GENDES) was developed prior to this program as part of the system performance code [Petrick et al (1970)]. In that code (Section II.1) the liquid velocity is held constant and the channel contour is calculated, so that it is of no value in analyzing experimental data. Three new codes were developed in connection with the experiments: ANLSIS, MHDPRE, and MHD9.

ANLSIS is the basic code used to process all of the raw experimental data. From that data, it calculates generator performance and the variation of the parameters (pressure, liqu'd velocity, gas velocity, etc.) along the channel.

MHDPRE is used to predict generator operation for given inlet conditions. The fluid equations are solved, and the load voltage and input pressure are varied to match the desired load resistances and exit pressure. Rather than solving Laplace's equation, an end resistance is assumed.

MHD9 is the most-detailed code; it solves both the fluid equations and Laplace's equation iteratively until convergence is obtained. This, an improved electrical model is used, and no end resistance is assumed. The inlet conditions are specified, and the load voltage varied to match a specified condition. MHD9 is an

expensive code to run, because of the detail and because convergence is not always obtained.

Facility Development

The Nak-nitrogen ambient·temperature facility, developed to test two-phase LMMHD generators, provides known flows of liquid (NaK) and gas (nitrogen) to the generator. It consists of a NaK loop and a nitrogen loop with a common mixer, generator test section, and separator/NaK storage tank. The NaK is recirculated, and the nitrogen is exhausted to the atmosphere from the separator tank through a secondary separator. The nitrogen exhaust line is equipped with a control valve and controller to sense and fix the generator exit pressure. The NaK loop includes three canned-rotor pumps in series with bypass valves, so that only one or two can be operated if desired, a turbine flow meter, control valves, and pressure gauges. The nitrogen loop comprises a heater and control system to heat the gas to the liquid temperature, a flowmeter, control valves, and pressure gauges. A dc electromagnet provides the magnetic field.

Throughout this program the facility has been continuously upgraded, to improve its characteristics and controlability, to provide a wider range of operationing parameters, and to provide improved instrumentation. In 1975-1976, the facility was completely rebuilt and most major components replaced, to allow operation at higher pressures and flow rates. Present capacities are 18 kg/s (330 gpm) NaK and 0.44 kg/s (800 scfm) nitrogen maximum at maximum system pressure of 2.0 MPa (275 psig) and maximum fluid temperature of 328 K (130°F).

The test section fits between conventional flanges, and is inserted into the (adjustable) air gap of the electromagnet. Instrumentation is provided to measure and control gas and liquid flow rates, pressures, and temperatures, and to measure (dc) generator voltages and currents, pressures along the generator channel, magnetic field strengths, and void fraction distributions along the generator. Auxiliary equipment includes 1) instrumentation for recording experimental data; 2) a dc electrogmagnet with a maximum flux density greater than 1.2 T at 0.09 m (3.5 in.) air gap and a working volume 0.41 m (16 in.) in diameter by an adjustable air-gap length; 3) a γ-ray void-fraction measuring system, and 4) a hot-film anemometry system.

Local Measurements

Initial measurements have been made of local flow parameters in a NaK-nitrogen two-phase LMMHD generator, using hot-film and resistivity probes. Although the results are preliminary, there is evidence that large electromagnetic force densities have a significant effect on the size and distribution of the gas bubbles or voids.

Foams

The use of surface-active agents in the liquid metal, to produce a more-stable foam flow in the LMMHD generator, reduces the slip loss, allows the generator to operate at higher average void fractions, and results in a more-efficient conversion system. A program to evaluate surface-active agents in liquid metals, especialy NaK, was initiated in 1976.

The feasibility of generating relatively stable bubbles, hence,
a foam, in liquid metals was demonstrated. These phenomena were documented
in both still and motion pictures. Surface tension measurements and foaming
experiments showed that viscosity is also a factor in promoting bubble
formation and persistence. Wetting and contact angle measurements were made
for stainless steel and carbon steel immersed in eutectic NaK.

Barium has been identified as an attractive additive for the
generation of foams with NaK, and bismuth is a back-up for barium. A
guiding hypothesis for understanding the phenomena contributing to
foamability in liquid metal systems has been developed, and basic
data on surface tension obtained. The next step is to test foams in
the LMMHD generator.

Analytical Studies

In the early phase of the program, the analytical work was
concentrated on developing the required comptuer codes and under-
standing the basic loss mechanisms. Subsequently, this work was
extended to more-detailed analytical studies.

The annular generator geometry has certain advantages, especialy
the lack of insulating walls and the ease of fabrication. The
equations were developed and solutions obtained for three cases--con-
stant velocity and no armature reaction, laminar flow with no armature
reaction, and armature reaction with constant velocity. Numerical
examples showed that 1) the attainable terminal voltages appear to
be very low, 2) flow reversal and large viscous loss occur at or
below the desired power densities, and 3) armature reaction effects
are important and compensation techniques appear impractical. Thus,

this annular geometry does not appear attractive for either generator or pump operation.

An analytical study of the liquid shunt (wall) layer sizes and losses showed that these losses are not expected to be significant for large generators, i.e., less than 1.0 % decrease in efficiency for Hartmann numbers in excess of 1000.

End current losses in LMMHD generators can be controlled by the proper choice of 1) channel aspect ratio, 2) magnetic flux density distribution outside of the electrodes, and 3) number and dimensions of insulating vanes. A computer code has been developed to calculate the end current loss as the above parameters are varied. Initial studies with this code have shown that generator efficiencies in excess of 0.8 are attainable.

Conclusion

The results obtained have provided basic data on two-phase flows in a magnetic field and demonstrated that high power density and good efficiency are attainable in small LMMHD generators. All indications are that large, high-efficiency LMMHD generators can be built.

REPORT DOCUMENTATION PAGE		READ INSTRUCTIONS BEFORE COMPLETING FORM
1. REPORT NUMBER ANL/MHD-79-1	2. GOVT ACCESSION NO.	3. RECIPIENT'S CATALOG NUMBER
4. TITLE *(and Subtitle)* EXPERIMENTAL TWO-PHASE LIQUID-METAL MAGNETOHYDRODYNAMIC GENERATOR PROGRAM		5. TYPE OF REPORT & PERIOD COVERED Final Report, October 1977 to September 1978
		6. PERFORMING ORG. REPORT NUMBER ANL/MHD-79-1
7. AUTHOR(s) M. Petrick, G. Fabris, E. S. Pierson, A. K. Fischer, C. E. Johnson, P. Gherson, P. S. Lykoudis, R. E. Lynch		8. CONTRACT OR GRANT NUMBER(s) N00014-78-F-0004
9. PERFORMING ORGANIZATION NAME AND ADDRESS Argonne National Laboratory 9700 South Cass Avenue Argonne, Illinois 60439		10. PROGRAM ELEMENT, PROJECT, TASK AREA & WORK UNIT NUMBERS Task No. NR099-404
11. CONTROLLING OFFICE NAME AND ADDRESS Office of Naval Research (Code 473) Department of the Navy Arlington, Virginia 22217		12. REPORT DATE April 1979
		13. NUMBER OF PAGES 208
14. MONITORING AGENCY NAME & ADDRESS(*If different from Controlling Office*) Same as 11		15. SECURITY CLASS. *(of this report)* Unclassified
		15a. DECLASSIFICATION/DOWNGRADING SCHEDULE

16. DISTRIBUTION STATEMENT *(of this Report)*

Approved for public release; distribution unlimited

17. DISTRIBUTION STATEMENT *(of the abstract entered in Block 20, if different from Report)*

18. SUPPLEMENTARY NOTES

19. KEY WORDS *(Continue on reverse side if necessary and identify by block number)*

armature reaction	liquid metals	quality
bubble parameter	load voltage	slip
end effects	local measurements	surfactants
foams	magnetohydrodynamics	two-phase
generator efficiency	pressure gradient	void fraction

20. ABSTRACT *(Continue on reverse side if necessary and identify by block number)*

The experimental results presented herein satisfy one major goal in demonstrating the technical feasibiilty of two-phase LMMHD (liquid-metal MHD), i.e., operating an MHD generator at power densities equal to or above that anticipated for practical power systems. Power densities of up to 32 MWe/m^3 and efficiencies higher than 0.6 at high void fractions were attained for a small 20-kWe generator. Slip ratio data, and more-extensive pressure distribution and voltage profile data are also given.

DD $_{1\ JAN\ 73}^{FORM}$ 1473 EDITION OF 1 NOV 65 IS OBSOLETE
S/N 0102-014-6601 ·

(3)

Barium has been identified as an attractive additive for the generation of foams with NaK, and bismuth is a back-up for barium. A guiding hypothesis for understanding the phenomena contributing to foamability in liquid metal systems has been developed, and basic data on surface tension obtained.

A computer code has been developed that will calculate the electrical end loss for any insulating vane geometry and magnetic flux density distribution, a significant accomplishment. Initial studies with this code have shown that generator efficiencies in excess of 0.8 are attainable.

Initial measurements of local flow parameters in a NaK-nitrogen two-phase liquid-metal MHD generator, using hot-film and resistivity probes, are reported. Although, the results are preliminary, there is evidence that large electromagnetic force densities have a significant effect on the size and distribution of the gas bubbles or voids.

All results are very encouraging for the development of large high-efficiency LMMHD generators.

Distribution for ANL/MHD-79-1

Internal:

J. A. Kyger	I. Pollack	G. Fabris
S. A. Davis	F. Schriener	P. V. Dauzvardis
K. D. Kuczen	E. S. Pierson (40)	D. Cohen
M. Petrick	E. G. Pewitt	J. Unik
W. C. Redman	S. Grammel	A. B. Krisciunas
K. E. Tempelmeyer	P. F. Dunn	ANL Contract File
B. Snyder	C. B. Reed	ANL Libraries (5)
C. Lenzo	G. Whittington	TIS Files (6)
	R. S. Smith	

External:

J. A. Satkowski, Office of Naval Research, Arlington (3)
B. Friedman, Office of Naval Research, Arlington (2)
Office of Naval Research Branch Office, Commanding Officer, Chicago
U. S. Naval Research Lab., Director, Washington (6)
Defense Documentation Center (12)
J. Huth, Naval Sea Systems Command, Washington
R. M. Forsell, Naval Sea Systems Command, Washington
B. Wolfson, Air Force Office of Scientific Research, Washington
Naval Underwater Systems Center, Technical Library, New London
B. Zauderer, General Electric Co. Valley Force Space Technology Center
M. E. Talaat, U. Maryland
R. H. Eustis, Stanford U.
Rand Corp., Technical Library, Santa Monica
D. G. Elliott, Jet Propulsion Lab.
J. Pidkowicz, U. S. Department of Energy, Oak Ridge
O. M. Friedrich, Jr., U. Texas at Austin
R. Hamilton, Institute for Defense Analyses, Arlington
J. Louis, Massachusetts Inst. Technology
Los Alamos Scientific Lab., Technical Library
Naval Surface Weapons Center, Technical Library, Dahlgren, Va.
U. S. Naval Postgraduate School, Library, Monterey
Naval Ocean Research and Development Activity, Technical Library, Bay St. Louis
Naval Ship Research and Development Lab., Special Projects Div., Annapolis
Naval Ship Research and Development Lab., Library, Annapolis
Naval Weapons Center, Propulsion Applied Research Group, Technical Library,
   China Lake, Calif.
R. Cooper, Air Force Aero Propulsion Lab., Wright Patterson AFB
Naval Surface Weapons Center, Technical Library, Silver Spring
L. Nichols, NASA Lewis Research Center
R. Rostenbach, National Science Foundation
H. Cheung, Lawrence Livermore Lab.
O. Loper, Lawrence Livermore Lab.
U. S. Marine Corps, Code CSY-3, Washington
J. C. Cochran, Atomics International
Knolls Atomic Power Laboratory
R. Janney, Avco Everett Research Lab.
J. B. Dicks, U. Tennessee Space Inst.
J. Rosciszewski, Air Vehicle Corp., San Diego
S. Demetriades, STD Research Corp., Pasadena

195

E. Resler, Jr., Cornell U.
E. Reshotko, Case Inst. Technology
H. Yeh, U. Pennsylvania
California Inst. Technology, Technical Library
H. E. Wilhelm, Colorado State U.
M. Hoffman, U. California, Davis
Energy Research Corp., Technical Library
R. L. Powell, National Bureau of Standards, Boulder
J. Wachtman, National Bureau of Standards, Washington
E. R. Lindgren, U. Florida
R. V. Vittucci, Naval Material Command, Washington
G. Donahue, Defense Advanced Research Projects Agency, Arlington
J. Kestin, Brown U.
R. Y. Pei, Rand Corp., Washington
S. Sacks, MHD Program Office, U. S. Department of Energy (2)
P. S. Lykoudis, Purdue U. (2)
P. Gherson, Purdue U. (2)
R. E. Lynch, Purdue U. (2)

DOE-TIC (27)
Manager, Chicago Operations and Regional Office, DOE
Chief, Office of Patent Counsel, DOE-CORO
V. H. Hummel, DOE-CORO
F. Herbaty, DOE-CORO
R. Selby, DOE-CORO
President, Argonne Universities Association
AUA Review Committee for Components Technology:
   P. F. Cunniff, U. Maryland
   W. E. Kessler, Commonwealth Associates
   C. H. Kruger, Jr., Stanford U.
   N. J. Palladino, Pennsylvania State U.
   N. C. Rasmussen, Massachusetts Inst. Technology
   M. A. Schultz, Pennsylvania State U.
   A. Sesonske, Purdue U.
   H. Thielsch, ITT Grinnell Corp.
   Y. C. L. S. Wu, U. Tennessee Space Inst.
DOE-MHD Division, Washington:
   J. Epstein
   J. Hopenfeld
   A. Liccardi
   R. Lightner
   J. Lynch
   M. Mintz
   J. H. Morris (3)
   L. Raring
   G. Rudins
   R. Shanklin
   D. Shelor
   M. Sluyter
   L. Sullivan
K. Ellingsworth, Office of Naval Research, Arlington
J. P. Clement, Georgia Inst. Technology
C. Kolb, Aerodyne Research, Inc., Bedford, Mass.
R. F. Starr, Arnold Engineering Development Center, Arnold A.F. Station, Tenn.